2010

Silicon on insulator microdosimetry for radiation protection in mixed radiation fields for aviation and space dosimetry

Dale A. Prokopovich
University of Wollongong

Silicon on Insulator Microdosimetry for Radiation Protection in Mixed Radiation Fields for Aviation and Space Dosimetry

A thesis submitted in fulfilment of the requirements
for the award of the degree
Doctor of Philosophy

From
University of Wollongong
by

Dale A. Prokopovich,
BSc. (Phys., Honours class II Division 1)(UOW)
BCompSc. (UOW)

Department of Engineering Physics
2010

Certificate of Originality

I declare that the work contained in this thesis is original and has not been submitted previously at any other institution. The work contained within is original and has not been copied or sourced from the work of others unless duly and clearly referenced. The intellectual content is of the author and contribution from others has been for style and expression only.

(Signed).....

(Dale A. Prokopovich)

Acknowledgments

The author would like to acknowledge the support and guidance of my supervisor Prof. Anatoly Rosenfeld (UOW) who has been instrumental in the research direction undertaken and the quality of the scientific findings within.

Dr. Mark Reinhard (ANSTO) for his overwhelming support during the period of my PhD. and contribution to the resources required for this undertaking.

Dr. Iwan Cornelius (UOW) for his overwhelming support in teaching me GEANT4 and the overwhelming support in arranging for experimental beam time and funding to support the experimentation.

Adam Sarbutt and Mark Hurry (ANSTO) for their assistance in preparing and repairing equipment required for many of the experiments undertaken in this thesis.

Dr. Susanna Guatelli (ANSTO) for the many informative conversations on the internal workings of GEANT4.

Dr. Rainer Siegele (ANSTO) for his seeming never tiring help in running the ANTARES Heavy Ion Microprobe and extreme patience in training me for my accelerator licence to allow solo operation of ANTARES and heavy ion Microprobe.

Stuart Hankin (ANSTO) for access and advice on the ^{252}Cf source used in this thesis.

Dr. Markus Fuerstner, Eduard Feldbaumer, Helmut Vinke, Chris Theis and Stefan Roesler (CERN) for the time and assistance using the CERN-EU High Energy Reference Field (CERF) and the FLUKA simulation results for the facility.

Dr. Graeme C. Taylor from the National Physical Laboratory in the UK for allowing the use of the HAWK TEPC data. Alex Hands (QinetiQ) for comparing PIN diode results taken at the CERF facility.

Dr Alexander Prokofiev (TSL) for his assistance in the use and preparation of the Quasi-monoenegetic neutron source in The Svedberg Lab at Uppsala university.

I would also like to thank my parents Tony and Christine Prokopovich as well as my brother Zane for the years of love, support and encouragement during the long undertaking of this thesis. I would also like to thank my fiancée Kathleen Ryan for her love and encouragement, especially during the final stages of the thesis writing and submission when it would have been very easy to get derailed.

Preamble

All of the experimental planning, work, simulations, computer coding and data collection presented within this thesis was performed by myself, Dale Prokopovich, with the following assistance:

The PIN diode experimental data collected for chapters 6 and 7 was collected with the assistance of Dr. Iwan Cornelius with all of the data processing and analysis performed by myself.

The HAWK TEPC data presented in chapter 6 was collected and given to me by Dr. Graeme Taylor for comparison with the SOI microdosimeter data.

The battery powered preamplifier and shaping amplifier system along with the associated custom length cabling, used for the SOI microdosimeter data collection was constructed by myself, however the battery power supplies and battery powered tail pulse generator used to test and calibrate the systems in the field were constructed by Mark Hurry. Adam Sarbutt constructed some specialist cabling required and was able to provide parts and advice on the construction of specialist components.

Dr. Rainer Siegele provided the ANTARES accelerator operation and beam focusing required for the IBIC data collection. The raw IBIC data was converted to ASCII list mode data for further processing using a program written by Dr. Siegele.

Publications

Relevant published first author publications:

- **D. A. Prokopovich**, M. I. Reinhard, I.M. Cornelius and A. B. Rosenfeld, "GEANT4 simulation of the CERN-EU High Energy reference Field (CERF) Facility" *Rad. Prot. Dosim.*, Vol. 141, No. 2, pp. 106–113 (2010).

- **D.A. Prokopovich,** M.I. Reinhard, I.M. Cornelius and A.B. Rosenfeld, "SOI Microdosimetry for Mixed Field Radiation Protection," *Rad. Meas*., 43, pp 1054-1058 (2008)

Relevant recently submitted first author publications:

- **D.A. Prokopovich,** M.I. Reinhard, I.M. Cornelius and A.B. Rosenfeld, "Response of a PIN diode and SOI Microdosimeter to the TSL Quasi-monoenergetic Neutron Field" Submitted to *IEEE. Trans. Nuc. Sci*., (2010)

- **D.A. Prokopovich,** M.I. Reinhard, G.C. Taylor, A. Hands and A.B. Rosenfeld, "Comparison of SOI Microdosimeter and Tissue Equivalent Proportional Counter Measurements at the CERF Facility" Submitted to *IEEE. Trans. Nuc. Sci*., (2010)

Relevant published first author conference proceedings:

- **D.A. Prokopovich**, M.I. Reinhard, G.C. Taylor, A. Hands and A.B. Rosenfeld, "Comparison of SOI Microdosimeter and Tissue Equivalent Proportional counter Measurements at the CERF Facility," *IEEE Nuclear Science Symposium and Medical Imaging Conferenc*e (NSS-MIC) Dresden, Germany 26-30 October (2009).

- **D.A. Prokopovich**, I.M. Cornelius, M.I. Reinhard and A.B. Rosenfeld, "Response of a PIN diode and SOI microdosimeter to the TSL quasimonoenergetic neutron field," *IEEE Nuclear Science Symposium and Medical Imaging Conferenc*e (NSS-MIC) Dresden, Germany 19-25 October (2008).

- **D.A. Prokopovich**, I.M. Cornelius, M.I. Reinhard and A.B. Rosenfeld, "Simulation of SOI Microdosimetry in High Energy Neutron Dominated Fields", *IEEE Nuclear Science Symposium and Medical Imaging Conferenc*e (NSS-MIC) Dresden, Germany 19-25 October (2008).

- **D.A. Prokopovich**, I.M. Cornelius, M.I. Reinhard and A.B. Rosenfeld, "Response of a SOI Microdosimeter to the CERF Reference Facility for Aviation Dosimetry," *Nuclear Science Symposium and Medical Imaging Conference*, Honolulu, Hawaii, USA, ISBN: 978-1-4244-9023-5, 27 Oct. – 3 Nov. (2007).

Relevant first author conference presentations:

- **D.A. Prokopovich**, M.I. Reinhard, I.M. Cornelius, A.J. Wroe and A.B. Rosenfeld, " SOI Microdosimeter Measurements at the CERF Reference Facility for Aviation Dosimetry," *The Annual Australian Experimental High Energy Physics Meeting (AEHEP2007)*, Sydney, 3-5 Dec. (2007).

- **D.A. Prokopovich**, M.I. Reinhard, I.M. Cornelius, R. Siegele and A.B. Rosenfeld, "Development of an improved CdZnTe based Compton suppression spectrometer for medical and security applications," Oral presentation to *8th Expert Evaluation & Control of compound Semiconductor Materials & Technologies* (EXMATEC'06), Cadiz, SPAIN, 14-17 May (2006).

- **D.A. Prokopovich**, M.I. Reinhard, I. Cornelius, R. Siegele, A.B. Rosenfeld, "Development of improved CdZnTe instrumentation for medical and security applications," *Australian Experimental HEP Consortium (AEHEPC) Workshop*, Melbourne, AUSTRALIA, 12-14 December, 2005.

- **Dale Prokopovich**, Dimitri Alexiev, Stuart Thomson, Anatoly Rosenfeld, "Uniformity of Deep Level Traps in Single Crystal Cadmium Zinc Telluride", RTSD Workshop, Rome, October, 2004

Relevant co-author publications:

- W.H. Lim, A.L. Ziebell, I. Cornelius, M.I. Reinhard, **D.A. Prokopovich**, A.S. Dzurak and A.B. Rosenfeld, "Cylindrical Silicon-on-Insulator Microdosimeter: Design, Fabrication and TCAD Modelling," *IEEE Trans. on Nuc. Sci*., vol. 56, no. 2, pp. 424-428 (2009).

- S. Guatelli, M. I. Reinhard, B. Mascialino**, D. A. Prokopovich**, A. S. Dzurak, M. Zaider and A. B. Rosenfeld, "Tissue equivalence correction in silicon microdosimetry for proton characteristics of the LEO space environment," *IEEE Trans. on Nuc. Sci*., vol. 55, no. 6, pp. 3407-3413 (2008).

- A.L. Ziebell, W. H. Lim, M. I. Reinhard, I. Cornelius, **D.A. Prokopovich**, R. Siegele, A. S. Dzurak and A. B. Rosenfeld, "Cylindrical Silicon-on-Insulator Microdosimeter: Charge Collection Characteristics," *IEEE Trans. on Nuc. Sci*., vol. 55, no. 6, pp. 3414-3420 (2008).

- Rainer Siegele, Mark Reinhard, **Dale Prokopovich**, Mihail Ionescu, David D. Cohen, Anatoly B. Rosenfeld, Iwan M. Cornelius, Andrew Wroe, Michael L.F. Lerch, A. Fazzi, A. Pola, S. Agosteo, "Characterisation of a □E–E particle telescope using the ANSTO heavy ion microprobe", *Nuc. Inst. Meth. B,* 260, pp. 270–275 (2007)

- A.J., Wroe, A.B. Rosenfeld, **D.A. Prokopovich**, M. Reinhard, R. Schulte, I. Cornelius and V. Bashkirov, "Microdosimetry within Heterogenous Tissue-Equivalent Structures," *IEEE Trans. Nuc. Sci. 53, No. 6, Dec (2006)*

Table of Contents

1. Introduction

2. Literature Review
   - 2.1. Introduction to Aviation Dosimetry
   - 2.2. Radiation Dosimetry / Microdosimetry
   - 2.3. Radiation Test Fields
     - 2.3.1. Californium 252
     - 2.3.2. The CERN EU High Energy Reference Field (CERF) Facility
     - 2.3.3. The Svedberg Lab (TSL)
   - 2.4. Monte Carlo Simulation

3. Experimental Methods
   - 3.1. Experimental Equipment
     - 3.1.1. SOI Microdosimeter
     - 3.1.2. PIN Diode
     - 3.1.3. Portable Nucleonic System
     - 3.1.4. Neutron Detection
   - 3.2. GEANT4 Simulation
     - 3.2.1. Geometry
     - 3.2.2. Materials Definitions
   - 3.3. Physics processes used for particle transport
   - 3.4. Primary generator
   - 3.5. Scoring of simulation results
   - 3.6. Conversion to microdosimetric spectra

4. SOI Microdosimetry of ^{252}Cf for Radiation Protection
   - 4.1. Introduction to ^{252}Cf Radiation Protection and Dosimetry
   - 4.2. Measurements
   - 4.3. GEANT4 Simulation
   - 4.4. Results
   - 4.5. Discussion

5. Simulation of the CERN-EU High Energy Reference Field (CERF) Facility
   - 5.1. Introduction to the CERF Facility
   - 5.2. Objective of GEANT4 Simulation of the CERF facility
   - 5.3. Method
     - 5.3.1. Monte Carlo Simulation
     - 5.3.2. Part 1 Simulation - Copper target geometry and setup
     - 5.3.3. Part 2 simulation - Facility additional geometry and setup
   - 5.4. Results
     - 5.4.1. Part 1 - Target Simulation
     - 5.4.2. Part 2 - Facility Simulation
     - 5.4.3. Neutron spectra dependence on irradiation position
     - 5.4.4. Calculation of ambient dose equivalent
   - 5.5. GEANT4 Comparisons
     - 5.5.1. GEANT4 Irradiation Position Physics List comparison
     - 5.5.2. GEANT4/IAEA data comparison

5.5.3. GEANT4/FLUKA comparison
5.6. Discussion

6. Response of SOI Microdosimetry to the CERN-EU High Energy Reference Field
6.1. Introduction
6.2. Method
6.2.1. The Facility
6.2.2. Instrumentation
6.2.3. Experimental Setup
6.2.4. GEANT4 Simulation
6.3. Results
6.3.1. SOI Microdosimeter
6.3.2. PIN Diode
6.4. Discussion

7. Response of SOI Microdosimetry and Planar Photodiode to the TSL Quasi-Monoenergetic Neutron Field
7.1. Introduction
7.2. Experimental Methods
7.2.1. Experimental configuration
7.2.1.1. SOI Microdosimeter
7.2.1.2. Planar silicon diode
7.2.2. GEANT4 Simulated response to the TSL Quasimonoenergetic neutron field
7.2.2.1. SOI Microdosimeter Simulation
7.2.2.2. Planar silicon PIN diode Simulation
7.3. Results
7.3.1. Experimental Results
7.3.1.1. SOI Microdosimeter
7.3.1.2. Silicon PIN diode
7.3.2. GEANT4 Simulated Results
7.3.2.1.SOI Microdosimeter
7.3.2.2. Silicon PIN diode
7.4. Discussion

8. Ion Beam Induced Charge Collection Analysis of SOI Microdosimeters
8.1. Introduction
8.1.1. Introduction to Ion Beam Induced Charge Collection (IBIC)
8.2. Experimental Method
8.3. Results
8.3.1. IBIC Characterisation and radiation damage
8.3.2. Bias Dependence Results
8.3.3. Angular Dependence Results
8.4. Discussion

9. Discussion
9.1. Recommendations for future solid state Microdosimetry development
9.2. Suggestions for future solid state microdosimetric designs
9.3. Future semiconductor materials to consider for semiconductor Microdosimetry

10. References

11. Appendix
A 3.1 C++ code for the conversion of energy deposition spectra into microdosimetric spectra
A 5.1 GEANT4 tracking of a single neutron inelastic interaction.
A 5.2 The neutron particle spectra and conversion coefficient
A 5.3 Published ambient dose equivalent conversion coefficients
A 8.1 Code to convert the listmode IBIC output into spectra, Median, Mode and Mean energy maps

Abstract

Radiation protection is used for determining the doses received by persons from a variety of sources. The recommendations for external radiation protection were outlined in ICRP Publication 51and ICRP Publication 60.

There is a growing need to measure the doses received from extraterrestrial sources at high altitudes. In the European Union (EU), flight staff are already classified as radiation workers following the European Commission Council Directive 96/29/EURATOM of 13 May 1996 defining the need for the exposure of the airline crew to the elevated levels of radiation to be monitored.

The radiation exposure from a mixed source can be measured using a regional microdosimetric approach. The advantage of this approach is that *a priori* knowledge of the type of radiation is not required.

The microdosimetric approach studied in this thesis is a solid state approach to microdosimetry using a Silicon on Insulator (SOI) design. The SOI Microdosimeter is advantageous over conventional low pressure gas chamber microdosimetry in that it does not require a constant supply of tissue equivalent gas or high voltages to operate and is physically small in size.

The mixed radiation fields tested in this dissertation are mixed neutron gamma sources (^{252}Cf, PuBe), the CERN-EU High Energy Reference Facility (CERF) field and the quasi-monoenergetic neutron source at Uppsala University.

1. Introduction

This thesis aims to verify the use of Silicon On Insulator (SOI) microdosimetry for application in aviation and space radiation environments. This is an extremely challenging radiation field for dosimetry application due to the high energy mixed particle nature of the environment. Recent European Commission Council Directive 96/29/EURATOM of 13 May 1996 require the reclassification of aviation employees to become radiation workers and require dosimetric record keeping. Current dosimetry technologies are not designed with such high energy mixed radiation fields in mind.

SOI microdosimetry offers an alternative to conventional dosimetry that could operate under the radiation environments encountered at aviation altitudes. The SOI microdosimeter also offers the advantage of being small, lightweight and requiring minimal power to operate. These advantages make SOI microdosimetry attractive for aviation and space applications.

Testing of the SOI microdosimeter, in a similar radiation environment to those encountered in aviation, measurements were performed at various accelerator facilities to recreate similar radiation field to those encountered at high altitude. In order to explain and verify the experimentally obtained data the Monte Carlo toolkit GEANT4 was used to simulate each of the experimental results.

Each of the experimental chapters investigates SOI microdosimetry in radiation fields from a neutron source (Chapter 4) as well as at CERN (Chapters 5, 6) and TSL at Uppsala University (Chapter 7). The thesis also undertakes to examine the properties of the SOI microdosimeter and suggest improvements for future work (Chapter 8, 9).

2. Literature Review

2.1 Introduction to Aviation Dosimetry

Interest in the radiation dose at jet airliner aviation altitudes has increased in recent years due to the potential for occupational exposure of aircrew and frequent flyers. Within the European Union, flight crew are considered occupationally exposed persons with respect to radiation exposure (European Council Directive 96/29/EURATOM, 1996). Article 42 of 96/29/EURATOM requires assessment and record keeping of aircrew exposure as well as limiting exposure using administrative methods (adjustment of flight routes or roster of aircrew etc.). The airlines are also responsible under Article 42 to inform aircrew of the risks associated with ionising radiation exposure at aviation altitudes and to keep records of the integral dose to each occupationally exposed individual.

Several methods are available for use in determining the dose associated with various aviation flight paths. The exposure of commercial aviation routes is estimated using software packages such as AVIDOS (Latocha et al., 2009) and CARI6 (Federal Aviation Administration, 2004) to estimate the dose prior to flight and more accurately estimate the dose accumulated post flight via the flight logs to obtain flight time, altitude and latitude corrections. These packages use accumulated data from cosmic radiation experiments and simulations of the radiation fields at aviation altitudes which then use modifiers such as flight path latitude, altitude, solar activity cycle, etc.

The detectors currently used for aviation radiation dosimetry are conventional dosimeters such as ionization chambers, conventional radiation detectors such as scintillators or semiconductors and Thermo-Luminescent Dosimeters (TLDs).

TLDs are not linear in their response to various types of radiation fields. The operation of a TLD relies on charge carriers (normally electrons) being excited by incident radiation into long lived deep level trapping states in the crystal. The most

common TLD crystal types are calcium fluoride and lithium fluoride with magnesium or manganese introduced to create the long lived trapping states. The amount of trapped charges within the TLD is proportional to the radiation exposure received by the crystal. The TLD is read out by heating the crystal which liberates the trapped charges which then release an optical photon during relaxation back to the ground state. Inconsistencies in the readout of TLDs under various mechanical and optical treatments have been observed for low dose rate radiation fields (German et al., 1999).

TLDs are currently widely used for radiation protection monitoring of occupationally exposed personnel and patients undergoing radiotherapy. The use of TLDs in mixed radiation fields is normally limited to neutron and gamma types of exposure, gamma due to direct excitation of electrons and neutron indirectly via the $^{6}Li(n, \alpha)$ reaction. Mixed field dosimetry requires multiple TLDs of different composition (neutron sensitive and neutron insensitive) covered by layers of various materials (Teflon, aluminium, lead, etc.) to elicit a different response from the TLD. The response from the combination of TLDs is then used to determine the dose contribution from the various field components. The sensitivity of TLDs to charged particle radiation is dependent on a light conversion factor. This produces a different response from proton irradiation when compared to the equivalent dose of gamma rays. The light conversion factor varies with both the charged particle type and energy requiring the charged particle energy and type to be known to compensate for the non linearity. TLDs have been used for proton therapy applications where the beam energy is known (Zullo et al., 2010).

The use of TLDs for high energy mixed field radiation is limited due to the factors outlined in the previous paragraphs. The use of TLDs in these environments has been examined (Schöner et al., 1999) showing significant variation in response due the different Lineal Energy Transfer (LET) values. The high energy charged particles encountered at aviation altitudes would require significant amounts of shielding to moderate or shield the particles from the TLDs to allow for accurate determination of the dose from the various field components. The energy range and type of charged particles at aviation altitudes is also a concern due to the non-linear nature of the light

conversion factor with charged particle energy and type. TLDs also have a limitation for aviation dosimetry due to only giving an integral dose measurement and cannot give a real time warning for increases in dose rates or the position and duration of dose variations.

An ionisation chamber consists of either a high or low pressure gas supply for the detection of radiation. Radiation deposits energy creating ionisation tracks though the gas in the chamber. The ions and electrons in the gas are drawn to the high voltage electrodes where the charge is collected. This charge is proportional to the energy deposited by the radiation within the gas. High pressure gas chambers rely on the full energy of the radiation to be deposited within the gas volume. Low pressure Tissue Equivalent Proportional Counters (TEPCs) only requires a portion of the energy from the radiation traversing the gas volume (Knoll, 2000).

Examples of ionisation chambers are a TEPC which is filled with low pressure tissue equivalent gas (such as methane) or high pressure xenon filled ionisation chamber for spectroscopy. The high pressure xenon chambers have the inherent danger of high pressure and being explosive if the external pressure lowers (as may happen on an aircraft). Low pressure gas, as found in TEPC chambers, has the limitation of either requiring a vacuum pump and controlled bleed of gas to maintain pressure or a completely sealed leak proof chamber at very low pressures. Due to the requirements for high voltages, a pressure vessel and potentially a gas supply can make these systems undesirable in the controlled environment of an aircraft (Perez-Nunez et al., 2010).

All gas filled ionisation chambers suffer from effects due to mechanical vibrations. Vibrations oscillate the fine wire electrodes making up the collection anode and cathodes which has the effect of modulating the electric field within the chamber. Harsh vibrations or shocks, such as those experienced during commercial aviation turbulence or take off and landing, can also potentially break or short the electrode wires.

Further limitations of the approach from some of these methods are due to the type of high energy mixed field radiation environment encountered at aviation altitudes.

Primary cosmic radiation interactions with the atmosphere produce secondary particles via electromagnetic and hadronic cascades resulting in a complex mixed radiation field. The mixed radiation field from the cascade varies with both altitude and latitude due to variation in atmospheric density and the magnetic field of the Earth in addition to the other modifying factors stated above (Bartlett et al., 2004). The mixed radiation field encountered at aviation altitudes contains high energy neutrons, gamma rays and charged particles (Lindborg et al., 2004; Mukherjee et al., 2002).

Dosimetry in aviation applications is challenging due to the mixed particle nature of the radiation field. The response of some detectors to neutrons and high energy charged particles is not well defined. This is due to the possibility of the charged particle not depositing the full energy within the detector volume or the neutron cross section of the detector material creating an over or under response.

2.2 Radiation Dosimetry / Microdosimetry

The biological effect of radiation on living cells has been investigated from the first discovery of radiation by Wilhelm Röntgen in 1895. Several of the early researchers in radiation discovered that exposure to the "invisible radiation" would lead to erythema. The earliest systematic investigation of the biological effects originated from discussion between Nikola Tesla and Elihu Thomson of the Edison labs where Tesla did not believe that the erythema was caused by "Roentgen ray" (x-ray) exposure but rather was due to ozone and small quantities of "nitrous acid" generated by the radiation near the skin creating a chemical burn as published in *Electrical Review*, 30 November 1896. Thomson did not agree with this and thought that the erythema was caused directly by the "Roentgen ray" exposure. This led Thomson to expose his hand to x-rays with all of his hand except the distal portion of his little finger covered by lead. The damage to the uncovered portion of his finger illustrated the origin of the erythema was from the radiation and not ozone as Tesla surmised as published in *Electrical Engineer*, 24 Nov. 1896.

On the 12th of December 1896, Wolfram Fuchs made the following recommendations on the limitation of exposure to radiation in a journal called Western Electrician. Fuchs recommendations were as follows:

1. Make the exposure as short as possible.
2. Do not place the x-ray tube closer to the body than 12 inches (30 cm).
3. Rub the skin carefully with Vaseline and leave a layer on the part that shall be exposed.

These guidelines were the first recognised radiation protection guidelines published (Lindell, B., 1996). The guidelines follow the still current principles for limiting radiation exposure by time, distance and shielding. The effectiveness of Vaseline as an x-ray shield is very limited however the assumption of the time was that radiation effects of dermatitis and erythema were confined to the skin.

David Walsh observed deeper tissue effects from "Roentgen ray" exposure during skiagraphy. Prior to this it was "generally assumed" that exposure to x-rays would not lead to deep tissue damage of bones and other organs and that the effects were confined to the skin. David Walsh published his findings in 1897 (Walsh D., 1897), only two years after the discovery of x-rays by Wilhelm Röntgen. His writing showed examples of deep tissue effects noticed by other doctors, such as organ shrinkage and pain relief of cancer patients from high exposures of the affected areas. These effects could not be explained if the "Roentgen rays" were not responsible for deep tissue damage.

Henri Becquerel reported in 1896 his discovery of the effects from uranium salts has having similar characteristics as "Roentgen rays" (Allisy et al., 1996). Tissue damage from naturally occurring radiation sources was observed when in 1901 when a vial of the newly discovered radium he carried in his vest pocket left a sunburn like skin burn (erythema) (Encyclopædia Britannica, 2007). The first systematic investigation and documentation of human exposure to gamma radiation occurred when Pierre Curie placed some radium salts onto his arm for 10 hours and then over the next 52 days he studied the resultant wound in detail and postulated that the effects of radiation from radium could be used for the treatment of cancer (Fröman, 1996).

Dosimetry of radiation and the biological effects caused by the effects of different types of radiation have been intensely investigated since these discoveries of the harmful effects of ionising radiation. Ionisation chambers have been in use since shortly after the discovery of radiation to determine the strength of radiation exposure. The ionisation chamber has since been extensively used for various applications from particle fluence counting to tissue equivalent dosimetry.

Conventional dosimetry relies on measuring the energy deposited on a macroscopic scale. The unit of absorbed dose is the Gray (Gy) and is measured in units of joules per kilogram (J/kg).

$$D = \frac{E}{m} \tag{1.1}$$

where D is the dose, E is the energy deposited in Joules and m is the mass of material exposed.

This is useful for measuring the overall amount of radiation dose that a person is exposed to but is limited in the ability to determine the effect from different types of radiation. This is due to the differing ionisation and production of secondaries that can change the biological effect of the radiation being measured. Different types of radiation can produce different biological effects as highly ionising radiation can have a dense ionisation trail deltas (secondary electrons).

From the absorbed dose, the term dose equivalent can be determined. The dose equivalent uses a quality factor as outlined in ICRP Publication 60 to weight the different types of radiation based on the biological effect of the particle type and energy of the radiation. The dose equivalent H is given by:

$$H = DQ \tag{1.2}$$

where the absorbed dose is given by D and Q is a dimensionless number called the quality factor used to weight the biological effect of the radiation. H is defined in

units of Sieverts (Sv). Q depends on LET as given in Table 2.1 from ICRP Publication 60 (1991). A comparison between some of the quality factor definitions is shown in Figure 2.1.

LET in water (keV/μm)	**Q**
< 10	1
10-100	0.32*L*-2.2
> 100	300/√*LET*

Table 2.1. The ICRP Publication 60 definition of the quality factor Q.

The quality factor gives the weighting dependence on the energy transfer properties of the radiation. The drawback of this method is that the LET can be mathematically defined as a property of the radiation but it is not an easily measurable quantity.

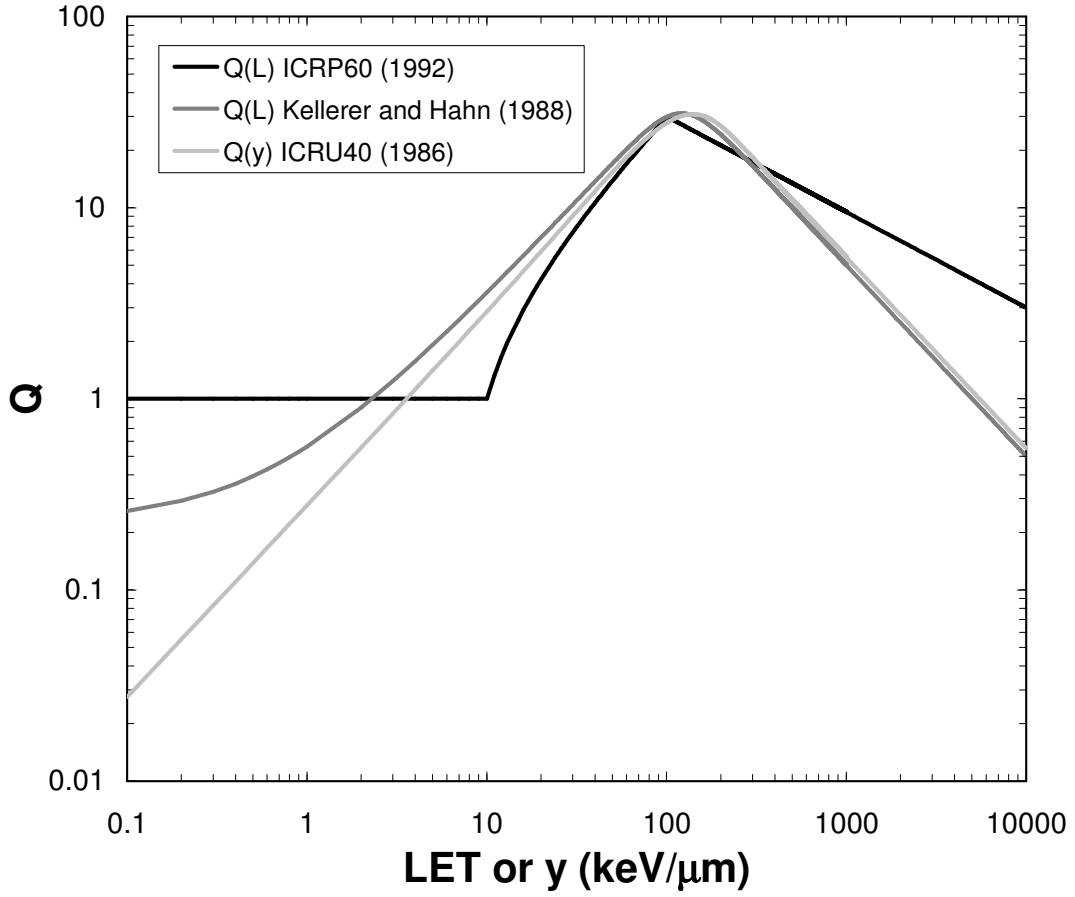

Figure 2.1. The quality factor Q as a function of LET as defined in ICRP Publication 60 and ICRU Publication 40. L in the legend refers to LET.

Publication 40 (1986) of the ICRU recommends a quality factor based on the lineal energy y, defined as

$$Q(y) = \frac{a_1}{y}\left[1 - \exp\left(-a_2 y^2 - a_3 y^3\right)\right] \qquad (1.3)$$

where $a_1 = 5510$ keV/μm

$a_2 = 5\text{x}10^{-5}$ μm^2/keV^2

$a_3 = 2\text{x}10^{-7}$ μm^3/keV^3

So y has units of keV/μm.

The advantage of using lineal energy deposition for the quality factor is that it is a directly measurable quantity unlike LET which is a property of the radiation; y is the lineal energy deposited in a 1 μm spherical region of tissue equivalent material.

The relationship between the lineal energy and LET is outlined by Kellerer and Hahn (1988) and shown in Figure 2.2.

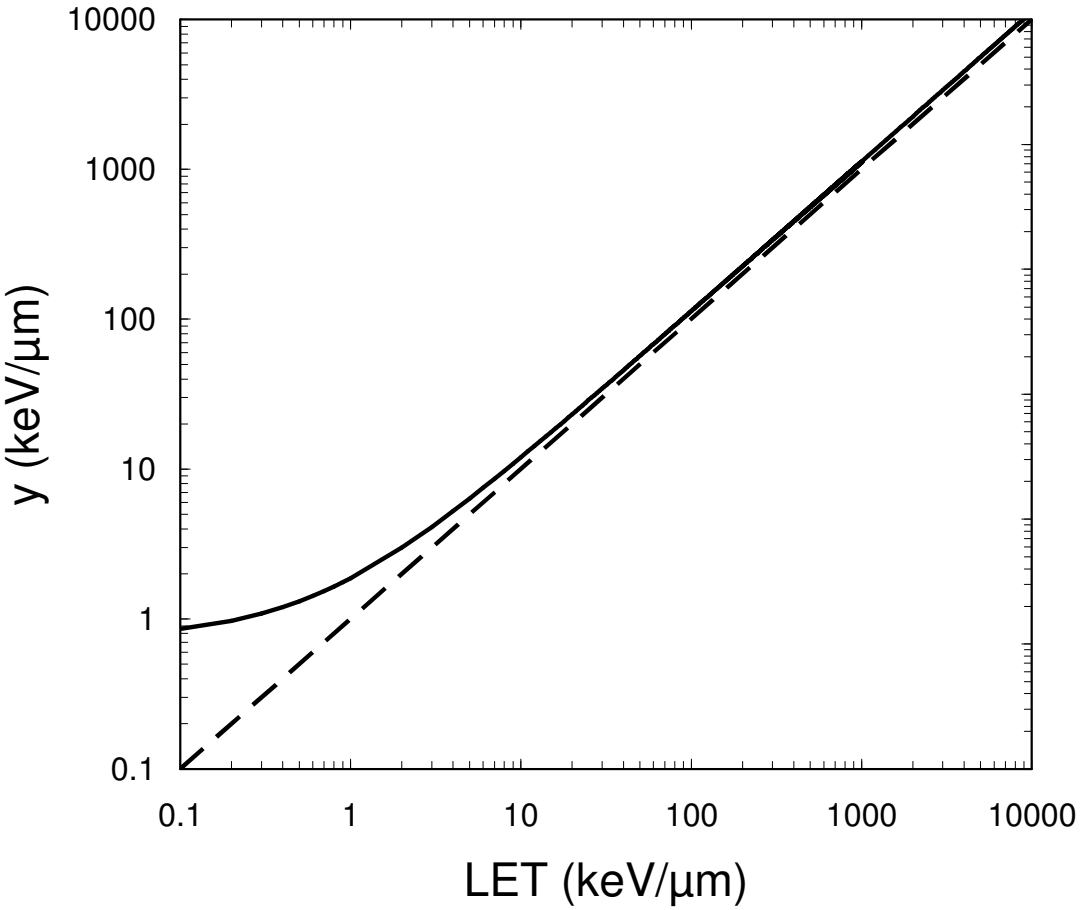

Figure 2.2. The quality relation between lineal energy and LET as used in quality factor calculations (Kellerer and Hahn, 1988); dashed line is for a 1:1 relation.

For the more penetrating types of radiation (gamma rays, neutron, and high energy charged particles), it is possible to estimate the dose from a given fluence of a type of radiation.

As can be seen from Figure 2.2, the relationship between lineal energy and LET is approximately linear except for values below a few keV/µm.

The recommendations of ICRP (ICRP Publication 60, 1991) is that the effects of Auger electrons emitted from atomic nuclei bound to DNA need to be determined using the techniques of microdosimetry or even nanodosimetry. It is not realistic to average the absorbed dose over the whole mass of the DNA as required for equivalent dose.

The field of microdosimetry was developed to understand the interactions of the various types of radiation on a cellular level. Early research in target theory showed that there is a requirement to have the size of the area of measurement to be comparable to the size of the cell under investigation. The earliest development of target theory (Dessauer et al., 1922; Crowther et al., 1924) identified the discrete energy transfer from individual ionisations. This work was limited in its capability to predict the damage due to a lack of information in the spatial distribution.

A substantial difference between conventional dosimetry and microdosimetry is the size of the volume used to measure the energy deposition from the radiation. The damage to a cell depends not just on the energy deposited on a macroscopic scale, as in conventional dosimetry, but on both the particle track structure and density as well as the charge and mass of the particle leaving the ionisation track.

The application of microdosimetry to radiation protection offers the capability to measure the equivalent dose for any arbitrary single or mixed radiation field. Steps to utilise a microdosimetric approach to real time dose equivalent assessment have been limited due to the unavailability of a portable instrument for this purpose.

The lineal energy is used in the regional microdosimetry approach (ICRU Report 36, 1983), in which energy deposition events from secondary charged particles are measured in a micron sized sensitive volume in terms of the lineal energy, y as given by:

$$y = \frac{\varepsilon}{\bar{l}} \tag{1.4}$$

where ε is the energy deposited in the volume by a single event and $\bar{l}$ is defined as the mean chord length in the volume of interest. Using this approach, the dose distribution can be determined using the relation:

$$d(y) = \frac{1}{\bar{y}_F} y f(y) dy \tag{1.5}$$

where $\overline{y_F}$ is the frequency-mean lineal energy and $f(y)$ is the lineal energy spectrum (Rossi and Zaider, 1996).

The frequency-mean lineal energy $\overline{y_F}$ and the dose-mean lineal energy $\overline{y_D}$ are given by (ICRP Publication 60, 1990):

$$\overline{y_F} = \int y f(y) dy \tag{1.6}$$

$$\overline{y_D} = \int y d(y) dy \tag{1.7}$$

For radiation protection applications, the dose equivalent *H* is given by:

$$H = \int Q(L) D(L) dL \tag{1.8}$$

where $Q(L)$ is the quality factor for tissue as defined in ICRP Publication 60 and *D(L)* is the dose distribution as a function of LET (ICRP Publication 51, 1987).

The quality factor in terms of either the LET (*L*) or lineal energy deposition (*y*) is related to the biological effectiveness of radiation in damaging or killing a living cell. The relationship to the absorbed dose is given as radiations with the same absorbed dose but different LET or lineal energy deposition can lead to a different biological effect.

The dose equivalent, *H*, can be given in terms of the lineal energy deposition (*y*) according to:

$$H = \int Q(y) y^2 f(y) d \log y \tag{1.9}$$

(ICRU Report 36, 1983; Rossi and Zaider, 1996) given that the relationship the transform the empirical function *Q(y)* to *Q(L)* is given by:

$$Q(L) = 0.3y\left[1 + \left(\frac{y}{137}\right)^5\right]^{-0.4} \quad (1.10)$$

Where:

$$y = \frac{9}{8}L + 0.75 \quad (1.11)$$

This gives y proportional to L following a linear relation (Brenner, 1989). This relation takes into account the dose contribution due to secondary delta rays but not straggling or nuclear spallation.

The difference between $Q(y)$ and $Q(L)$ is related to the spectrum of delta electrons which do not necessarily deposit all energy within the specified micron sized sensitive volume in regional microdosimetery. The $Q(y)$ for determination of the dose equivalent was introduced in ICRU Report 40 (1986). A small difference of approximately 5% is observed by using $Q(L)$ or $Q(y)$ in the above integral from other neutron dose equivalent measurements in proton therapy (Wroe et al, 2007).

For the investigations in this thesis, Silicon on Insulator (SOI) Microdosimetry was used to measure the microdosimetric qualities of various high energy neutron dominated fields. The SOI Microdosimeter consists of an array of micron sized cells fabricated on a semiconductor on insulator base (Rosenfeld A.B. et al., 1999).

The SOI Microdosimeter uses the regional microdosimetry approach. This is achieved by measuring the energy deposition from secondary charged particles in a cellular sized sensitive volume. SOI Microdosimeters have previously been successfully tested in a number of radiation fields including proton therapy, fast neutron therapy, boron neutron capture therapy (BNCT) (Bradley et al., 2001) and recently in the Space Heavy Ion Radiation field at the NASA Radiation Facility (Wroe et al., 2007).

The regional microdosimetry approach is advantageous as no prior knowledge of the type of radiation present is required. This is useful in situations where the radiation field is not clearly understood, difficult to measure or time varying. The radiation field encountered at high altitudes falls into all three categories due the high energy

particles and cascades composing the field, in addition to the variance due to effects of the solar cycle and flares modifying the field and the effect of altitude.

2.3 Radiation Test Fields

2.3.1 Californium 252

Californium 252 is a manufactured isotope which undergoes 96.9% alpha particle emission with the remaining 3.1% decay undergoing spontaneous fission. The spontaneous fission results in the emission of a neutron continuum with the peak neutron emission intensity at 1 MeV. The half-life of ^{252}Cf is 2.645 years, the primary alpha decay of ^{252}Cf decays into ^{248}Cm, another 91.61% pure alpha emitter with a 8.39% spontaneous fission component and a half life of 3.40 years, which then decays into ^{244}Pu another pure alpha emitter with a long half life (8.08×10^7 years) and a very small (0.121%) spontaneous fission component. The remnants of the spontaneous fission result in an increased gamma emission from the fission products (Asaro et al., 1955).

The strong neutron emission of ^{252}Cf has several medical applications for certain neutron cancer therapy treatments and industrial applications such as bore hole logging and prompt gamma neutron activation analysis, security applications and neutron radiography.

Radiation protection around these industrial applications as well as the dose from medical ^{252}Cf seeds for both patients and the medical staff handling and administering the therapy is very important. Conventional neutron dosimetry requires bulky hydrogenous material to thermalise high energy neutrons surrounding a thermal neutron detector. These detectors are not easily portable and can suffer from problems due to the neutron energy range for accurate dose determination. Due to reflections of surrounding materials, thermal neutrons that may interact within the human body may be shielded by the thick thermalising hydrogenous layer. These neutron dosimeters also need to be complemented with a gamma ray dosimeter to give the total dose in a mixed radiation field.

SOI Microdosimetry is extremely suited to these types of mixed fields as the type of radiation does not need to be known unlike for conventional dosimeters.

2.3.2 The CERN EU High Energy Reference Field (CERF) Facility

Within the European Union, flight crew are considered occupationally exposed persons with respect to radiation exposure (European Council Directive 96/29/EURATOM, 1996). Dosimetry in such radiation fields requires instrumentation to be calibrated in a characterised field with similar particle energy spectra. The CERN-EU High Energy Reference Field (CERF) (Mitaroff A. et al., 2002) facility located on the H6 beam line at the Prévessin site of CERN is designed for the purpose of testing radiation dosimeters in a neutron dominant field with similar characteristics to that encountered at aviation altitudes. This facility produces high energy neutron dominated mixed radiation field. In addition to the neutron and photon component, there is also a high energy charged particle component in the total radiation field (Mitaroff et al., 2002).

The field is created through the bombardment of a 50 cm long copper target with a mixed hadron beam of momentum 120 GeV/c comprised of 35% protons, 61% pions and 4% kaons. The total number of particles incident on the copper target are measured by an air filled Precision Ionisation Chamber (PIC). One PIC count corresponds to $2.2 \times 10^4 \pm 10\%$ primary hadrons incident on the copper target.

Irradiation positions are available on the side and top of the nominally 80 cm thick concrete shielding, the density of which is used to replicate density profile of the upper atmosphere (Bartlett et al., 2004). The CERF facility has a total of twenty irradiation positions, with four positions available at the side (CS1-4) and sixteen positions available on top (CT1-16). This allows for the calibration of dosimetry instrumentation for radiation protection applications in aviation as well as for other high energy physics facilities like the Large Hadron Collider (LHC).

2.3.3 The Svedberg Lab (TSL)

The Svedberg Lab (TSL) in Uppsala Sweden is an accelerator facility used for research, medical and industrial applications. The accelerator used for the TSL facility is the Gustaf Werner cyclotron (Reistad et al., 1993). This cyclotron is used to produce

positive ion beams for a variety of research and electronics testing applications. For protons the accelerator is capable of accelerating a high flux of protons, up to $6x10^{13}$ particles per second, with proton energies up to 180 MeV. The protons from the cyclotron can then be directed down any number of different beam lines depending on the usage such as proton therapy, biological irradiations, proton beams, quasimonoenergetic and recently "Atmosperic-like Neutrons from thIck TArget" (ANITA) spectral neutron beams and single event upset integrated circuit testing.

The TSL facility provides a quasimonoenergetic neutron field through the $^{7}Li(p, n)^{7}Be$ reaction (Prokofiev et al., 2006). The irradiation of this target with energetic protons produces a quasimonoenergetic neutron beam. Due to a magnet bending away any charged particles in the beam after the target the beam only consist of neutrons in the particle beam.

2.4 Monte Carlo Simulation

GEANT4 (GEometry ANd Tracking) (Agostinelli et al., 2003; Allison et al., 2006) is a Monte Carlo toolkit used to simulate the passage of radiation in matter. Monte Carlo works by using a random number generator to select between a set of probable outcomes during particle transport. The particle transport takes place in a series of discrete steps, where between each step the random number generated will select a process to apply to the particle (i.e. ionisation, scattering, decay, nuclear processes, etc.) or not applying any process and allow the particle to continue to the next step. Once a large number of these particle tracks or "histories" has been built up, a statistical representation of the particle behaviour can be inferred.

Construction of a geometry consisting of a sensitive volume and the surrounding geometry for scattering and secondary emission allows for an approximation of the experimental system. The energy deposition events from ionisation, recoils, scattering, nuclear processes etc. within the sensitive volume are accumulated and can give a detector response that can be compared to an experimental situation.

3. Experimental Methods

3.1 Experimental Equipment

The equipment used in the experimentation was designed to be portable and lightweight. This necessitated building custom equipment to perform the experimentation as standard Nuclear Instrumentation Module (NIM) rack nucleonic equipment is too bulky and heavy with significant power consumption requirements.

3.1.1 SOI Microdosimeter

The SOI (Silicon On Insulator) microdosimeter consists of an array of individual p-n junction "cells". Each of the square p-n junctions is either 10 μm x 10 μm or 100 μm x 100 μm and is fabricated on either a 2, 5 or 10 μm thick SOI wafer. The pitch of the array of cells is 30 μm in both lateral dimensions. The SOI microdosimeters are fabricated on a p-type SOI layer utilising a reverse biased n^+ junction and a p^+ common ohmic contact. The SOI microdosimeters were fabricated by Fujitsu Research Laboratories Ltd. in Japan. An outline of the 10 μm p-n junction SOI microdosimeter is shown in Figure 3.1.

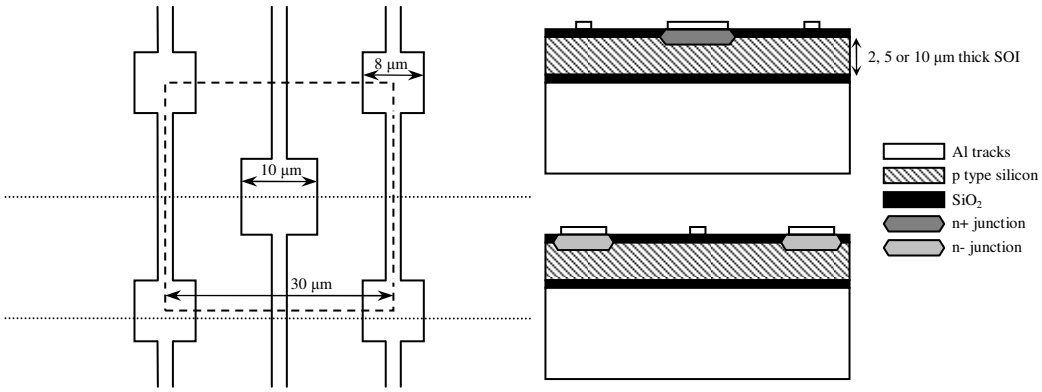

Fig 3.1. Left: A schematic of an SOI Microdosimeter unit cell (dashed square). The dotted lines show the position of the profile cuts on the right. Right: A profile cut (top) though the central n^+ region of the unit cell and a profile cut (bottom) though the shared p^+ contacts of a unit cell.

Each of these cells has individual charge collection from the sensitive volume under the n+ region. For readout, all cells are connected in parallel to increase the total overall sensitive area/volume. Only the 10 μm x 10 μm p-n junction devices were used in the experimental program outlined in this thesis.

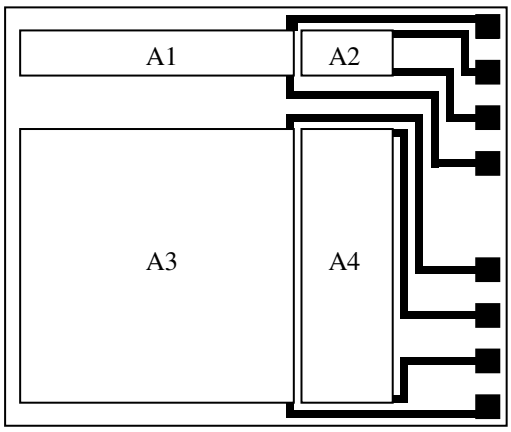

Fig 3.2. An outline of the SOI Microdosimeter arrays. Arrays A1 and A2 are 100 μm x 100 μm p-n junctions and Arrays A3 and A4 are 10 μm x 10 μm p-n junctions. The Array dimensions are: A1 3612 x 626 μm, A2 1214 x 626 μm, A3 3612 x 3626 μm, A4 1214 x 3626 μm

The arrays on a single SOI Microdosimeter chip are shown in Figure 3.2. Arrays A1 and A2 were considered unsuitable for the experimentation outlined in this thesis due to the large 100 μm x 100 μm p-n junctions compared to the SOI thickness. The large cells would result in large energy depositions from oblique charged particle strikes producing incorrect results for fields resulting in a large solid angle of charged particles. The fields tested within this thesis can potentially produce such particles from either the field itself at the CERF facility or from the angle of recoil protons.

A3 was only working for one of the available SOI Microdosimeters. The large area of 13 mm^2 produced a large capacitance which resulted in a noise level equivalent to 10 keV/μm. The large noise level in A3 resulted in the array being unusable for low lineal energy measurements. Low LET radiation such as that expected to be encountered at the CERF facility or from high energy recoil protons expected to be encountered at the TSL facility would be within the noise on A3.

Array A4 with either a 5 or 10 μm thick SOI was used in the experimentation. The 5 μm thick SOI was used for the majority of the measurements in this thesis with the exception of the CERF Facility measurements outlined in Chapter 6. The 10 μm thick SOI was used for the CERF facility measurements due to the low LET nature of the radiation environment being measured. The area of the A4 array is 4.4 mm^2 of 10 μm p-n junctions with an equivalent noise of 1-3 keV/μm depending on SOI thickness. This resulted in the best compromise between noise and sensitive area during low fluence acquisitions.

3.1.2 PIN Diode

The silicon PIN diodes used were model S3590-09 from Hamamatsu and were 300 μm thick planar windowless photodiodes with an active area of 1 cm^2. These photodiodes were chosen due to their implanted windowless front contact and good charge collection characteristics. The photodiodes were mounted on a white ceramic carrier. The white ceramic was the same type as that used for the SOI microdosimeter packaging and minimises the hydrogenous material that could cause scattering in a neutron field.

3.1.3 Portable Nucleonic System

The nucleonic system used to acquire data was designed to be portable for data acquisition at the location of the various neutron dominated fields. The SOI Microdosimeter data acquisition system consisted of:

- A regulated battery powered detector bias supply and a regulated power supply for the pre and shaping amplifier system.
- Charge and shaping amplifiers combined together in an electromagnetically shielded housing with the SOI Microdosimeter.
    - A CREMAT CR110 rev. 2 charge sensitive preamplifier mounted on a CR-150-AC evaluation board
    - A CREMAT CR200-1μs shaping amplifier mounted on a CR-160 evaluation board

- The output of the shaping amplifier was digitised using an AMPTEK Pocket MCA 8000A. This is capable of acquiring data for 24 hours on two AA sized batteries.
- A laptop computer running AMPTEK ADMCA software to interface with the AMPTEK Pocket MCA
- An in house built tail pulse generator was used to test and calibrate the system at the various experimental locations.

The overall system weighed approximately 1.5 kilograms without laptop computer or batteries in the power supply. Including batteries and laptop the entire system weighed approximately 5 kilograms. An image of the SOI Microdosimeter, preamplifier and shaping amplifier system can be seen in Figure 3.3.

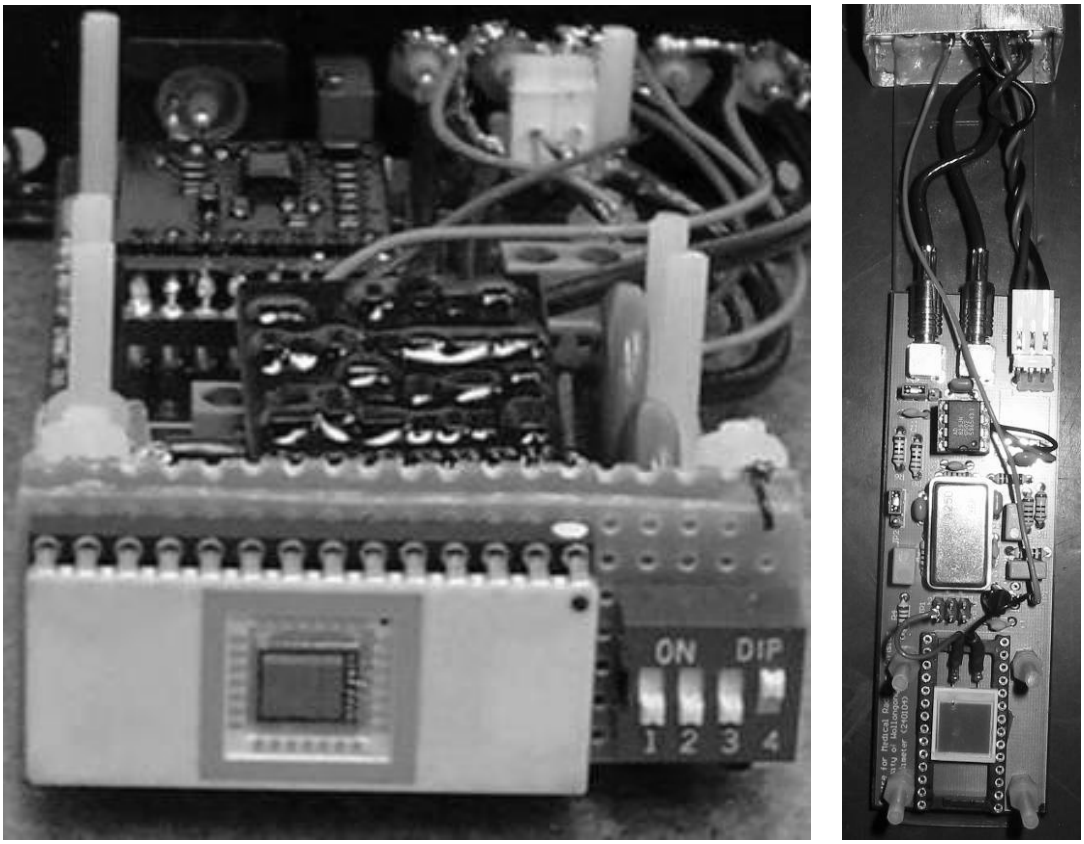

Fig 3.3. Left: A photo of the CREMAT based SOI Microdosimeter system. Right: A photo of the AMPTEK A250 based PIN photodiode system.

The system for data acquisition from the PIN diode used an AMPTEK A250 preamplifier coupled to the PIN diode as seen in the right hand image of Figure 3.3.

For the TSL measurements the output of the preamplifier was inverted using an AD 829 Inverting amplifier. The output of the AD 829 was then input into a set of AMPTEK A275 shaping amplifiers mounted on a PC 275 test board. The reason for inverting the preamplifier signal prior to shaping was that the AMPTEK A275 on the PC 275 test board shaping amplifier circuit can only take a positive input and the preamplifier signals from the PIN diode though the AMPTEK A250 were negative.

For all of the other experiments using the PIN diode, the shaping amplifier was changed to a CREMAT CR200-1μs shaping amplifier mounted on a CR-160 evaluation board. This allowed the negative preamplifier pulse from the AMPTEK A250 preamplifier to be directly input into the shaping amplifier without requiring the intermediate inverting amplifier. This both reduced power consumption and simplified the data acquisition system.

The bias supply for the PIN diode was created in-house to provide a very low ripple (<10 mV p-p ripple) -100 V from two 9 V batteries that is able to supply bias continuously for over 5 days. The battery supply for the amplifiers of both systems ran off eight C sized cells and was able to supply power for over 48 hours continuously.

3.1.4 Neutron Detection

The experimental configuration for neutron detection in mixed fields involved placing low density polyethylene (LDPE) in front of the detector surfaces to produce recoil protons. Measurements subtracting the response of the bare detector from the response of the detector covered with a LDPE converter give a response proportional to the fast neutron component of the fields.

The neutrons also create recoil nuclei from the silicon in and around the sensitive volume of the detectors. Above 1 MeV the cross section for the major isotope of silicon, ^{28}Si, increases above the cross section for hydrogen. This results in a significant contribution to the energy deposition spectrum due to silicon recoils for a thick silicon sensitive volume such as the PIN diode. For the thin sensitive volume for

the SOI Microdosimeter in comparison to the thickness of the LDPE layer, silicon recoils are not as significant.

Subtraction of the bare from the LDPE covered SOI microdosimeter measurements are not as effective due to the low probability for silicon recoils within such a relatively small sensitive volume resulting only in single high energy deposition events. A comparison between the bare and LDPE covered SOI Microdosimeter measurements allow for an estimation of the recoil proton contribution after rebinning onto a logarithmic scale. Subtracting the bare spectrum from the LDPE covered detector reduces the contribution from silicon recoils in the thick PIN diode detector.

3.2 GEANT4 Simulation

The GEANT4 (GEometry ANd Tracking) toolkit (Agostinelli S. et al., 2003) (Allison J. et al., 2006) is a Monte Carlo toolkit developed by CERN under the RD44 collaboration for high energy physics experiment simulation. The Monte Carlo method of simulation for radiation transport relies on the probability of certain interactions occurring during the radiation movement through matter. At each step there is a random number generated which depending upon the probability determined by the cross-section will decide on the type of interaction to take place.

GEANT4 uses the C++ object oriented programming language to develop an open source set of libraries that are then used to produce a program specific to the simulation requirements. The object oriented nature of GEANT4 allows for inheritance of pre-built objects with the user requirements implemented. These user requirements are the geometry, materials, primary generator, physics and action classes (from the overall run and events down to individual steps of the radiation through the simulation). Using this inheritance it is possible to build a simulation specifying and controlling precisely the simulation requirements.

For each of the experimental measurements performed in this thesis a complimentary set of GEANT4 simulations was undertaken to compare and contrast to the experiment. A good agreement with the experimental measurements then allows for further analysis of the results that would be difficult if not impossible with

experimental measurements. This allows characteristics such as the origin of the energy deposition event, the type of particle depositing the energy and the type of interaction that caused the energy deposition (i.e. electron ionisation, nuclear recoil, etc.)

3.2.1 Geometry

GEANT4 allows for the geometry to be constructed from three dimensional Constructive Solid Geometry (CSG) primitives (box, twisted box, cone, elliptical cone, tube, twisted tube, elliptical tube, ellipsoid, sphere, spherical shell, generic trapezoid, twisted trapezoid, wedge, parallelepiped, hyperbolic volume, tetrahedra, torus, polycon and polyhedra). CSG solids can have Boolean operators (union, subtraction and intersection) performed on them to allow for complex and flexible geometries to be constructed.

The geometry can also be constructed from Boundary REPresented Solids (BREPS) consisting of Bezier surfaces, B-Splines or NURBS (Non-Uniform-Rational-B-Splines) surfaces. These advanced geometries are mainly used with more geometrically complex or “organic” designs exported into GEANT4 from Computer Aided Design (CAD) programs. The drawback of BREPS is that the computation time is significantly increased due to the increasing number of polygons and complexity.

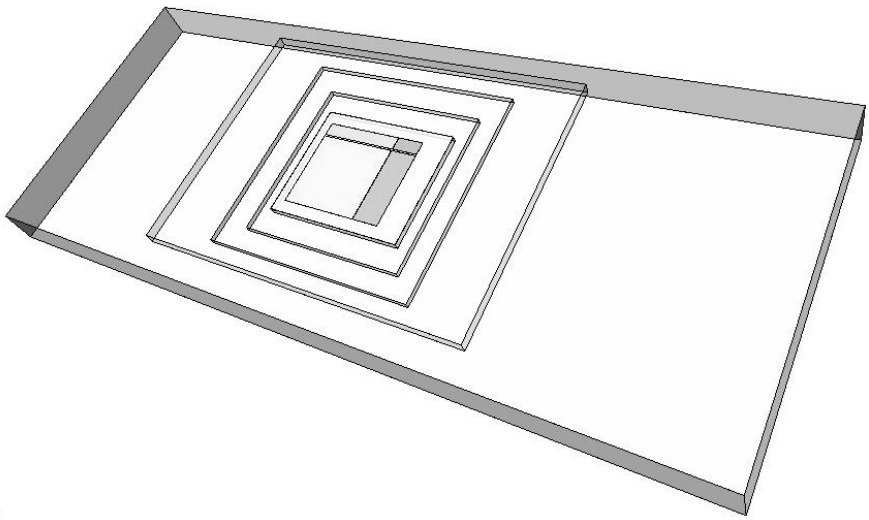

Fig 3.4. The geometry of the SOI Microdosimeter used in the GEANT4 simulations. The four arrays can be seen on the substrate with a transparent 0.5 mm LDPE converter on the surface of the ceramic chip carrier.

The geometry used for the SOI Microdosimeter is shown in Figure 3.4. The simulations in this research were constructed using CSG primitives and Boolean operations. The advantage of using CSG primitive is the ability to pass simple messenger class commands to the detector construction class to modify the geometry.

Using messenger classes in the GEANT4 simulations allowed for changes in the thickness of the sensitive volume and LDPE converter as well as being able to remove the LDPE converter altogether. The materials making up the geometry could also be changed in this way. The messenger class allowed for these modifications to be made between variations in the simulation without requiring manual editing of the code and recompiling.

3.2.2 Materials Definitions

The materials defined and associated with the geometric solids were optimised to include the isotopic compositions of the constituent materials used in the various detector structures. The isotopic abundance of the various materials was taken from the NIST Atomic Weights and Isotopic Compositions database (NIST, Physical Reference Data Website, accessed December 14th 2007) to allow for accurate neutron interactions in the sensitive volumes.

The SOI Microdosimeter geometry composition was defined using the composition as outlined in the thesis by Peter Bradley (Bradley, P. D., 2000) and surrounding ceramic chip packaging. This allowed accurate simulation of the response of the SOI Microdosimeter and included the accurate contribution of neutron inelastic events originating in the silicon of the device itself.

3.3 Physics processes used for particle transport

The physics used in the simulation was the QGSP_BIC_HP physics list packaged with the GEANT4 toolkit. This physics lists tracks all particles of interest in this simulation for the energy range of interest (neutrons down to thermal energies, alphas, protons, deuterons, tritons, generic ions from recoils and inelastic interactions and electromagnetic physics).

GEANT4 uses range cuts to determine the limit for tracking of the particles in a simulation. This is achieved through calculation of the minimum energy required in each material for a given step size. The minimum energy range cut for electromagnetic and hadronic interactions in the physics lists used was 990 eV.

For the simulations involving the SOI microdosimeter, the tracking cut for the simulation was set to a range of 1 μm to allow for a minimum of 5 steps in the sensitive volume of the SOI microdosimeter. The simulations involving the PIN diode used a 5 μm step size to allow 60 steps within the sensitive volume.

3.4 Primary generator

All of the GEANT4 simulations read in a sample spectrum which is used to produce a normalised cumulative probability distribution which is then used to sample the energy using a random number generator. This produces a radiation field with the same energy distribution as the sampled spectrum. The sampled spectra were taken from neutron reference spectra in IAEA TRS 403 and from simulated results that were used to produce the input reference spectra for other simulations.

The sampled beam was then randomly positioned within a specified field size to create a broad beam. This broad beam of sampled energies could then be angled to allow for variations of the beam relative to the detector. For the californium simulations the beam was randomly angled to accommodate the angular variation from the source to detector distance.

3.5 Scoring of simulation results

The energy deposition events in the simulation were scored by defining a sensitive volume within the detector geometry. Any radiation passing though the sensitive volume that also deposits energy within the sensitive is recorded. This is done on an event by event basis and is performed within the EventAction class. The following characteristics were recorded for each energy deposition:

- Total energy deposited within the volume for a given event
- The type(s) of radiation contributing to the energy deposition
- The contribution to the energy deposition from each type of radiation
- If required the momentum direction and position of the interaction can be stored

The energy deposition events were histogrammed to produce the energy deposition spectra. The ranges of the spectra were selected to cover the same energy range as the experimental measurements with same bin granularity (conversion gain). Events occurring outside of this energy range were still tallied and were used to determine whether an increase or decrease in gain was required in the experimental measurements.

3.6 Conversion to microdosimetric spectra

The energy deposition spectra produced by both the experimental measurements and the GEANT4 simulations were converted to microdosimetric spectra. The C++ code for the conversion of a calibrated energy deposition spectrum to a microdosimetric spectrum is given in Appendix A3.1.

The procedure followed by the code is the same as the procedures outlined in the literature review and outlined in ICRU report 36 and the book “Microdosimetry and Its Applications” (Rossi and Zaider, 1996). The graphic of microdosimetric data is performed as a plot of the lineal energy spectra as a function of $yd(y)$ versus y in keV/μm.

4. SOI Microdosimetry of Cf-252 for Radiation Protection

4.1 Introduction to ^{252}Cf Radiation Protection and Dosimetry

Radiation protection in mixed neutron/gamma fields produced by radioisotope sources is important in a number of industrial applications where such isotopes are utilised such as bore hole logging and prompt gamma neutron activation analysis, security applications and neutron radiography. Online monitoring of the dose equivalent received from a neutron/gamma source would permit real time dosimetry in industrial and medical applications.

A Silicon On Insulator (SOI) microdosimeter has been used to experimentally determine the microdosimetric spectra from a ^{252}Cf source which can be converted to dose equivalent. Simulations of the response of a SOI microdosimeter to the ^{252}Cf source using GEANT4 have also been performed.

The neutron (IAEA TRS 403, 2001) and gamma ray spectra are given in Figure 4.1. The neutron spectrum peaks at around 2 MeV and extends from approximately 10 keV up to approximately 10 MeV. Since its discovery, ^{252}Cf has been used as an important source of fast neutrons in various industries. Originally it was used as a seed source of neutrons which when thermalised were used to "kick-start" certain types of nuclear reactors. Currently the majority of ^{252}Cf sources are in use for various forms of neutron radiography, both fixed and portable, in a variety of industries (weapons components, turbine blades, high pressure pipes, etc.). Another application is for isotopic identification from Prompt Gamma Neutron Activation Analysis (PGNAA) used for bore hole logging, ore identification and explosive compound detection. It is also used for delayed neutron scanning of fuel rods to determine enrichment and uniformity as well as for the spent rods to determine the burn up (Martin, 2000). In medicine it has been trialled for use to treat various cancers by ^{252}Cf brachytherapy seed implantation of a tumour doped with elements with a high thermal neutron capture cross section, such as ^{10}B (Ghassoun et al., 2010).

Neutron sources made from ^{252}Cf are very strong neutron emitters for their size with 1 mg of ^{252}Cf emitting 2.3×10^9 neutrons/s with up to 10% of the dose coming from a

gamma component. For industrial neutron radiography and PGNAA sources there can be several mg of ^{252}Cf to allow for enough signal in the radiography equipment or PGNAA in a reasonable time.

The environment around the source can significantly affect the quality factor of the neutron radiation. The dose to personnel around these sources changes significantly with themalisation of the neutrons by surrounding hydrogenous material. Reflections from surrounding hydrogenous materials can increase the dose to personnel (Falcão et al., 2007) using a strong neutron source for applications such as bore hole logging. For a strong source surrounded by hydrogenous material the neutron field can be approximated to be isotropic. A microdosimetric approach for online personal dosimetry would be suitable for these conditions due to not requiring knowledge of the particle direction, type or energy.

In the current study the applicability of the SOI microdosimeter for radiation protection applications was trialled using mixed neutron-gamma fields produced by the radioisotope neutron source ^{252}Cf in free air geometry.

4.2 Measurements

The SOI microdosimeter consists of an array of p-n junction "cells" of micron size with individual charge collection. For readout all cells are connected in parallel to increase the total overall sensitive volume. Response of the SOI microdosimeter is related to charge collection in a single cell under the assumption that no pile up occurs due to multiple hits occurring within the array during the shaping time. This assumption is valid for all practical applications with the SOI microdosimeter arrays used. Data acquisition, including the SOI microdosimeter chip, was pocket sized and included an Amptek MCA 8000A.

The activity of the ^{252}Cf neutron source at the time of measurement was 34.5 MBq with a neutron emission rate of 4.0×10^6 n/s in 4π. The gamma component of the field produced by the source was measured with an HPGe detector and is shown in Figure 4.1. As the ^{252}Cf source ages, the gamma background changes and increases in activity due to the gamma emission from the multiple spontaneous fission products.

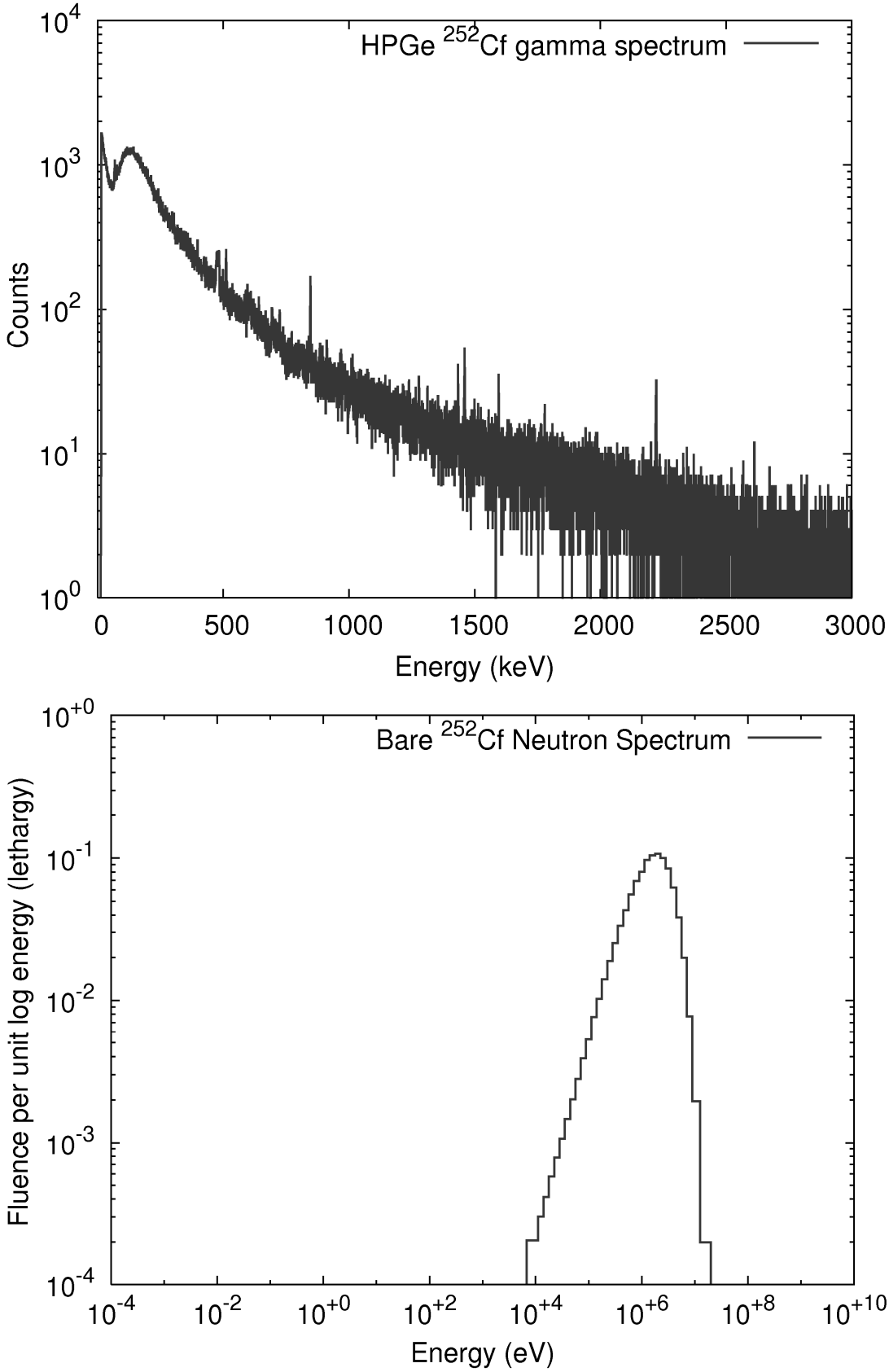

Fig 4.1. Top: The pulse height spectrum from a HPGe detector exposed to the ^{252}Cf source. Bottom: The neutron spectrum of ^{252}Cf source as given by IAEA TRS 403.

In order to produce recoil protons from the neutron field, which could readily be detected by the SOI microdosimeter, a Low Density PolyEthylene (LDPE) converter was placed in front of the device entry window. The LDPE converter used was obtained from Goodfellow Cambridge Ltd. UK. It was 0.5 mm thick with a density of 0.92 g/cm^{-3}.

Recoil protons produced within the LDPE with energies above 440 keV can be expected to deposit a portion of their energy within the sensitive volume of the SOI microdosimeter contributing to a lineal energy spectrum. For energies below 440 keV the recoil protons will be stopped within the LPDE layer failing to reach the sensitive volume of the SOI microdosimeter. A proton edge located at around 88 keV/μm for normally incident protons on the 5 μm thick SOI microdosimeter corresponding protons of 440 keV energy incident on the SOI device can be expected.

In addition to the proton recoil component there is also a contribution from silicon recoil events produced by direct interaction of neutrons with the silicon nuclei of the device via elastic and inelastic nuclear reactions.

The spectrum recorded from the SOI microdosimeter was converted into lineal energy spectra for analysis. These spectra were then used to obtain further understanding of the different components of the mixed radiation field as part of an evaluation as to the suitability of this technology for radiation protection applications involving neutron emitting radioisotopes.

4.3 GEANT4 Simulation

The experiments were simulated using the GEANT4 Simulation toolkit (Agostinelli et al., 2003; Allison et al., 2006).

The geometry was optimised to include the isotopic compositions of the constituent materials used in the SOI microdosimeter and surrounding chip mounted packaging. This allowed accurate simulation of the response of the SOI microdosimeter and included the contribution of neutron inelastic events originating in the silicon of the device itself.

The physics used in the simulation was the QGSP_BIC_HP physics list packaged with the GEANT4 toolkit. This physics list tracks all relevant particles in this investigation for the energy range of interest (neutrons down to thermal energies, alphas, protons, deuterons, tritons, generic ions from recoils and inelastic interactions and electromagnetic physics). For these simulations the range cut for the simulation was set to a range of 1 μm to allow for a minimum of 5 steps in the sensitive volume of the SOI microdosimeter. The simulation neutron source term was generated by sampling a reference neutron spectrum of the ^{252}Cf as shown in Figure 4.1. The source neutrons were approximated by a parallel beam normally incident on the SOI microdosimeter front face. The simulation was run using the same number of primary neutrons ($1.2x10^8$) incident on the area of the SOI microdosimeter as calculated for the experiment.

Due to simulation time constraints, a number of approximations were made to reduce the processing time. Firstly backscatter events from the surrounding environment were not considered. A possible source of errors with this approximation is the slight angular variations of incident protons due to the presence of a finite sized source in close proximity to the device (10 cm distance from source to SOI microdosimeter). Backscatter events would lead to a slight increase in the neutron fluence passing through the sensitive volume of the SOI microdosimeter without passing though the LDPE converter. These backscattered neutrons from the environment will have a very low probability of interacting directly in the SOI microdosimeter sensitive volume and will not significantly contribute due to the lineal energy spectrum in comparison to the interactions from the primary source neutrons.

Secondly source encapsulation consisting of a thin stainless steel capsule was neglected. A simulation was undertaken to investigate the source encapsulation on the neutron spectrum and was shown to have a negligible effect on the emitted neutron spectrum from the source.

The energy deposition events were log binned and converted to lineal energy spectra using knowledge of the average chord length of the SOI microdosimeter cells.

4.4 Results

The microdosimetric spectra obtained from the SOI microdosimeter in free air geometry with and without a 0.5 mm LDPE neutron converter are shown in Figure 4.2. Components of the spectra attributable to gamma rays, protons, neutron inelastic interaction products and neutron elastic silicon recoils are shown.

The maximum neutron energy expected from a ^{252}Cf source is approximately 10 MeV. Using the equation to determine the energy for a recoil nucleus

$$E_R = \frac{4A}{(1+A)^2}(\cos^2\theta)E_n \qquad (4.1)$$

where E_R is the energy of the elastically recoiled nucleus, E_n is the energy of the incoming nucleus, A is the atomic number and θ is the direction of the recoil nucleus relative to the direction of the incoming neutron. From Equation 4.1 the corresponding maximum silicon recoil energy is 1.33 MeV (determined for A = 28 and using θ=0 to give $E_{MaxRecoil} = 0.133\ E_{neutron}$) which corresponds to an event with a lineal energy in a 5 µm chord length SOI microdosimeter of approximately 266 keV/µm. The silicon recoil energy for the average neutron energy of 1 MeV corresponds to an event with a lineal energy of approximately 26.6 keV/µm. The silicon ion range of this energy Si ion is much less than the dimensions of the device sensitive volume meaning all energy is deposited within the device.

For the case of the bare microdosimeter, the contribution from the silicon recoils and inelastic neutron reaction products can be seen as the component of the spectrum above 15 keV/µm. The gamma ray component is associated with lineal energy events below 15 keV/µm. The noise threshold of the SOI microdosimeter limited the microdosimetric spectrum to above 6 keV/µm therefore only part of the gamma ray component of the microdosimetric spectrum is observable.

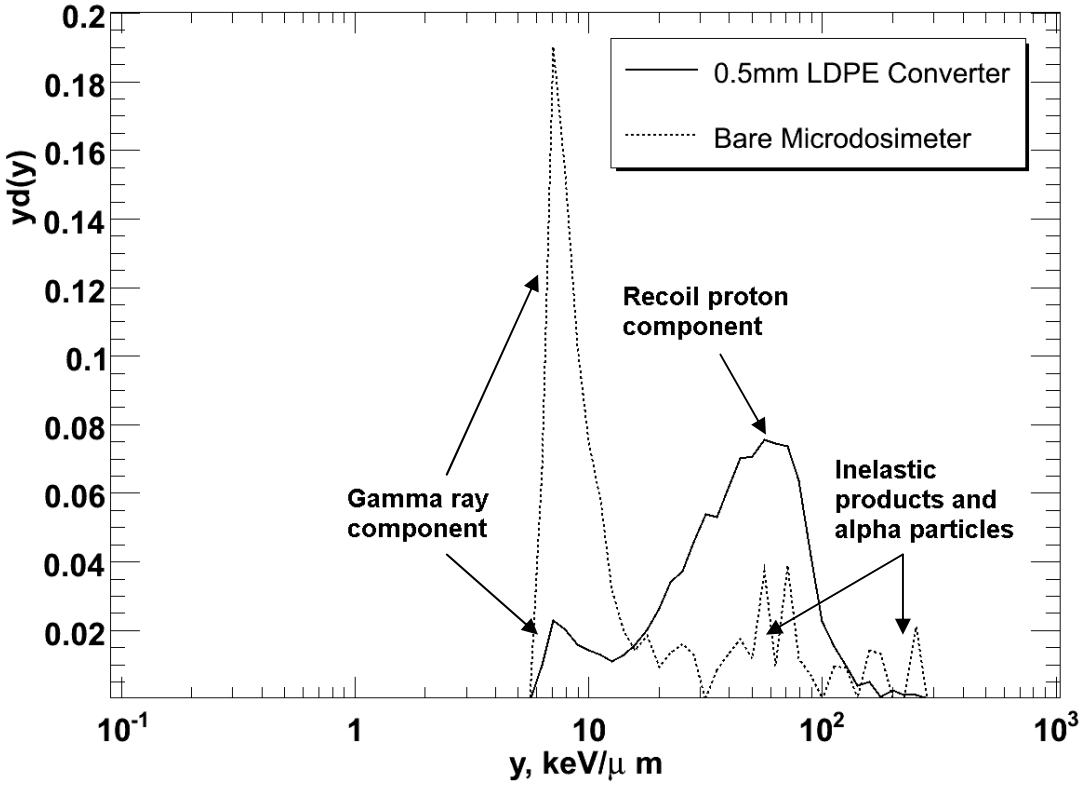

Fig 4.2. Normalised microdosimetric spectra obtained using a 5µm SOI microdosimeter. The different components of the field with the LDPE can be seen: below 15 keV/µm is the gamma ray component; between 15-100 keV/µm is primarily recoil protons; and above 100 keV/µm is the inelastic reaction and alpha particle contribution. Note: The gamma ray component of the two spectra is the same but appear different due to the integral of the spectra being normalised to 1.

To understand the contribution of the gamma component of the field to the microdosimetric spectra, a 6.4 mm lead plate was placed in front of the SOI microdosimeter to attenuate the gamma component from the source and surrounds without significant attenuation of the neutron component of the field. The thickness of the lead plate was several half value layers for the average gamma ray energy of 177 keV (6.4 mm of lead corresponds to approximately a single half value layer for 750 keV gammas) (Berger et al., 2010).

The microdosimetric spectrum for this situation can be seen in Figure 4.3.

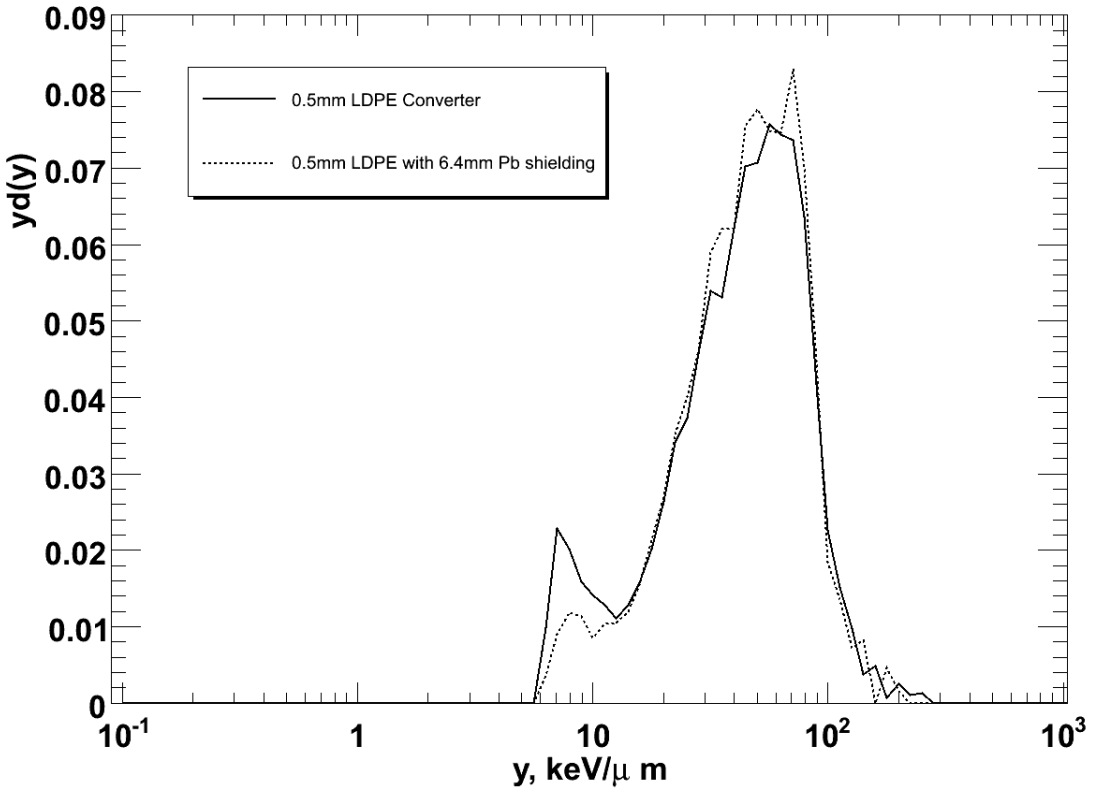

Fig 4.3. Microdosimetric spectra obtained using a 5 µm SOI microdosimeter with a 0.5 mm thick LDPE converter. The difference between the spectra is seen in the gamma ray component below 15 keV/µm. Both spectra were normalized to unity.

A reduction of events with lineal energies below 20 keV/µm was observed for the lead shielded case when compared to the unshielded case. Gamma rays directly from the source and gamma rays produced via neutron inelastic reactions with the source container were attenuated in the lead and a reduction in the spectrum can be seen in Figure 4.3. It is possible that some of the gamma ray component observed in the microdosimetric spectrum originates from neutron interactions in the lead as well as the small amount of gamma rays penetrating the lead from the source.

Subtraction of the bare SOI microdosimeter spectrum from the spectrum of the SOI microdosimeter with the LDPE converter provides a spectrum made up of predominantly recoil proton events. The normalised microdosimetric spectrum for this situation compared to the spectrum without subtraction is shown in Figure 4.4.

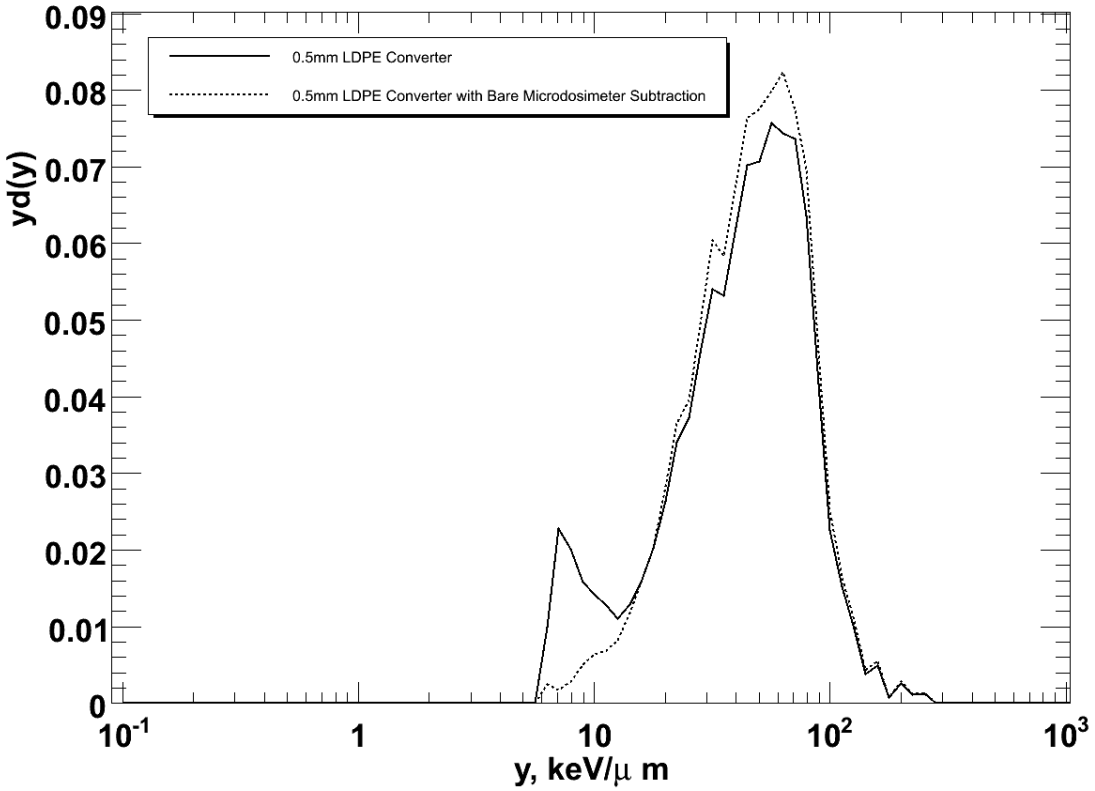

Fig 4.4. Microdosimetric spectra obtained using a 5 μm SOI microdosimeter with a 0.5 mm thick LDPE converter and the same spectrum with the bare SOI microdosimeter results subtracted. Both spectra were normalized to unity.

The subtraction removes the gamma interaction component associated with direct gamma-ray interactions within the sensitive volume as well as the inelastic silicon reaction products associated with direct neutron interactions within the silicon based sensitive volume. This gives the microdosimetric spectrum of the products from the LDPE only.

From the Spectra in Figure 4.4, removal of the gamma contribution below 15 keV/μm is observed. The removal of this component from the spectrum shows that the majority of the gamma component is due mainly to Compton interactions of gamma rays with the silicon sensitive volume. This indicates that interactions of the gamma rays in the LDPE are not contributing to the microdosimetric spectra. The ratio of the mass energy-absorption coefficient $\left(\frac{\mu_{en}}{\rho}\right)$ for silicon to polyethylene, at energies between approximately 200 keV and 5 MeV, is approximately 0.90 ± 0.08 (NIST). The absence of LDPE build-up does not produce a large difference in the deposited spectra from secondary electrons. The small ratio of coefficients will not significantly influence the

gamma component of the microdosimetric spectrum based on the dose equivalent for low LET radiation.

The contribution from inelastic neutron reaction products due to neutron interactions with the silicon of the SOI microdosimeter is negligible within the 5 μm thick sensitive volume. This would not be the case in a thicker silicon sensitive region such as that of a typical photodiode. Simulation of the SOI microdosimeter both with and without the LDPE converter is shown in Figure 4.5. The distribution of the lineal energy depositions due to the silicon recoils in the sensitive volume is centred at approximately 20 keV/μm. This contribution is very minimal when compared to the contribution from recoil protons and silicon recoils also shown in Figure 4.5.

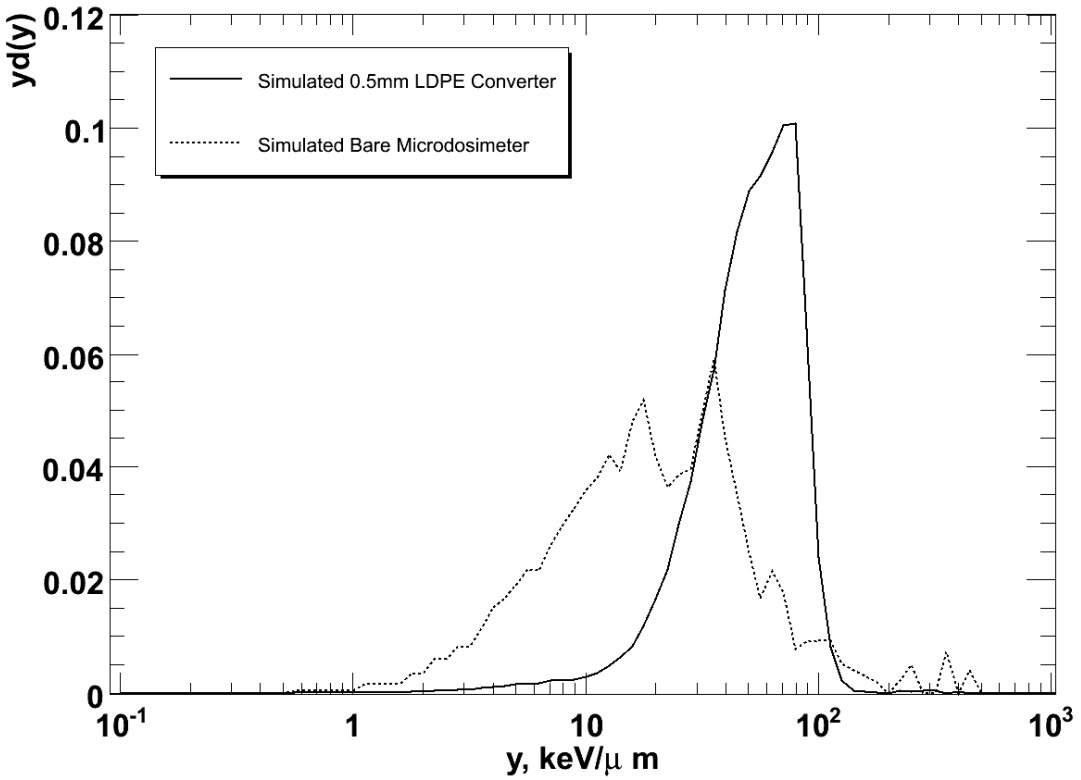

Fig 4.5. GEANT4 simulation results of the SOI microdosimeter. The simulation incorporated the gamma component of the source. Both spectra were normalized to unity.

The results from the GEANT4 simulation agree well with the experimental results given the approximations made in the simulation. The comparison between the

GEANT4 simulations of the 0.5 mm LDPE converter, with the simulated bare device subtracted, compares well with the experimental results for the same situations.

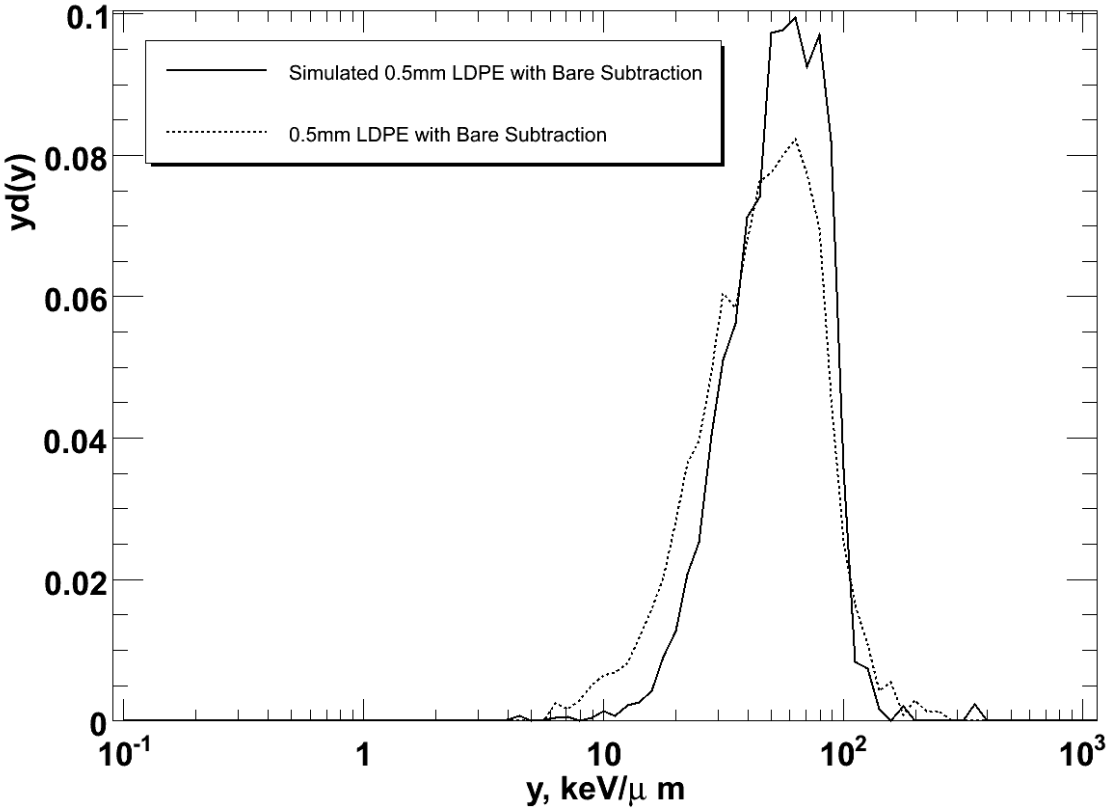

Fig 4.6. Comparison between the experimental and GEANT4 simulation proton recoil results of the SOI microdosimeter with the bare component subtracted. Both spectra were normalized to unity.

The difference between the spectra in Figure 4.6 can be attributed to ambient scattered neutrons from nearby materials. The spectrum used for the simulation was an idealised neutron spectrum from a bare ^{252}Cf metal without any moderation or scattering obtained from IAEA TRS 403. By comparison, the experimental conditions would have been subject to attenuation of low energy neutrons by the container wall and possibly contributions from scattered neutrons from the concrete floor. The increase in the lower energy neutron component of the source spectrum in the experimental situation will increase the relative contribution of low LET events observed.

The SOI microdosimeter data is also in good agreement with previously published ^{252}Cf data taken with a Tissue Equivalent Proportional Counter (TEPC) (Dicello J.F. et al.,

1972) and a TEPC based on a Gas Electron Multiplier (GEM) (Farahmand M. et al., 2004) (see Figure 4.7).

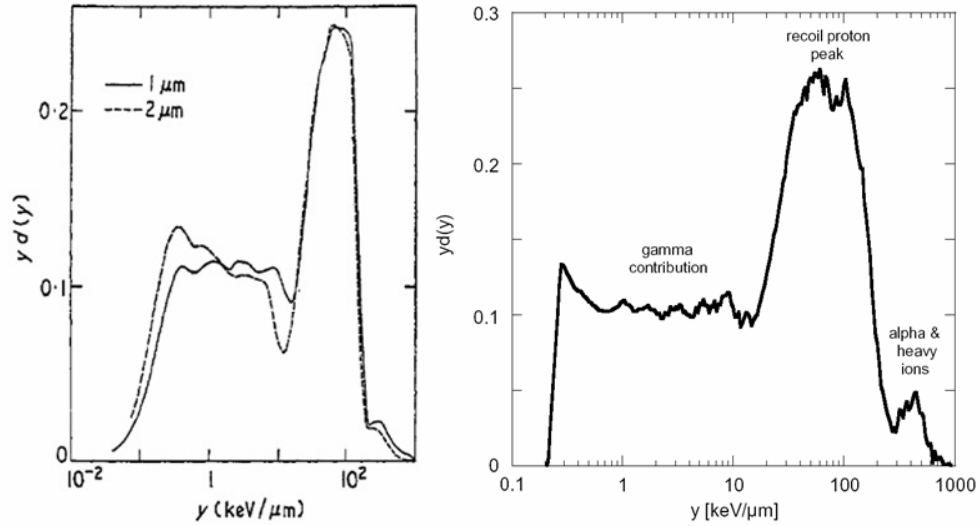

Fig 4.7. Published microdosimetric spectra of a ^{252}Cf source. Left: conventional TEPC taken from J. F. Dicello et al. Phys. Med. Biol., 1972, Vol. 17, No. 3, 345-355. Right: TEPC measurement with a TEPC based on a GEM taken from M. Farahmand et al. Rad. Prot. Dosim., 2004, Vol. 110, No 1-4, 839-843.

The SOI Microdosimeter has also been previously tested in a Fast Neutron Therapy Field and is in good agreement with these measurements (Bradley et al. 2001).

4.5 Discussion

The SOI microdosimeter response to a ^{252}Cf source was shown to be in reasonably good agreement with the experimentally determined microdosimetric spectra obtained using other methods (Dicello et al., 1972 and Farahmand et al., 2004).

Due to the thin 5 μm width of the sensitive volume of the SOI microdosimeter, the contribution to the spectrum from inelastic neutron interactions with silicon nuclei is small in comparison to thicker (350 um) P-I-N silicon photodiodes with a LDPE converter. The contribution from the neutron inelastic events in the silicon sensitive volume, being small in comparison to events from the recoil protons, is a significant advantage for radiation protection applications.

The subtraction of the bare SOI microdosimeter contribution from the spectrum for 0.5 mm LDPE shows that the measured gamma contribution is mostly due to Compton interactions in the silicon of the detector and not from the LDPE converter.

Taking into account that the efficiency of the converter is of the order of 10^{-3}, the small active area of the SOI microdosimeter (2.262 mm^2) is a limiting factor for real time dosimetry in low dose rate neutron field in radiation protection applications. However, a stacked design of SOI microdosimeters with an array area of 1 cm^2 each, which is currently under development, is designed to address this issue.

The signal to noise ratio of the SOI microdosimeter together with the signal processing electronics is a limiting factor for observing low LET events. However, this is currently being addressed in the next generation SOI microdosimeter with internal amplification of deposited charge within the sensitive volume (Ziebell et. al, 2007).

5. Simulation of the CERN-EU High Energy Reference Field (CERF) Facility

5.1 Introduction to the CERF Facility

The CERN-EU High Energy Reference Field (CERF) (Mitaroff et al., 2002), located at the Prévessin site of CERN, is used in the calibration and characterisation of active and passive dosimeters for space and aviation applications. The facility produces a mixed radiation field dominated by neutrons which mimics the radiation field found at jet airliner cruising altitudes.

The field is produced via the irradiation of a thick copper target by a 120 GeV/c positive hadron beam. The primary radiation emitted from the target passes through a nominally 80 cm thick concrete layer adjacent to and on top of the target. The effect of the concrete results in energy moderation, secondary particle production and particle attenuation to produce a radiation field adjacent to the concrete layer. The characteristics of this radiation field are relevant to aviation dosimetry. The neutron component of the field has been previously shown (Mitaroff et al., 2002) to be similar for dosimetry applications to the types of neutron dominated fields encountered at aviation altitude. Different positions surrounding the concrete layer provide stable fields with respect to the characteristic particle energy fluence for dosimeter testing. The irradiation positions at the CERF facility are divided up into positions on the side and top of the concrete shielding. Four irradiation positions are available at the side concrete shield (CS1-4) and sixteen are available on the top (CT1-16). Field variations at each position vary slightly depending on both the angular distribution of the particles created from the target as well as the variation in the thickness of the concrete due to the chord created by the angle of the irradiation position relative to the copper target. Due to the angle subtended by the irradiation positions, the relative thickness of the concrete varies from approximately 80 cm, for positions perpendicular to the target, to approximately 120 cm for the furthest positions.

This field has previously been modelled via the FLUKA Monte Carlo simulation package with the equivalent dose per primary particle on target determined from the neutron spectra (Theis et al., 2005). The values obtained are used to calibrate neutron

dosimeters for aviation applications. The facility dosimeter calibration is made under the assumption that the calibration field is typical of the radiation field for aviation applications. No account is taken for wide variations in the field characteristics associated with different altitudes and latitudes.

5.2 Objective of GEANT4 Simulation of the CERF facility

Experimental observations of the field at the CERF facility with silicon detectors by this author (see Chapter 6) indicated that the field contained a significant component of charged particles not recognised in the facility description (Mitaroff et al., 2002). The additional charged particle component may potentially contribute significantly to the actual dose equivalent at different irradiation positions within the facility not currently accounted for in the existing calibration factors. This can lead to errors in calibration depending on the actual magnitude of the neglected charged particle component and the sensitivity of the particular instrumentation to the high energy charged particle components.

In order to improve the understanding of the CERF field and contribute to improved calibration factors it was identified as important to carry out further studies to quantify the charged particle component and to understand its impact on particle dosimetry instrumentation.

5.3 Method

5.3.1 Monte Carlo Simulation

GEANT4 (Agostinelli et al., 2003) was used to model and simulate the CERF facility. The use of GEANT4 was chosen to complement published past studies concerning the CERF facility obtained using FLUKA (Mitaroff et al., 2002). Simulations were performed to determine the particle energy fluence of all field components at each of the 20 designated irradiation positions at the CERF facility. Another important objective was to determine the equivalent dose rate at each of the irradiation positions for each of the separate components of the mixed field.

The version of GEANT4 used for this simulation was GEANT4.8.2.p01 with both the QGSP_BIC_HP and QGSP_BERT_HP physics lists. These physics lists were chosen on the basis of being most suited for the particles and energy range to be covered (GEANT4 Reference Physics Lists, http://geant4.web.cern.ch/geant4/support/proc_mod_catalog/physics_lists/referencePL.shtml). The Binary Cascade and Bertini Cascade contained within these physics lists were both considered suitable for this application and were compared to published experimental data. GEANT4 refers to all high energy photon radiation, regardless of origin (i.e. X-rays, fluorescence, bremsstrahlung, high energy particle decay, etc.) as "gammas".

The simulation was divided into two parts. In part 1, the primary mixed hadron beam impinging on the copper target was simulated. The radiation field components emerging from the target were recorded to investigate the primary target radiation field. In part 2, the primary radiation field from the target was transported through the concrete of the facility to determine the components of radiation field at each of the 20 designated irradiation positions. This was done to illustrate the differences between the field produced by the target and the final field at the irradiation positions.

5.3.2 Part 1 Simulation - Copper target geometry and setup

The simulation geometry consisted of a copper target of 50 cm length and 7 cm diameter. The mixed positive hadron beam consisted of 61% positive pions, 35% protons and 4% positive kaons.

In routine operations at CERF, the fluence of the primary hadron beam is monitored using a free air precision ionisation chamber (PIC) in terms of particle count. A single PIC count corresponds to $2.2 \times 10^4 \pm 10$ % primary particles impinging on the target. PIC counts are used as a reference when discussing the radiation field intensity and dose at the CERF facility. This is preferable to other approaches due to the pulsed nature of the primary beam and the total number of particles that can be counted. The Super Proton Synchrotron (SPS) has a supercycle of 42.0 seconds with a spill of 14.4 seconds into the north area beamline, where the CERF facility is located. The average number of PIC counts per spill for measurements can be set using apertures. All

measurements related to the beam are recorded in PIC counts and the simulation results are similarly normalised to PIC counts for comparison purposes.

The target material was created using the NIST Physical Reference Data, Atomic Weights and Isotopic Compositions (NIST, Physical Reference Data Website, accessed December 14th 2007) database for the isotopic definition of natural abundance copper.

The primary beam was modelled as having a radially symmetric Gaussian fluence distribution impinging the end of the target and centred at the copper target cylinder axis. The copper target diameter was within three standard deviations of the beam profile. The target simulation scoring was performed by enveloping the target cylinder in a micron thick scoring volume (with material composition of air) which scored any particles leaving the copper cylinder. The particles were killed upon leaving the copper cylinder and entering the scoring volume in order to prevent double tallying of particles travelling along the scoring volume or backscattered into the scoring volume.

Tallying of the particles produced by the target was achieved by recording the type and energy of the particles. The results were histogrammed for each particle type using logarithmic binning over an energy range of 1 meV to 1 TeV to ensure all particles were completely tallied. Any particles that entered the scoring volume with an energy outside of this established range were recorded and counted in an additional bin to ensure that any such particles were not ignored by the simulation. During the investigation no particles were observed outside of the binning energy range.

5.3.3 Part 2 simulation - Facility additional geometry and setup

The second simulation involved transporting this secondary radiation field through the concrete layer at both the top and side positions relative to the target. The geometry and composition of the top and side walls were nominally 80 cm thick concrete for the facility. The target and concrete shielding materials were created using the NIST Physical Reference Data, Atomic Weights and Isotopic Compositions (NIST, Physical Reference Data Website, accessed December 14th 2007) database for the isotopic definitions for each of the elements. The concrete elemental composition was

provided by the CERF facility organisers (via private email correspondence with Markus Fuerstner) and was identical to those used in the earlier published FLUKA simulations.

The radiation was tallied using 50 x 50 cm^2, 1 micron thick scoring volumes placed at each of the 20 irradiation positions, 16 on the top (labelled CT1-CT16) and 4 on the side (labelled CS1-CS4). Each of these scoring volumes tallied the particle energy and type and then killed the particle to prevent multiple tallying of the same particle. The GEANT4 geometry used for the CERF facility simulations can be seen in Figure 5.1.

The scoring volumes on the top concrete shielding and copper target were placed with a slight anti-clockwise rotation of 3.45 degrees when viewed from above. This rotation reflects the actual CERF facility beam lines fanning out from the beam entry point to each of the experimental beam lines. The CERF facility is on the H6 beam line which is at the slight angle with respect to the concrete walls used to construct the target area of the facility.

The geometry of the facility simulation was optimised by having killing volumes on the opposite side of the target from the concrete walls and at the opposite end from the beam direction. These killing volumes were to ensure that the particles exiting the copper target in the opposite direction to the walls were removed from the field. This assumes that there is no significant contribution to the field from high angle scattering of radiation from the opposing concrete walls.

A simulation was constructed taking into account the opposing walls, concrete side positions entry labyrinth and concrete beam stop. However the execution time of this simulation required an unfeasible amount of CPU time, even parallelised on the available computing cluster, (approximately four years on a single 3 MHz CPU) to obtain adequate statistics for the analysis required. The simulation with additional geometry was not used to produce quantitative results. However, to provide a basis for rejecting simulation of these facility features a low statistics simulation was used which incorporated these features which revealed its effect on the field at the irradiation positions was negligible.

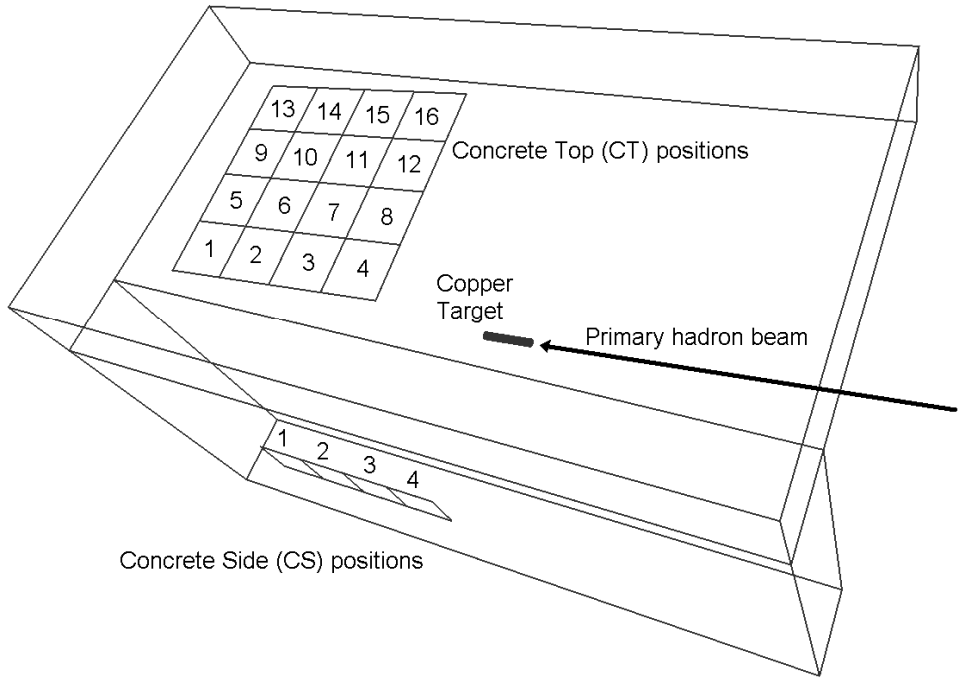

Figure 5.1. A 3D visualisation of the GEANT4 geometry for the CERF facility. Note the four irradiation positions on the side (CS1-4) and 16 positions on top (CT1-16).

Particles emitted from the target in the direction away from the concrete walls were killed to further reduce simulation execution time. The drawback of this is that the estimated minimal contribution from backscattered neutrons from the floor and opposite wall is not tallied, nor is any contribution from the concrete side irradiation position access concrete labyrinth partition. The effect of neglecting these geometric components is a slight decrease in the mid range neutron particle spectra for neutrons between 10^{5} and 10^{-1} eV. This is shown by the neutron particle count using the more accurate short simulation that included these features when compared with the final simulation geometry.

5.4 Results

5.4.1 Part 1 - Target simulation

The target simulation was executed for $2x10^5$ primary hadrons which is equivalent to 9.09 ± 0.91 PIC counts. Table 5.1 shows the total number of particles produced within the copper target, simulated for both of the physics lists of interest (QGSP_BIC_HP and QGSP_BERT_HP). The majority of the particles produced by the copper target were primarily photons with, an order of magnitude less, neutrons and electrons. A slight increase of the neutron, proton and pion components by the Bertini model was observed which was expected due to the differences in the way they handle protons and pion interactions in the 0-9.9 GeV energy range (Bolshakova et al., 2008), (GEANT4 Physics Reference Manual).

Particle Type	**Total number of particles QGSP_BERT_HP**	**Total number of particles QGSP_BIC_HP**	**Physics list ratio**
Photon	6.98×10^8	7.12×10^8	0.98
Neutron	4.38×10^7	3.34×10^7	1.31
Electron	1.07×10^7	1.09×10^7	0.99
Positron	5.70×10^6	5.83×10^6	0.98
$Pion^-$	1.95×10^6	1.72×10^6	1.14
$Pion^+$	1.94×10^6	1.74×10^6	1.11
Proton	1.87×10^6	1.49×10^6	1.26
$Kaon^+$	7.35×10^4	6.96×10^4	1.06
$Kaon^-$	3.10×10^4	3.07×10^4	1.01
$Muon^+$	2.11×10^4	2.32×10^4	0.91
$Muon^-$	5.55×10^3	5.69×10^3	0.98
Deuteron	1.19×10^4	1.61×10^5	0.07
Triton	4.25×10^3	5.78×10^4	0.07
Alpha	6.05×10^2	3.24×10^3	0.19
He^3	4.50×10^1	7.20×10^1	0.63

Table 5.1. a) The total number of particles produced during simulation of the copper target for $2x10^5$ primaries.

Particle fluences of the same orders of magnitude for the majority of particles was produced by both physics lists. However for the heavier particles (deuteron, triton and alphas) there was approximately an order of magnitude higher production by the physics list using the Binary Cascade model over the physics list using the Bertini

Cascade model. For the He^3 particles the difference in number escaping the target, while still large, is less than double. These particles are not important for the characterisation of the field outside the concrete shielding at each of the irradiation positions as, regardless of which physics list is used, none of these heavier particles are capable of passing through the air gap and concrete layer to the external irradiation positions. For any further studies on the effects of dosimetry within the target chamber, to study effects of dosimeters without atmospheric shielding and cascades, a thorough investigation of the physics processes accuracy would need to be undertaken.

The energy spectra for each component of the radiation escaping the target is shown in the graphs presented in Figures 5.2 to 5.8. The spectra are binned logarithmically from 0.1 meV to 1.0 TeV to cover the large dynamic range observed. The energy ranges of the particles escaping from the target are from the beam energy of 120 GeV/c down to approximately 10 keV for the charged particles and down to 0.01 eV for the neutrons. Several differences between the spectra of the two physics lists used can be observed.

The components of the neutron particles escaping from the target are compared in Figure 5.2. These spectra show a significant difference between the two physics lists employed. In both of the neutron spectra there is a low energy thermal peak of neutrons produced in the energy range of 0.01 – 1 eV. The QGSP_BERT_HP physics list produces approximately 64% more particles in this energy range than the QGSP_BIC_HP list. A sharp neutron peak is observable at 1 keV. The peak is caused by pion inelastic interactions producing 1 keV neutrons and protons near the limit of overlap of the high and lower energy models (Daquino, 2006). This peak is an artefact of the inelastic processes occurring during the pion-nucleus interactions and is only seen in the neutron spectra due to the ability of neutrons of that energy to escape the target unlike the protons. The artefact is produced from the LEP (Low Energy Parameterised) together with the LElastic (Low Energy elastic) models to ensure the balancing of the energy and isotope number when using these parameterised models. The two physics models predict a significantly different peak intensity. For the QGSP_BIC_HP physics list, the evaporation peak dominates the spectrum and is the most intense feature, while the QGSP_BERT_HP list shows this peak as over an order

of magnitude less intense. From this it can be seen that the QGSP_BERT_HP physics list performs better with respect to artefact production than the QGSP_BIC_HP physics list which grossly overestimates the production of 1 keV neutrons and protons.

The developers of GEANT4 are currently investigating the models used in the physics lists to remove the production of this artefact (private communication with Alexander Howard, Gunter Folger and Alberto Ribon, GEANT4 testing and quality assurance working group) but it is still present as of the models used in GEANT4.9.4.p01 (released 25 February 2011). The Fritof model is intended to be released in a future version of GEANT4 which will eliminate the requirement for the parameterised model generating the artefact.

A broad neutron peak at approximately 1 MeV can be observed with a less intense broad peak present at approximately 100 MeV. These broad peaks dominate the spectra in the QGSP_BERT_HP physics list simulation. The energy range from 1 keV to 30 MeV has the QGSP_BERT_HP physics list producing more neutrons than the QGSP_BIC_HP list. Above 30 MeV both of the physics lists produce comparable results.

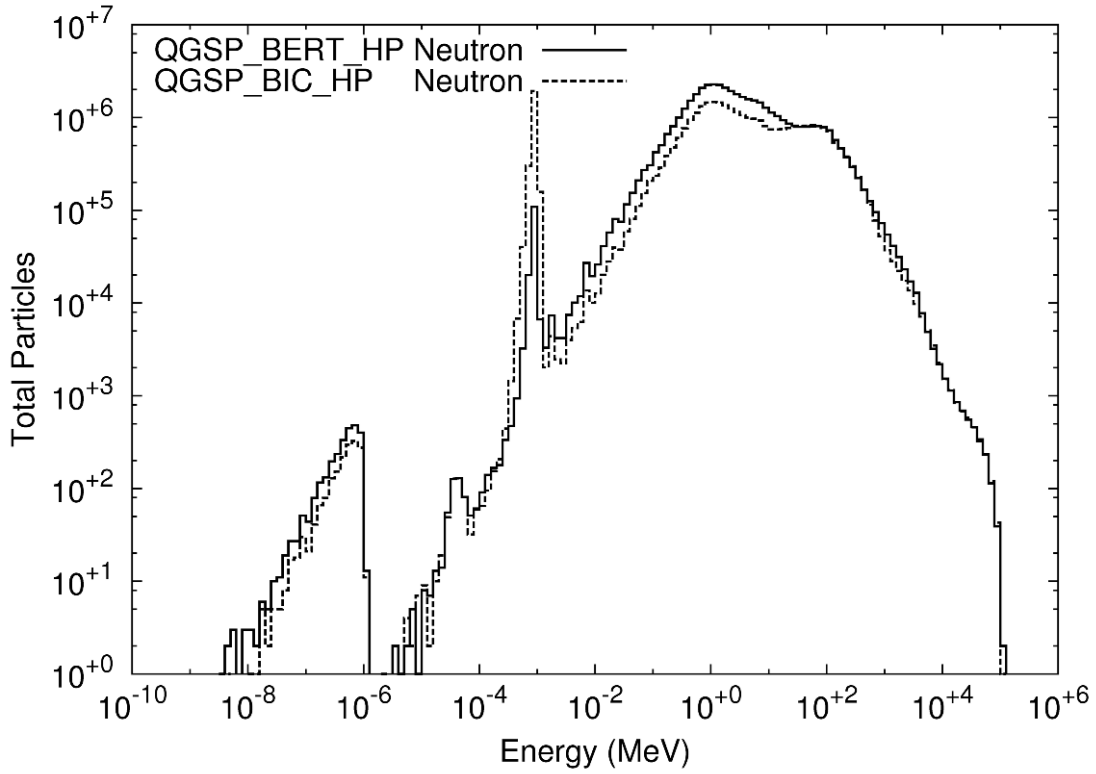

Figure 5.2. Energy spectra of neutrons produced from the copper target for both the QGSP_BERT_HP and QGSP_BIC_HP Physics lists.

High energy inelastic interactions within the target, from any type of incident particle, are the principle source of neutron production. An example of a reaction path for a neutron inelastic interaction with a copper nucleus and the production of secondaries is shown in equation 5.4.1. The kinetic energy in MeV of each particle in the laboratory frame of reference is shown below each corresponding reaction component.

$$ {}^{1}_{0}n + {}^{63}_{29}C \rightarrow {}^{56}_{26}Fe + {}^{4}_{2}He + {}^{1}_{1}p + {}^{1}_{0}n + {}^{1}_{0}n + {}^{1}_{0}n + \gamma + \gamma \qquad (5.4.1) $$

256	0		1.3	6.43	5.72	48.3	44.7	110.0	3.61	5.06	Energy (MeV)

The sum of the kinetic energies from the secondary particles produced in the inelastic interaction is 225.12 MeV. The reaction is endoergic with energy required to exceed the relevant nuclear binding energies.

The GEANT4 tracking output from the inelastic interaction illustrated in equation 5.4.1 is shown as Listing 5.1.1 in Appendix 5.1.

The proton, positive pion and positive kaon spectra (shown in Figures 5.3-5.5) all display the presence of a sharp peaked feature at approximately 120 GeV. This originates from the primary beam either being elastically scattered into the scoring volumes or passing with minimal ionisation energy loss through the length of the copper target to the scoring volume at the end of the target.

The proton spectra, as shown in Figure 5.3, show a broad peak at approximately 200 MeV. While both physics lists employed in the simulation resulted in a similarly shaped peak, the QGSP_BIC_HP physics list produced a higher number of events in this feature. The lowest energy tallied for the protons each simulation was well above the production cut level of 1 keV.

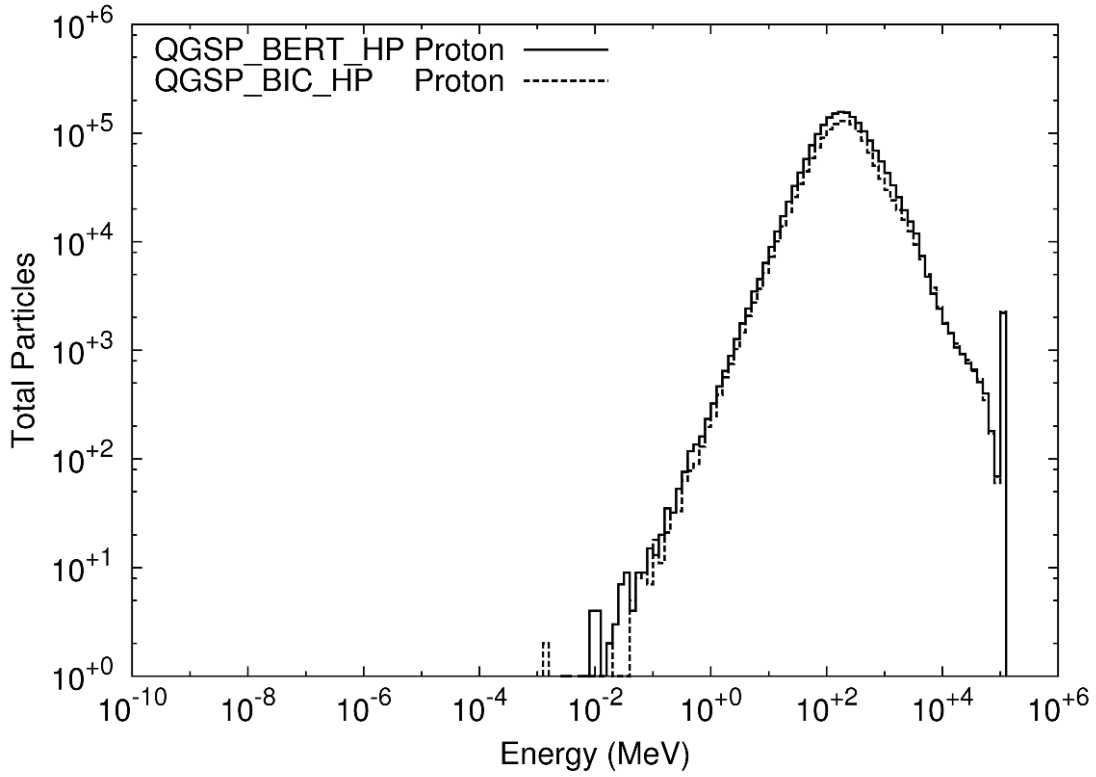

Figure 5.3. The proton energy spectra for the QGSP_BERT_HP and QGSP_BIC_HP physics lists for the simulation of the mixed hadron beam on the copper target. The highest energy filled bin is a result of the 120 GeV/c primary particles elastically scattering at the edge of the copper target into the scoring region.

The positive and negative pion spectra display similarities to the proton spectrum with the peak maximum occurring at approximately 350 MeV. The spectra for the pions resulting from the simulations of both physics lists are shown in Figure 5.4. An observable difference between both simulations is a greater production rate of positive and negative pions for the case of the simulation employing the QGSP_BERT_HP physics list in the energy range of 200 MeV to 2 GeV.

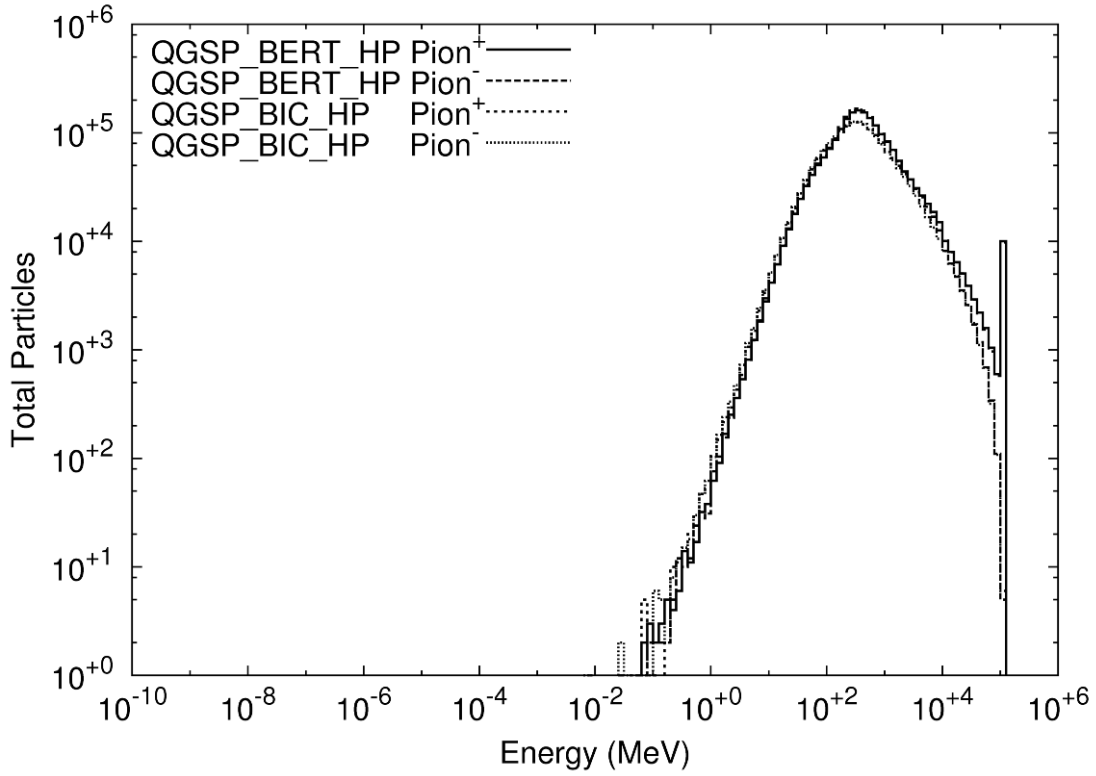

Figure 5.4. The positive and negative pion energy spectra for the QGSP_BERT_HP and QGSP_BIC_HP physics lists for the simulation of the mixed hadron beam on the copper target. The highest energy filled bin is a result of the 120 GeV/c primary particles elastically scattering at the edge of the copper target into the scoring region.

The kaon spectra contain two broad peaks associated with the positive and negative kaons centred at approximately 1 GeV. Simulations employing either physics list resulted in approximately twice the number of positive kaons than negative kaons under the observed broad energy peak. As seen in Figure 5.5 the distribution of the positive kaons is wider by approximately 85 MeV and slightly reduced in peak intensity by approximately 280 counts in the peak as produced by the QGSP_BERT_HP physics list compared the QGSP_BIC_HP physics list. The additional width in the peak produced by QGSP_BERT_HP is only at lower energies, the higher side of the peaks produced by both physics lists is practically identical. A

similar skewing of the peaks comparatively by both physics lists is shown in the negative kaon spectra although to a lesser extent.

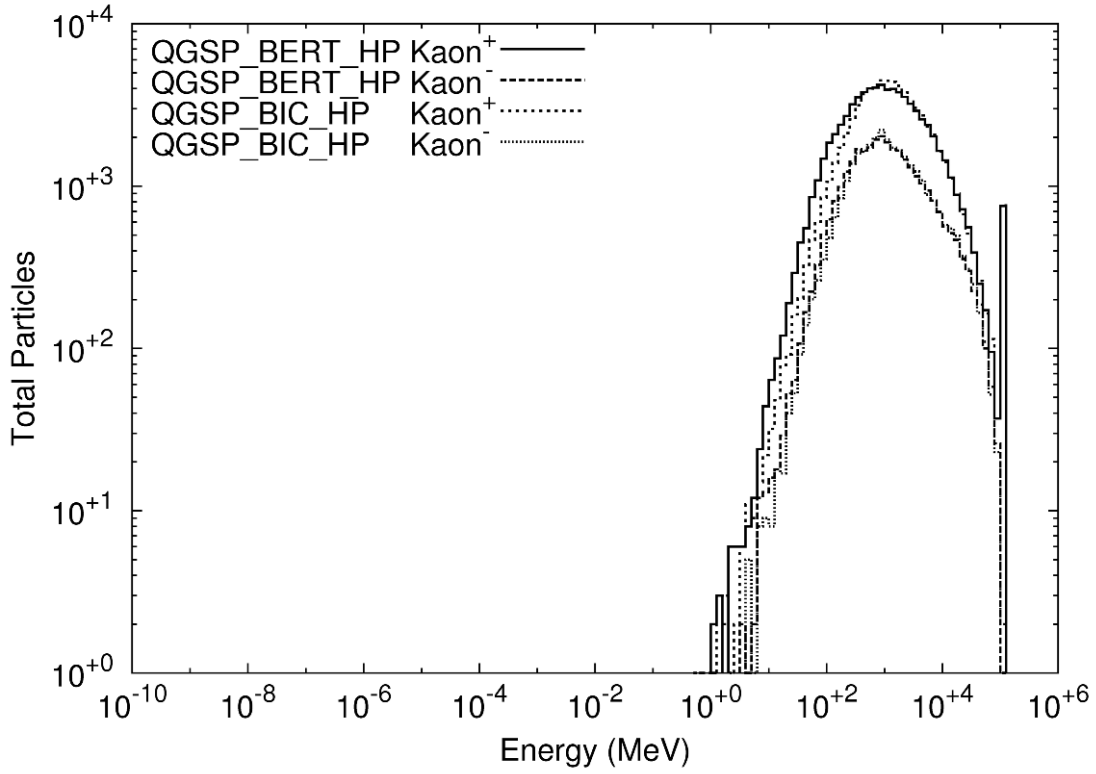

Figure 5.5. The positive and negative kaon energy spectra for the QGSP_BERT_HP and QGSP_BIC_HP physics lists for the simulation of the mixed hadron beam on the copper target. The highest energy filled bin is a result of the 120 GeV/c primary particles elastically scattering at the edge of the copper target into the scoring region.

The muon spectra shown in Figure 5.6 reveal the presence of a broad positive and negative muon peak. Two narrow energy peaks are apparent on the lower energy side of the broader energy peak centred at energies of 4.13 MeV and 152.5 MeV in the positive muon spectra. One of the processes undertaken by both positive pions and the positive kaons is the decay to a positive muon plus a muon neutrino. The pions and kaons from the primary beam have sufficient time to decay due to the relatively long flight time of the primary beam to reach and interact with the target. This would adequately explain the presence of the muon background experienced at the facility from the positive pion and kaon decays occurring further upstream in the beamline. Multiple positive pion and kaon energy loss interactions in the target can decrease the kinetic energy of the particle, if the particle does not escape the target, to very low energy (non-relativistic speeds) resulting in the assumed decay of the particles into a

muon and muon neutrino. The non-relativistic positive pion mean lifetime is τ = (2.6033 ± 0.0005) x 10^{-8} s and the positive kaon mean lifetime is τ = (1.2380 ± 0.0021) x 10^{-8} s.

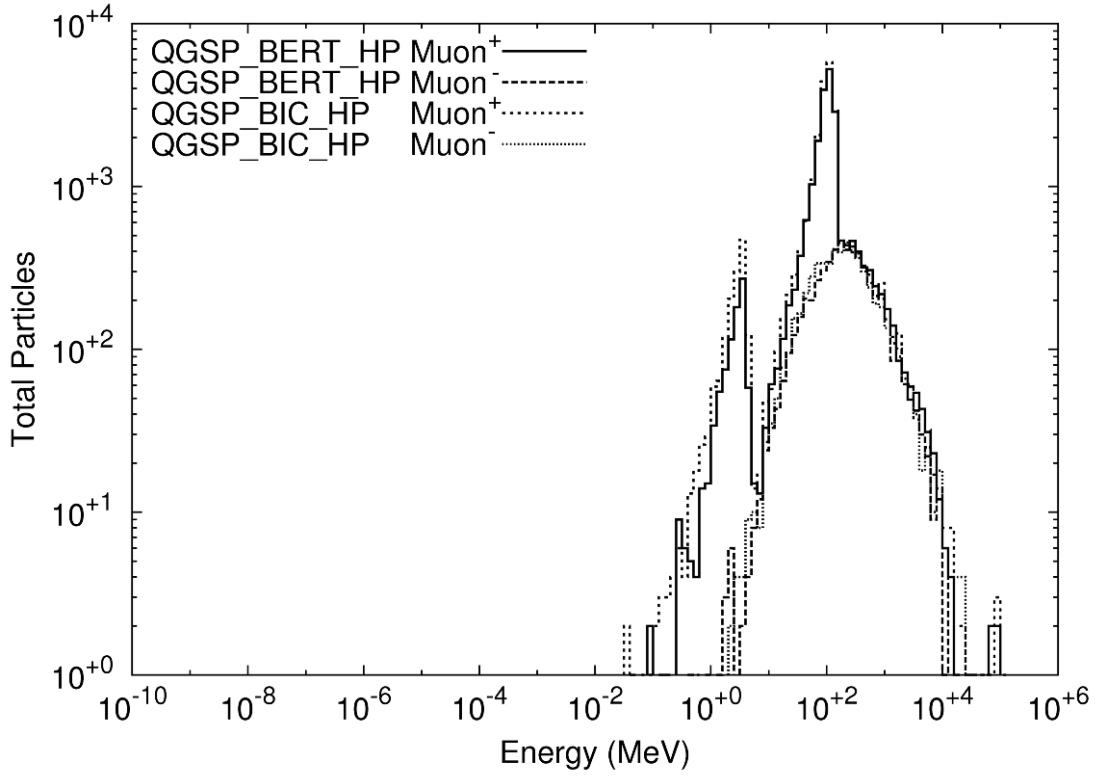

Figure 5.6. The positive and negative muon energy spectra for the QGSP_BERT_HP and QGSP_BIC_HP physics lists for the simulation of the mixed hadron beam on the copper target. The two observable sharp peaks are the result of positive pion and kaon decay from the primary beam.

The energy calculations for the positive muon decays are show below. Constants and decay scheme are referenced from Amsler et al. (2008).

Rest energies of the particles of interest are:

$\mu^+ = 105.658367 \pm 0.000004$ MeV (5.4.2)

$\pi^+ = 139.57018 \pm 0.00035$ MeV (5.4.3)

$K^+ = 493.677 \pm 0.016$ MeV (5.4.4)

Pion decay is given by:

$$\pi^+ \rightarrow \mu^+ + \nu_\mu \qquad (5.4.5)$$

This decay has a branching fraction of (99.98770 ± 0.00004) %. Assuming a centre of mass frame of reference, the particle decay Q value is given by summing the rest mass energies:

$$m_\pi c^2 = m_\mu c^2 + m_\nu c^2 + Q \qquad (5.4.6)$$

$$139.57 = 105.66 + 0.0 + Q \qquad (5.4.7)$$

Assuming a negligible rest mass for the muon neutrino, this gives a Q value of Q = 33.91 MeV for the decay. Therefore the kinetic energy carried by the muon and the muon neutrino is given by:

$$Q = KE_\mu + E_\nu \qquad (5.4.8)$$

where E_ν is the energy carried off by the neutrino. Since the muon neutrino is considered to have negligible mass the relativistic energy expression is given by

$$E_\nu = pc \qquad (5.4.9)$$

The momentum relationship is given by

$$(pc)^2 = KE_\mu + 2KE_\mu m_\mu c^2 \qquad (5.4.10)$$

Substituting equation 5.4.8 into equation 5.4.10 allows *pc* to be expressed in terms of *Q (5.4.11).*

$$pc = \frac{Q^2 + 2Qm_\mu c^2}{2(Q + m_\mu c^2)} \qquad (5.4.11)$$

This gives a muon neutrino energy of E_ν = 29.79 MeV. Substituting E_ν back into equation (5.4.8) gives the positive muon component of the decay energy.

KE_μ = 33.91 - 29.79 = 4.12 MeV (5.4.12)

This energy corresponds to the lower energy peak feature seen in the positive muon spectra for both physics lists revealed in Figure 5.6. The differences between the two simulations with differing physics lists associated with this peak are due to the differing way that pion decay is handled between the Bertini and Binary Cascade models.

In a similar manner the higher energy peak can be shown to be a result of positive kaon decay by solving the decay energy:

$$K^+ \rightarrow \mu^+ + \nu_\mu \quad (5.4.13)$$

which has a decay fraction of (63.54 ± 0.14) % and a Q value of Q = 388.01 MeV. The final energy of the decay product positive muon is:

KE_μ = 388.01 – 235.52 = 152.48 MeV (5.4.14)

The next highest percentage decay fraction for positive kaon decay is $K^+ \rightarrow \pi^+ + \pi^0$ with a decay fraction of (20.68 ± 0.13) % and a Q value of 219.12 MeV. A feature attributable to this reaction path would occur at approximately 110 MeV is not easily observable in the spectra due to the low decay fraction in the presence of the higher statistical events.

Any neutral pions created during the decays and multiple particle interactions occurring in the target promptly decay due to a very short lifetime. The mean lifetime of a neutral pion is $\tau = (8.4 \pm 0.6) \times 10^{-17}$ s with a primary decay path of $\pi^0 \rightarrow 2\gamma$ with a decay fraction of 98.798 ± 0.032 %. This decay results in the simulation of any neutral pion created to primarily decay within a single step to two photons with a total

energy of the neutral pion rest mass energy plus its kinetic energy. An example of such a decay with the associated energies below is the decay of a neutral pion with 625 MeV KE by two photons with energies of 131 and 447 MeV. The remainder of the energy comes from the conversion of the neutral pion rest mass energy of 134.9766 ± 0.0006 MeV.

Creation and decay of other short lived exotic particles of either neutral or charged states, lambda, eta, tau, sigma, etc. created from inelastic interactions occur frequently, at least once per primary. These exotics usually decay within a single step into other particles that decay rapidly to more stable products such as pions, muons, protons, neutrons, electrons and positrons.

Figure 5.7 shows the electromagnetic (photon, electron and positron) components of the field. Only the results from the QGSP_BERT_HP physics list are displayed as both physics lists used the standard electromagnetic model and produced identical results. The production energy cut-off for the electromagnetic interactions in the standard model is at 990 eV. This means that electrons, positrons and photons below this energy will not be produced as secondary particles. Particles were tracked down to energies below this value with an energy range cut of 70 µm. This corresponds to an electron energy cut of 990 eV and photon energy cut of 20.5152 keV within the copper target.

The electron and positron continuum are comparable from approximately 100 GeV down to 60 MeV. From 60 MeV and lower energies the two spectra differ where the photon component of the field results in the production of photoelectrons at significantly lower energies. This results in a statistical peak feature occurring in the electron spectrum due to the 511 keV annihilation photons, seen in the photon spectra, increasing the photoelectron component below this energy. Since the photon energy cut-off is at 20.52 keV the predominant electron generation mechanism at lower energies is ionisation from charged particle interactions. The ionisation electrons with low energies are produced close to the scoring volume as a result of charged particles which escape the target. This accounts for the increase in electron contribution from below the photon threshold down to the electron production threshold of 990 eV. The

positron component remains smooth and continuous to a lower energy limit of around 10 keV.

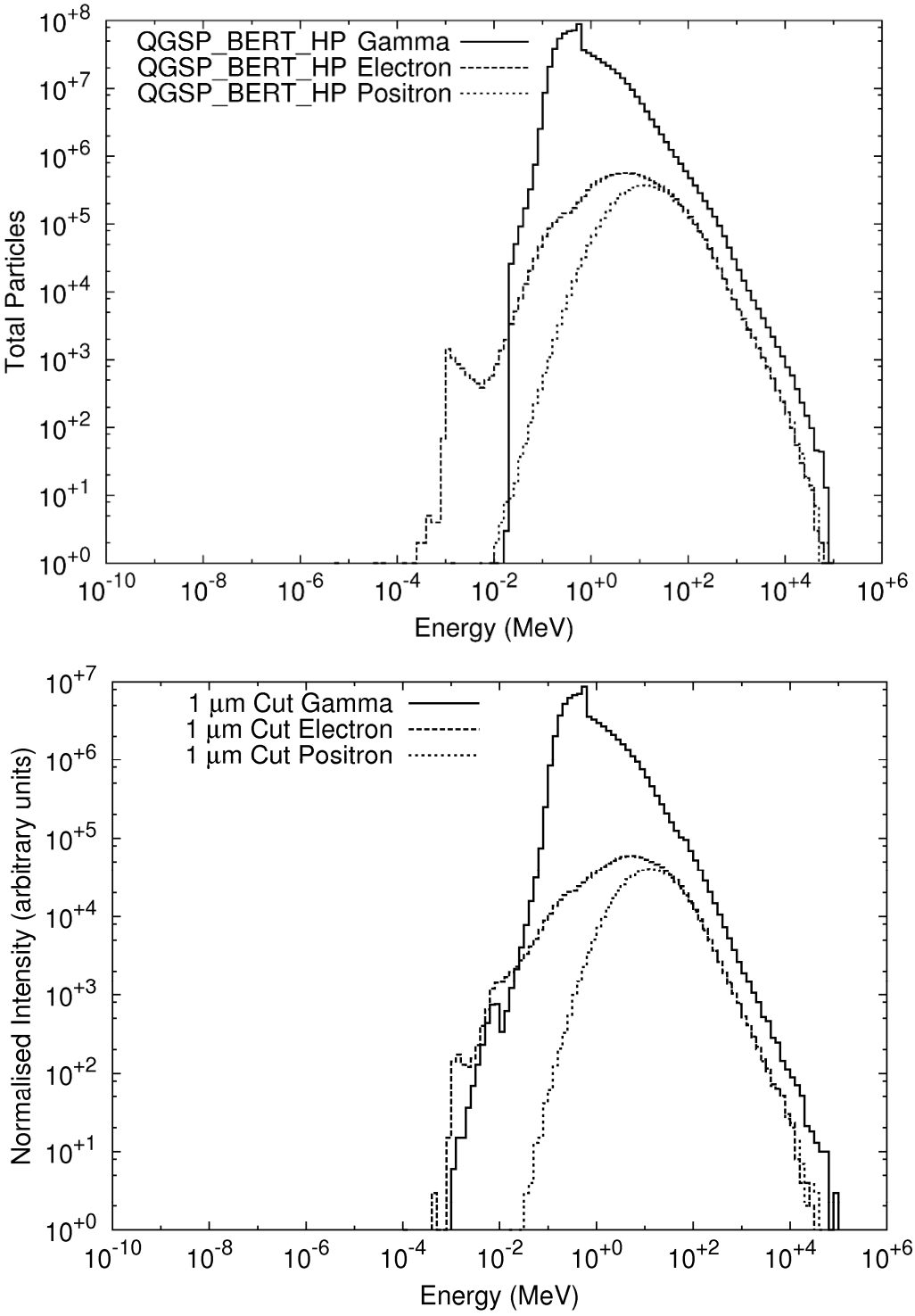

Figure 5.7. Top: Simulation of the mixed hadron beam on the copper target with default range cut of 70 µm. The electromagnetic processes were the same for both physics lists used and spectra are the same for both. Bottom: The photon and electron comparison of different cuts for the electromagnetic component affected by the reduction of range cuts to 1 µm. The photon and electron components of the field are the only components affected by the reduction of the cuts from the default value.

The simulation was rerun using a factor of 10 reduced primaries particles, with a reduced cut value due to the significantly increased simulation time compared to the default cut values. The time required rerunning the simulation with the reduced production cuts and lower number of primaries was increased by approximately 16 times compared to the original simulation with the default range cut value of 70 µm. The re-run simulation involved 2×10^4 primary particles incident on the target with a reduced range cut value of 1 µm. For the rerun simulation the energy production cuts were reduced to the minimum value of 990 eV for both of the photon and electron components. The rerun comparison shows that the electron component becomes continuous down to the production threshold. The photon, electron and positron results of the re-run simulation are also shown in Figure 5.7. The ionisation electron contribution can no longer be seen due to the greater contribution from the photoelectron contribution down to the production threshold.

In the re-run simulation, the photon component now continues down to the 990 eV cut value. The electron contribution from photoelectrons continues to be dominant down to the 990 eV cut threshold. The contribution of ionisation electrons from the interactions of the charged particles with the electrons can no longer be readily observed.

It can be concluded that the effect of lowering the cut value to simulate the low energy components of these spectra will not affect the final spectra at the irradiation positions behind the concrete shielding. The cut value of 70 µm is suitable to simulate the facility field, due to the increased simulation time required to simulate the field using reduced cut values. Electrons require above approximately 400 keV to transverse the air gap between the target and the inside of the concrete shielding and energy above several GeV to transverse the concrete shielding.

The scoring of heavier ions produced near the surface of the copper target is shown in Figure 5.8. There are significant differences for all of the heavier particle production between the two simulations with the different physics lists. This is due to known inaccuracies in the physical models employed by both physics lists which is an issue requiring, and currently receiving attention (private communication with Alexander

Howard, Gunter Folger and Alberto Ribon, GEANT4 testing and quality assurance working group). It is important to state however that the effects of these particles produced by high energy collisions is not normally important in most high energy physics simulations due to the short ranges of the particles concerned (e.g. 2.77 mm in copper for 1 GeV alpha particles).

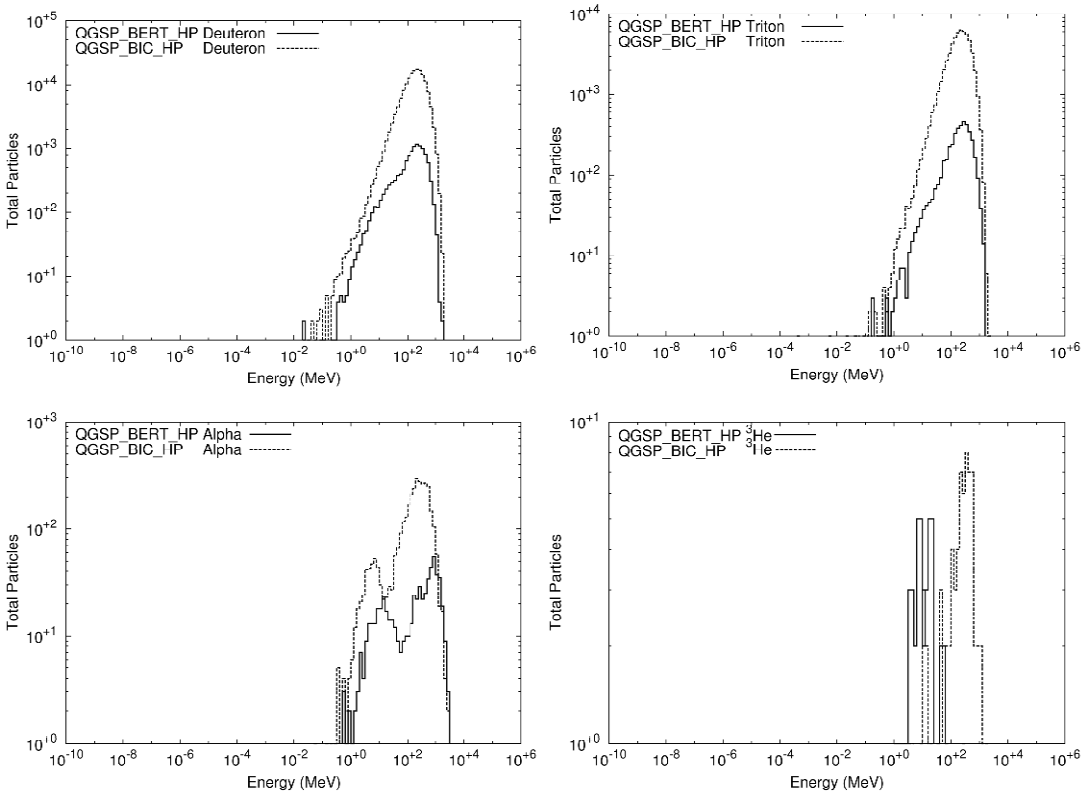

Figure 5.8. Comparison of the heavy particles (A>1) produced by the target using the QGSP_BIC_HP and QGSP_BERT_HP physics lists. These particles show the greatest difference between the particle production in the Bertini and Binary Cascade models. The particles illustrated from the top left hand side clockwise are Deuterons, Tritons, Alphas and ^{3}He.

The interactions producing these particles and the spectra of each only become important if dosimetry or spectroscopy is to be performed inside the target chamber in order to simulate the effect of high energy space radiation without the moderation and cascades of the concrete wall simulant of the upper atmosphere. Experiments have been undertaken at the CERF facility looking at activation within and around the target by using a sliced target and effects of activations of samples around the target and then comparing to activation results from FLUKA simulations. This was performed as part of an activation study for the commissioning of the LHC for high

energy radiation protection of accelerator areas and calibration for the beam loss monitors (BLM) (Brugger, M., et al. 2005).

The hadron component of the target is primarily neutrons, however secondary interactions from the higher energy components (above hundreds of MeV) of all the secondary charged particles will contribute to the field produced at each of the irradiation positions.

5.4.2 Part 2 - Facility Simulation

The simulation of the facility produced the energy spectra for each of the particles encountered at each of the 20 designated irradiation positions. The tallied results for each of the particles and positions resulted in 180 output files being produced per simulation. The output files consisted of 9 particle spectra (neutron, photon, proton, electron, positron, positive pion, negative pion, positive muon and negative muon) for each of the 20 positions. These particles were the main components of the field reaching the irradiation position sampling volumes. The spectra were logarithmically binned covering an energy range from 1 meV to 1 TeV. The neutrons and charged particles were strongly moderated or attenuated by the concrete shielding and as such only high energy charged particles were tallied at each of the designated irradiation positions.

Due to long simulation times required to produce the results, the simulation was executed for 1×10^5 primary hadrons which is equivalent to 4.54 ± 0.45 PIC counts. The mean execution time per primary particle was 8.7 ± 6.2 seconds.

The concrete side position 1 (CS1) results are presented here as a representative sample spectrum for each of the different particles. This position was chosen as all of the experimental measurements to be presented in subsequent chapters were obtained at side positions due to the higher particle fluence necessary for good experimental statistics. In chapter 6 results of experimental measurements taken at positions CS1 and CS3 are presented. The spectra for each of the irradiation positions are very similar with no large differences apparent. Section 5.4.3 presents a comparison of the spectra with the largest positional differences.

Results for the neutron, photon and proton particles encountered at irradiation position CS1 are shown in Figure 5.9.

The neutron spectrum is shown to cover the energy range from a maximum at approximately 1 GeV down to 1 meV. The neutron spectra reveals not only a significant high energy neutron peak at approximately 100 MeV but also a significant intensity thermal neutron peak at approximately 0.05 eV. There is a continuum of neutron energies between the thermal and high energy peaks covering a range from approximately 0.1 eV up to 0.1 MeV. From 0.1 MeV to approximately 10 MeV there are several sharp neutron features.

The proton component of the spectrum can be seen to be a relatively low intensity peak centred at approximately 100-200 MeV in energy. This peak position shifts to lower energies and lower intensities for more lateral irradiation positions compared to those located further downstream from the target i.e. positions adjacent to the target have a much lower proton energy and intensity than forward positions. This is to be expected due to the greater forward momentum of the higher energy particles from the target. The consequence of this is that the proton component will give rise to a significantly different contribution to energy depositions in dosimeters under test at different positions. Although the proton component of the field is orders of magnitude lower in fluence than the neutron, photon, electron and positron components, it is the heaviest charged particle produced at the irradiation sites.

The standard electromagnetic model was employed in the simulation meaning that low energy electromagnetic processes were not simulated. The cut-off value used for photons in concrete, the material adjacent to the sampling volumes, was 10 keV. The photon spectrum ranges from approximately 20 keV up to approximately 200-300 MeV depending on position. The 511 keV electron-positron annihilation peak can be seen as a sharp, single bin width, peak below the 1 MeV tic mark on the scale. Above this energy variations can be seen up to approximately 6.5 MeV. This is due to neutron and charged particle reactions within the wall materials resulting in gamma photons to be emitted from the relaxation of excited radionuclides in the concrete. The high energy photon intensity drops off rapidly above approximately 7 MeV. The high

energy photons result from high energy antiparticle annihilations and from unstable heavy particles decaying with modes that produce one or more high energy photons. An example of this is the neutral pion reaction channel expressed as $\pi^0 \rightarrow 2\gamma$ associated with a decay fraction of 98.798 ± 0.032 % and a mean lifetime of τ = (8.4 ± 0.6) x 10^{-17} s), producing photons with energies greater than 110 MeV. The energy cut for photon production was 20 keV set to be just below the threshold of photon production and photon attenuation from the copper target in the concrete.

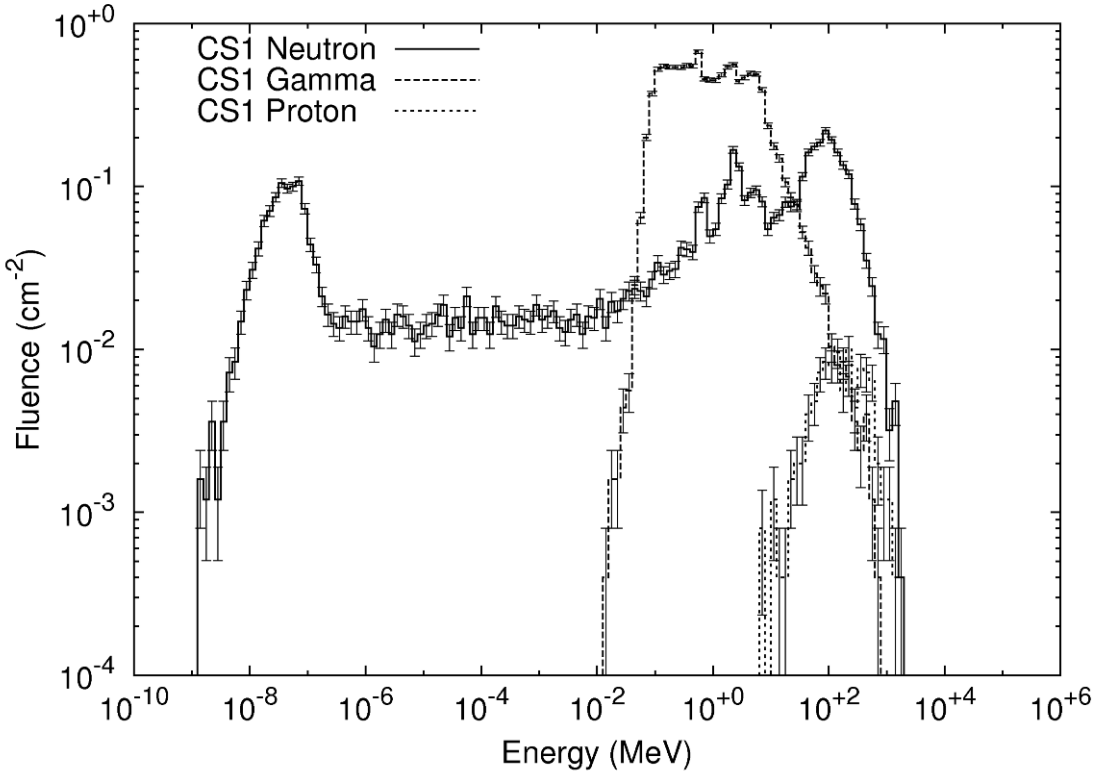

Figure 5.9. The GEANT4 neutron, proton and photon spectra at irradiation position CS1 for 10^5 primary hadrons incident on the copper target using the QGSP_BERT_HP physics list. Error bars are root mean square error for each bin.

The electron and positron components are shown in Figure 5.10. The electron component of the spectrum peaks between 2 and 4 MeV and does not appear to have an appreciable variation in peak position over the different irradiation positions. The electrons have a broad distribution of energy with a width of approximately 17 ± 1 MeV with energies in a range from tens of keV to hundreds of MeV. The electron contribution to the spectra is of low LET especially at higher energies. Although the total number of electrons in the field is larger than the proton or pion contribution, the low LET means that depending on the detection method used for dosimetry (active or

passive, energy deposition threshold, density of dosimeter sensitive volume, etc.) it may not contribute significantly to the measured dose.

The positron component of the field is lower in intensity and higher in peak energy than the electron component. This is due to the increased annihilation probability for the lower energy positrons in the field through the concrete wall. The average peak of the positron component is approximately 17 ± 8 MeV with a maximum energy comparable to the electron component.

The remaining components of the field make up a relatively minor component to the overall CERF facility mixed radiation field particle fluence. The positive and negative pion components are much lower in intensity and peak at around 250 ± 50 MeV. Both the positive and negative pion components of the field cover the same energy range and peak position.

The muon components are shown in Figure 5.11. Due to the low number of both positive and negative muons recorded, the positive and negative muon components of the field can not be reliably resolved into a peak without resorting to greater simulation statistics. The muon component is a relatively insignificant portion of the total field. In some irradiation positions, no observable record of any muons was evident for the number of primaries simulated, and is not expected to make a significant contribution to the overall dose received from the field.

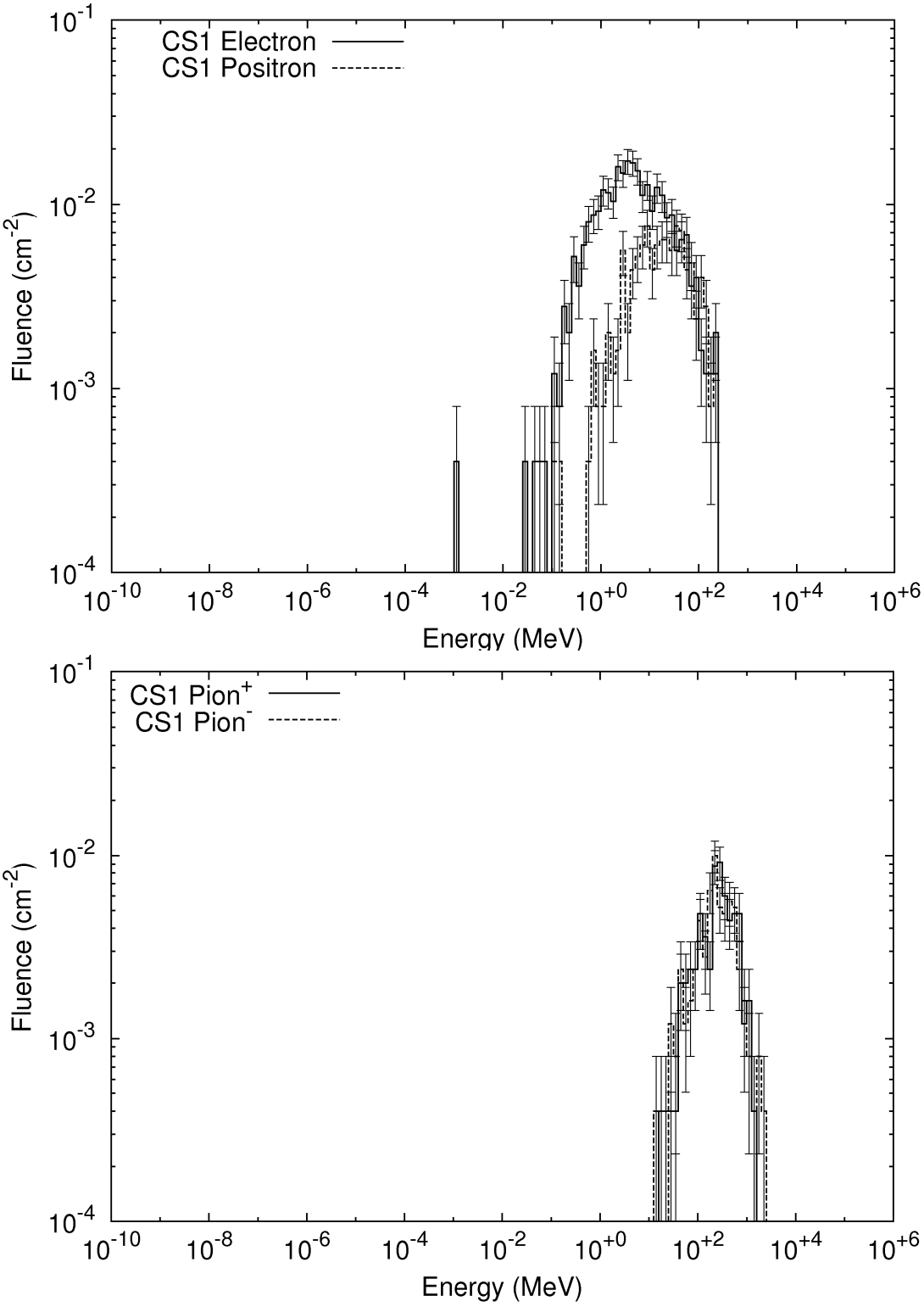

Figure 5.10. The GEANT4 electron, positron (top) and pion (bottom) spectra at irradiation position CS1 for 10^5 primary hadrons incident on the copper target using the QGSP_BERT_HP physics list. Error bars are the root mean square error for each bin.

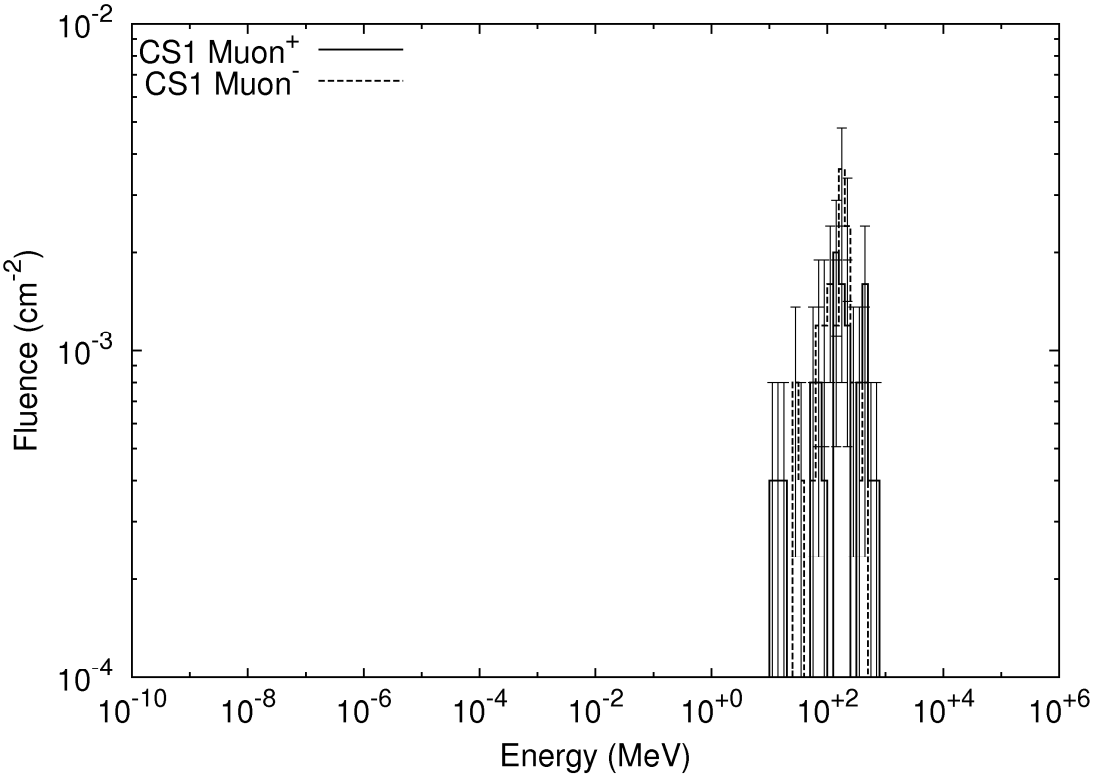

Figure 5.11. The GEANT4 muon spectra at irradiation position CS1 for 10^5 primary hadrons incident on the copper target using the QGSP_BERT_HP physics list. Error bars are the root mean square error for each bin.

The simulation was executed using the QGSP_BIC_HP and QGSP_BERT_HP physics lists. The overall shape and peak position of the spectra did not vary significantly between the two physics lists. The main difference between the recorded particle spectra is the total number of particles recorded for the same number of initial primaries.

A comparison between the two physics lists for the irradiation positions is given in section 5.5.1. Tables 5.2 and 5.3 summarise the total number of particles per PIC count per square centimetre for each of the particles encountered at each position. Table 5.2 is for the QGSP_BIC_HP physics list and Table 5.3 is for the QGSP_BERT_HP physics list. The difference between the total particles produced by each physics list is that the QGSP_BERT_HP physics list produces on average more hadrons, pions and muons than the QGSP_BIC_HP physics list which can be seen in Table 5.6.

	Neutron	Proton	Photon	Electron	Positron
CS1	$6.81\times10^{-1} \pm 7.74\times10^{-3}$	$9.59\times10^{-3} \pm 9.19\times10^{-4}$	$1.75\times10^{0} \pm 1.24\times10^{-2}$	$4.17\times10^{-2} \pm 1.92\times10^{-3}$	$1.40\times10^{-2} \pm 1.11\times10^{-3}$
CS2	$8.40\times10^{-1} \pm 8.60\times10^{-3}$	$1.21\times10^{-2} \pm 1.03\times10^{-3}$	$2.14\times10^{0} \pm 1.37\times10^{-2}$	$4.51\times10^{-2} \pm 1.99\times10^{-3}$	$1.62\times10^{-2} \pm 1.19\times10^{-3}$
CS3	$9.79\times10^{-1} \pm 9.28\times10^{-3}$	$1.24\times10^{-2} \pm 1.04\times10^{-3}$	$2.34\times10^{0} \pm 1.43\times10^{-2}$	$4.87\times10^{-2} \pm 2.07\times10^{-3}$	$1.64\times10^{-2} \pm 1.20\times10^{-3}$
CS4	$9.19\times10^{-1} \pm 8.99\times10^{-3}$	$1.11\times10^{-2} \pm 9.88\times10^{-4}$	$2.04\times10^{0} \pm 1.34\times10^{-2}$	$4.16\times10^{-2} \pm 1.91\times10^{-3}$	$1.02\times10^{-2} \pm 9.48\times10^{-4}$
CT1	$3.41\times10^{-1} \pm 5.48\times10^{-3}$	$4.31\times10^{-3} \pm 6.16\times10^{-4}$	$7.62\times10^{-1} \pm 8.19\times10^{-3}$	$1.51\times10^{-2} \pm 1.15\times10^{-3}$	$5.46\times10^{-3} \pm 6.93\times10^{-4}$
CT2	$3.80\times10^{-1} \pm 5.78\times10^{-3}$	$4.66\times10^{-3} \pm 6.41\times10^{-4}$	$8.63\times10^{-1} \pm 8.71\times10^{-3}$	$1.86\times10^{-2} \pm 1.28\times10^{-3}$	$5.54\times10^{-3} \pm 6.98\times10^{-4}$
CT3	$4.03\times10^{-1} \pm 5.96\times10^{-3}$	$3.78\times10^{-3} \pm 5.77\times10^{-4}$	$8.75\times10^{-1} \pm 8.78\times10^{-3}$	$1.76\times10^{-2} \pm 1.24\times10^{-3}$	$4.75\times10^{-3} \pm 6.47\times10^{-4}$
CT4	$3.82\times10^{-1} \pm 5.80\times10^{-3}$	$3.17\times10^{-3} \pm 5.28\times10^{-4}$	$8.02\times10^{-1} \pm 8.40\times10^{-3}$	$1.60\times10^{-2} \pm 1.19\times10^{-3}$	$3.34\times10^{-3} \pm 5.42\times10^{-4}$
CT5	$4.02\times10^{-1} \pm 5.95\times10^{-3}$	$5.02\times10^{-3} \pm 6.64\times10^{-4}$	$9.32\times10^{-1} \pm 9.06\times10^{-3}$	$1.87\times10^{-2} \pm 1.28\times10^{-3}$	$6.78\times10^{-3} \pm 7.72\times10^{-4}$
CT6	$4.50\times10^{-1} \pm 6.29\times10^{-3}$	$4.66\times10^{-3} \pm 6.41\times10^{-4}$	$1.09\times10^{0} \pm 9.77\times10^{-3}$	$2.24\times10^{-2} \pm 1.40\times10^{-3}$	$5.81\times10^{-3} \pm 7.15\times10^{-4}$
CT7	$4.91\times10^{-1} \pm 6.57\times10^{-3}$	$5.98\times10^{-3} \pm 7.26\times10^{-4}$	$1.11\times10^{0} \pm 9.86\times10^{-3}$	$2.16\times10^{-2} \pm 1.38\times10^{-3}$	$5.90\times10^{-3} \pm 7.20\times10^{-4}$
CT8	$4.65\times10^{-1} \pm 6.39\times10^{-3}$	$4.84\times10^{-3} \pm 6.53\times10^{-4}$	$9.83\times10^{-1} \pm 9.30\times10^{-3}$	$1.96\times10^{-2} \pm 1.31\times10^{-3}$	$4.93\times10^{-3} \pm 6.59\times10^{-4}$
CT9	$3.84\times10^{-1} \pm 5.81\times10^{-3}$	$6.51\times10^{-3} \pm 7.57\times10^{-4}$	$9.23\times10^{-1} \pm 9.01\times10^{-3}$	$1.81\times10^{-2} \pm 1.26\times10^{-3}$	$5.19\times10^{-3} \pm 6.76\times10^{-4}$
CT10	$4.48\times10^{-1} \pm 6.28\times10^{-3}$	$4.84\times10^{-3} \pm 6.53\times10^{-4}$	$1.05\times10^{0} \pm 9.63\times10^{-3}$	$2.12\times10^{-2} \pm 1.37\times10^{-3}$	$6.69\times10^{-3} \pm 7.67\times10^{-4}$
CT11	$4.82\times10^{-1} \pm 6.51\times10^{-3}$	$5.72\times10^{-3} \pm 7.09\times10^{-4}$	$1.09\times10^{0} \pm 9.80\times10^{-3}$	$2.24\times10^{-2} \pm 1.41\times10^{-3}$	$5.90\times10^{-3} \pm 7.20\times10^{-4}$
CT12	$4.54\times10^{-1} \pm 6.32\times10^{-3}$	$5.19\times10^{-3} \pm 6.76\times10^{-4}$	$9.90\times10^{-1} \pm 9.33\times10^{-3}$	$1.99\times10^{-2} \pm 1.32\times10^{-3}$	$5.10\times10^{-3} \pm 6.70\times10^{-4}$
CT13	$3.30\times10^{-1} \pm 5.39\times10^{-3}$	$4.49\times10^{-3} \pm 6.28\times10^{-4}$	$7.52\times10^{-1} \pm 8.14\times10^{-3}$	$1.47\times10^{-2} \pm 1.14\times10^{-3}$	$4.58\times10^{-3} \pm 6.35\times10^{-4}$
CT14	$3.75\times10^{-1} \pm 5.75\times10^{-3}$	$5.46\times10^{-3} \pm 6.93\times10^{-4}$	$8.48\times10^{-1} \pm 8.64\times10^{-3}$	$1.78\times10^{-2} \pm 1.25\times10^{-3}$	$5.63\times10^{-3} \pm 7.04\times10^{-4}$
CT15	$4.01\times10^{-1} \pm 5.94\times10^{-3}$	$4.58\times10^{-3} \pm 6.35\times10^{-4}$	$8.42\times10^{-1} \pm 8.61\times10^{-3}$	$1.77\times10^{-2} \pm 1.25\times10^{-3}$	$5.46\times10^{-3} \pm 6.93\times10^{-4}$
CT16	$3.67\times10^{-1} \pm 5.69\times10^{-3}$	$4.40\times10^{-3} \pm 6.22\times10^{-4}$	$7.85\times10^{-1} \pm 8.31\times10^{-3}$	$1.48\times10^{-2} \pm 1.14\times10^{-3}$	$4.14\times10^{-3} \pm 6.03\times10^{-4}$

	Positive Pion	Negative Pion	Positive Muon	Negative Muon
CS1	$3.52\times10^{-3} \pm 5.57\times10^{-4}$	$3.78\times10^{-3} \pm 5.77\times10^{-4}$	$1.50\times10^{-3} \pm 3.63\times10^{-4}$	$1.76\times10^{-3} \pm 3.94\times10^{-4}$
CS2	$2.55\times10^{-3} \pm 4.74\times10^{-4}$	$3.96\times10^{-3} \pm 5.90\times10^{-4}$	$9.68\times10^{-4} \pm 2.92\times10^{-4}$	$1.94\times10^{-3} \pm 4.13\times10^{-4}$
CS3	$3.08\times10^{-3} \pm 5.21\times10^{-4}$	$2.38\times10^{-3} \pm 4.57\times10^{-4}$	$1.14\times10^{-3} \pm 3.17\times10^{-4}$	$8.80\times10^{-4} \pm 2.78\times10^{-4}$
CS4	$8.80\times10^{-4} \pm 2.78\times10^{-4}$	$7.92\times10^{-4} \pm 2.64\times10^{-4}$	$4.40\times10^{-4} \pm 1.97\times10^{-4}$	$6.16\times10^{-4} \pm 2.33\times10^{-4}$
CT1	$7.04\times10^{-4} \pm 2.49\times10^{-4}$	$9.68\times10^{-4} \pm 2.92\times10^{-4}$	$6.16\times10^{-4} \pm 2.33\times10^{-4}$	$7.92\times10^{-4} \pm 2.64\times10^{-4}$
CT2	$7.92\times10^{-4} \pm 2.64\times10^{-4}$	$7.04\times10^{-4} \pm 2.49\times10^{-4}$	$4.40\times10^{-4} \pm 1.97\times10^{-4}$	$3.52\times10^{-4} \pm 1.76\times10^{-4}$
CT3	$5.28\times10^{-4} \pm 2.16\times10^{-4}$	$4.40\times10^{-4} \pm 1.97\times10^{-4}$	$8.80\times10^{-5} \pm 8.80\times10^{-5}$	$4.40\times10^{-4} \pm 1.97\times10^{-4}$
CT4	$4.40\times10^{-4} \pm 1.97\times10^{-4}$	$4.40\times10^{-4} \pm 1.97\times10^{-4}$	$1.76\times10^{-4} \pm 1.24\times10^{-4}$	$0.00\times10^{0} \pm 0.00\times10^{0}$
CT5	$7.92\times10^{-4} \pm 2.64\times10^{-4}$	$1.50\times10^{-3} \pm 3.63\times10^{-4}$	$6.16\times10^{-4} \pm 2.33\times10^{-4}$	$7.04\times10^{-4} \pm 2.49\times10^{-4}$
CT6	$9.68\times10^{-4} \pm 2.92\times10^{-4}$	$1.32\times10^{-3} \pm 3.41\times10^{-4}$	$3.52\times10^{-4} \pm 1.76\times10^{-4}$	$3.52\times10^{-4} \pm 1.76\times10^{-4}$
CT7	$5.28\times10^{-4} \pm 2.16\times10^{-4}$	$5.28\times10^{-4} \pm 2.16\times10^{-4}$	$1.76\times10^{-4} \pm 1.24\times10^{-4}$	$1.76\times10^{-4} \pm 1.24\times10^{-4}$
CT8	$1.76\times10^{-4} \pm 1.24\times10^{-4}$	$5.28\times10^{-4} \pm 2.16\times10^{-4}$	$8.80\times10^{-5} \pm 8.80\times10^{-5}$	$0.00\times10^{0} \pm 0.00\times10^{0}$
CT9	$9.68\times10^{-4} \pm 2.92\times10^{-4}$	$1.76\times10^{-3} \pm 3.94\times10^{-4}$	$1.23\times10^{-3} \pm 3.29\times10^{-4}$	$7.92\times10^{-4} \pm 2.64\times10^{-4}$
CT10	$8.80\times10^{-4} \pm 2.78\times10^{-4}$	$1.23\times10^{-3} \pm 3.29\times10^{-4}$	$5.28\times10^{-4} \pm 2.16\times10^{-4}$	$3.52\times10^{-4} \pm 1.76\times10^{-4}$
CT11	$5.28\times10^{-4} \pm 2.16\times10^{-4}$	$4.40\times10^{-4} \pm 1.97\times10^{-4}$	$2.64\times10^{-4} \pm 1.52\times10^{-4}$	$3.52\times10^{-4} \pm 1.76\times10^{-4}$
CT12	$2.64\times10^{-4} \pm 1.52\times10^{-4}$	$5.28\times10^{-4} \pm 2.16\times10^{-4}$	$2.64\times10^{-4} \pm 1.52\times10^{-4}$	$8.80\times10^{-5} \pm 8.80\times10^{-5}$
CT13	$8.80\times10^{-4} \pm 2.78\times10^{-4}$	$8.80\times10^{-4} \pm 2.78\times10^{-4}$	$1.58\times10^{-3} \pm 3.73\times10^{-4}$	$5.28\times10^{-4} \pm 2.16\times10^{-4}$
CT14	$8.80\times10^{-4} \pm 2.78\times10^{-4}$	$7.92\times10^{-4} \pm 2.64\times10^{-4}$	$3.52\times10^{-4} \pm 1.76\times10^{-4}$	$3.52\times10^{-4} \pm 1.76\times10^{-4}$
CT15	$4.40\times10^{-4} \pm 1.97\times10^{-4}$	$7.92\times10^{-4} \pm 2.64\times10^{-4}$	$4.40\times10^{-4} \pm 1.97\times10^{-4}$	$2.64\times10^{-4} \pm 1.52\times10^{-4}$
CT16	$1.76\times10^{-4} \pm 1.24\times10^{-4}$	$4.40\times10^{-4} \pm 1.97\times10^{-4}$	$0.00\times10^{0} \pm 0.00\times10^{0}$	$8.80\times10^{-5} \pm 8.80\times10^{-5}$

Table 5.2. The QGSP_BIC_HP particles per cm^2 per PIC count for each irradiation position.

	Neutron	Proton	Photon	Electron	Positron
CS1	$1.17x10^{0} \pm 1.01x10^{-2}$	$2.14x10^{-2} \pm 1.37x10^{-3}$	$2.51x10^{0} \pm 1.49x10^{-2}$	$5.94x10^{-2} \pm 2.29x10^{-3}$	$2.29x10^{-2} \pm 1.42x10^{-3}$
CS2	$1.34x10^{0} \pm 1.09x10^{-2}$	$1.73x10^{-2} \pm 1.24x10^{-3}$	$2.90x10^{0} \pm 1.60x10^{-2}$	$6.48x10^{-2} \pm 2.39x10^{-3}$	$2.31x10^{-2} \pm 1.43x10^{-3}$
CS3	$1.42x10^{0} \pm 1.12x10^{-2}$	$1.14x10^{-2} \pm 1.00x10^{-3}$	$3.07x10^{0} \pm 1.64x10^{-2}$	$6.96x10^{-2} \pm 2.47x10^{-3}$	$2.22x10^{-2} \pm 1.40x10^{-3}$
CS4	$1.16x10^{0} \pm 1.01x10^{-2}$	$6.34x10^{-3} \pm 7.47x10^{-4}$	$2.51x10^{0} \pm 1.49x10^{-2}$	$4.87x10^{-2} \pm 2.07x10^{-3}$	$1.64x10^{-2} \pm 1.20x10^{-3}$
CT1	$5.45x10^{-1} \pm 6.92x10^{-3}$	$7.13x10^{-3} \pm 7.92x10^{-4}$	$1.10x10^{0} \pm 9.86x10^{-3}$	$2.28x10^{-2} \pm 1.42x10^{-3}$	$6.95x10^{-3} \pm 7.82x10^{-4}$
CT2	$5.57x10^{-1} \pm 7.00x10^{-3}$	$5.10x10^{-3} \pm 6.70x10^{-4}$	$1.14x10^{0} \pm 1.00x10^{-2}$	$2.39x10^{-2} \pm 1.45x10^{-3}$	$8.71x10^{-3} \pm 8.76x10^{-4}$
CT3	$5.41x10^{-1} \pm 6.90x10^{-3}$	$3.26x10^{-3} \pm 5.35x10^{-4}$	$1.12x10^{0} \pm 9.92x10^{-3}$	$2.14x10^{-2} \pm 1.37x10^{-3}$	$6.34x10^{-3} \pm 7.47x10^{-4}$
CT4	$4.54x10^{-1} \pm 6.32x10^{-3}$	$2.02x10^{-3} \pm 4.22x10^{-4}$	$9.54x10^{-1} \pm 9.16x10^{-3}$	$1.96x10^{-2} \pm 1.31x10^{-3}$	$6.51x10^{-3} \pm 7.57x10^{-4}$
CT5	$6.38x10^{-1} \pm 7.50x10^{-3}$	$8.71x10^{-3} \pm 8.76x10^{-4}$	$1.36x10^{0} \pm 1.10x10^{-2}$	$2.89x10^{-2} \pm 1.59x10^{-3}$	$1.02x10^{-2} \pm 9.48x10^{-4}$
CT6	$6.57x10^{-1} \pm 7.61x10^{-3}$	$7.13x10^{-3} \pm 7.92x10^{-4}$	$1.44x10^{0} \pm 1.13x10^{-2}$	$2.99x10^{-2} \pm 1.62x10^{-3}$	$1.15x10^{-2} \pm 1.01x10^{-3}$
CT7	$6.48x10^{-1} \pm 7.55x10^{-3}$	$3.96x10^{-3} \pm 5.90x10^{-4}$	$1.39x10^{0} \pm 1.10x10^{-2}$	$3.12x10^{-2} \pm 1.66x10^{-3}$	$9.42x10^{-3} \pm 9.10x10^{-4}$
CT8	$5.39x10^{-1} \pm 6.89x10^{-3}$	$3.08x10^{-3} \pm 5.21x10^{-4}$	$1.16x10^{0} \pm 1.01x10^{-2}$	$2.52x10^{-2} \pm 1.49x10^{-3}$	$7.83x10^{-3} \pm 8.30x10^{-4}$
CT9	$6.20x10^{-1} \pm 7.38x10^{-3}$	$7.57x10^{-3} \pm 8.16x10^{-4}$	$1.33x10^{0} \pm 1.08x10^{-2}$	$3.12x10^{-2} \pm 1.66x10^{-3}$	$1.06x10^{-2} \pm 9.68x10^{-4}$
CT10	$6.75x10^{-1} \pm 7.71x10^{-3}$	$6.07x10^{-3} \pm 7.31x10^{-4}$	$1.43x10^{0} \pm 1.12x10^{-2}$	$3.01x10^{-2} \pm 1.63x10^{-3}$	$1.26x10^{-2} \pm 1.05x10^{-3}$
CT11	$6.41x10^{-1} \pm 7.51x10^{-3}$	$5.46x10^{-3} \pm 6.93x10^{-4}$	$1.36x10^{0} \pm 1.09x10^{-2}$	$2.72x10^{-2} \pm 1.55x10^{-3}$	$7.83x10^{-3} \pm 8.30x10^{-4}$
CT12	$5.62x10^{-1} \pm 7.03x10^{-3}$	$2.2x10^{-3} \pm 4.22x10^{-4}$	$1.15x10^{0} \pm 1.01x10^{-2}$	$2.67x10^{-2} \pm 1.53x10^{-3}$	$6.51x10^{-3} \pm 7.57x10^{-4}$
CT13	$5.25x10^{-1} \pm 6.80x10^{-3}$	$6.69x10^{-3} \pm 7.67x10^{-4}$	$1.08x10^{0} \pm 9.74x10^{-3}$	$2.15x10^{-2} \pm 1.37x10^{-3}$	$8.36x10^{-3} \pm 8.58x10^{-4}$
CT14	$5.57x10^{-1} \pm 7.00x10^{-3}$	$4.93x10^{-3} \pm 6.59x10^{-4}$	$1.17x10^{0} \pm 1.01x10^{-2}$	$2.49x10^{-2} \pm 1.48x10^{-3}$	$8.01x10^{-3} \pm 8.39x10^{-4}$
CT15	$5.21x10^{-1} \pm 6.77x10^{-3}$	$3.43x10^{-3} \pm 5.50x10^{-4}$	$1.14x10^{0} \pm 1.00x10^{-2}$	$2.34x10^{-2} \pm 1.44x10^{-3}$	$7.39x10^{-3} \pm 8.07x10^{-4}$
CT16	$4.60x10^{-1} \pm 6.36x10^{-3}$	$2.20x10^{-3} \pm 4.40x10^{-4}$	$9.15x10^{-1} \pm 8.98x10^{-3}$	$1.72x10^{-2} \pm 1.23x10^{-3}$	$4.22x10^{-3} \pm 6.10x10^{-4}$

	Positive Pion	Negative Pion	Positive Muon	Negative Muon
CS1	$1.37x10^{-2} \pm 1.10x10^{-3}$	$1.34x10^{-2} \pm 1.08x10^{-3}$	$2.46x10^{-3} \pm 4.66x10^{-4}$	$3.26x10^{-3} \pm 5.35x10^{-4}$
CS2	$1.34x10^{-2} \pm 1.08x10^{-3}$	$1.76x10^{-2} \pm 1.24x10^{-3}$	$2.99x10^{-3} \pm 5.13x10^{-4}$	$3.78x10^{-3} \pm 5.77x10^{-4}$
CS3	$1.09x10^{-2} \pm 9.80x10^{-4}$	$1.05x10^{-2} \pm 9.60x10^{-4}$	$2.64x10^{-3} \pm 4.82x10^{-4}$	$1.50x10^{-3} \pm 3.63x10^{-4}$
CS4	$5.63x10^{-3} \pm 7.04x10^{-4}$	$6.34x10^{-3} \pm 7.47x10^{-4}$	$1.14x10^{-3} \pm 3.17x10^{-4}$	$1.32x10^{-3} \pm 3.41x10^{-4}$
CT1	$4.49x10^{-3} \pm 6.28x10^{-4}$	$4.66x10^{-3} \pm 6.41x10^{-4}$	$1.14x10^{-3} \pm 3.17x10^{-4}$	$2.02x10^{-3} \pm 4.22x10^{-4}$
CT2	$4.84x10^{-3} \pm 6.53x10^{-4}$	$3.61x10^{-3} \pm 5.63x10^{-4}$	$1.14x10^{-3} \pm 3.17x10^{-4}$	$1.32x10^{-3} \pm 3.41x10^{-4}$
CT3	$2.99x10^{-3} \pm 5.13x10^{-4}$	$3.34x10^{-3} \pm 5.42x10^{-4}$	$8.80x10^{-4} \pm 2.78x10^{-4}$	$5.28x10^{-4} \pm 2.16x10^{-4}$
CT4	$1.23x10^{-3} \pm 3.29x10^{-4}$	$1.14x10^{-3} \pm 3.17x10^{-4}$	$5.28x10^{-4} \pm 2.16x10^{-4}$	$5.28x10^{-4} \pm 2.16x10^{-4}$
CT5	$6.86x10^{-3} \pm 7.77x10^{-4}$	$5.37x10^{-3} \pm 6.87x10^{-4}$	$1.94x10^{-3} \pm 4.13x10^{-4}$	$1.76x10^{-3} \pm 3.94x10^{-4}$
CT6	$5.63x10^{-3} \pm 7.04x10^{-4}$	$4.05x10^{-3} \pm 5.97x10^{-4}$	$1.23x10^{-3} \pm 3.29x10^{-4}$	$1.67x10^{-3} \pm 3.84x10^{-4}$
CT7	$3.78x10^{-3} \pm 5.77x10^{-4}$	$3.34x10^{-3} \pm 5.42x10^{-4}$	$1.06x10^{-3} \pm 3.05x10^{-4}$	$1.23x10^{-3} \pm 3.29x10^{-4}$
CT8	$2.11x10^{-3} \pm 4.31x10^{-4}$	$2.29x10^{-3} \pm 4.49x10^{-4}$	$7.92x10^{-4} \pm 2.64x10^{-4}$	$4.40x10^{-4} \pm 1.97x10^{-4}$
CT9	$5.10x10^{-3} \pm 6.70x10^{-4}$	$6.42x10^{-3} \pm 7.52x10^{-4}$	$1.76x10^{-3} \pm 3.94x10^{-4}$	$1.67x10^{-3} \pm 3.84x10^{-4}$
CT10	$4.66x10^{-3} \pm 6.41x10^{-4}$	$5.37x10^{-3} \pm 6.87x10^{-4}$	$1.85x10^{-3} \pm 4.03x10^{-4}$	$1.76x10^{-3} \pm 3.94x10^{-4}$
CT11	$4.14x10^{-3} \pm 6.03x10^{-4}$	$3.96x10^{-3} \pm 5.90x10^{-4}$	$2.02x10^{-3} \pm 4.22x10^{-4}$	$1.23x10^{-3} \pm 3.29x10^{-4}$
CT12	$1.32x10^{-3} \pm 3.41x10^{-4}$	$2.29x10^{-3} \pm 4.49x10^{-4}$	$9.68x10^{-4} \pm 2.92x10^{-4}$	$8.80x10^{-4} \pm 2.78x10^{-4}$
CT13	$4.40x10^{-3} \pm 6.22x10^{-4}$	$4.40x10^{-3} \pm 6.22x10^{-4}$	$1.94x10^{-3} \pm 4.13x10^{-4}$	$1.23x10^{-3} \pm 3.29x10^{-4}$
CT14	$3.26x10^{-3} \pm 5.35x10^{-4}$	$4.05x10^{-3} \pm 5.97x10^{-4}$	$1.41x10^{-3} \pm 3.52x10^{-4}$	$1.41x10^{-3} \pm 3.52x10^{-4}$
CT15	$2.55x10^{-3} \pm 4.74x10^{-4}$	$3.26x10^{-3} \pm 5.35x10^{-4}$	$1.06x10^{-3} \pm 3.05x10^{-4}$	$1.32x10^{-3} \pm 3.41x10^{-4}$
CT16	$1.85x10^{-3} \pm 4.03x10^{-4}$	$1.32x10^{-3} \pm 3.41x10^{-4}$	$1.76x10^{-4} \pm 1.24x10^{-4}$	$2.64x10^{-4} \pm 1.52x10^{-4}$

Table 5.3. The QGSP_BERT_HP particles per cm^2 per PIC count for each irradiation position.

5.4.3 Neutron spectra dependence on irradiation position

The results for the neutron and proton fluence from several irradiation positions are seen in Figure 5.12. All of the positions were recorded simultaneously for the same number of primary particles. The different irradiation positions have a different solid angle, subtended through the concrete wall, from the target and as such significant differences in field intensity and energy is to be expected.

The positions chosen for graphing in Figure 5.12 were selected as they best illustrate the greatest variation in both the absolute fluence and difference in energy spectra. The most significant difference in energy was observed in the heavy charged particles such as the proton and pion components where both energy and fluence is increased at forward "downstream" irradiation positions. Changes in the energy spectra for the electromagnetic component were not observed for the different irradiation positions.

The neutron results reveal that position CS1 is associated with the highest neutron energy edge while position CT16 is associated with the lowest. This is attributable to the slight rotation of the side irradiation positions with respect to the target giving rise to position CS1 to be slightly more inline, with the target "downstream" of the beam resulting in slightly higher energy particles incident. The intensity of the main peak for the top positions does not appear to be as strongly correlated with position as for the side positions. This gives a slightly more uniform distribution of neutron field on the top positions due to the top positions being parallel to the beam direction.

The irradiation position with the highest neutron fluence overall is position CS3. The positions with the highest ratio of neutron to other particle components are the irradiation positions CS4 for the side and CT16 for the top positions. The spectra for each of these positions show minimal variations. As such it is mainly the ratio of the neutron to the other components of the field that should be taken into account in dosimetry measurement considerations.

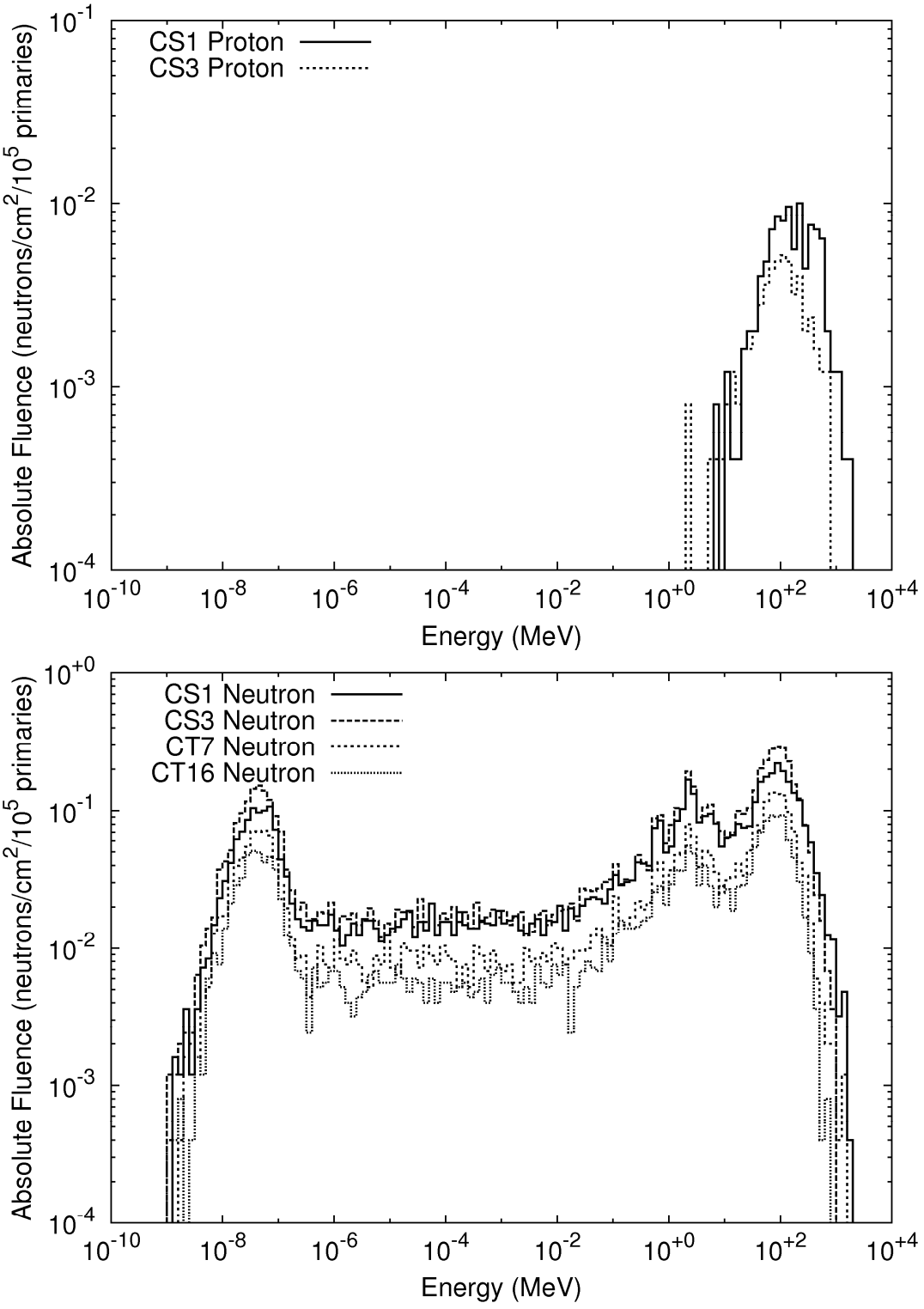

Figure 5.12. Selected irradiation position proton and neutron spectra. The proton spectra (top) shows the slight shift to higher proton energies at downstream (CS1) irradiation positions. The neutron spectra (bottom) shows the spectra with the most significant differences for both the top and side positions.

5.4.4 Calculation of ambient dose equivalent

ICRP Publication 60 (ICRP, 1991), only recently superseded by ICRP Publication 103 (ICRP, 2007), recommended a number of different sets of dosimetric definitions for radiation protection. The dosimetry value of interest for radiation protection applications for monitoring an area where a strongly penetrating radiation field is present is the ambient dose equivalent, $H^*(d)$, where d is defined as the depth of measurement within the ICRU sphere. The ambient dose equivalent value is used for radiation protection purposes as recommended by ICRU publication 39 and 40 (ICRU, 1985, 1988). This quantity is defined as the dose in a defined ICRU sphere (ICRU, 1980), at a recommended depth for most penetrating fields of 10 mm, on the radius opposing the direction of an extended radiation field. This is written as $H^*(10)$ to define the depth of measurement in the ICRU sphere.

The ambient dose equivalent was calculated for the particles observed at each irradiation position. The calculations were performed using published (Pelliccioni, 2000) fluence to ambient dose equivalent conversion factors. This was performed over the range of energies for which these factors exist. Some of the spectra had particles binned with energies outside of the range of the conversion factors. This was mostly for the lower energies of charged particles such as protons and electrons. By definition the values outside of the conversion factors for fluence to ambient dose equivalent are defined to be zero due to the lower energy particles not being able to penetrate sufficiently into the ICRU sphere to deposit energy in the relevant region to necessitate dosimetry consideration. This is important to consider for the charged particles in the field. There is a significant increase in the dose conversion for lower energy charged particles before going to zero due to the range of the charged particles being less than the relevant energy deposition region in the ICRU sphere. The ambient dose equivalent for each irradiation position using both QGSP_BERT_HP and QGSP_BIC_HP physics lists is tabulated in Tables 5.2 & 5.3.

	Neutron	Proton	Photon	Electron	Positron	$Pion^+$	$Pion^-$	Total	Percent Neutron	Percent Other
CS1	167.61	12.26	9.53	9.21	3.82	3.18	3.43	209.04	75.28%	24.72%
CS2	208.22	16.04	11.75	10.06	4.46	2.41	3.64	256.57	76.78%	23.22%
CS3	241.28	18.31	13.12	10.93	4.40	2.87	2.28	293.19	78.49%	21.51%
CS4	225.71	16.11	11.53	8.57	2.73	0.77	0.72	266.15	82.08%	17.92%
CT1	84.91	6.96	4.24	3.30	1.59	0.64	0.99	102.62	79.14%	20.86%
CT2	94.75	7.49	4.79	3.91	1.62	0.77	0.72	114.04	79.64%	20.36%
CT3	10.44	4.91	4.91	3.74	1.34	0.48	0.45	116.27	84.24%	15.76%
CT4	93.66	5.58	4.45	3.33	0.91	0.43	0.42	108.79	83.85%	16.15%
CT5	101.79	6.72	5.11	4.28	1.97	0.74	1.36	121.96	80.18%	19.82%
CT6	111.85	6.73	6.05	5.24	1.52	0.87	1.37	133.63	80.52%	19.48%
CT7	121.99	8.77	6.24	4.80	1.76	0.51	0.51	144.59	81.48%	18.52%
CT8	113.72	6.16	5.57	4.33	1.46	0.17	0.52	131.93	83.99%	16.01%
CT9	95.99	8.80	5.06	3.55	1.59	0.87	1.64	117.50	77.60%	22.40%
CT10	110.19	5.66	5.90	5.05	1.78	0.84	1.11	130.53	81.54%	18.46%
CT11	119.27	7.86	6.19	4.81	1.73	0.52	0.42	140.80	81.95%	18.05%
CT12	111.78	7.44	5.54	4.53	1.49	0.24	0.55	131.56	82.31%	17.69%
CT13	82.30	6.16	4.12	2.98	1.27	0.82	0.85	98.50	80.32%	19.68%
CT14	93.94	7.99	4.70	4.31	1.47	0.83	0.74	113.98	78.67%	21.33%
CT15	96.53	5.74	4.82	3.84	1.54	0.40	0.73	113.60	82.33%	17.67%
CT16	91.41	7.17	4.41	3.33	1.19	0.19	0.49	108.19	81.65%	18.35%

Table 5.4. The QGSP_BIC_HP simulated ambient dose equivalent for each of the particle types using the conversion factor from (Pelliccioni, 2000) at each irradiation position. Values are in pSv/cm^2/PIC count. Error in the dose values is approximately 10%.

	Neutron	Proton	Photon	Electron	Positron	$Pion^+$	$Pion^-$	Total	Percent Neutron	Percent Other
CS1	284.73	28.05	13.08	13.77	6.85	12.58	12.34	371.40	69.56%	30.44%
CS2	327.26	22.16	15.38	14.27	6.79	12.35	16.25	414.46	73.35%	26.65%
CS3	338.20	16.01	16.73	15.19	6.47	10.14	10.04	412.79	77.95%	22.05%
CS4	267.51	9.25	13.79	10.47	4.67	5.37	6.20	317.28	81.39%	18.61%
CT1	133.70	8.15	5.84	4.89	2.05	4.11	4.38	163.11	78.0%	22.0%
CT2	135.39	5.71	6.12	5.54	2.42	4.60	3.30	163.08	79.55%	20.45%
CT3	128.73	5.09	6.09	5.05	1.83	2.81	3.26	152.86	81.25%	18.75%
CT4	108.35	2.85	5.28	4.51	1.93	1.24	1.07	125.22	84.42%	15.58%
CT5	152.28	10.28	7.27	6.39	3.16	6.39	5.17	190.95	74.61%	25.39%
CT6	158.85	9.82	7.80	6.63	3.56	5.23	3.70	195.58	76.87%	23.13%
CT7	150.71	5.53	7.60	6.65	2.75	3.64	3.19	180.06	80.52%	19.48%
CT8	126.94	4.46	6.40	5.23	2.28	2.06	2.20	149.57	82.17%	17.83%
CT9	149.04	10.07	7.05	6.88	3.10	4.63	5.82	186.60	74.80%	25.20%
CT10	163.78	8.45	7.69	7.01	3.76	4.32	5.03	20.04	77.86%	22.14%
CT11	149.40	7.79	7.49	6.30	2.45	3.93	3.83	181.19	78.72%	21.28%
CT12	130.40	2.70	6.29	5.57	1.91	1.31	2.32	150.50	84.58%	15.42%
CT13	128.33	8.32	5.68	4.74	2.46	4.11	4.07	157.70	77.11%	22.89%
CT14	134.03	8.16	6.31	5.05	2.21	3.11	3.87	162.73	78.58%	21.42%
CT15	122.86	6.80	6.27	4.91	2.21	2.42	3.11	148.58	79.06%	20.94%
CT16	108.72	2.91	4.99	3.34	1.33	1.69	1.34	124.33	85.64%	14.36%

Table 5.5. The QGSP_BERT_HP simulated ambient dose equivalent for each of the particle types using the conversion factor from (Pelliccioni, 2000) at each irradiation position. Values are in pSv/cm^2/PIC count. Error in the dose values is approximately 10%.

A graph of the range of the conversion factors to the spectra of the CERF facility filed can be seen in Appendix A.5.1. There is a slight discrepancy between the conversion factors outlined by Pelliccioni and the values provided in ICRU Report 57 (ICRU, 1998) and ICRP Publication 74 (ICRP, 1996), which supersedes the commonly used factors outlined in ICRP Publication 51 (ICRP, 1987), for the neutron to ambient dose equivalent conversion coefficients. For consistency, and to ensure the complete energy range of interest is covered, the conversion coefficients by Pelliccioni have been used for all conversions. The variation between the reference conversion coefficients of Pelliccioni and the ICRP and ICRU are shown in Appendix A.5.2.

The calculation of the ambient dose equivalent for the positive and negative muon component of the CERF field is omitted from tables 5.4 and 5.5 due to the negligible (< 0.1%) contribution to the overall dose. This is both due to the very low particle fluence and the relatively low conversion factor for muons compared to other particles present in the field.

The findings in this work regarding the ambient dose equivalent values for the CERF facility designated irradiation positions reveal a non-negligible dose attributable to components of the field other than neutrons. Depending on the irradiation position there is an approximate 15-30% component of non-neutron dose. Failure to account for this component in instrument calibrations could be problematic. Consideration of variations in the charged particle contributions to dose at different positions may also be needed. The concrete top positions show lower charged particle ambient dose equivalent than that of the concrete side positions CS1 and CS1 which are rotated slightly forward with respect to the target.

Tables 5.4 and 5.3 display the ambient dose equivalent contributions from different radiation field components for all of the different designated irradiation positions. The different charged particle components of the varying fields will result in different dosimetric responses depending on the type of dosimeter. Dosimeters based on moderators and thermal neutron detection reactions ^{6}LiF, ^{3}He, ^{10}B are generally insensitive to, or have a threshold set to filter out, low LET charged particles. Dosimeters based on spectroscopic detectors with a low discriminator threshold, such as semiconductor and scintillator type detectors, will respond to the charged particle

components resulting in higher doses than expected or measured using a neutron sensitive instrument.

Measurement of the full energy of all charged particles in a detector, in order to perform fluence based dosimetry, is difficult if not impossible due to the very high energies (up to several GeV). Conventional dosimetry techniques for mixed neutron gamma fields are generally not equipped or designed to appropriately respond to high energy charged particles.

Methods to overcome the implicit complications of dosimetry in a mixed radiation field are to utilise either 1) a detector capable of discriminating the different types of high energy radiation, 2) multiple detectors designed to detect particular components of the radiation field or 3) a dosimeter that is radiation type insensitive for dose measurement where the response can be characterised in terms of the total ambient dose equivalent.

Method three can be achieved through use of the regional microdosimetry approach. The application of microdosimetric techniques to the CERF facility radiation field is suitable for use as it only requires the lineal energy deposition of the field components. The high energies involved within the charged particle components will only deposit a portion of the energy on a microdosimetric scale.

The microdosimetric spectrum should be capable of differentiating the field components based on the lineal energy deposition. This is due to the various field component particles having a different linear energy transfer (LET) for the same total particle energy i.e. a 100 MeV pion and a 100 MeV proton will deposit different energies in a microdosimeter while having the same total energy. This will be covered further in Chapter 6.

5.5 GEANT4 Comparisons

5.5.1 GEANT4 Irradiation Position Physics List comparison

The simulations described above suggest further considerations of the effects of different physics lists are important. In a further series of simulations four different hadronic physics lists were selected and implemented in the simulations to contrast any irregularities between the different theoretical ways GEANT4 handles the physical processes involved. The different physics lists were selected on the basis of their validity for interactions in the energy range of interest. The physics lists selected were:

(1) QGSP_BIC_HP,
(2) QGSP_BERT_HP,
(3) LHEP_BIC_HP,
(4) LHEP_BERT_HP.

All physics lists included the high precision low energy neutron models (as indicated by the _HP suffix). The acronym QGSP stands for Quark Gluon String Precompound and LHEP stands for Low and High Energy Parameterization. The principle point of difference between the four lists was the use of either the Bertini cascade model or Binary cascade model, as indicated by BERT and BIC respectively. This affects how high energy pion interactions are handled. Since the primary beam consisted of 61% 120 GeV/c pions, the results for the Bertini and binary cascade models would be expected to show variations in results where notable discrepancies between the models are apparent. The older LHEP physics lists were included to compare against the newer QGSP lists.

The total number of particles produced by the simulations at CS1 with each of the physics list is shown in Table 5.6. Variations in the total number of particles produced between each of the different physics lists were observed.

The ratios of the total number of particles for each field component appear similar regardless of the physics list used. The Bertini Cascade model produced the highest number of total particles for each component.

	Neutron	**Photon**	**Proton**	**Electron**	**Positron**	**Pion Total[1]**	**Muon Total[1]**
QGSP_BIC_HP	7736	19933	109	474	159	83	37
QGSP_BERT_HP	13276	28531	243	675	260	308	65
LHEP_BIC_HP	8768	20509	152	470	174	104	43
LHEP_BERT_HP	10914	22070	144	488	169	109	40

Table 5.6. The GEANT4 simulated number of particles at position CS1 for 10^5 primary hadrons on target (4.55 PIC counts). [1]Muon and pion totals are the sum of $muon^+$, $muon^-$, $pion^+$ and $pion^-$ number of particles respectively.

The conversion to ambient dose equivalent for each of the physics lists revealed that the QGSP_BERT_HP reproduced the closest ambient dose equivalent to published irradiation position results (Mitaroff, A., 2002). This is shown in section 5.4.4.

The normalised contribution to the neutron, photon, electron and proton energy fluence at position CS1 is shown in Figure 5.13 (a-d). No significant variation in the spectra for the various particles in the field between the four physics models investigated was evident. This illustrates that the main difference between the different physics lists tested was the total fluence of particles produced and the secondary reactions in the materials of the CERF facility geometry.

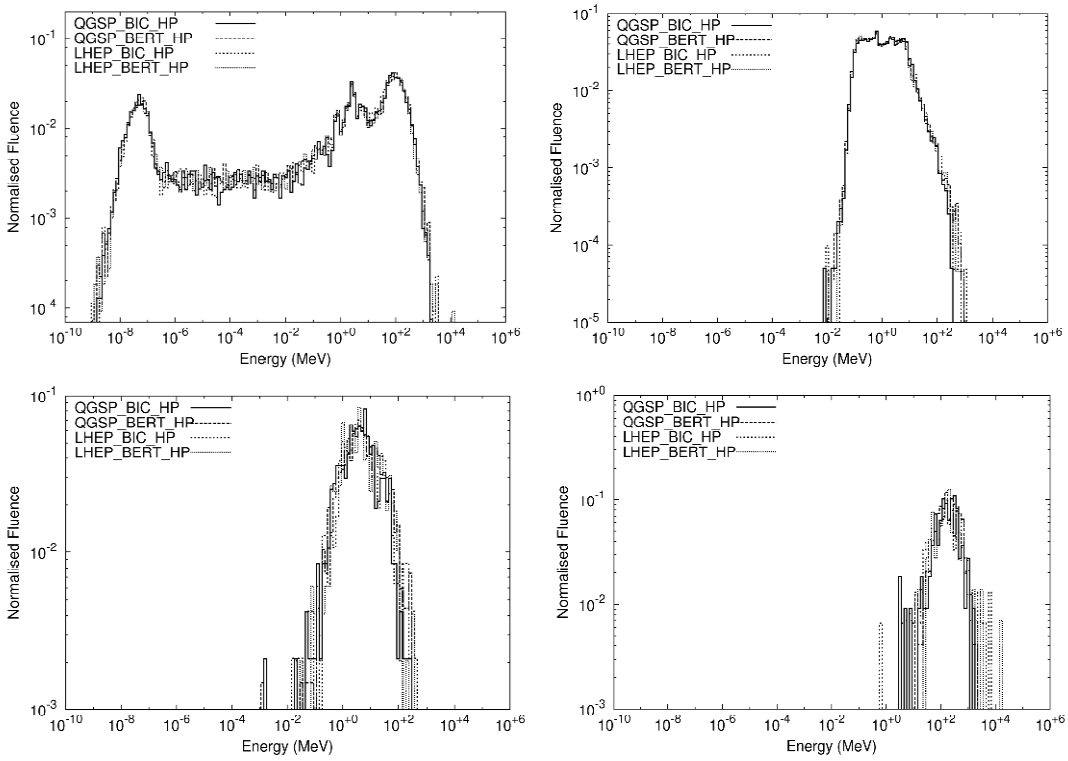

Figure 5.13. Comparison of the different physics models used in the GEANT4 simulation for irradiation position CS1. Clockwise from top left the particles are a) neutrons b) photons c) electrons and d) protons. The spectra are normalised to unity under each spectrum.

All of the physics lists examined utilised the same standard electromagnetic model for their electromagnetic interactions. As expected, the electromagnetic components of the field only show variations due to the hadronic interactions producing secondary electromagnetic components of the spectrum.

5.5.2 GEANT4/IAEA data comparison

Comparison of the results for the concrete side positions of the GEANT4 simulation with the concrete side spectrum from the International Atomic Energy Agency (IAEA) Compendium of Neutron Spectra, TRS 403 is shown in Figure 5.14.

The results of the neutron spectra attained from the GEANT4 simulation are in good agreement with the published IAEA reference spectrum, collected using experimental Bonner sphere measurements (IAEA TRS-403, 2001). The main difference between the two spectra is apparent within the energy region from approximately 0.1 eV to 0.5 MeV.

The GEANT4 simulated data underestimates the number of events within the continuum. This explained by the incomplete geometry utilised for the simulation which did not take into account the concrete labyrinth walls and floor for neutron scatter. These walls and floor were left out due to the unacceptably long simulation time if included (ref. section 5.3.3). There is also variation between the two spectra at the higher energies above approximately 500 MeV. This is likely to be attributable to limitations in the unfolding code where the minimal set of inputted data points from the Bonner spheres leads to inaccuracies at high energies for the fluence in this region.

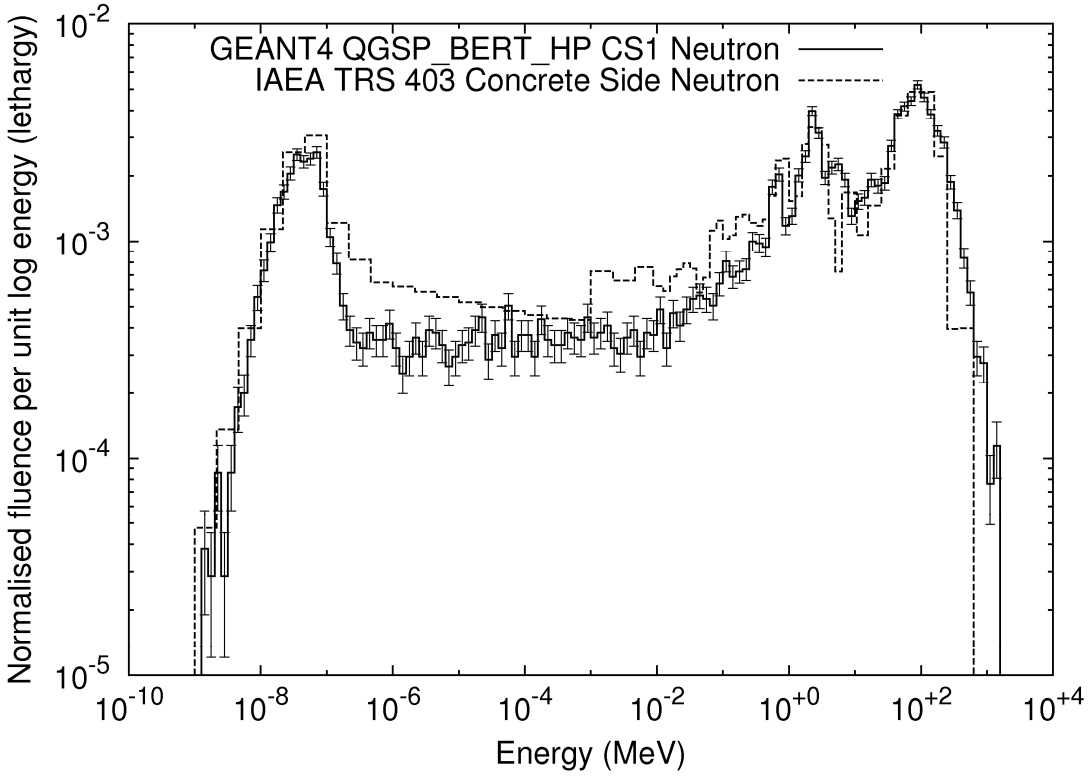

Figure 5.14. Comparison of the GEANT4 simulated output from the position CS1 with the IAEA TRS 403 Compendium of Neutron Spectra for the listed CERF concrete side spectrum. The spectra are normalised to total fluence for comparison. The GEANT4 error bars are the root mean square error.

The main peak in the spectrum at 100 MeV as well as the sharper peaks at 500 keV to 5 MeV is apparent in both spectra. The thermal neutron peak from simulation is well reproduced. The thermal peak, although not significantly contributing to the total dose when compared to the higher neutron energies, can potentially increase the response of a detector depending on the cross section of the materials composing the sensitive volume. Depending on the reaction with the thermal neutron i.e. fission, alpha

emission, de-excitation, it is possible to deposit much higher energies in the sensitive volume than the incident thermal neutron energy.

5.5.3 GEANT4/FLUKA comparison

The GEANT4 simulation was compared with the results from the previously published FLUKA simulation (Mitaroff et al., 2002). The FLUKA data were obtained via private communication with M. Fuerstner, C. Theis and H. Vincke. The data for the different components of the spectrum have been compared using the data from the both simulation toolkits and the results for each are presented in Figures 5.15 to 5.18.

The comparison between the GEANT4 and FLUKA spectra demonstrate a good agreement for the majority of the CERF field components in both energy and shape of the CERF spectra components for which comparison was available. The components of the field for which there were no direct comparison possible were the electron, positron and charged muon components. The FLUKA simulation for the electron and positron components only tallied the total number of particles for both components combined together, which was much lower in normalised magnitude than any single bin for either of the electron or positron components of the GEANT 4 data (see top graph of Figure 5.10). The FLUKA simulation did not tally any charged muon component unlike the GEANT4 simulation (see Figure 5.11).

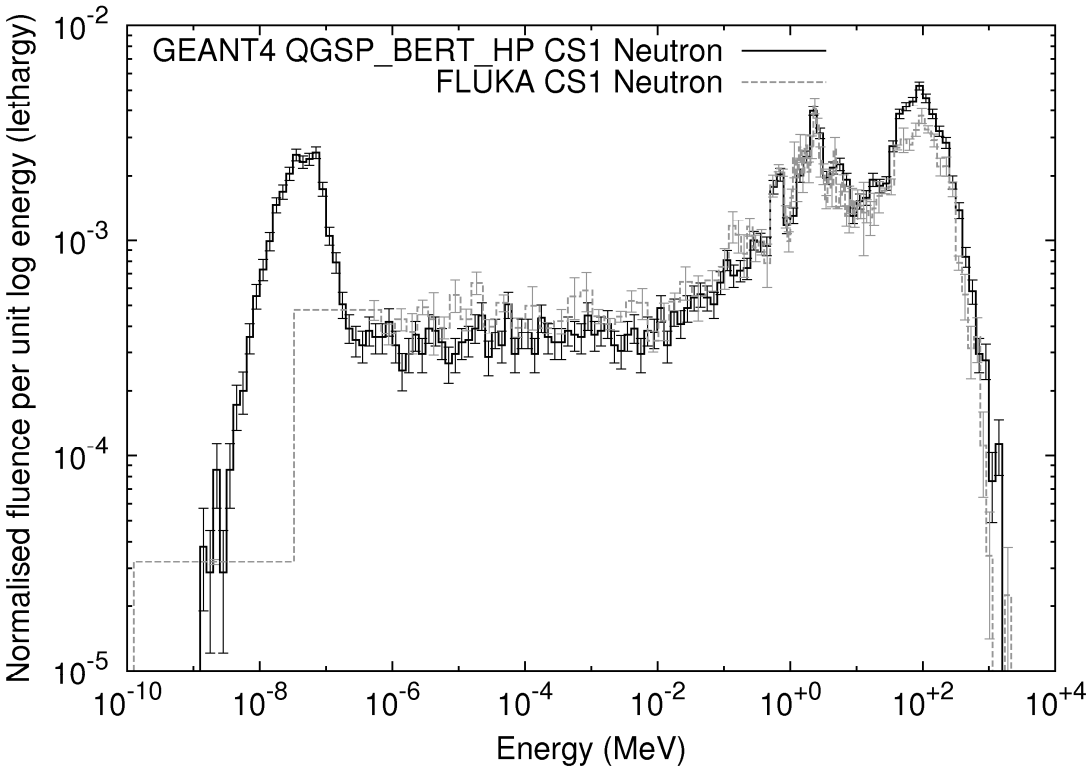

Figure 5.15. Comparison of the neutron spectra predicted by the GEANT4 and FLUKA Monte Carlo simulations for position CS1. The spectra are normalised to the area of the neutron spectrum equal to unity for comparison.

The neutron spectra were normalised to obtain unity area under the curve for both the FLUKA and GEANT4 simulation results. This normalisation factor was then used for each of the different components of the field to give a relative comparison to the neutron component of the field.

Comparison between the FLUKA and GEANT4 neutron spectra at CS1 revealed a satisfactory fit for the majority of the neutron energy range, from approximately 1 eV to 50 MeV, with only a few minor statistical variations attributable to the different number of primary particles used for the different simulations and the different spectrum binning. The FLUKA data appears to have a comparatively reduced component for the main peak at about 100 MeV. The FLUKA simulation did not take into account thermal neutron transportation and binning, as the thermal energy peak in the GEANT4 spectrum centred at 0.05 eV is not seen at all in the FLUKA neutron spectrum, due to low energy limitations below 1 eV.

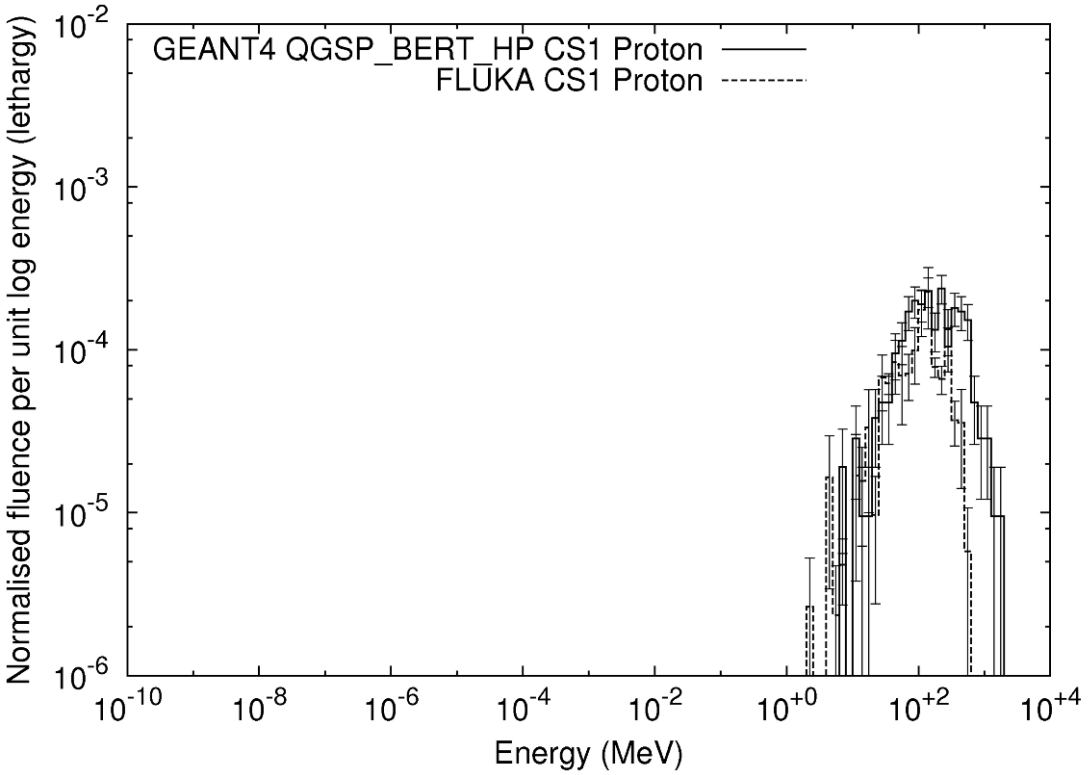

Figure 5.16. Comparison of the proton spectra for the GEANT4 and FLUKA Monte Carlo simulations for position CS1. The spectra are normalised to the area of the neutron spectrum equal to unity for comparison.

The comparison between the proton components of the spectrum are shown in Figure 5.16. The uncertainties for both of the GEANT4 and FLUKA simulations are relatively large due to the low number of protons produced compared to the gamma and neutron components. However both GEANT4 and FLUKA reveal a proton component centred at approximately 100 MeV. The GEANT4 proton spectrum has higher energy particles in the spectrum with the maximum recorded particle energy of approximately 1.7 GeV while the maximum recorded particle energy in the FLUKA simulation was approximately 560 MeV. This is due to the difference in the physics models used to simulate the proton transport and high energy interactions.

The significance of this comparison of the CERF facility proton component is that both GEANT4 and FLUKA show a reasonable high energy proton component at the CERF facility. This can potentially lead to differences in readings with dosimeters due to proton-nucleus reactions with light nuclei contributing to different energy depositions depending on detector composition.

The photon component of the CERF facility field is shown in Figure 5.17. The FLUKA simulation tracks the photon component down to an energy of only 100 keV, although below this the spectrum in the GEANT4 simulation the intensity of events drops off significantly. The majority of the two spectra are comparable to each other with the FLUKA simulation data showing slightly lower photon intensity and a larger statistical fluctuation due to lower total simulation statistics.

In both photon spectra the 511 keV electron-positron annihilation peak can be seen with an apparent slight shift between the different spectra due to the size and position of the binning. The high energy component above approximately 6 MeV of the FLUKA simulation has a few unusual features not apparent in the GEANT4 simulation; this can be explained due to relatively lower statistics in the FLUKA simulation than the GEANT4 simulation.

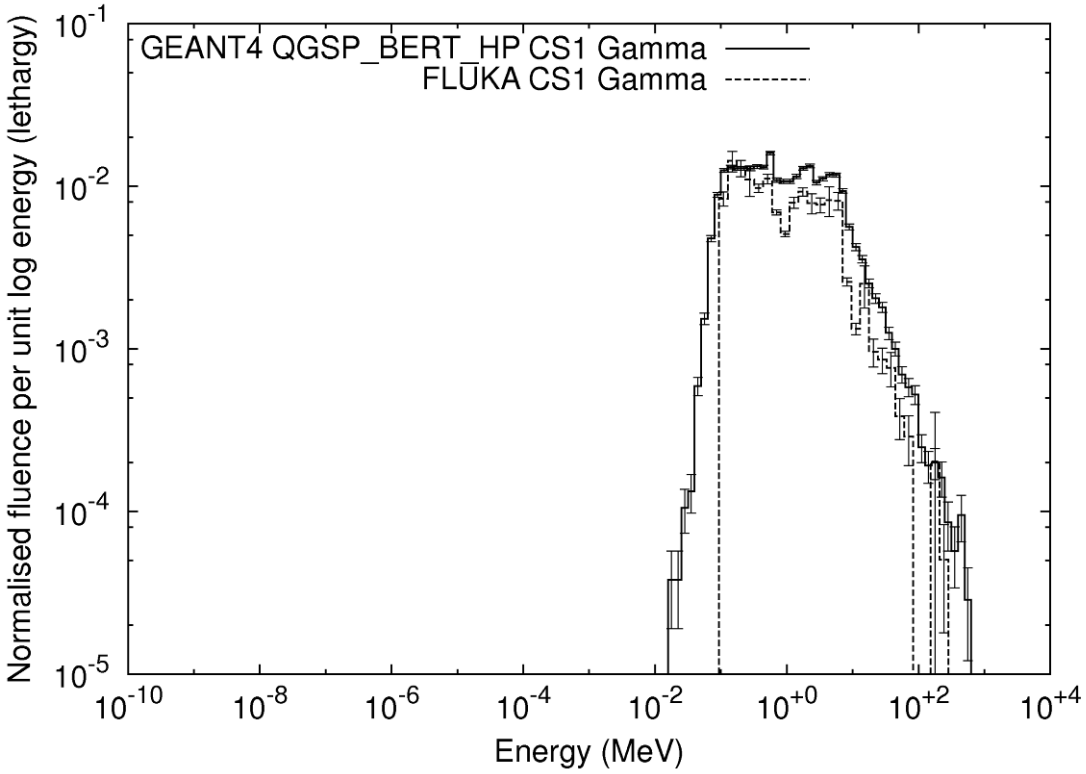

Figure 5.17. Comparison of the proton spectra predicted by the GEANT4 and FLUKA Monte Carlo simulations for position CS1. The spectra are normalised to the area of the neutron spectrum equal to unity for comparison.

Pion spectra from FLUKA and GEANT4 are shown in Figure 5.18. The total charged pion component normalised to the neutron field component is comparable in both energy and intensity to the proton component of the CERF facility field.

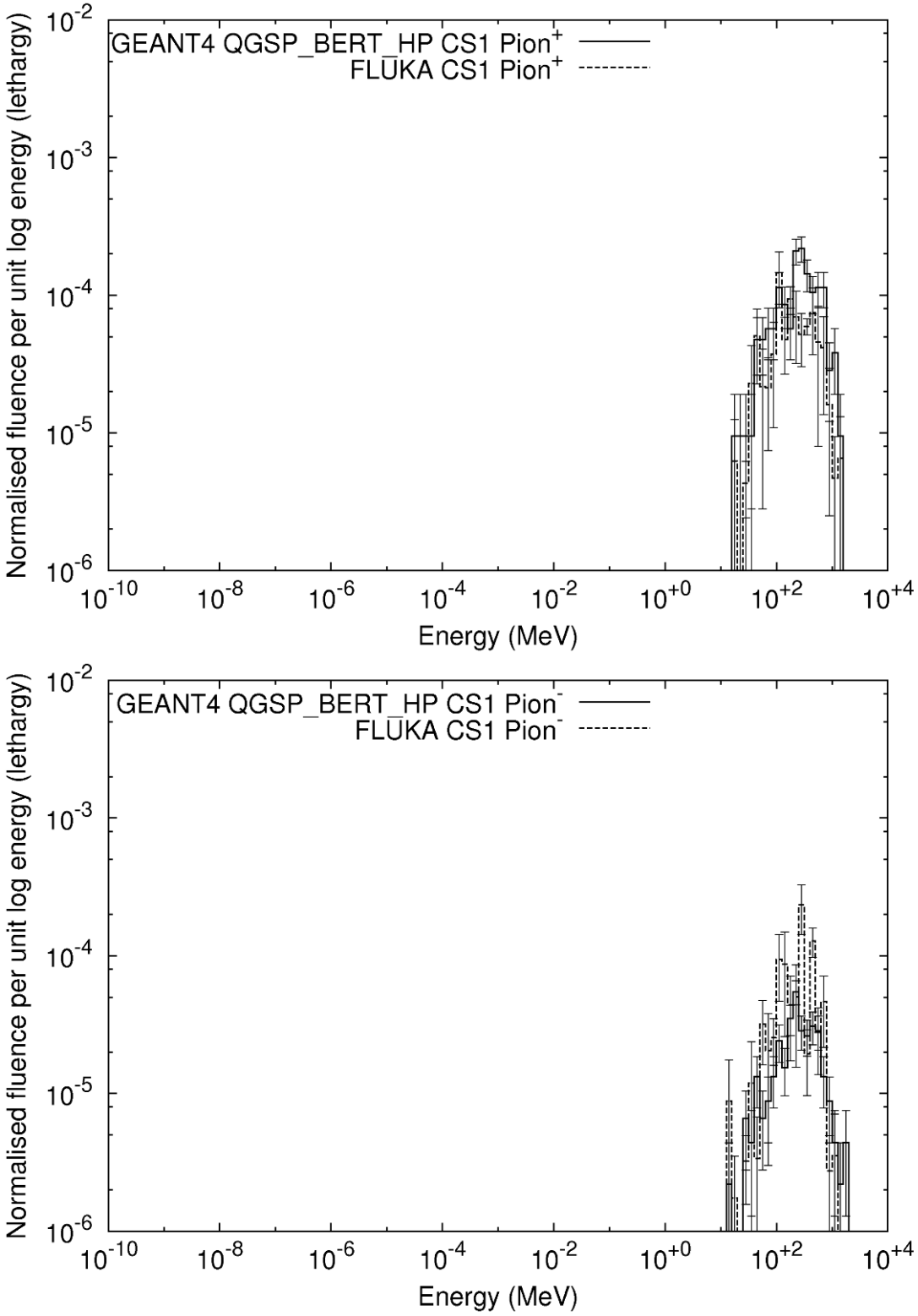

Figure 5.18. Comparison of the pion spectra predicted by the GEANT4 and FLUKA Monte Carlo simulations for position CS1. top: positive pion, bottom: negative pion.

The spectra are normalised to the area of the neutron spectrum equal to unity for comparison.

The GEANT4 and FLUKA spectra for both the positive and negative pion components of the field are almost identical in the energy range covered. Relative to the FLUKA component, the GEANT4 simulation results were lower in total intensity for the negative pion component and higher intensity for the positive pion component.

Statistically the pion spectra for both the GEANT4 and the FLUKA simulations overlap within the range of the error bars.

The comparison between the GEANT4 and FLUKA simulations are mostly in good agreement with only slight discrepancies between them. Further simulation of the field taking into account the electron and positron components of the CERF facility using FLUKA would be beneficial as these components are significant in the GEANT4 simulation.

The important comparison of the neutron spectra revealed that GEANT4 compares well with the standard simulated spectrum used at the facility as the reference spectrum.

5.6 Discussion

The simulation of the CERF facility using GEANT4 has provided a useful understanding and validation of the types of radiation present at the CERF facility. Other than the inevitable gamma radiation component for any high energy radiation field, the next most dominant component of the field is the neutron component. The neutron component of the field produced by the GEANT4 simulation agrees well with both of the IAEA TRS 403 and published FLUKA reference data for the neutron field component. The GEANT4 toolkit appears to offer additional information than FLUKA in being able to predict not only the high energy component of the neutron spectrum but also the significant thermal energy component of the neutron field.

The GEANT4 simulation also predicts a significant high energy charged particle component of the field. The total non-neutron component of the field can contribute

up to approximately 20-30% of the ambient dose equivalent dependent on the irradiation position used. Results from silicon PIN diodes and SOI microdosimeters experiments, presented in the next chapter, with farther elucidate the charged particle contribution.

The side irradiation positions display a slight increase in both particle energy and charged particle fluence. This is due to the side positions being rotated with an angle of 3.45° into the direction of the primary beam with an energy and fluence increase expected due to the increased forward projections of particle production within the target in the laboratory frame of reference. A similar increase in energy, but lower fluence, is also seen in the forward top concrete positions due to the higher energy particles having a conserved momentum in the beam direction.

Of the different physics lists tested, the QGSP_BERT_HP physics list produces the closest match to the previously published values of ambient dose equivalent. The QGSP_BERT_HP physics list has both a good spectral match to published simulated and experimental measurements in addition to the closest comparison for measured doses at the different irradiation positions, hence total particle fluence. This physics list is thus to be considered the most suitable physics list for simulating the types of particles and energies involved with the CERF facility.

The spectra produced using the GEANT4 simulation of the CERF facility with the QGSP_BERT_HP physics list is used in the next chapter to simulate the response of detectors to the CERF facility radiation field. The component particle spectra for each irradiation position can be used to determine the response of a detector to each particle type.

6. Response of SOI Microdosimetry to the CERN-EU High Energy Reference Field (CERF)

6.1 Introduction

As outlined in chapter 5, the CERF Facility produces a radiation field similar to those encountered at aviation altitudes. Testing of semiconductor (Spurný et. al., 2007) and tissue equivalent proportional counter (Rollet et. Al., 2004) detectors at the facility are under ongoing study. This chapter outlines the first testing of the CERF field using Silicon On Insulator (SOI) microdosimeter devices to determine the microdosimetric qualities of the radiation field.

The complex radiation field produced at the CERF facility is difficult to measure in terms of absorbed doses from the separate components of mixed radiation fields consisting of neutrons, photons and charged particles. The CERF facility radiation field is valuable for being able to produce a radiation field for the calibration and testing of dosimeters capable of measuring the dose equivalent in an aviation radiation environment. A SOI microdosimeter is suited to these types of radiation environments as explained in this chapter. For microdosimetry, the composition of the particles in the field is not required to be known while microdosimetric spectra can be easy converted into dose equivalent for any type of radiation field.

Both a SOI microdosimeter and silicon PIN diodes were used to investigate the radiation field properties. The SOI microdosimeter is used to determine the lineal energy spectrum of the field and to produce a microdosimetric analysis of the field using a bare SOI microdosimeter. The contribution from neutrons via recoil protons was also studied by the placement of a thick layer of Low Density PolyEthylene (LDPE) over the SOI microdosimeter and PIN diode.

6.2 Method

6.2.1 The Facility

A SOI microdosimeter of 10 μm thick sensitive volume was selected to permit measurement of low LET particles anticipated to be present in the field based on the results of the GEANT4 simulations (Chapter5).

The CERF field has previously been modelled via FLUKA simulations (Theis et al., 2005) (Hajek et. al., 1999). In these studies the equivalent dose per primary particle on the target was determined from the neutron spectra. It is these values that are used to calibrate the facility for use with neutron dosimeters for aviation applications. These calibration factors are performed using only the neutron contribution under the assumption that the neutron energy spectrum at altitude does not significantly change with altitude/latitude. Chapter 5 has indicated that the assumption of only neutron contribution to dosimetric calibration at the facility requires both a simulated and experimental assessment.

To maximise data collection, all experimental measurements were performed at irradiation position CS3 which provided the highest dose per PIC of all available positions at CERF. The particle fluence at CS3 was 4.62 ± 0.04 particles per PIC count per square centimetre. At 10^4 PIC counts per 14.4 second spill this results in 3.2×10^3 $cm^{-2}s^{-1}$ particles. 66.51% of the total field consists of photons, leaving only 10^3 neutrons and other charged particles per square centimetre per second during a spill. A spill was in a supercycle (period between spills) of 42 seconds, resulting in an average of approximately 370 neutrons and charged particles per square centimetre per second when averaged out over the entire duration of the run.

This rate of fluence at CS3 allowed, for the SOI microdosimeter array A4 with sensitive area 4.4 mm^2, to have approximately sixteen neutrons and charged particles per square centimetre per second incident upon the detector sensitive area. This allowed the SOI microdosimeter to be capable of measuring the field, in a practical time of 24 hours of continual beam, by having approximately 14×10^6 neutrons and charged particles

incident on the detector surface. The side positions, as shown in Chapter 5, are associated with a higher than average facility contribution to dose from charged particles in the field. This results in position CS3 having 2.5 times more neutrons and charged particles than the average of the top positions.

6.2.2 Instrumentation

Measurements of the microdosimetric spectra within CERF were obtained with recently developed SOI microdosimeters (Rosenfeld A.B., 1999) as well as a conventional HAWK Tissue Equivalent Proportional Counter (TEPC). The results provide improved understanding of the microdosimetric properties of the CERF field as well as demonstrating the usefulness of SOI microdosimeters for such measurements.

The contribution of charged particles present within the CERF neutron dominated radiation field is also investigated through measurements obtained with silicon PIN diodes.

The HAWK TEPC is designed to be a portable radiation environmental monitor for use in obtaining microdosimetric measurements of high energy neutron dominated fields (Far West Technologies Inc., 2000). The HAWK TEPC consists of a 5 inch gas proportional counter with an A150 conductive tissue equivalent plastic wall. The HAWK TEPC is filled to a propane gas pressure of 2 micron tissue equivalent site size (7 Torr).

6.2.3 Experimental Setup

The SOI microdosimeter and HAWK TEPC were placed sufficiently close to one another so as to validate a working assumption that both instruments were exposed to the same field. Data was acquired simultaneously.

The system used to collect the SOI microdosimetry data was designed to be lightweight, battery powered and portable. Data acquisition consisted of a CREMAT charge sensitive preamplifier and shaping amplifier and an AMPTEK Pocket MCA 8000a.

SOI microdosimeter measurements were performed with and without the presence of a 45 mm thick low density polyethylene (LDPE) converter layer (density 0.92 g/cm^3) placed in front of the device. The converter was used to produce a recoil proton component associated with elastic reactions of the incident neutrons. The acquisition time for all measurements was 30 hrs within a high intensity field of 1x10^4 PIC counts per spill for a total of 2x10^7 PIC counts. The pulse-height spectrum acquired from each irradiation was then processed into a lineal energy spectrum for interpretation.

TEPC measurements within the CERF facility have been performed previously (Rollet, et. al. 2007) and simulated using the FLUKA Monte Carlo code (Rollet et. al., 2004).

PIN Dosimeter diode measurements were performed subsequent to the SOI microdosimeter and HAWK TEPC measurements at the same field position. Measurements with and without a 12.5 mm thick LDPE converter layer were made. The duration of the PIN diode measurements was 2.5 hours each at 1x10^4 PIC counts per spill. This resulted in a total exposure of 1.93x10^6 PIC counts for each measurement.

6.2.3 GEANT4 Simulation

GEANT4 (GEometry ANd Tracking) (Agostinelli et al., 2003) (Allison et. al., 2006) version 4.8.2.p01 was used to model and simulate response of the SOI microdosimeter detector geometry to the CERF field. The CERF facility was simulated using GEANT4 to determine the energy spectra for each of the particles produced at each of the irradiation positions as discussed in Chapter 5.

The particle spectra from the previous simulation of the CERF facility were used as the input spectra into a GEANT4 simulation to model the response of a SOI microdosimeter to the various components of the field for the same configuration as the experiment. The PIN diode response was also simulated in this manner.

The geometry of the GEANT4 simulation for the SOI microdosimeter and PIN diode took into account both the isotopic composition of the elements used for the device

fabrication and the accurate physical geometry of the SOI microdosimeter and surrounding microchip packaging.

The physics list selected for use in the simulation was the QGSP_BERT_HP physics list. This list has been applied successfully in past simulations of the CERF facility with good agreement to published dose rate values as well as experimental measured neutron spectral data and FLUKA simulations (see Chapter 5, Section 5.5).

6.3 Results

6.3.1 SOI Microdosimeter

The acquisitions with the SOI microdosimeter, both with and without the LDPE converter, were taken for the same PIC count exposure for approximately the same exposure duration of approximately 30 hours. The total PIC exposure for each measurement, either with or without the LDPE layer, was $2x10^7$ total PIC counts.

The comparison of the lineal energy deposition for the measurement with and without the 45 mm LDPE layer is shown in Figure 6.1. Both of the spectra are normalised to unity area under the curve.

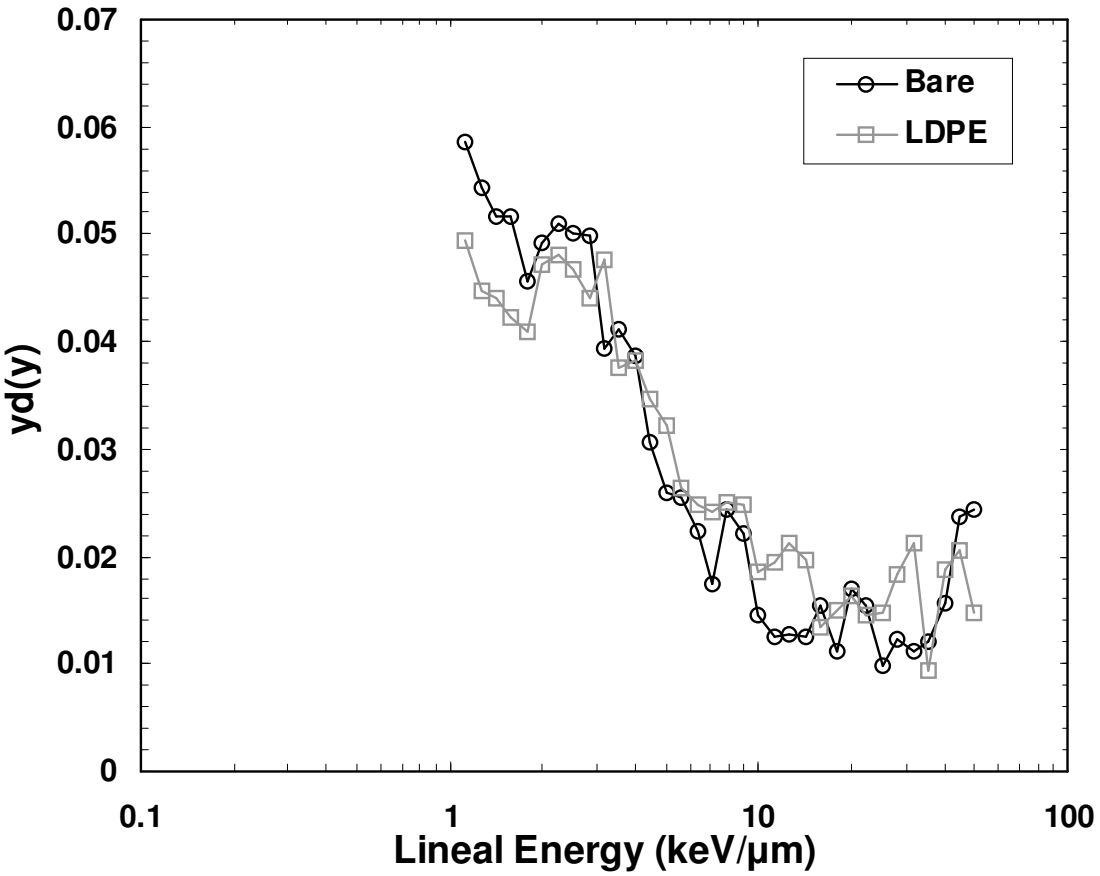

Fig. 6.1. Comparison of the normalised lineal energy spectrum with and without 45 mm LDPE converter in front of the SOI microdosimeter. Uncertainties of up to 20% are expected due to the small sensitive area of the SOI microdosimeter.

The addition of LDPE to the front of the SOI microdosimeter results in a relative decrease in low lineal energy depositions below 3-4 keV/µm and a slight relative increase in lineal energy deposition events above this energy. There are two explanations for this observation.

1) The energy fluence of primary protons from the mixed radiation field incident on the detector assembly with the 45mm LDPE present are moderated to lower energies giving rise to the observed relative increase in high lineal energy events.

2) The additional recoil proton component resulting from the interaction of the neutrons with the LDPE contributes to the observed increase in high lineal energy events. This will also harden the neutron component of the field reducing low energy deposition silicon recoils. Elastic and inelastic neutron cross sections for hydrogen and silicon are discussed in chapter 7.

The implication of the minimal change observed in the lineal energy deposition spectrum when the LDPE layer is placed in front of the SOI microdosimeter is that the majority of the energy deposition events are occurring due to direct interactions of charged particle component of radiation field with the sensitive volume. It is mainly due to the small charged particle and gamma components of the field dominating the energy deposition events occurring in the sensitive volume of the SOI microdosimeter compared to the events occurring due to recoil protons from neutrons in the field.

A direct comparison of the LET spectrum from the HAWK TEPC with the SOI microdosimeter lineal energy deposition spectrum, adjusted for tissue equivalency, is presented in Figure 6.2.

The SOI microdosimetric spectrum has been adjusted using the geometric tissue equivalence scaling factor for silicon to tissue dose conversion (ζ=0.63) (Bradley et al., 1998) and the SOI microdosimeter charge collection efficiency (CCE) (80% at the 10 V bias used) (Cornelius et al., 2003). This allows for the most equitable comparison between the TEPC and the silicon based SOI microdosimeter.

The SOI microdosimeter measurements are range bound at both the low and high lineal energy regions when compared to the HAWK TEPC. The lower limit in lineal energy of the SOI microdosimeter of approximately 1 keV/μm is set by the noise threshold. An upper limit of approximately 70 keV/μm in silicon is established by the gain setting of the pulse processing circuitry. The HAWK overcomes the range limitation through the use of two separate MCAs with different gain settings allowing for a wide range of measurement in tissue equivalent lineal energies from 0.2 keV/μm to over 1 MeV/μm. A lower noise threshold is also apparent.

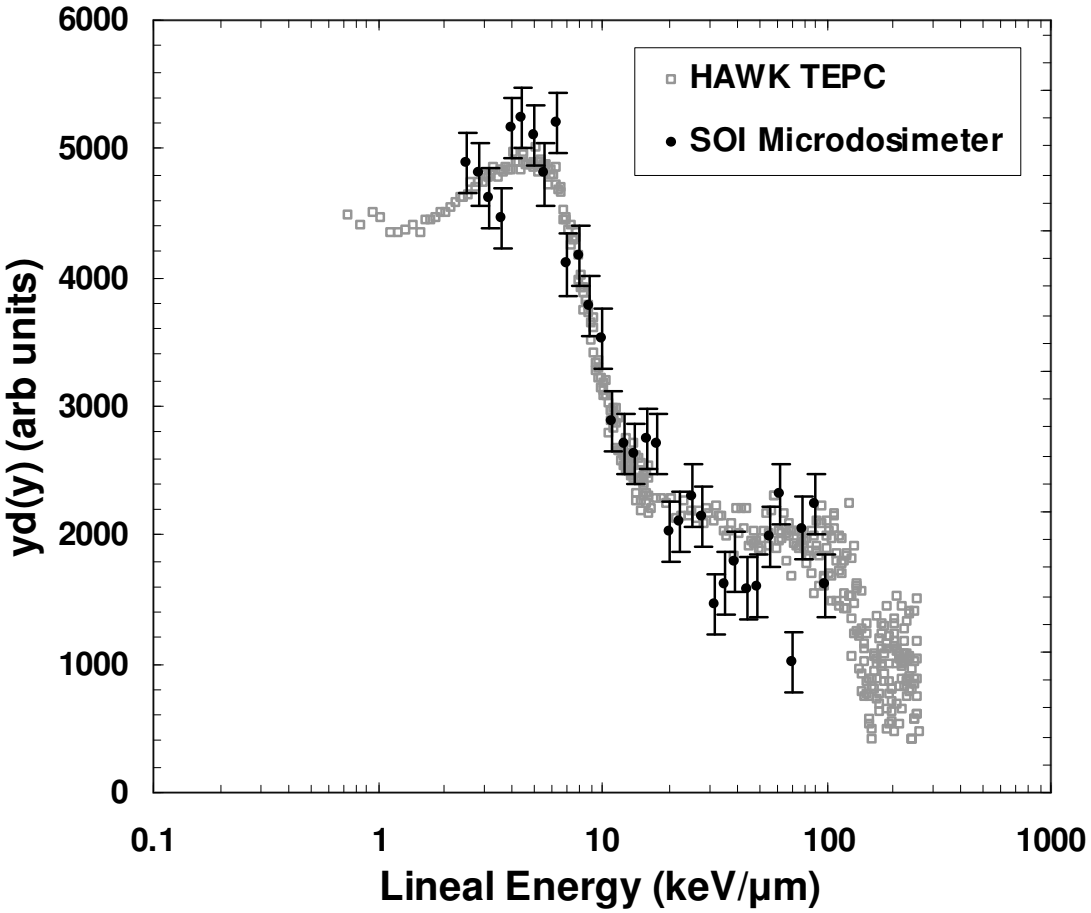

Fig. 6.2. Comparison of the lineal energy spectra as obtained with the SOI microdosimeter and HAWK TEPC.

The TEPC SOI microdosimeter comparison shows a reasonable agreement between the two measurements with all spectral features reproduced. Low statistics in the SOI microdosimeter measurement associated with the small sensitive volume is apparent. The HAWK TEPC data was provided "as is" without error estimation, however due to the large detector size and acquisition time errors are estimated to be significantly smaller than for the SOI microdosimeter. The results obtained with the SOI microdosimeter are also in agreement with previously published tissue equivalent proportional counter results (Rollet et. al. 2005; Badhwara et. al., 2002).

The energy deposition in the SOI microdosimeter was simulated in GEANT4 for each component of the radiation field at the facility as simulated in Chapter 5. The outputs of the SOI microdosimeter for each field component were converted to lineal energy

deposition spectra of yd(y) vs lineal energy. The components of the field, as well as the total energy deposition for the total field for the bare and LDPE covered SOI microdosimeter, are shown in Figures 6.3 and 6.4. The rebinning of the simulated total microdosimetric spectrum was normalised to unity. The contribution from each of the components of the field were normalised to the relative contribution from the particle type compared to the total microdosimetric spectrum.

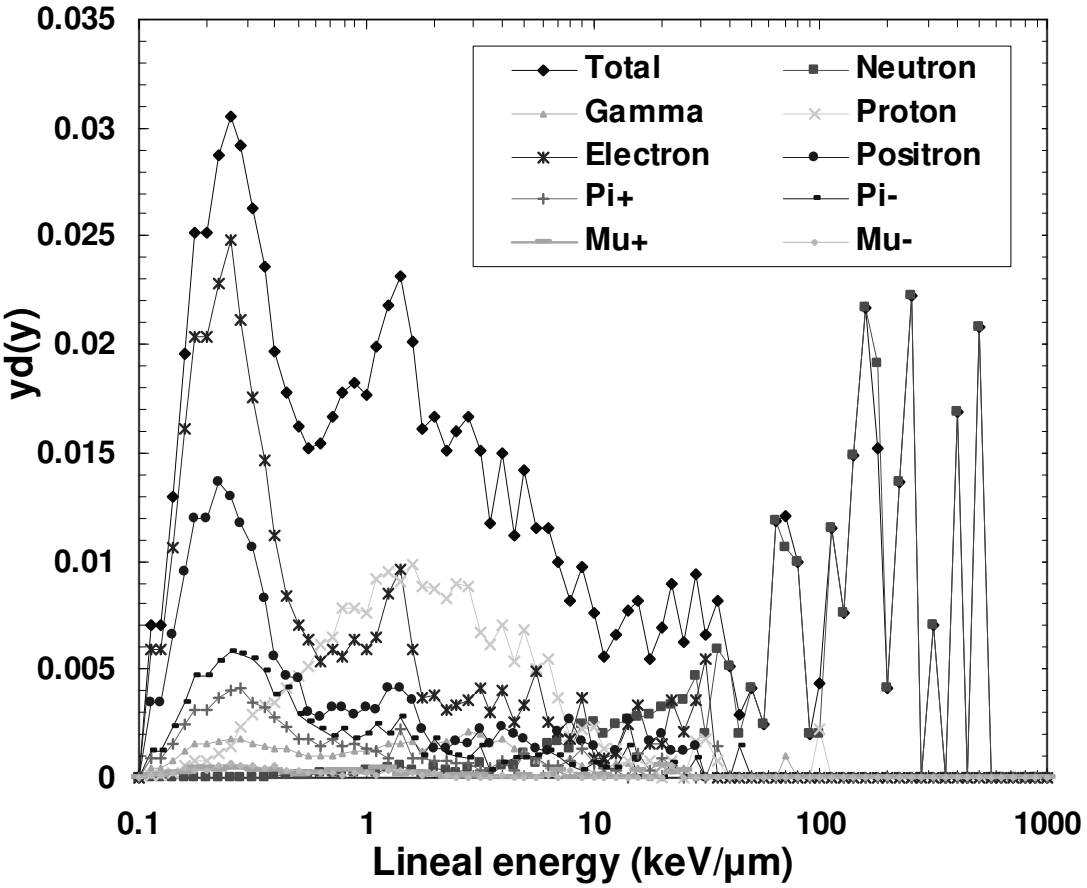

Fig. 6.3. The GEANT4 simulated bare SOI microdosimeter lineal energy spectrum. The components of the CERF facility field comprising of the total detector response are shown.

The bare SOI microdosimeter simulation shown in Figure 6.3 illustrates the direct contribution due to direct interactions from the CERF facility field. Above 10-40 keV/µm the lineal energy deposition is mostly associated with the silicon recoil reactions from neutrons in the sensitive volume of the SOI microdosimeter. The major component in the bare SOI microdosimeter spectrum in the mid range lineal energies, from 1.5-7 keV/µm, is due to direct proton contributions from the CERF facility field

(ie., not recoil protons due to neutrons). Below 0.6 keV/μm the field is dominated by the contribution from electrons and positrons in the field. The peak seen at 1.4 keV/μm is due to the range of electrons in 10 μm of silicon having a maximum lineal energy deposition of 1.7 keV/μm corresponding to the maximum lineal energy component of the peak. Higher lineal energy depositions come from electrons with a longer chord length through the sensitive volume as well as electrons above 50 MeV where the electron-nuclear interactions begin to dominate and lead to much higher lineal energy deposition events.

The simulated results from the SOI microdosimeter with the 45 mm of LDPE converter layer are shown in Figure 6.4.

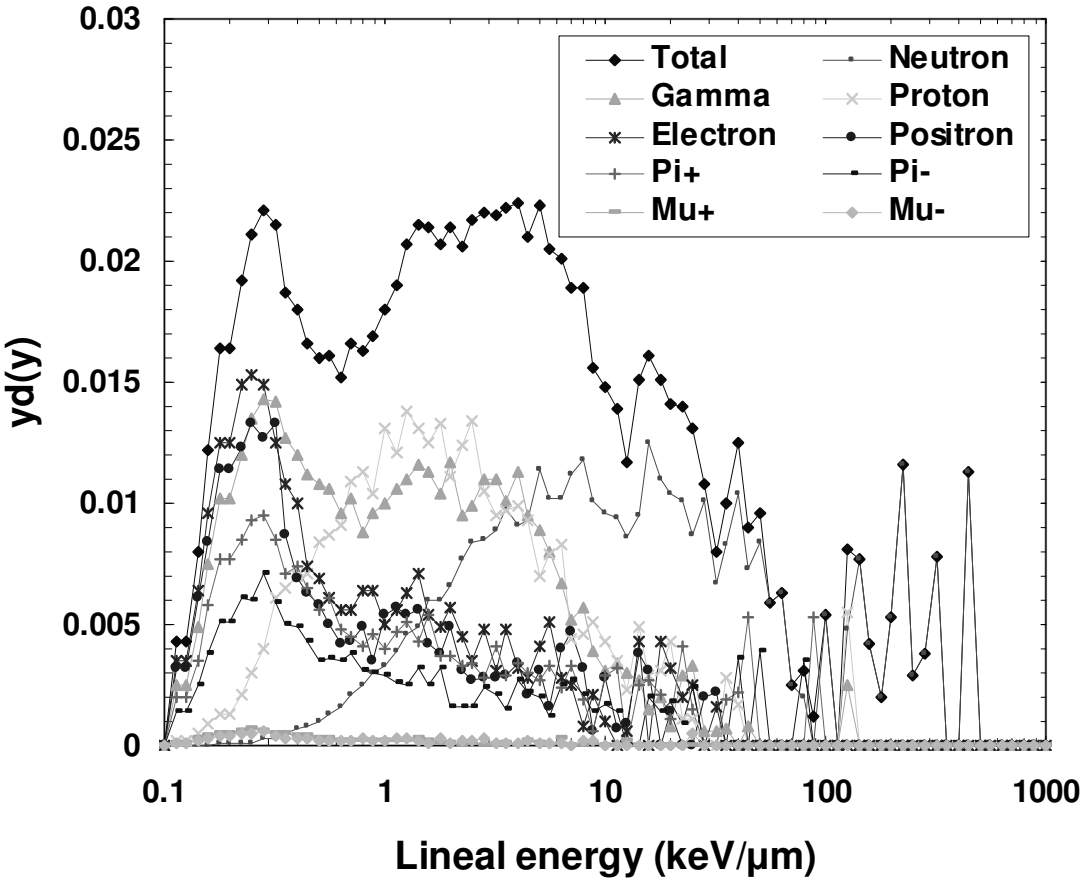

Fig. 6.4. The GEANT4 simulated SOI microdosimeter lineal energy spectrum with a 45 mm LDPE converter. The components of the CERF facility field comprising of the total detector response are shown.

With the addition of the LDPE converter the neutron component dominates above 5 keV/μm due to the addition of proton recoils.

Even with the addition of this recoil proton component the majority of the lineal energy deposition events are from the other charged particle and gamma components of the field.

The gamma component of the spectrum is enhanced in the 0.3 keV/μm peak and above due to the contribution of photoelectrons generated in the LDPE layer. The presence of the LDPE layer moves the lineal energy depositions of the low LET particles to higher lineal energies as evidenced by the electron and positron spectra. This occurs due to both the moderation of the particle energy resulting in a shift to higher lineal energy deposition and additional scatter from the LDPE layer resulting in a longer chord length. This is from energy deposition of particles originally normal to the device prior to interacting within the LPDE layer are scattered before passing through the sensitive volume at an oblique angle.

The simulated LDPE covered SOI microdosimeter shows an increased contribution from the proton recoils due to the neutron field component in mid range, 1.4 - 30 keV/μm, compared to the bare spectra. This shows more of a significant change than seen in the experimental comparison. The comparisons between the simulated spectra are shown in Figure 6.5.

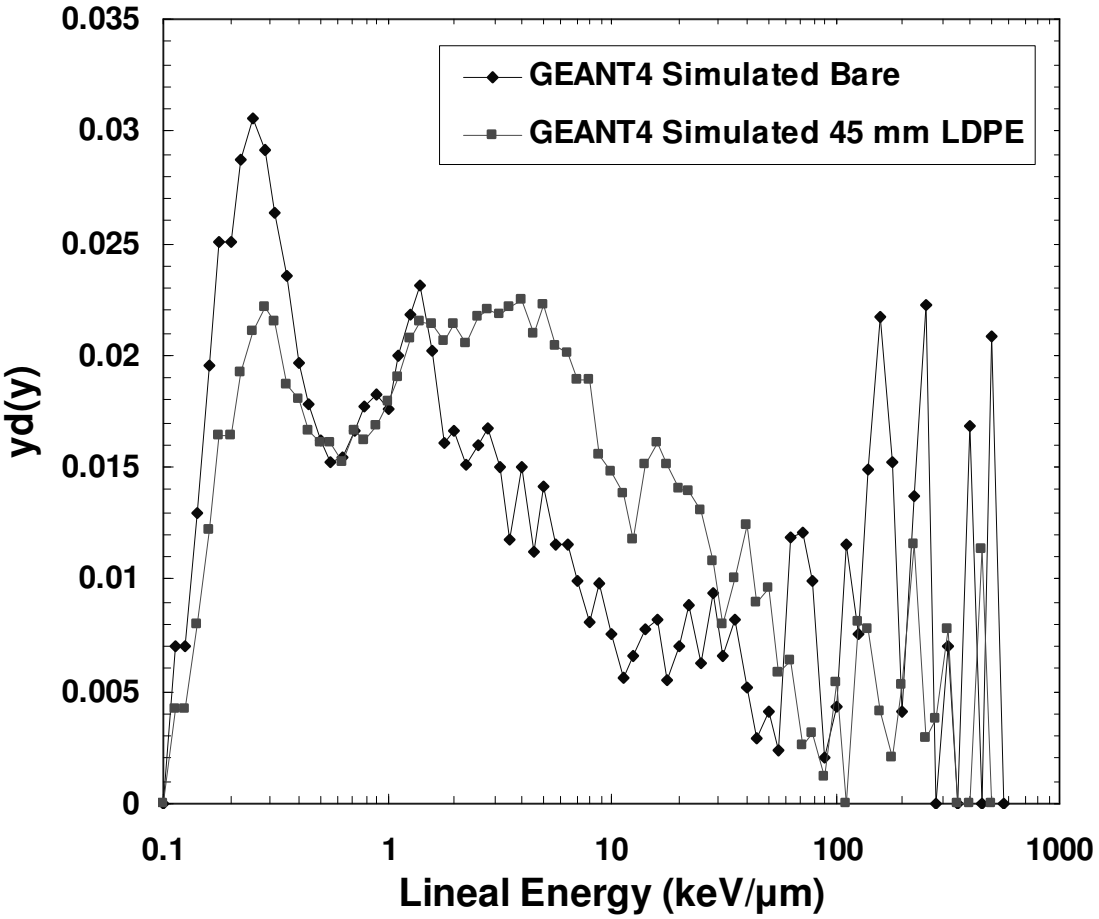

Fig. 6.5. Comparison of the GEANT4 simulated SOI microdosimeter lineal energy spectra with and without a 45 mm LDPE converter.

The increase in contribution of energy deposition events corresponding to lineal energies between 1.4 and 30 keV/µm in the simulated LDPE covered SOI microdosimeter can be attributed to the recoil proton component. The increase of this recoil proton component in the simulated response is, as described in Chapter 5, due to limitations on the simulation time, the direction of the field used in the simulation is normal to the front surface of the LDPE and SOI microdosimeter geometry. The field at the facility contains an angular distribution of particles due to cascades and moderation in the concrete wall, resulting in a slight increase in oblique strikes from proton recoils.

There is a relative reduction in the low energy peak due to the gamma and low LET particle components of the field due to the addition of the LDPE layer. This is mainly due to the interactions of gammas and electrons in the LDPE volume scattering and losing energy resulting in both a higher LET and longer path lengths due to more

oblique strikes from the scatter. This results in an increase in the lineal energy depositions from approximately 1.5 to 10 keV/µm.

The comparison of the GEANT4 simulated and experimental measurement with the bare SOI microdosimeter are shown in Figure 6.6. The spectra were normalised over the range of the lineal energies covered by the experimental measurements.

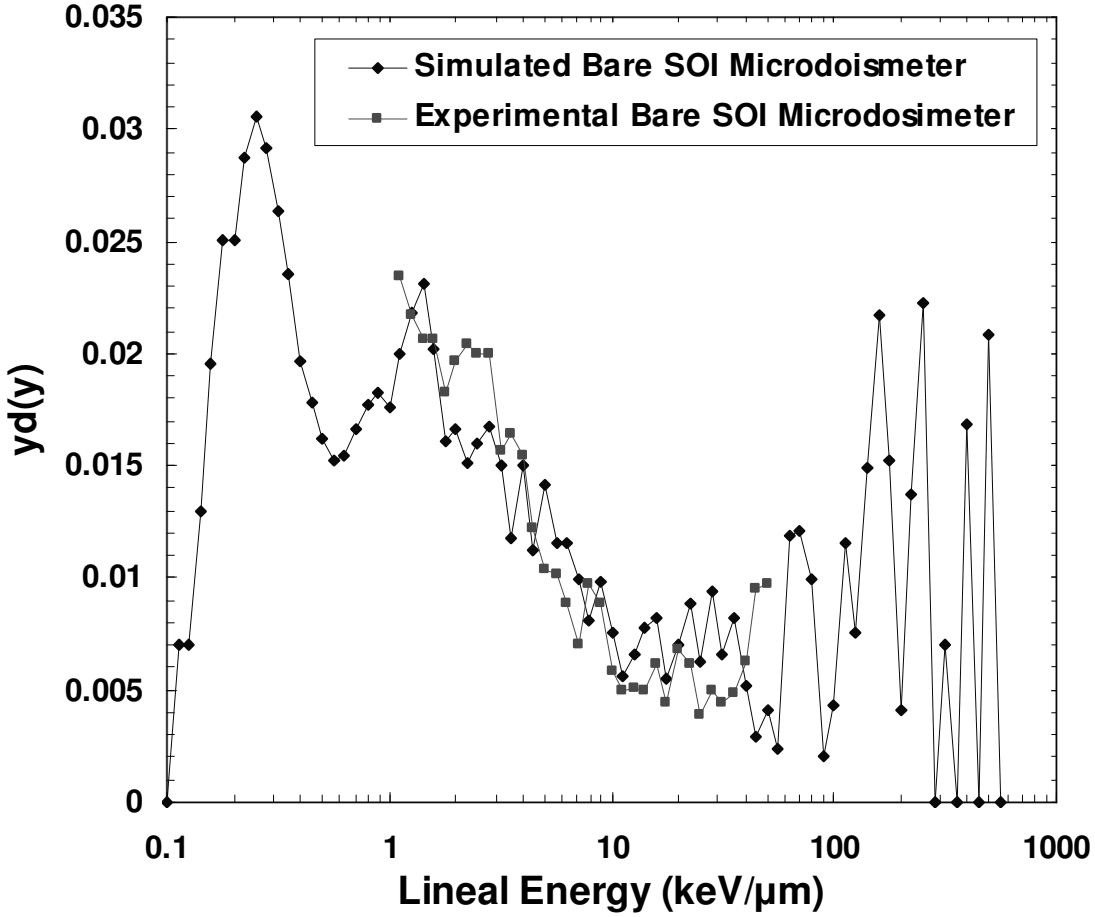

Fig. 6.6. Comparison of the GEANT4 simulated and experimentally measured bare SOI microdosimeter lineal energy spectra.

The simulated and experimental measurements for the bare SOI microdosimeter correspond well over the range of measurement. This indicates that over the range of measurement from 1 to 50 keV/µm the majority of the contribution to the spectrum comes from the non-neutron components of the field as illustrated in Figure 6.3 where the proton and electron components make up the majority of the contribution to the lineal energy deposition up to 10 keV/µm.

The neutron inelastic silicon recoil contribution begins to contribute significantly at energies above 10 keV/µm where silicon recoils begin to dominate.

The comparison of the GEANT4 simulated and experimental measurement with the LDPE converter are shown in Figure 6.7. The simulated data is shows an increase in the lineal energy depositions from 3.5 to 30 keV/µm compared to the experimental results.

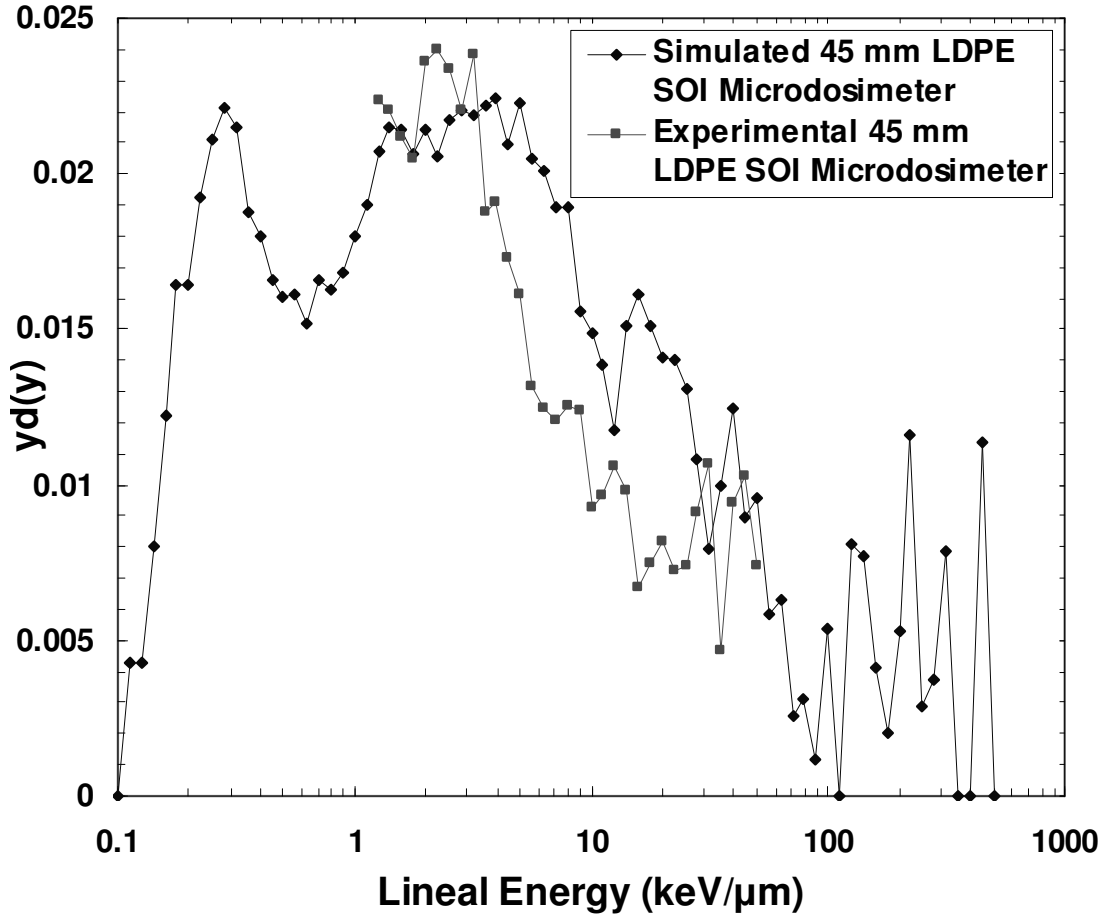

Fig. 6.7. Comparison of the GEANT4 simulated and experimentally measured 45 mm LDPE covered SOI microdosimeter lineal energy spectra.

The explanation of this difference in the simulated and experimental lineal energy deposition spectra is due to the increase in the recoil proton component in the simulated lineal energy spectrum. The angular distribution of the recoil protons from a normally incident neutron beam, as in the simulated case, produces recoils with a lower energy at longer chord length distributions and hence a higher lineal energy deposition for these events. The primary neutrons from the experimental case where there was an angular

distribution will allow for lower lineal energy deposition events for direct recoils at an angle.

The simulation also may have overestimated the contribution from secondary electrons originating in the LDPE layer, as shown in Figure 6.4, as being the main contributor to the discrepancy between the experimental and simulated data.

The comparison between the GEANT4 simulated results to the experimental data agrees well for the scenario of the SOI microdosimeter without the LDPE converter layer. There is a discrepancy between the results of the simulated and experimental SOI microdosimeter with the LDPE layer. This shows an increase in the contribution to the microdosimetric spectrum for the simulated result in the mid lineal energy range of 3.2 to 30 keV/μm, the cause of this is due to the angular distribution of the generated neutron-proton recoils. These appear to show the contribution from the charged particles to be a significant portion of the detector response in the CERF facility field.

These results are supported by 300 μm thick PIN diode measurements taken with and without an LDPE converter. These results are shown in the next section (6.3.2).

6.3.2 PIN Diode

The 300 μm PIN diode measurements were taken with and without a 12.5 mm thick LDPE converter. Each exposure was performed for precisely 2.5 hours live time at $1x10^4$ PIC counts per spill for a total exposure of $1.93x10^6$ PIC counts.

The bare PIN diode recorded a total of $2.86x10^5$ energy depositions while the LDPE covered diode recorded $2.65x10^5$ energy deposition events. There are $1.66x10^4$ more energy deposition events in the bare PIN diode than the LDPE covered PIN diode. The reduction of counts for the LDPE covered PIN diode is due to the LDPE layer acting as shielding for the moderate to lower energy neutrons below approximately 35 MeV.

Proton recoils produced by neutrons from this energy and below, depending on the position within the LDPE layer at which the recoil proton was generated, are likely to be absorbed within the LDPE layer before reaching the sensitive volume of the PIN

diode. The results of these measurements and a subtraction of the bare measurement from the LDPE covered PIN diode measurement are shown in Figure 6.8.

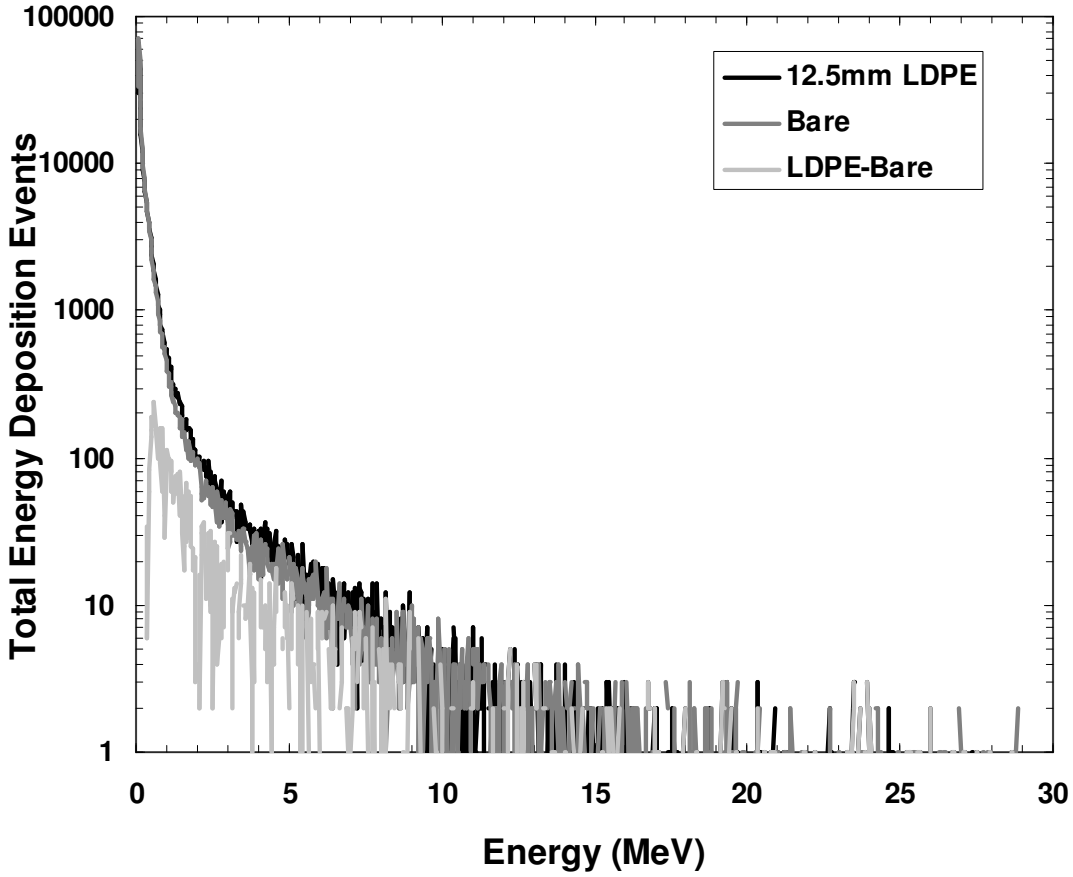

Fig. 6.8. Experimental PIN diode results for a bare PIN diode and covered with 12.5 mm LDPE converter. There are 1.66×10^4 more total counts in the bare PIN diode than in the LDPE covered case. Each of the measurements was for 2.5 hours at 1×10^4 PIC counts per spill.

These measurements show a decrease in energy deposition events below approximately 330 keV in the LDPE covered PIN diode, compared to the bare PIN diode, and a relative increase in energy deposition events above this energy. The difference between the LDPE and bare PIN diode measurement can be seen clearly in Figure 6.9.

The difference at 330 keV in the ratio of LDPE covered to bare PIN diode measurements corresponds to the minimum lineal energy deposition from the recoil protons in 300 μm of silicon. The events from 330 keV and below are from maximum energy (E_{max}) proton recoils from approximately 135 MeV neutrons and higher in

energy in the 300 μm thickness of silicon. Below 330 keV the bare PIN diode produces more events compared to the LDPE converter scenario, as it is not being shielded and moderated from the neutrons by the LDPE layer.

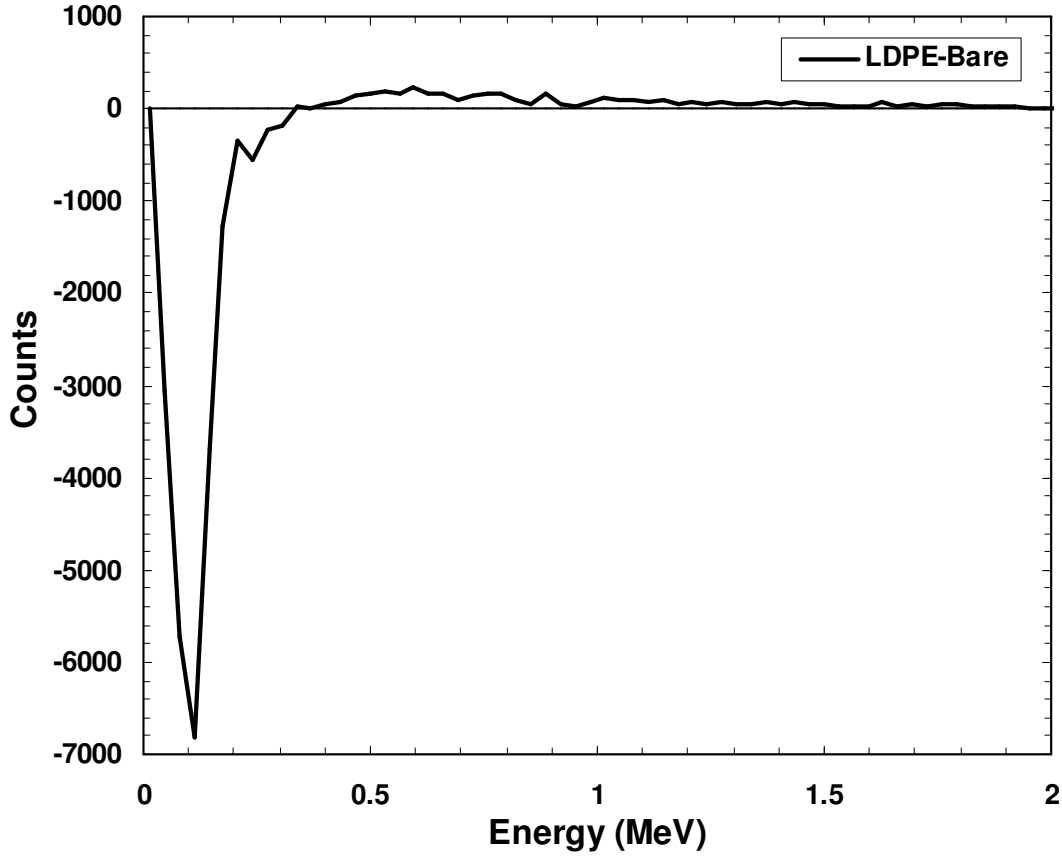

Fig. 6.9. The difference between the LDPE covered and bare PIN diode measurements.

The minimal difference between the PIN diode measurements with and without an LDPE converter indicates the presence of a significant component of charged particles in the field contributing to the observed energy deposition spectra. The lack of a clear separation between the bare and LDPE converter covered PIN diode measurements is suggestive of a significant contribution from charged particles in the CERF facility field.

These results are different from those given in chapter 7, where the same experimental configuration was used to measure the lineal energy spectrum for a 174.35 quasimonoenergetic neutron beam. This is shown in Figure 6.10 where the significant

recoil proton component can be clearly seen, including the 6 MeV proton "knee". This further supports the notion of a significant charged particle component in the CERF radiation field.

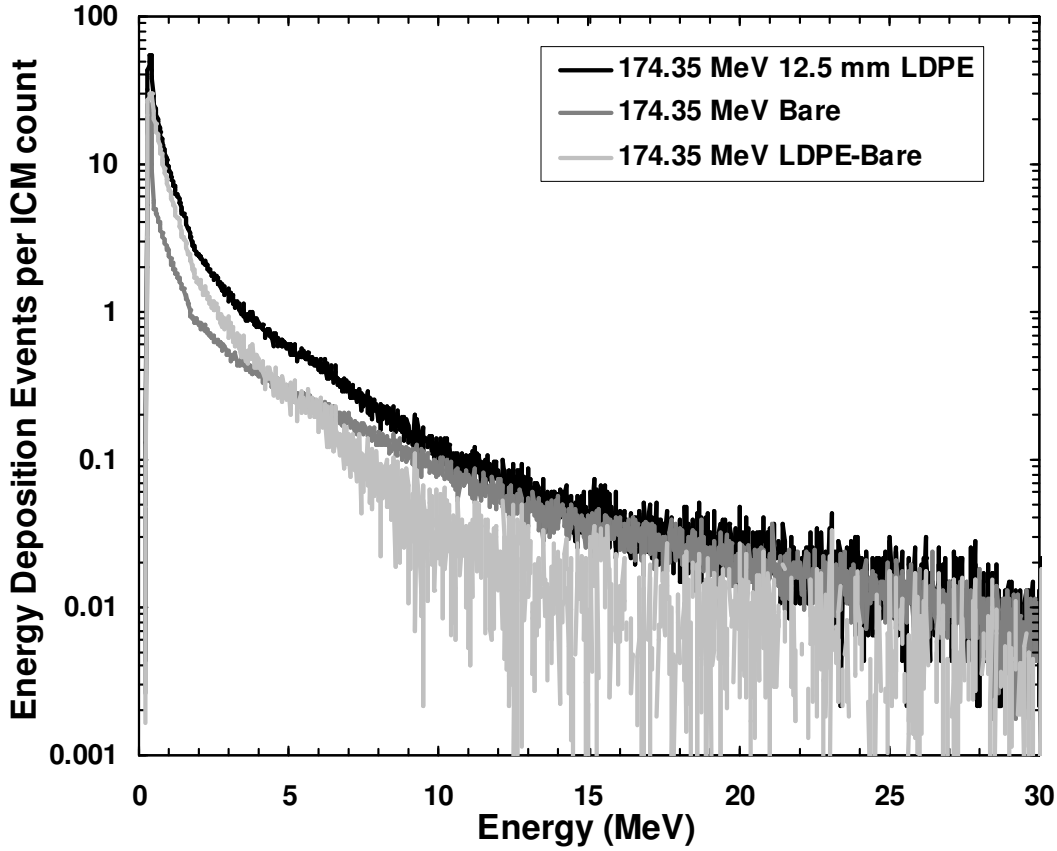

Fig. 6.10. Energy deposition in a 300 μm thick PIN diode with and without an LDPE converter in a comparable energy (174.35 MeV) quasimonoenergetic neutron beam.

GEANT4 was used to simulate the PIN diode response to the CERF radiation field for the cases with and without an LDPE converter. The input particle composition for the PIN diode simulations is the same as used for the SOI microdosimeter simulations.

The results of the simulation show a similar response to the total field as for the experimental measurements. The results of the GEANT4 simulated response of the PIN diode are shown in figure 6.11. The subtraction of the response of the bare energy deposition from the LDPE covered scenario shows a similar result as in the experimental results shown in figure 6.8.

The simulated subtraction of the bare from the LDPE results show a similar relative excess in bare counts at energies below the minimum energy deposition for a recoil proton. This is seen in the GEANT4 simulation as the LDPE layer shielding the sensitive volume of the PI diode from the low energy neutrons below a few MeV. The LDPE layer will also scatter any neutrons not stopped in the LDPE from creating silicon recoil energy deposition events in the sensitive volume.

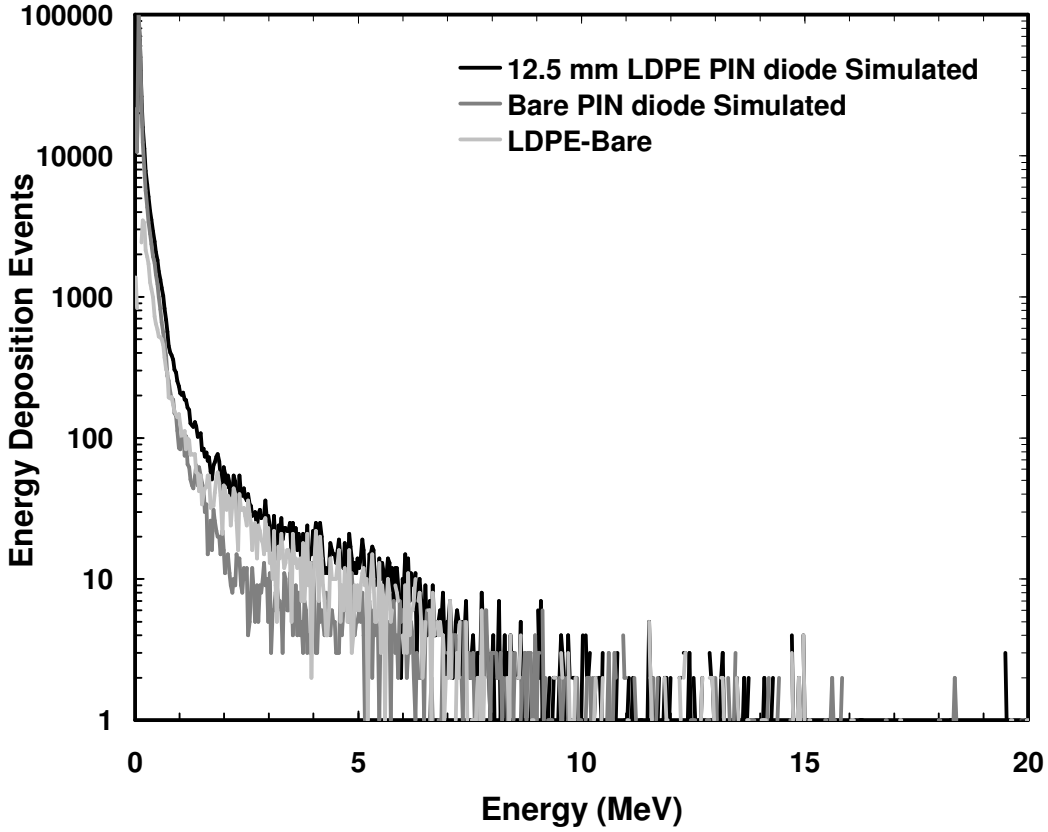

Fig. 6.11. GEANT4 total simulated response to the CERF facility field for both a bare and LDPE covered PIN diode.

The simulations were performed for each component of the radiation field. The response of the bare PIN diode to each particle in the field is shown in figure 6.12 and in figure 6.13 the response of the 12.5 mm thick LDPE covered diode is given.

These simulations indicate that the primary contribution to the energy deposition spectrum below 2 MeV in the bare PIN diode case comes from proton interactions. Above this energy, and up to about 6 MeV, the proton and neutron components are

comparable. It is only above 6 MeV that silicon recoil events from neutrons are the dominant contribution.

The other components of the field (electrons, positrons, pions and muons and gammas) only begin to make a significant contribution below 550 keV. Below this energy the total energy deposition curve increases away from the proton energy deposition curve.

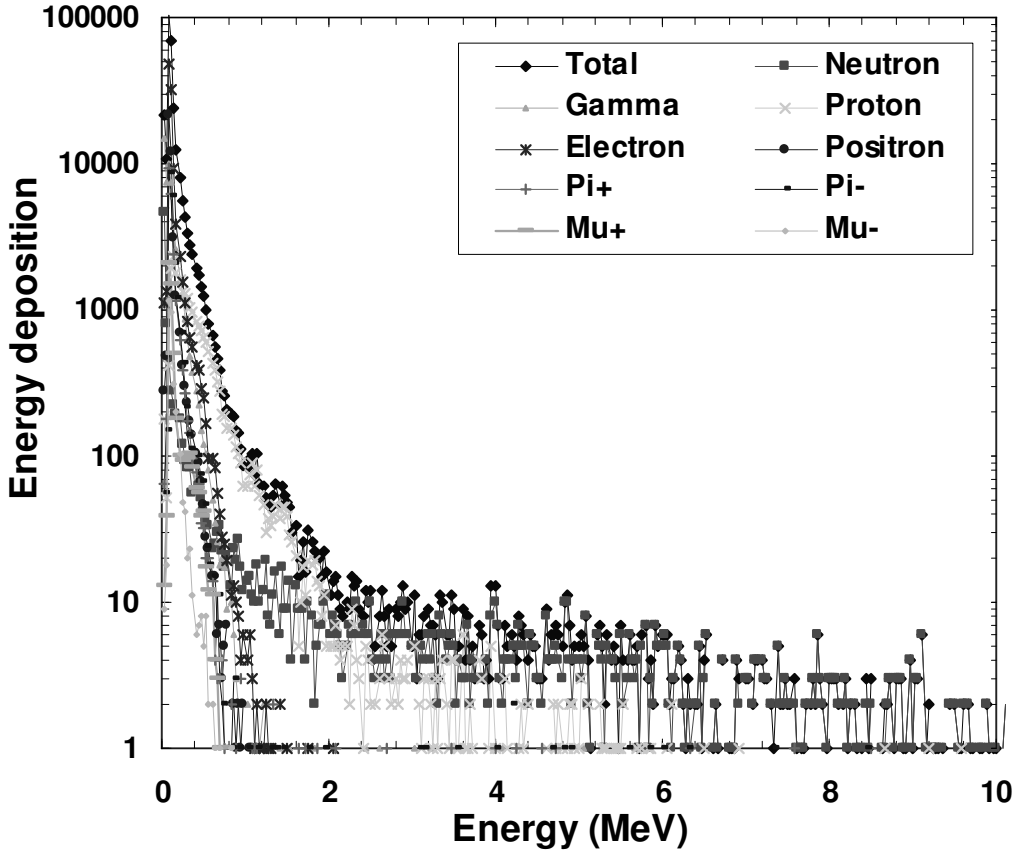

Fig. 6.12. GEANT4 simulated response of a bare PIN diode to the CERF facility field for each of the particles present in the field.

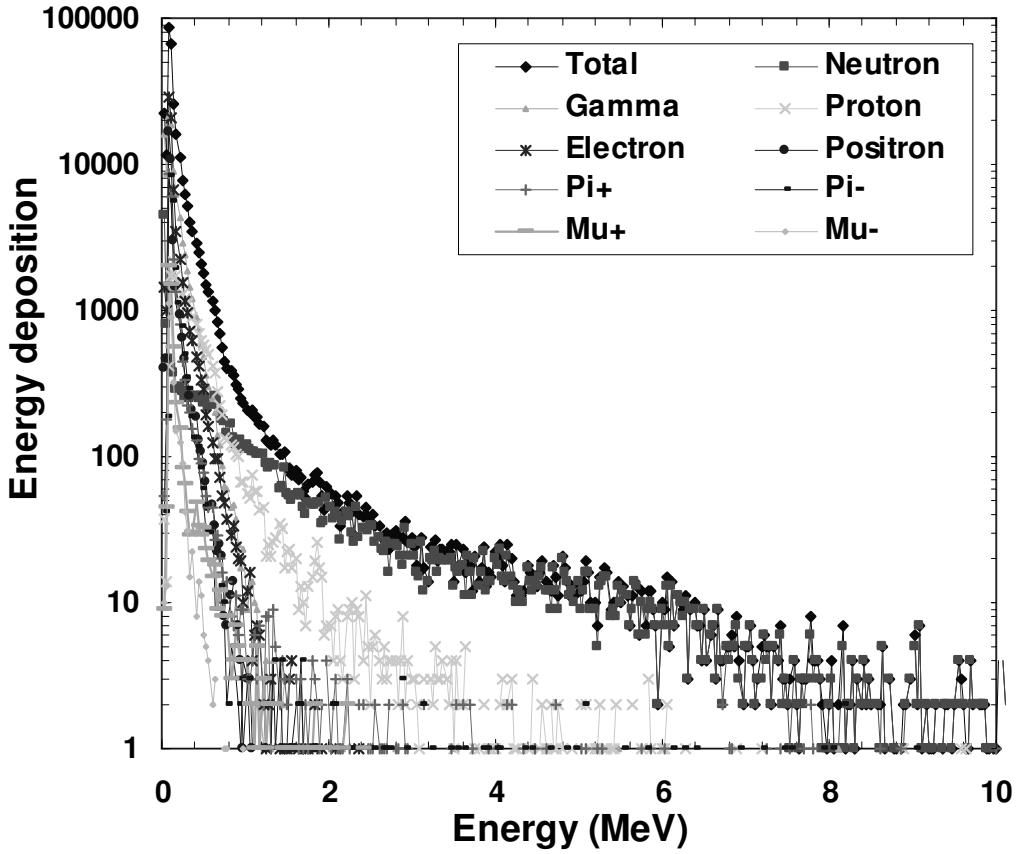

Fig. 6.13. GEANT4 simulated response of a 12.5 mm LDPE covered PIN diode to the CERF facility field for each of the particles present in the field.

The results from the scenario where the LDPE converter is placed in front of the PIN diode indicates that above 1 MeV the recoil protons from the neutron component are the major contribution to the total response. Below 2 MeV the proton component still makes a significant contribution to the total energy deposition in the PIN diode. Noteworthy in figure 6.13 is the start of a 6 MeV maximum energy deposition "knee" from the proton recoils. This "knee" cannot be easily observed in the experimental measurements due to the limited statistics.

For a microdosimetric approach to apply to a detector, the majority of the energy deposition events must originate outside of the sensitive volume only depositing a portion of the total energy. These types of events are classified as crossers as they cross the sensitive volume. The energy deposition events in the PIN diode were also tallied into the particle categories of starter, crosser, stopper and insider, for each of the different particle types in the field. These categories are dependant on the origin and endpoint of the particle depositing the energy relative to the sensitive volume. A starter

is from an energy deposition event that originates within, and then escapes, from the sensitive volume. A crosser is from an energy deposition event both originating and escaping from outside of the sensitive volume. A stopper is an energy deposition event that originates outside of the sensitive volume but does not escape. An insider is an energy deposition event that origin and endpoint are both inside of the sensitive volume. Figure 6.14 shows these events for the bare PIN diode and figure 6.15 shows the same for the LDPE covered scenario.

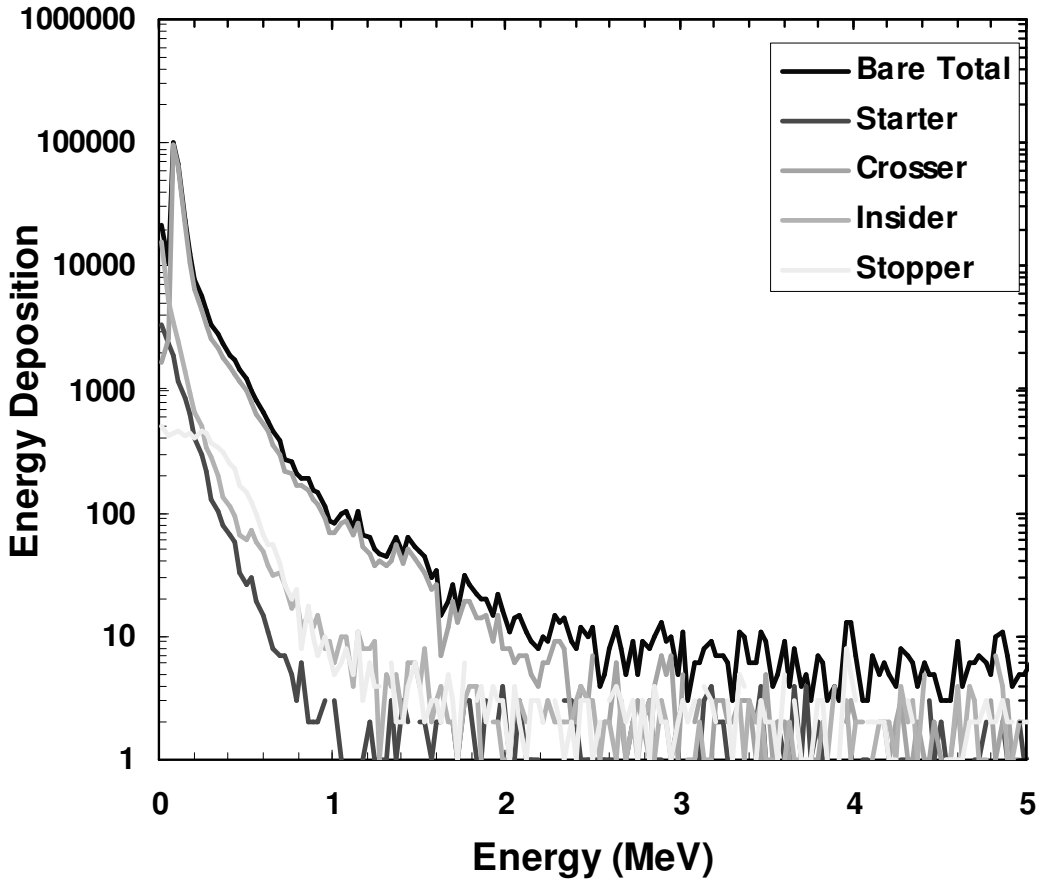

Fig. 6.14. GEANT4 simulated bare PIN diode energy deposition classified into starter, stopper, crosser and insider.

The bare PIN diode simulation reveals that the majority of the particles depositing energy in the sensitive volume originate outside of the sensitive volume and cross through it. This indicates that the majority of energy deposition events below 2.4 MeV are crossers and are depositing energy in the PIN diode. Crossers remain dominant from a lineal energy deposition of 8 keV/μm down to approximately 60 keV, which

corresponds to a lineal energy deposition of 0.2 keV/μm. Below 60 keV insiders and starters begin to dominate the spectrum.

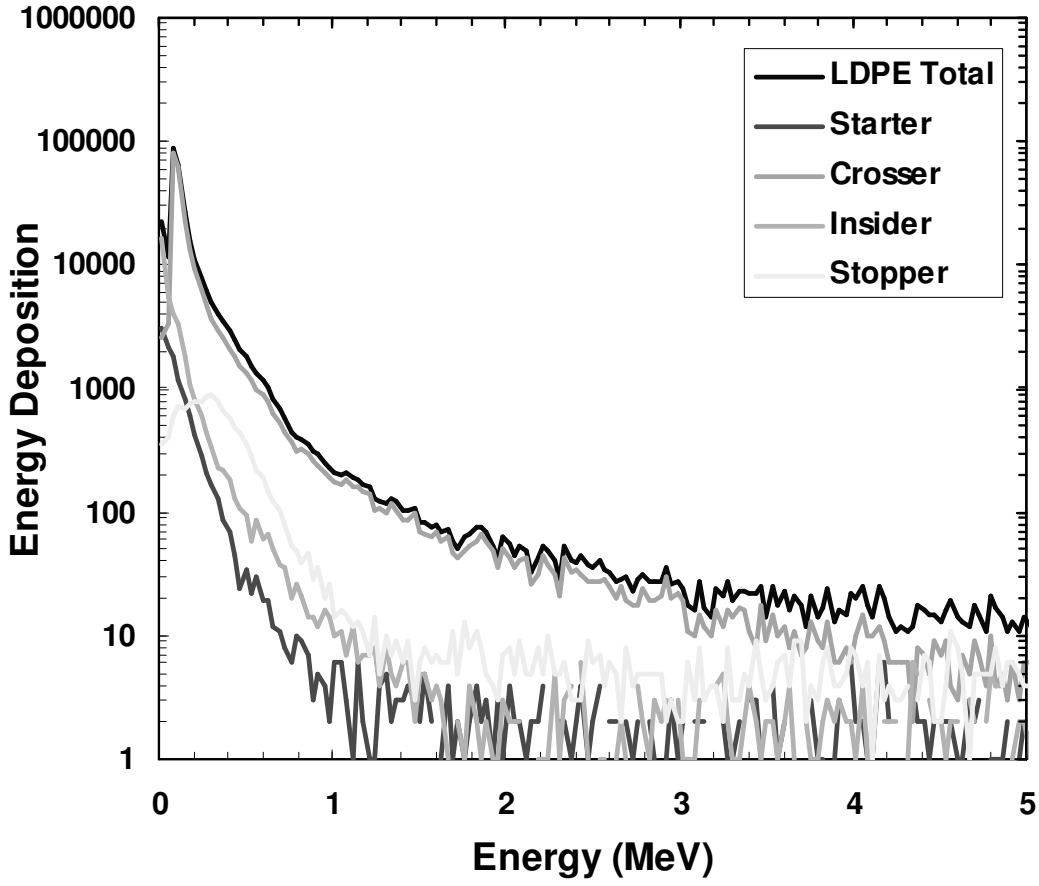

Fig. 6.15. GEANT4 simulated 12.5 mm LDPE covered PIN diode energy deposition classified into starter, stopper, crosser and insider.

Covering the PIN diode with LDPE increased the dominant crosser component attributable to the recoil proton component out to approximately 3 MeV, which corresponds in the region of 10 keV/μm. At higher lineal energies the stopper component becomes significant. The 6 MeV region of the spectrum, where stoppers dominate, corresponds to 20 keV/μm.

The maximum detected experimental energy deposition events were around 33-36 MeV with the maximum energy threshold on amplifier and MCA set at 66 MeV. This maximum energy corresponds to the maximum silicon recoil energies associated with neutron elastic and inelastic reactions.

Over 60 keV crossers are the dominant contribution to the spectrum. From these lineal energy deposition events it is possible to convert the spectrum to a microdosimetric spectrum.

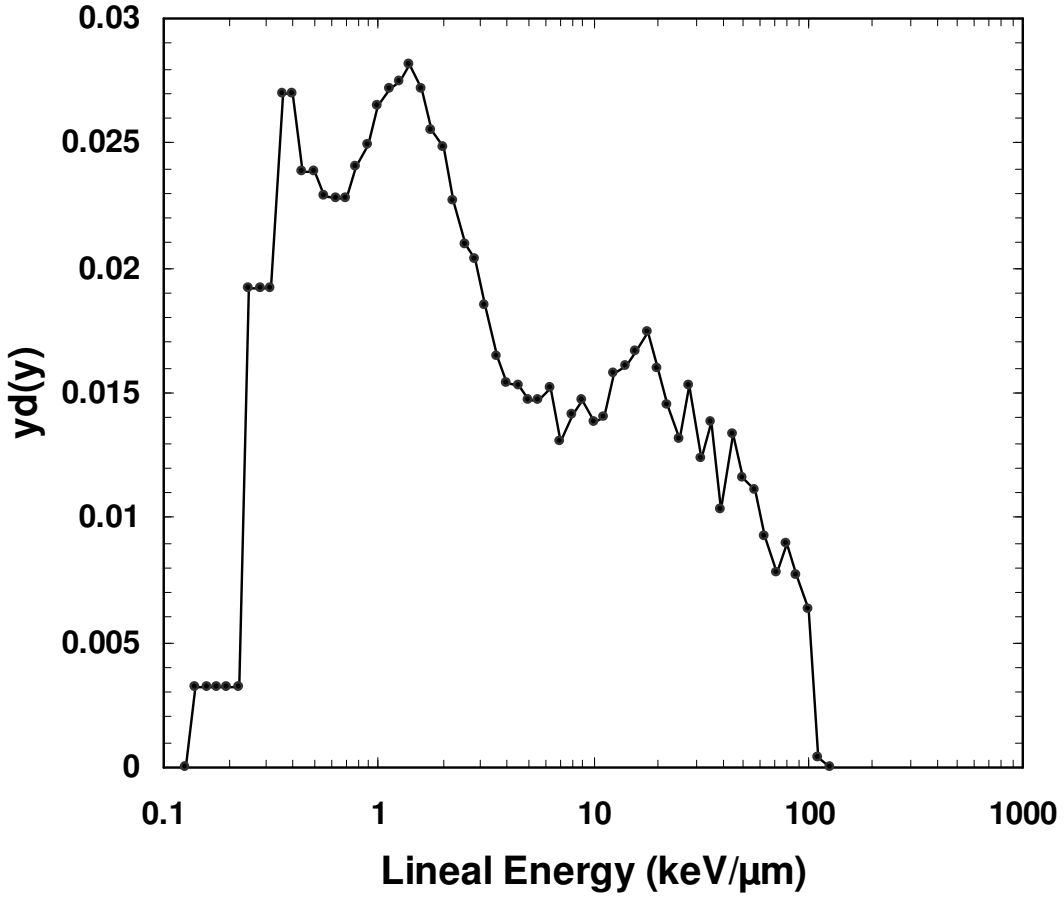

Fig. 6.16. Experimental lineal energy deposition spectrum from a bare PIN diode in the CERF facility field.

The conversion of the bare PIN diode to a microdosimetric spectrum is shown in figure 6.16. Due to having the beam normal to the surface of the diode the mean chord length used was the 300 µm thickness of the PIN diode. The assumption of having majority crosser events is valid from 0.2 keV/µm to approximately 7-8 keV/µm for the bare PIN diode from the simulated results. Above this lineal energy the spectrum is dominated by stopper events.

The microdosimetric spectrum for the 12.5 mm LDPE covered PIN diode measurement is illustrated in Figure 6.17. A feature of interest in the spectrum is the peak followed by a drop in lineal energy deposition events at 20 keV/µm. An explanation for this feature is that it corresponds to the 6 MeV proton edge for maximum energy deposition events in the 300 µm sensitive volume of the PIN diode.

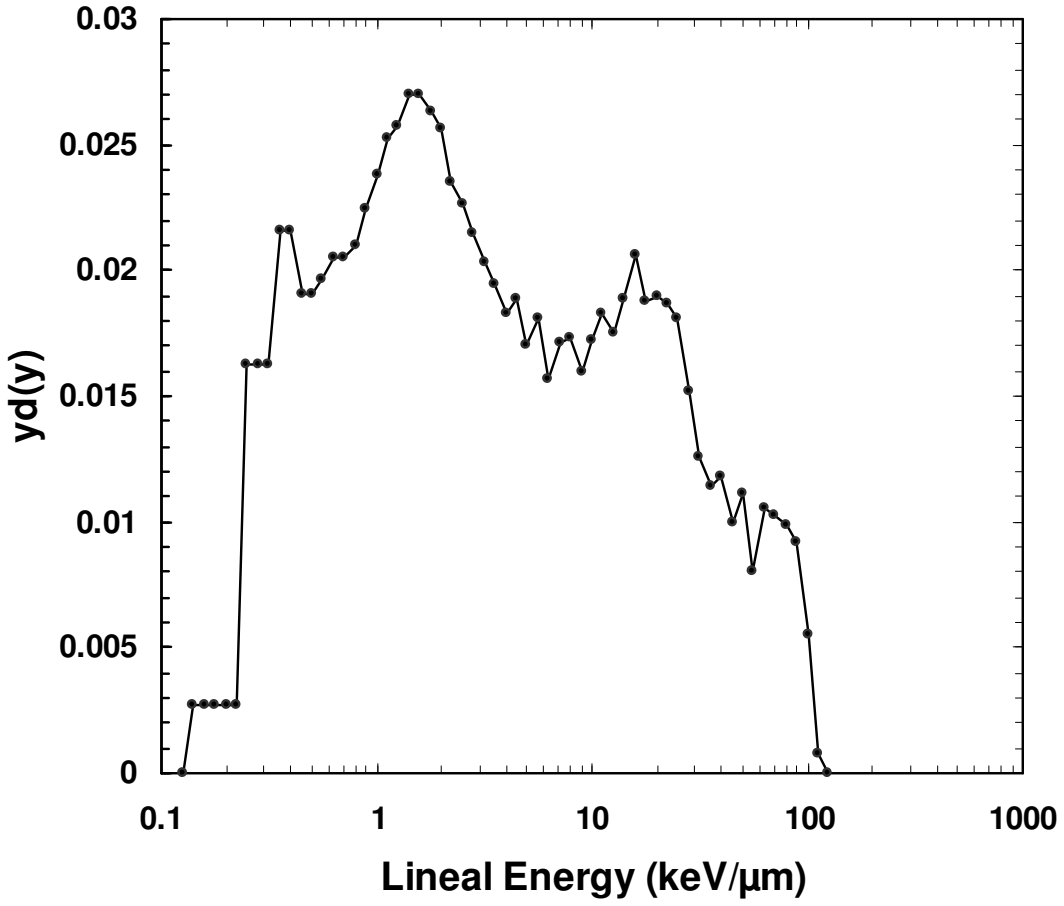

Fig. 6.17. Experimental lineal energy deposition spectrum from a 12.5 mm LDPE covered PIN diode in the CERF facility field.

The proton edge artefact and the limit on the upper and lower range of the lineal energy deposition events restrict the application of PIN diodes to microdosimetric analysis. The range over which the measurements are valid show a good agreement to the experimentally obtained measurements using the HAWK TEPC and SOI microdosimeter.

The GEANT4 simulated PIN diode results were also converted to microdosimetric spectra for comparison. Both the bare and LDPE covered PIN diode simulations are

shown in Figure 6.18. These results compare well with the experimental lineal energy deposition spectra shown above.

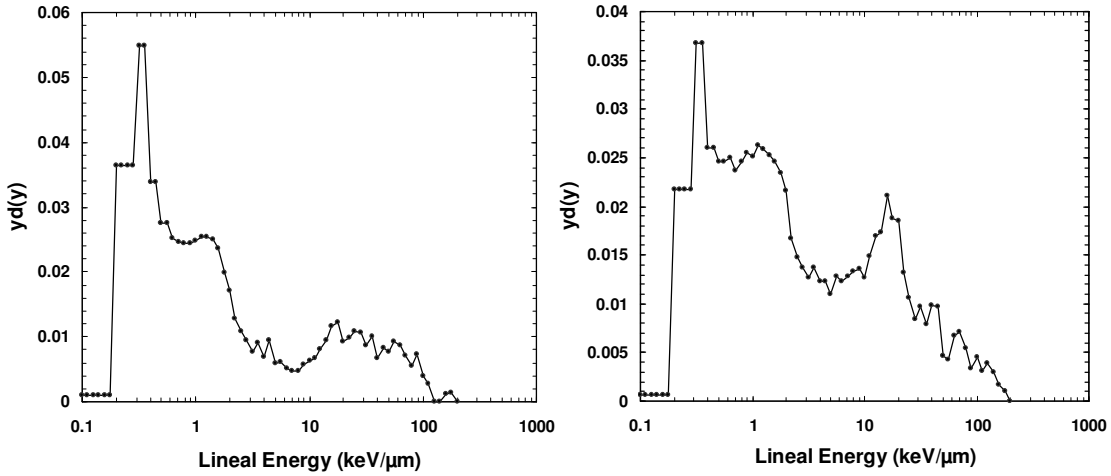

Fig. 6.18. GEANT4 simulated lineal energy deposition spectra for a bare (left) and 12.5 mm LDPE covered (right) PIN diode in the CERF facility field.

The proton edge artefact at 20 keV/µm and the contribution from the higher energy stopper type of events can be seen clearly in the simulated result. The "peaks" at the lower energies below 0.4 keV/µm are from the conversion process to logarithmic binning from the linear binning of the measurements. This amplitude of this peak is also due to the contribution in the energy deposition spectrum at around 80 keV from the low LET particles (gamma, electrons, positrons etc.). The conversion of the PIN diode energy deposition to microdosimetric spectra, under the assumption that the majority of interactions do not stop and deposit full energy in the sensitive volume, shows a similar shape to the SOI microdosimetric spectrum (simulation and experimental) as well as the HAWK data. The main difference is that in comparison to the SOI microdosimeter and TEPC measurements there is a much higher probability for full energy deposition events within the PIN diode. This is due to both the larger sensitive volume and the large area of 1 cm^2 compared to the 300 µm thickness resulting PIN diode energy deposition being extremely sensitive to angular orientation of the incident radiation. The conversion to microdosimetric spectra of the PIN diode measurements only holds for high energy radiation fields normal to the detector surface.

6.4 Discussion

Microdosimetric spectra at the CERF facility were measured with a novel SOI microdosimeter and a conventional HAWK TEPC. These measurements were

performed at the same position in the field to provide a simple comparison to one another. Simulations of the experimental setup for the SOI microdosimeter and PIN diode were also performed.

After applying the geometric tissue equivalence conversion factor, the comparison between the lineal energy deposition spectra shows a good agreement for the lineal energy range of the SOI microdosimeter measurement. These measurements also show a good agreement to the GEANT4 simulated results for the lineal energy deposition spectra.

The results indicate there was no significant difference between the energy depositions recorded in a bare SOI microdosimeter when compared to the case when a LDPE converter was employed to produce recoil protons from the neutron component of the CERF field. These results indicate a reasonable but important contribution from charged particles in the CERF field.

The results of the PIN diode measurements and GEANT4 simulations agree well with the conclusions of the TEPC and SOI microdosimeter measurements. These show a significant contribution from the charged particles in the field. Conversion of the PIN diode data to microdosimetric spectra shows good agreement with the TEPC and SOI measurements for the valid region of lineal energies in the CERF facility field. However artefacts in the spectra due to the thickness of the sensitive volume make this technique limited in application compared to SOI microdosimetry.

7. Response of SOI Microdosimetry and Planar Photodiode to the TSL Quasimonoenergetic neutron field

7.1 Introduction

The Svedberg Lab (TSL) at Uppsala University is an accelerator facility used for research, medical and industrial applications. The accelerator used for the TSL facility is the Gustaf Werner cyclotron (Reistad et al., 1993). This cyclotron is used to produce positive ion beams for a variety of research and electronics testing applications. For protons the accelerator is capable of accelerating a high flux of protons, up to $6x10^{13}$ particles per second, with proton energies up to 180 MeV. The protons from the cyclotron can then be directed down any number of different beam lines depending on the application such as proton therapy, biological irradiations, proton beams, quasimonoenergetic and more recently "Atmosperic-like Neutrons from thIck TArget" (ANITA) spectral neutron beams and single event upset integrated circuit testing. The schematics for the "Blue Hall" used for proton and neutron experimentation is shown in Figure 7.1. The beam can be dedicated to a particular beam line and configuration or it can be set up in a beam sharing mode with the proton therapy facility, where preference is given to the proton therapy beam line for short durations, to give therapy fractions, and is then redirected back to the "D-Line" in the blue experimental hall for neutron experiments.

For the experiments described here a quasimonoenergetic neutron field was produced via the $^{7}Li(p, n)^{7}Be$ reaction (Prokofiev, A.V., 2006). The thickness of the lithium target was selected to be 1, 2, 4, 8.5 or 23.5 mm thick depending on the proton energy. The lithium target was irradiated with a high fluence of protons with energies of 49.5 MeV with a 4 mm thick lithium target and 178.7 MeV protons with a 23.5 mm thick lithium target to produce the quasimonoenergetic neutron field.

The beam contains a negligible component of charged particles on account of the thickness of the lithium target and the small cross section for proton-nucleus interactions to produce energetic secondary charged particles. Any charged particle component downstream from the lithium target is bent away from the axis of the neutron beam, using a magnet, into a beam dump. If the magnet was not used to redirect

the charged particle component down to a beam dump, the field at the irradiation positions would, depending on the distance from the target and the energy used, most likely contain a mix of charged particles and neutrons. The beam is dumped down a 10 meter line to a heavily shielded, water-cooled, graphite beam dump which is used as a faraday cup to measure the transmitted proton flux.

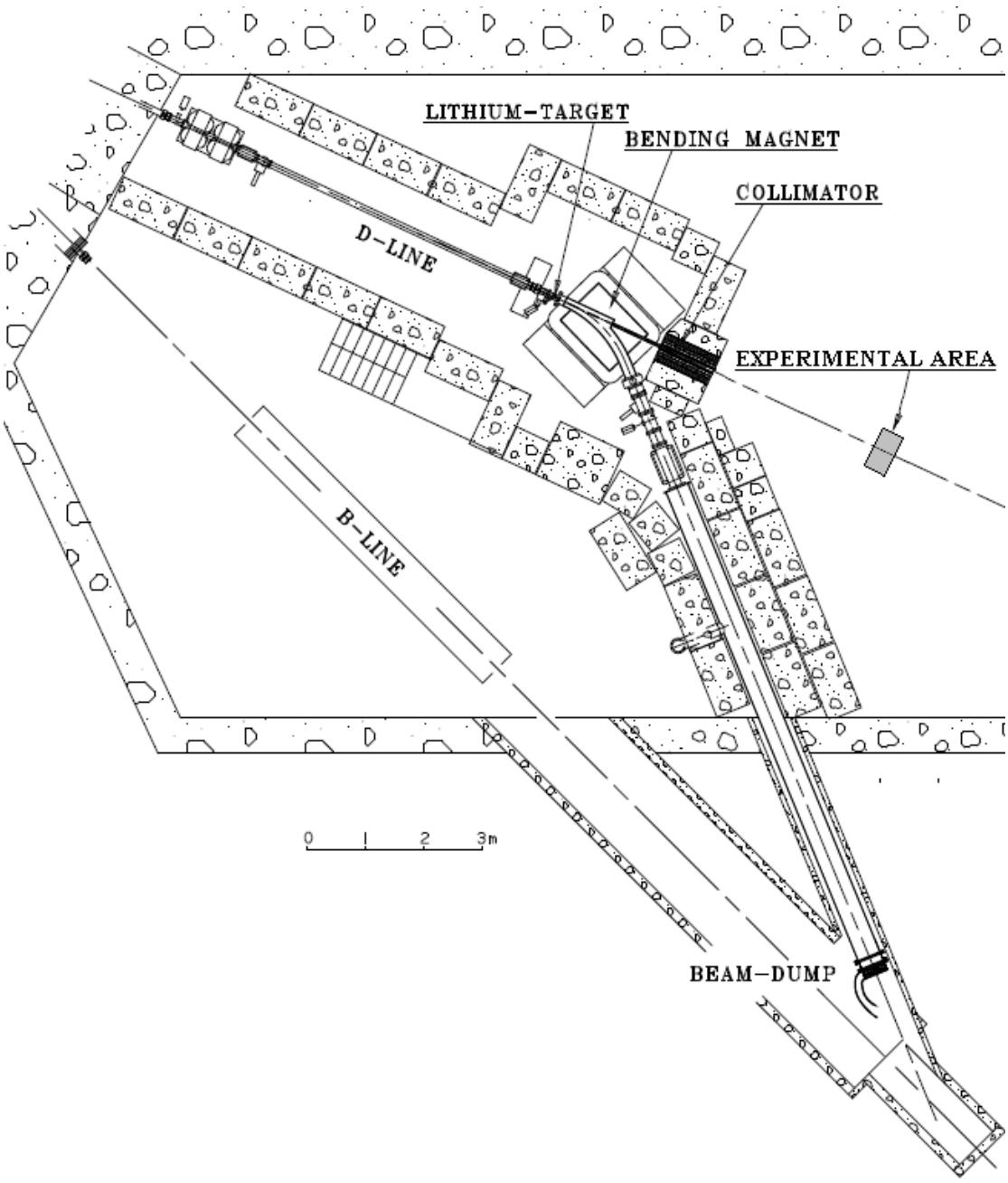

Figure 7.1. Schematic of the neutron beam line at TSL. The experiment was located at 6 meters from the lithium target along the D-Line. The bending magnet for charged particles and collimation are indicated along the beam line axis. (Prokofiev et al., 2006)

The two neutron spectra used had nominal mean quasimonoenergetic peak energy of 46.5 ± 1.1 MeV for the 49.5 MeV incident proton beam and 174.35 ± 2.45 MeV for the 178.7 MeV incident protons. Peak to continuum fluence ratios for both beams was approximately 0.55. The spectra supplied for the two energies used in this experiment are shown in Figure 7.2. Due to the spectrum having this "tail" of lower energy neutrons the beam is referred to as quasimonoenergetic.

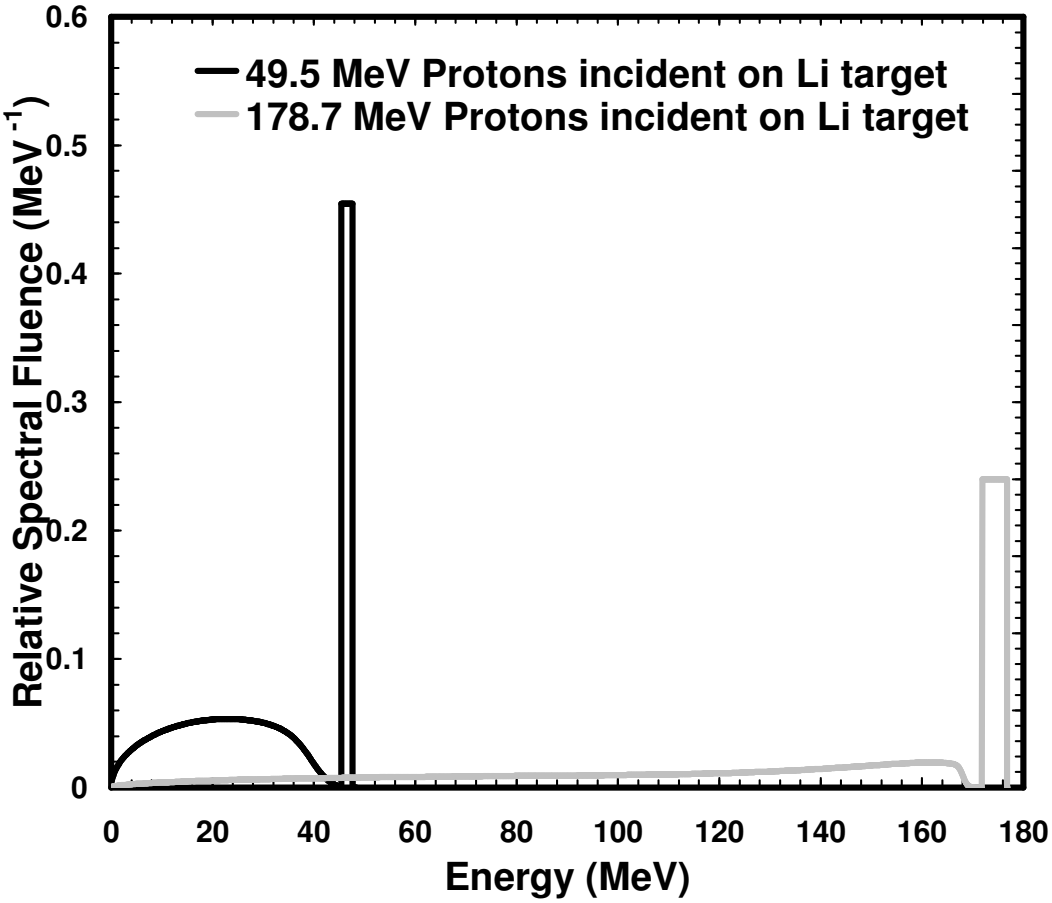

Figure 7.2. The supplied spectra of the two beam energies used in the experiments. The peak to tail ratio for the two energies used is 0.6 for the 49.5 MeV incident protons and 0.72 for the 178.7 MeV incident protons on the lithium target. The thickness of the 7Li target was 4 mm for the 49.5 MeV incident protons and 23.5 mm for the 178.7 MeV incident protons.

The initial beam diameter could be set using a series of interchangeable collimator sleeves 100 cm long with an outer diameter of 50 cm and were constructed from iron. There was a range of inner collimator sleeve diameters available ranging from 2 cm to 30 cm in diameter. The collimator sleeve used for these experiments had a 27 cm inner

diameter. The closest edge of the collimator sleeve is set at 300 cm from the ^{7}Li target. The detectors are set up 300 cm from the collimator resulting in a total distance from the ^{7}Li target to the detectors was 600 cm. The angular beam spread was approximately 0.46° leading to a beam diameter of 31.8 cm at the measurement position.

7.2 Experimental Methods

7.2.1 Experimental configuration

The detectors were irradiated in the user area of the blue hall at TSL (Figure 7.1). The detectors were mounted at a distance of 6 meters from the Li target and aligned with the collimated neutron beam using rotating laser alignment to ensure accurate placement of the detectors within the field. The beam diameter of 31.8 cm at the irradiation position was sufficient to irradiate both the PIN diode and the SOI microdosimeter simultaneously. A "Beams-eye" view photograph of the experimental setup can be seen in Figure7.3.

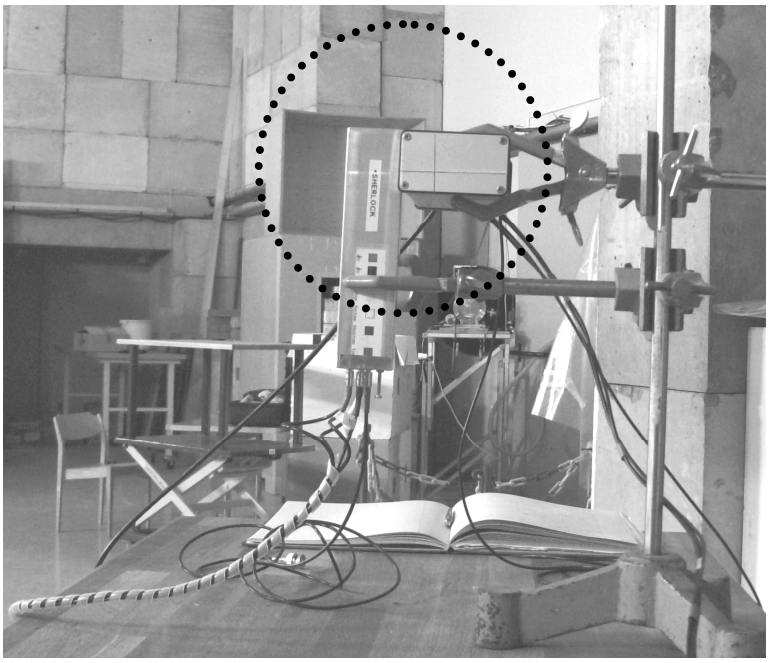

Figure 7.3. A "beams-eye view" photograph of the experimental setup showing the planar silicon diode equipment on the left (designated "Sherlock") and the SOI microdosimeter equipment on the right. The dotted black circle indicates the approximate area of the beam at the irradiation position. The markings on the detector casings indicate the location of the centre of the detectors (A spot on the left hand side detector, just before the "S" of the Sherlock label, and a cross on the right hand side detector).

The two detector systems used for these experiments were designed to be battery powered and portable. These systems were designed to operate continuously and perform reliably for extended periods of time (greater than 24 hours) as would be expected in an aviation application.

The planar silicon diode device electronics were constructed using an Amptek A250 preamplifier system in a long aluminium probe casing. The entry window for this system was made up of 0.8 mm of aluminium with room to accommodate a maximum thickness of 12.5 mm LDPE in front of the detector. The preamplifier output of the probe case, designated “Sherlock”, was then fed into Amptek shaping amplifiers, based on the A275 hybrid chip, mounted on a PC275 test board. The shaped output of this system was then read out through a patch cable to the control room using an Amptek Pocket MCA 8000a.

The SOI microdosimeter electronics used a Cremat CR-110 preamplifier directly coupled to a Cremat CR-200 shaping amplifier with a 1 μs shaping time. This system was designed to be an initial prototype for a complete battery powered dosimetry system. The output of the shaping amplifier was fed through a patch cable to an Amptek Pocket MCA 8000a. The entry window of the SOI microdosimeter electronics enclosure was made from 1.6 mm of aluminium. A thinner, but more mechanically fragile, aluminium window could be fitted to the system if required however the original box window thickness was effectively transparent to the high energy neutrons used in this experiment at both energies. This could be seen by examining the cross sections for neutrons for the energy spectrum used, approximately 1.7 barns for the 49.5 MeV peak neutrons and approximately 0.61 barns for the 178.7 MeV peak neutrons (Figure 7.4). This is the same configuration as used in the previous chapter 6 at the CERF facility for taking portable measurements with the SOI microdosimeter.

The systems were powered using a regulated battery power supply, with +/- 6 Volts for the electronics supply rails. The photodiode bias voltage was supplied from a custom built, very low ripple (order of 10 mV p-p ripple on the output), adjustable battery powered high voltage supply to fully deplete the Hamamatsu photodiode at +100 V.

The SOI microdosimeter was biased using a battery powered +10 V stable regulated bias supply. The supply rails for the electronics had a drain of approximately 70 mA per supply rail and were capable of lasting approximately 48 hours before the battery cells (C size batteries) required replacing. The bias supplies for each of the detectors were able to operate continuously for a minimum of two weeks and were powered by two standard 9 V batteries.

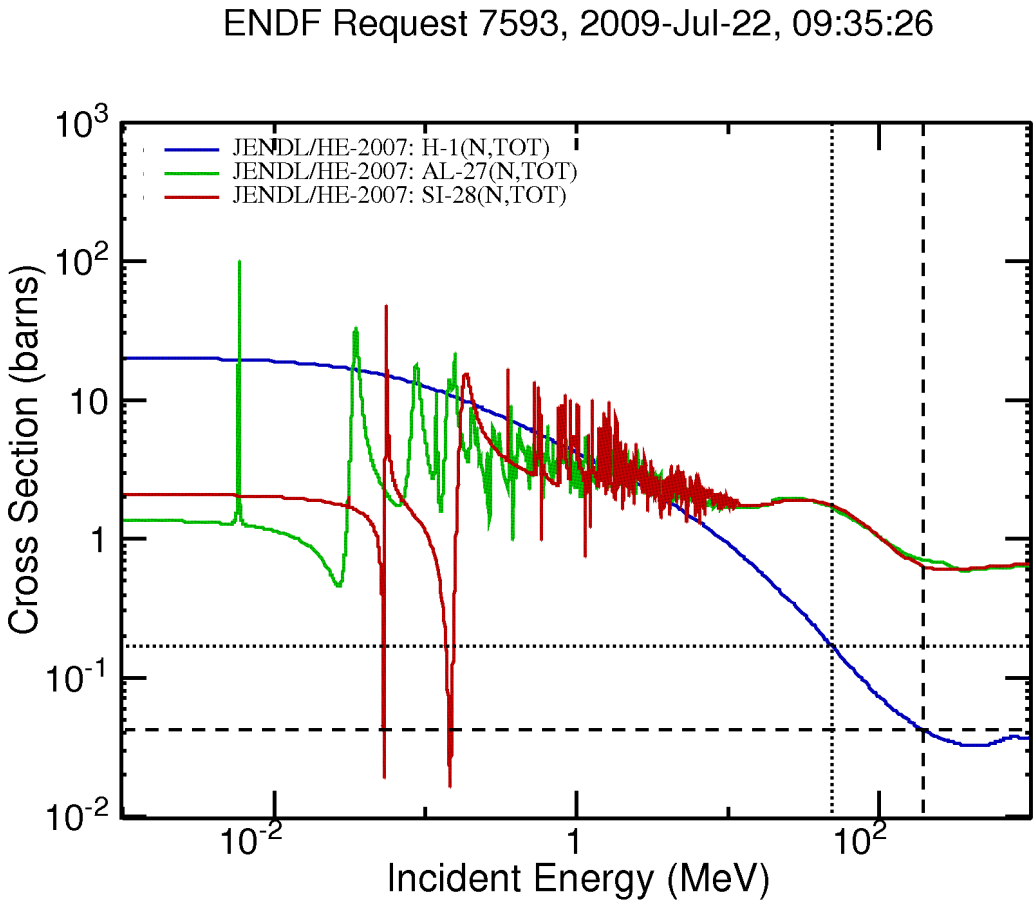

Figure 7.4. The evaluated total neutron cross section (ENDF, 2009) for 27Al (100% natural abundance), 28Si (92.23% natural abundance) and 1H (99.99% natural abundance). These cover the primary elements of interest for the detector system. The points of most interest are the points for the main neutron peak energies 46.5 MeV (approximately 1.75 barns for both 28Si and 27Al and 0.14 barns for 1H) and 174.35 MeV (approximately 0.61 barns for 28Si, 0.75 barns for 27Al and 0.046 barns for 1H).

A Low Density Polyethylene (LDPE) layer (density ρ = 0.94 g·cm^{-3}) was used to produce recoil protons from the incident quasimonoenergetic neutron beam via the

^{1}H(n, p)n' elastic scattering reaction. The energy of a particle due to elastic recoil from a neutron interaction, in the laboratory coordinate system, is given by the equation:

$$E_R = \frac{4A}{(1+A)^2}(\cos^2\theta)E_n \qquad (7.2.1)$$

Where E_R is the energy of the recoiling particle, A is the mass number of the target particle relative to the incident neutron mass, θ is the angle of the recoil relative to the original direction of the incident neutron and E_n is the energy of the incident neutron (Knoll, 2000).

Elastic neutron recoils from heavier nuclei, such as the carbon in the LDPE or the silicon in the detector sensitive volume, will only transfer a fraction of the energy from the neutron to the nucleus as given by the $\frac{4A}{(1+A)^2}$ factor. From this ratio is can be seen that the maximum energy transfer to a carbon-12 nucleus (98.9% natural abundance) is 28.4% of the initial neutron energy and that the maximum energy transfer to a silicon-28 nucleus (92.23% natural abundance) is 13.3% of the initial neutron energy.

For proton elastic recoils from the LDPE typical mass $A = 1$, therefore the energy of the recoil proton depends solely on the angle of recoil where the maximum energy of the proton occurs at $\theta = 0^\circ$ resulting in $E_p = E_n$. The angular distribution probability, $P(E_p)$, as a function of the proton recoil energy is uniform, at a value of $\frac{1}{E_n}$, and therefore produces a flat angular distribution ending at the maximum recoil energy of $E_p = E_n$. This relation holds for reasonably low energies ($E_n < 10$MeV) and can still be approximated up to energies of about 300 MeV, above which inelastic processes would begin to occur and would need to be taken into account.

For protons of sufficient energy such that they traverse the detector sensitive volume depositing only a portion of the energy in the detector (ΔE), the spectra will be dependent on the chord length distribution of the sensitive volume. To collect the full energy deposition of a maximum recoil energy proton the thickness of a silicon

sensitive volume would be required to be 10.7 mm thick for the 46.5 MeV neutron beam and 109.62 mm for the 174.35 MeV neutron beam (SRIM, 2008).

Energy loss within the LDPE layer needs to be taken into account. A thin layer of LDPE would result in a recoil proton with the full recoil energy being sampled by the detector sensitive volume. However, the elastic recoil cross section is small requiring a relatively thick layer to provide sufficient neutron detection efficiency. An excessively thick LDPE converter layer results in protons produced close to the surface of the LPDE losing a considerable amount of energy traversing the remaining LDPE thickness. Charged particle equilibrium occurs when the thickness of the LDPE converter corresponds to the maximum range of the highest energy elastic recoil protons in the LDPE layer. For charged particle equilibrium to occur the LDPE converter layer would be required to be 19.4 mm thick for the nominally 46.5 MeV neutron beam and approximately 205.5 mm thick for the nominally 174.35 MeV neutron beam.

For these ideal thicknesses of detector and converter, this would produce a full range of theoretical energy depositions from the maximum energy deposition down to the minimum energy deposition. However the required thickness of both detector and LDPE converter necessary to produce an idealised response are not feasible. The resultant requirement for microdosimetry from a neutron field is to sample the ΔE of the recoil protons produced in the converter layer. This converter layer will simulate a certain depth in tissue for the microdosimetric sampling. To minimise the sampling of full energy particles or variances due to angular distribution uncertainties from the elastic recoil protons the sensitive volume of the detector should be small with a well defined chord length distribution.

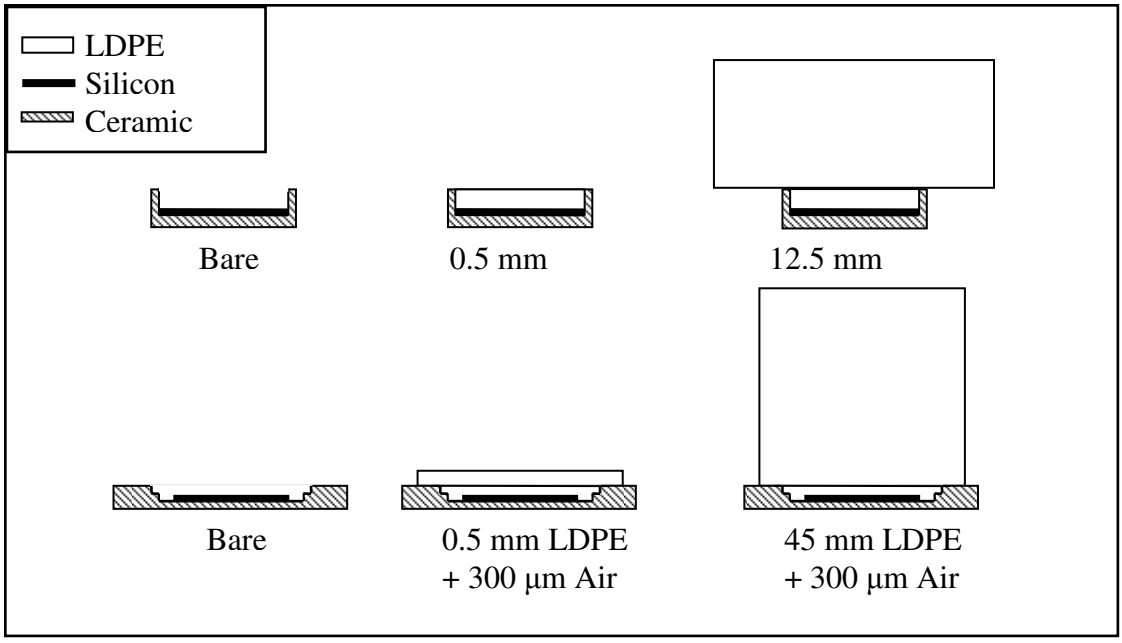

Figure 7.5. Profile cross-sections of the three thicknesses of LDPE converter used for the PIN photodiode (upper) and SOI microdosimeter (lower).

The LDPE thicknesses for the SOI microdosimeter experiments were 45.0 mm, 0.5 mm and bare SOI microdosimeter. For the PIN photodiode the thickness used were 12.5 mm, 0.5 mm and bare PIN photodiode. The maximum thicknesses of the LDPE were mechanically limited by the available room in the aluminium detector enclosures. The 0.5 mm thicknesses were used to act as a thin hydrogenous material and minimise proton energy losses in the LDPE volume. The lineal energy of the recoil protons above approximately 440 keV in energy were measured in the sensitive volume of the SOI microdosimeter below this energy the full energy of the proton would be deposited in the detector volume. However due to a 300 μm air gap between the lower surface of the LDPE and the upper surface of the SOI microdosimeter (necessary to avoid damaging the bonding wires and surface tracks) protons below 440 keV lose all their energy in this air gap. The PIN photodiode did not have such a large air gap as the LDPE was able to be in direct contact with the windowless surface of the PIN photodiode.

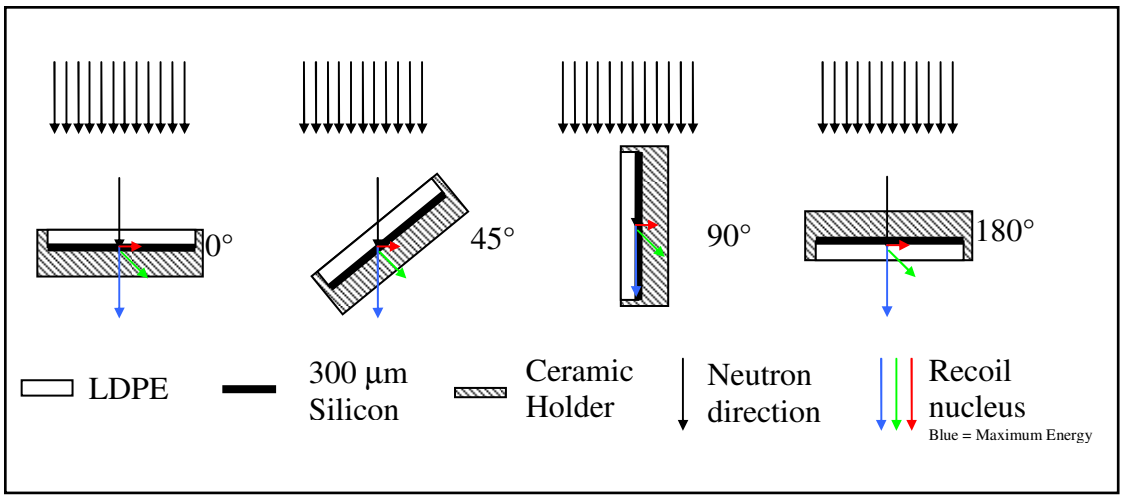

Figure 7.6. The rotation of the planar silicon diode relative to the quasimonoenergetic neutron beam direction. Illustrated in the example of the 0.5 mm thick LDPE in contact with the Si PIN photodiode. The recoil nucleus arrows indicate the relative energy dependant on the angle of scatter from maximum elastic recoil energy transfer (blue), half maximum energy elastic recoil (green) and minimum recoil energy (red).

The PIN diode was also rotated at different angles (0°, 45°, 90°, 180°) with respect to the normal incidence of the neutron beam to determine the angular response. This rotation was performed for each of the different LDPE converter thicknesses and quasimonoenergetic beam energies. From Figure 7.6 and the elastic recoil equation

7.2.1.1 SOI Microdosimeter

The SOI microdosimeter used for these experiments was 5 µm thick with 30 x 30 µm cell dimensions. The larger area 30 x 30 µm cell array (14,400 cells) was used for these experiments, at the expense of slightly increased noise, to increase the total area and hence the detection efficiency of the SOI microdosimeter system. The smaller SOI microdosimeter arrays (4800 cells), used in other chapters, have a noise threshold of approximately 1 keV/µm while the noise of this larger array in this experimental configuration is 3.5 keV/µm.

For the SOI microdosimeter, each experimental measurement was performed with both a high shaping amplifier gain and then repeated with a low shaping amplifier gain. The two measurements were then amalgamated together to cover approximately three orders of magnitude in range for the lineal energy deposition events, while preserving the fine binning for the low lineal energy deposition events when converted to a logarithmic

scale for plotting of microdosimetric lineal energy deposition. The energy deposition range covered by this method extended from the noise threshold limit of 17.5 keV (3.5 keV/μm) through to 18.89 MeV (3.78 MeV/μm).

The maximum expected energy deposition event is from a silicon elastic recoil event of 10.6 MeV which corresponds to a measured lineal energy deposition of 2,120 keV/μm. The minimum neutron energy required to impart this much energy in the silicon volume is approximately 80 MeV, which can only occur in the 174.35 MeV quasimonoenergetic neutron beam. For the 46.5 MeV quasimonoenergetic beam the maximum energy deposition is expected to be 6.19 MeV which corresponds to a recorded lineal energy deposition of 1,238 keV/μm. Energy depositions recorded in the SOI microdosimeter above these energies can only occur due to multiple interactions during the integration time of the processing electronics and, less likely, exothermic inelastic neutron-silicon interactions.

7.2.1.2 Planar silicon diode

The 300μm thick planar silicon photodiode used in these experiments was a Hamamatsu S3590-09 windowless PIN diode with dimensions of 1 cm x 1 cm x 300 μm. The diode was calibrated using the alpha particles from thin electroplated ^{421}Am (5.486 MeV major emission) and ^{148}Gd (3.184 MeV) sources under vacuum. This was done to test both the energy resolution of the detectors and calibrate the energy scale to be used in the experiment. Additional energy calibration points were generated using a calibrated battery powered portable tail pulse generator to inject charge into the preamplifier front end. These also allowed the electronics to the tested for the large energy depositions, and hence charge, expected during the experimentation.

Saturation of the pulse shaping electronics occurred for pulse heights corresponding to energy depositions greater than approximately 26 MeV, below this the pre and shaping amplifiers were linear in operation for the selected gain. The maximum expected energy deposition in the PIN diode is from the 174.35 MeV quasimonoenergetic neutron beam due to a silicon recoil of 23.3 MeV, which is within the limits of the preamplifier saturation.

An LDPE converter was able to be placed in front of the PIN diode to produce proton recoils from the field. The limit for the maximum physical thickness of the LDPE converter was 12.5 mm due to the interior dimensions of the aluminium probe housing used to contain the PIN diode and preamplifier circuit. A 0.5 mm thick piece of LDPE was able to be placed directly contacting the surface of the PIN photodiode and occupy the space to the top of the edge of the ceramic diode holder. A 12 mm LDPE block could then be placed to contact the upper surface of the 0.5 mm LDPE layer. This allowed for two different thicknesses of LDPE to be used, 0.5 mm and 12.5 mm.

Each of the different thicknesses of LDPE converters, and bare PIN diode, were measured not only for normal incidence but also for different angles of 0, 45, 90 and 180 degrees at each of the beam energies. This was done to test the angular response of the planar diode to a parallel neutron field. If the recoil proton enters the 300 micron thick photodiode perpendicular to the surface with energy greater than 6.07 MeV then the full energy of the proton will not be measured and only the ΔE of the proton will be measured. Conversely if the proton enters at an angle of 45 degrees to the surface then the maximum energy deposition is expected to be 7.43 MeV and any higher will result in only a ΔE being recorded.

7.2.2 GEANT4 Simulated response to the TSL Quasimonoenergetic neutron field

GEANT4 (GEometry ANd Tracking) (Agostinelli et al., 2003; Allison et al., 2006) was used to model and simulate the experimental arrangement for both the SOI microdosimeter and PIN diode.

The geometric and isotopic compositions of the different detector configurations were accurately modelled. The isotopic composition for each of the elements present in the simulation was defined using the NIST Physical Reference Data for the Atomic Weights and Isotopic Compositions (Coursey et al., 2005). This allowed accurate simulation of the neutron inelastic interactions in all of the materials that could produce a secondary charged particle to interact in the detector sensitive volume.

The GEANT4 physics list used for these simulations, QGSP_BIC_HP, was suitable to model the neutron and charged particle interactions, with the high precision neutron model used to simulate accurate interactions from fast neutrons down to thermal energies.

The spectra used as input for the primary neutron beam was sampled from the neutron spectra provided by TSL, shown in Figure 7.2, for both of the quasimonoenergetic energies used. This was done to accurately model the interactions from not only the high energy monoenergetic component but also the "tail" continuum which would contribute appreciably to the energy deposition spectrum.

The output of both of the simulations were scored into a linearly binned histogram with an additional channel to sum any energy deposition events that exceeded the maximum binning energy of 20 MeV for the SOI microdosimeter simulation and 66 MeV in the PIN diode simulation.

7.2.2.1 SOI Microdosimeter Simulation

The GEANT4 simulation of the SOI microdosimeter used the same isotopic composition and geometry as outlined in Chapter 3. The array used for these measurements was the A3 array, the largest array on the SOI microdosimeter. The simulation included the three different converter scenarios, bare, 0.5 mm LDPE and 45 mm LDPE.

The results from these simulations were processed into microdosimetric spectra for comparison to the experimentally measured data. The simulation was set to cover the same energy range and binning width as the experimentally acquired data.

7.2.2.2 Planar silicon PIN diode Simulation

The geometry of the PIN diode included the silicon sensitive volume with dimensions of 1 cm^2 surface area with a 300 μm thickness. This was backed with a simulated 1 mm thick ceramic (composition Al_2O_3) mechanical PIN diode support. The support was included in the geometry due to the rear side angular irradiation simulations, in order to

simulate any secondary charged particle production in the ceramic from inelastic neutron interactions.

The simulated geometry of the PIN diode to the planar quasimonoenergetic neutron field was simulated for each of the different thicknesses of LDPE converter used in the experiment. For each of the different thicknesses of LDPE converter the beam was oriented in each of the different angular directions (0°, 45°, 90°, 180°) relative to the simulated geometry.

The field surface area was consistent for each of the angles and the simulated total number of primary neutrons was comparable to the total flux for each of the measurements as measured on the Ionisation Chamber Monitor (ICM).

7.3 Results

7.3.1 Experimental Results

For each of the comparable measurements (beam energy, converter thickness and angle), the experimental results were acquired for identical acquisition times (in the case of measurements taken at the same beam energy) and similar number of ICM counts (limited by ICM measurement certainty). This was done to ensure the total integrated neutron flux was the same for each measurement.

The fluence of the 174.35 MeV quasimonoenergetic neutron beam was lower than the 46.5 MeV quasimonoenergetic beam due to that beam sharing energy requiring to be shared with the proton therapy beam line, which resulted in very short duration beam outages while proton therapy treatments was were taking place.

7.3.1.1 SOI Microdosimeter

The energy deposition measurements taken with the SOI microdosimeter were converted to microdosimetric spectra for analysis. The comparison of the microdosimetric spectra, of the bare SOI microdosimeter, for both beam energies used are shown in Figure 7.7.

There was a slightly larger silicon recoil contribution in the bare SOI microdosimeter measurements from the 46.5 MeV beam energy due to the silicon elastic recoil cross section having a maxima just below this energy and dropping significantly at higher energies.

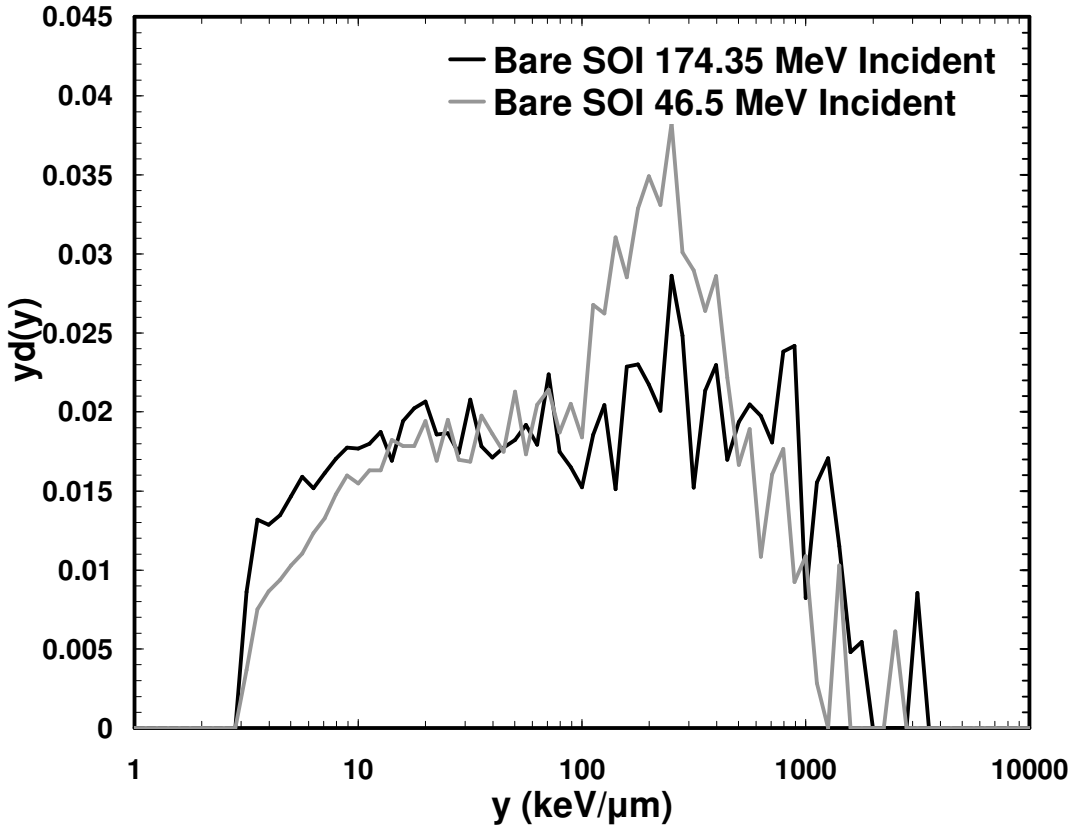

Figure 7.7. Microdosimetric spectra with spectra from the bare SOI microdosimeter irradiated with 46.5 MeV and 174.35 MeV neutrons

The contribution to the energy depositions for this setup is expected to mostly be from the recoil silicon component which, for the 46.5 MeV beam, is 6.18 MeV with a range in silicon of 3.5 µm, less than the 5 µm thickness of the SOI microdosimeter cell used for the measurements. This corresponds to a maximum lineal energy being recorded of approximately 1240 keV/µm for direct high energy recoils and a much higher probability of "Insider" types of events.

For the higher energy beam, any direct recoil from neutrons above approximately 79 MeV will have a range of 5 µm in silicon, and this will lead to a maximum energy deposition of approximately 3030 keV/µm. Any silicon recoils from energies greater

than 79 MeV, such as encountered in the 174.35 MeV nominal quasimonoenergetic beam, will produce significantly lower energy depositions due to only a small ΔE component from a "Starter" type event occurrence. This is shown in the bare SOI microdosimetric spectra of yd(y), in Figure 7.7, as the higher energy beam contribution produces a flatter appearing distribution due to the lower energy beam contributing to higher apparent lineal energy deposition events.

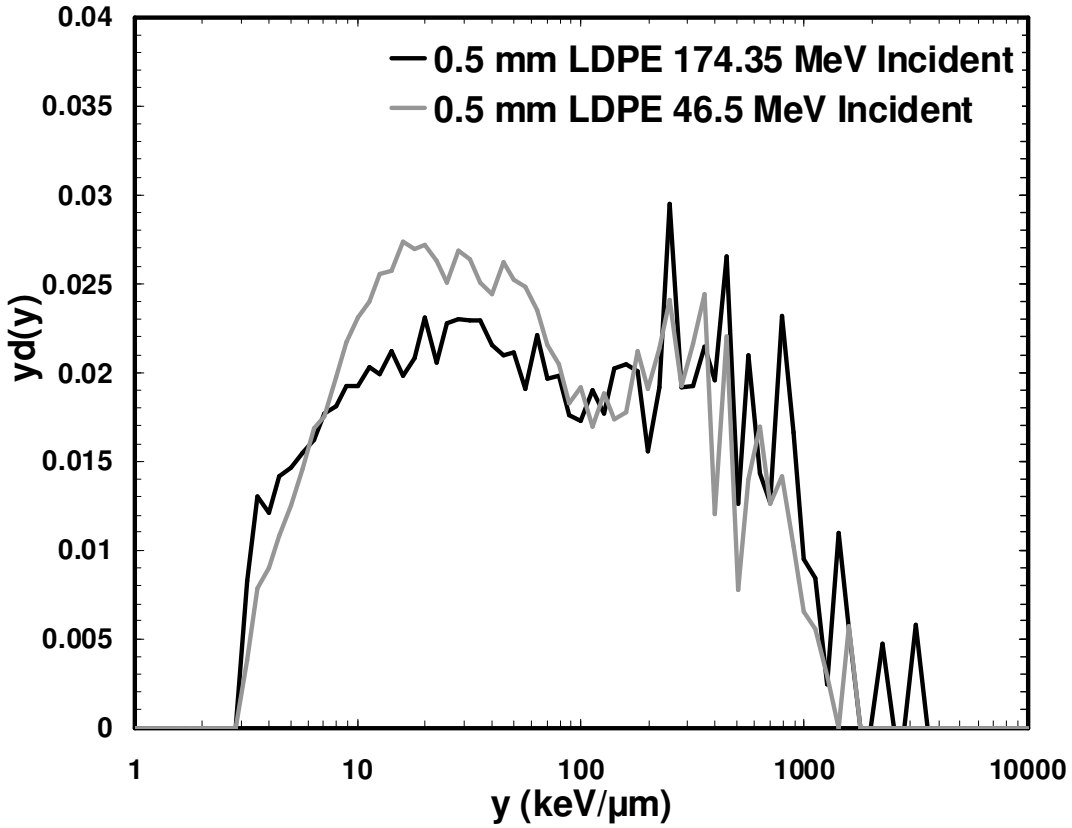

Figure 7.8. Microdosimetric spectra with a 0.5 mm LDPE converter irradiated with 46.5 MeV and 174.35 MeV neutrons

For the 174.35 MeV neutron beam the maximum silicon recoil energy is 23.2 MeV which would lead to a recorded lineal energy deposition of approximately 4600 keV/μm. The range of a 23.2 MeV silicon recoil in silicon is approximately 9 μm which is longer than the mean chord length of the SOI microdosimeter sensitive volume. The maximum lineal energy deposition from the 174.35 MeV neutron beam is therefore approximately 3600 keV/μm for the mean chord length of the SOI microdosimeter used.

The different thickness LDPE converter microdosimetric spectra are shown in Figure 7.8 (0.5 mm LDPE) and Figure 7.9 (45 mm LDPE).

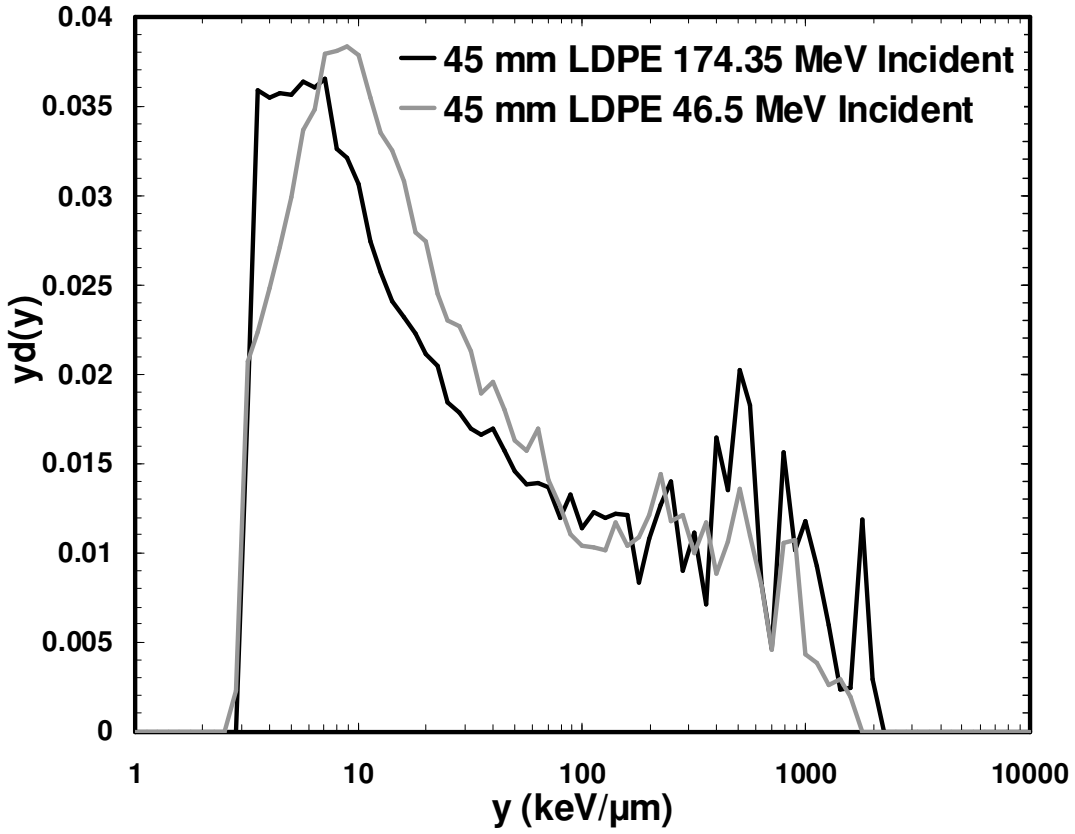

Figure 7.9. Microdosimetric spectra with the 45 mm LDPE converter irradiated with 46.5 MeV and 174.35 MeV neutrons

For each of the measurements using a LDPE converter the recoil proton component occurs below approximately 100 keV/µm. The 46.5 MeV quasimonoenergetic neutron beam produces higher lineal energy deposition events than the 174.35 MeV beam. This is most apparent in the measurements taken with the 45 mm LDPE converter measurements, as shown in Figure 7.9.

The lower lineal energy is due to protons that originate further inside the LDPE converter from the detector surface having a higher LET, after losing energy traversing the LDPE, however there is a higher probability of these lower energy protons stopping within the sensitive volume. This would lead to an underestimation in energy for these types of events.

The larger magnitude of the proton component in Figure 7.9 is due to the significantly thicker layer of LDPE. This is unlike in Figure 7.8 where the LDPE layer is only 0.5 mm and is only two orders of magnitude thicker than the sensitive volume. For the neutron energies used the total cross section for the hydrogen nuclei is approximately an order of magnitude lower than the silicon-28 cross section.

The recoil protons from the 46.5 MeV quasimonoenergetic beam are at charged particle equilibrium in the 45 mm LDPE converter unlike the 0.5 mm LDPE converter for the same beam energy. This implies that for the conditions of charged particle equilibrium that the proton energies sampled by the SOI microdosimeter are from full energy proton recoils occurring near the surface adjacent to the SOI microdosimeter down to low energy recoils from protons losing energy in the LDPE volume. The implications of this are that at charged particle equilibrium there will be a fraction of recoil protons depositing their total remaining energy in the sensitive volume. Full proton energy deposition would only occur for proton energies below approximately 450 keV. For recoil proton energies above approximately 450 keV only a partial energy deposition will occur resulting in the expected lineal energy depositions.

For the SOI microdosimeter mean chord length, the maximum total energy deposition from the recoil protons is approximately 90 keV/μm. This is in good agreement with the microdosimetric spectra shown in Figures 7.8 and 7.9. This can be seen as the limit of the proton recoils for both neutron beam energies and different LDPE thicknesses.

The 174.35 MeV quasimonoenergetic beam was not in charged particle equilibrium for any of the measurements. For charged particle equilibrium to occur at the higher energy beam, a thickness of more than 200 mm LDPE would be required. This amount of LDPE is not feasible for a portable SOI microdosimetry system and is larger than the complete portable battery powered SOI microdosimeter system.

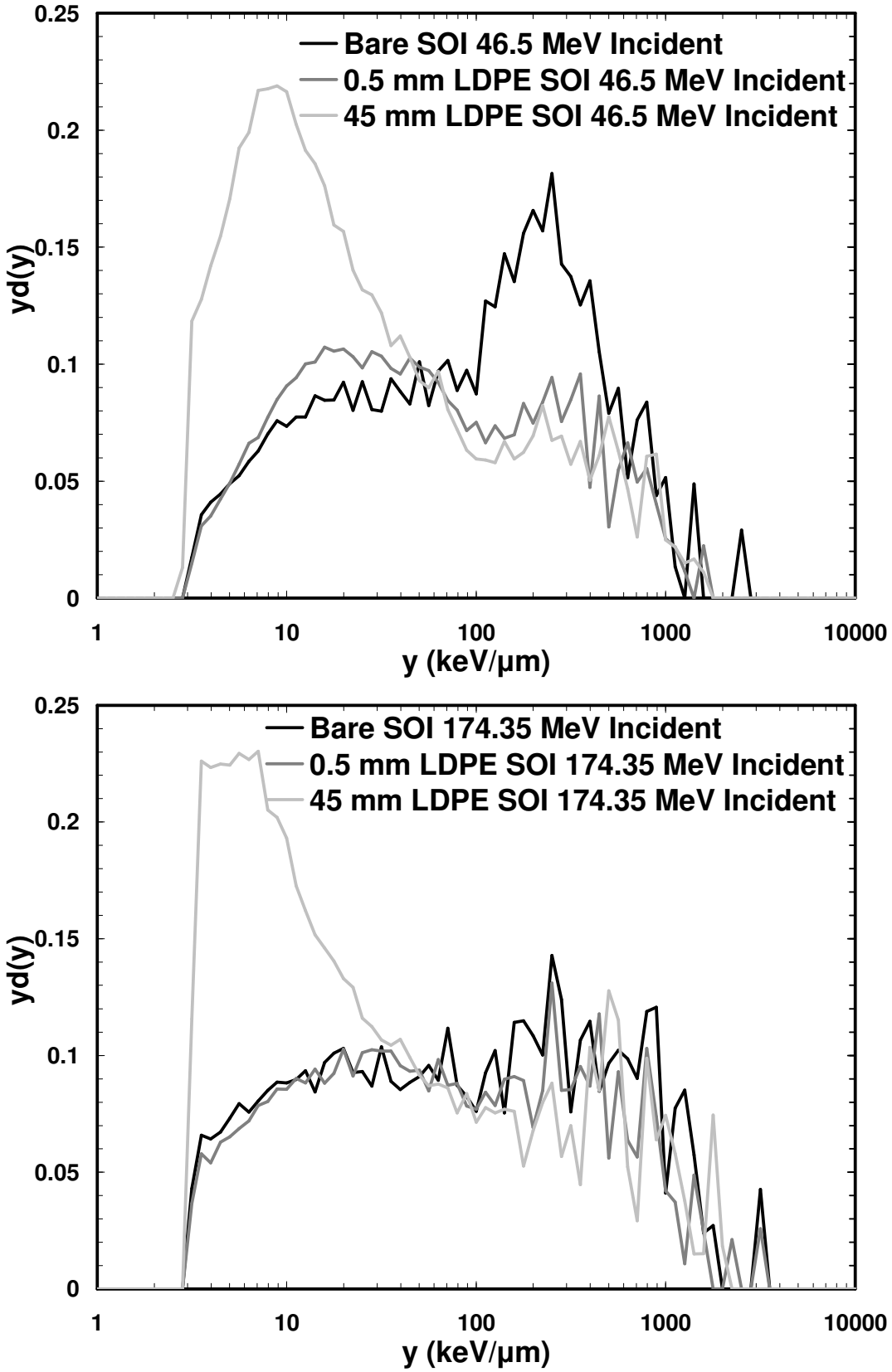

Figure 7.10. The comparison of the different LDPE thicknesses used in the SOI microdosimeter measurements. The 46.5 MeV quasimonoenergetic beam measurements are at the top and the 174.35 MeV quasimonoenergetic beam measurements are at the bottom

The component due to the Si recoils occurs over the full lineal energy range measured, as shown by the bare SOI microdosimeter measurements in Figure 7.7. The lineal energy depositions from the silicon recoils remain significant in all of the measured spectra for lineal energies greater than the maximum recoil proton lineal energy of approximately 90 keV/μm.

7.3.1.2 Silicon PIN diode

The results of the PIN diode experimental measurements were collected and analysed for the different thicknesses of LDPE converter as well as for angular rotation of the pin diode with each of the different thicknesses of LDPE converter. The PIN diode response for each of the experimental configurations was then simulated in GEANT4 for comparison to the experimental data.

Silicon PIN diode results for different LDPE thickness

The deposited energy spectrum obtained with a PIN diode is shown in Figures 7.11 for the 46.5 MeV quasimonoenergetic neutron beam with different thicknesses of LDPE. The PIN diode energy deposition spectra for different LDPE converter thicknesses with the 46.5 MeV quasimonoenergetic neutron beam show an increasing contribution from recoil protons between approximately 700 keV and 8 MeV. A peak can be observed at 1.1 MeV from the recoil protons with a continuum ending at a recoil proton 'shoulder' starting at approximately 6.2 MeV. This corresponds to the maximum energy deposition from the recoil protons in a 300 μm thick silicon volume and is a gradual shoulder due to the angular distribution of the recoils leading to a maximum energy deposition of approximately 8 MeV from angular proton recoils.

The LDPE charged particle equilibrium for 46.5 MeV neutrons occurs at 19.4 mm of LDPE. None of the PIN diode measurements occurred at charged particle equilibrium due to the maximum possible LDPE thickness of 12.5 mm. This means that a proton recoil generated from the opposing side of the LDPE layer from the detector would only lose approximately 16.5 MeV in the 12.5 mm of LDPE before entering the detector. The remaining 30 MeV would then deposit just 1.03 MeV in the PIN diode. This produces the peak observable in Figure 7.11.

A consequence of the maximum energy loss of 16.5 MeV in the LDPE for the 46.5 quasimonoenergetic beam is that almost all of the energy deposition events due to partial energy loss resulting in a ΔE spectrum for both quasimonoenergetic neutron beams. Normally incident proton recoils with energies below approximately 6 MeV, can be expected to deposit all of their energy in the sensitive volume of the PIN diode. The only recoil protons that will contribute to full energy deposition events in the PIN diode are recoils from the tail below the monoenergetic neutron peak. These protons will be stopped within the sensitive volume and contribute their full energy, *E*, within the PIN diode.

A recoil proton generated in the LDPE directly adjacent to the detector with 46.5 MeV would deposit 730.5 keV in the PIN diode. This corresponds to the lowest possible energy deposition events recorded in the PIN diode from proton recoils. Events recorded below this energy are due to prompt gamma radiation induced by inelastic events in the surrounding environment.

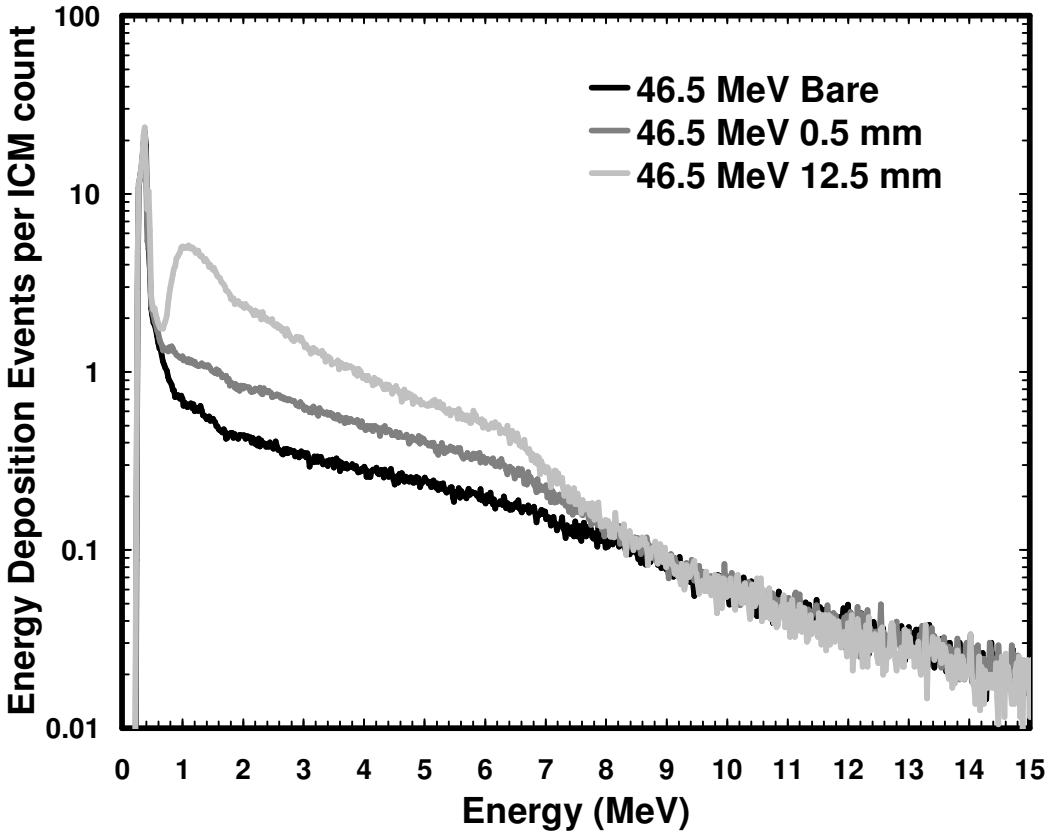

Fig. 7.11. Experimental energy deposition event spectrum for a 300 μm PIN diode with LDPE converter of given thickness irradiated with top: 46.5 MeV quasi-monoenergetic neutrons.

The PIN diode measurements for the 174.35 MeV quasimonoenergetic beam energy are shown in Figure 7.12. The minimum energy deposition for a proton recoil, produced adjacent to the detector surface, in the PIN diode is 277 keV. The energy loss of a 174.35 MeV proton in 12.5 mm of LDPE is 6.1 MeV leading to a maximum energy deposition for a normally incident 168.25 MeV proton of 283.57 keV in 300 μm thick silicon. These recoil proton energies coincide with low energy peak in the spectrum just above the noise threshold produced from the prompt gamma ray emission events. The amplitude of the low energy peak is increased relative to the 0.5 mm LDPE and bare PIN diode responses due to the addition of the proton recoil and gamma ray components.

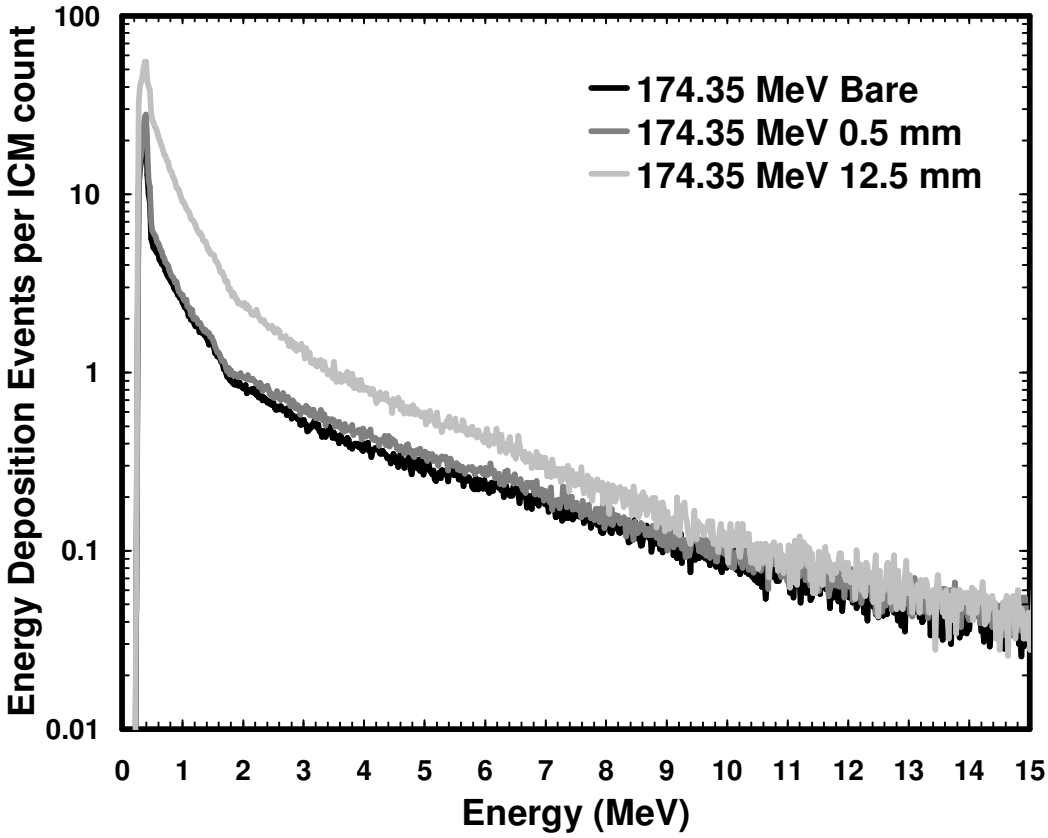

Fig. 7.12. Experimental energy deposition event spectrum for a 300 μm PIN diode with LDPE converter of given thickness irradiated with 174.35 MeV quasi-monoenergetic neutrons.

The spectra above this low energy peak are in a continuum due to higher energy depositions from oblique proton recoils and silicon recoils within the PIN diode.

The 0.5 mm thick LDPE converter showed only a very slight increase in detector response compared to the bare PIN diode. This is due to the significant decrease in proton elastic recoil cross section at these higher energies.

Silicon PIN diode results for different irradiation angles

Angular response measurements of the PIN diode with different converter thicknesses were taken for both of the quasimonoenergetic neutron beam energies used. Figures 7.13 and 7.14 show the response of the PIN diode as a function of angle for the with respect to the incident 46.5 MeV and 174.35 MeV quasimonoenergetic neutron beams.

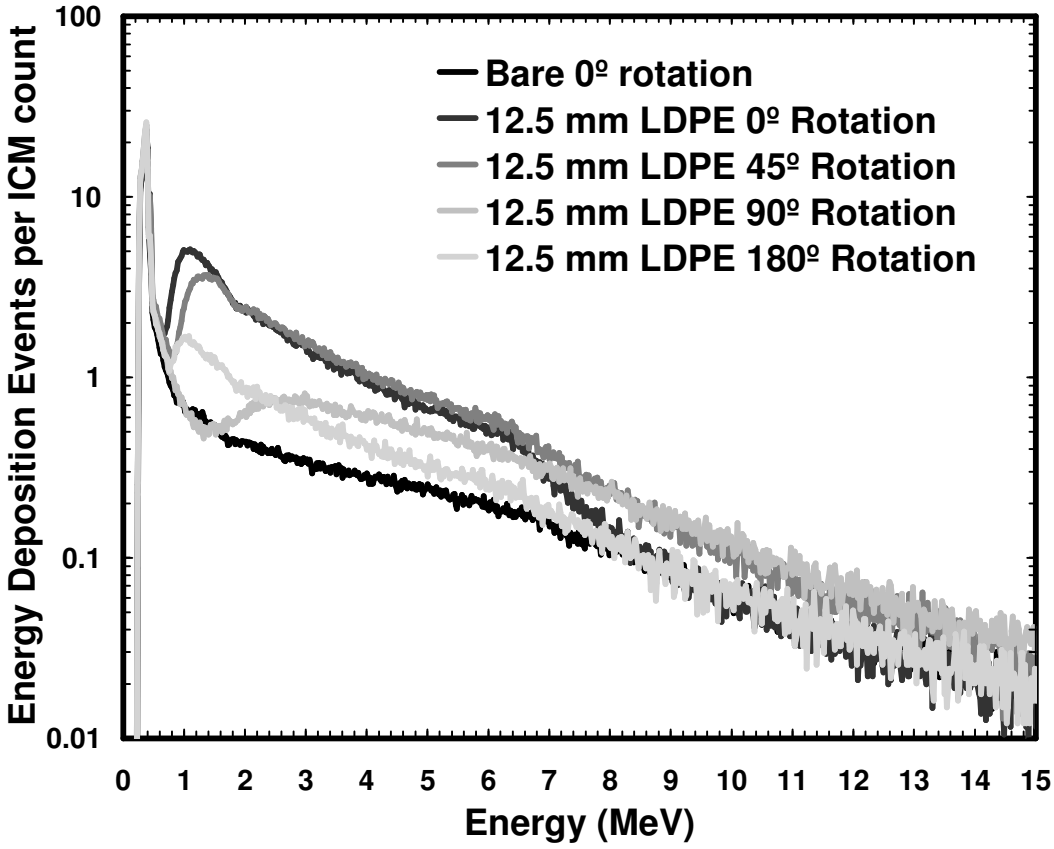

Fig. 7.13. Energy deposition event spectrum for a 300 μm PIN diode with 1.25 cm LDPE irradiated with various angles of incidence for the 46.5 MeV quasi-monoenergetic neutron beam.

The PIN diode rotation results show that due to the geometric rotational asymmetry of the PIN diode structure there is a related variation in energy deposition. Due to the energy deposition dependence on the recoil angle, the energy deposition spectrum varies significantly.

The low energy recoil proton peak seen in the 12.5 mm LDPE spectrum at normal incidence moves to higher energies in the 45° and 90° angular energy deposition measurements. This is from the minimum energy deposition events increasing in energy due the maximum recoil proton energy now traversing a longer chord length of 424 μm through the PIN diode at a 45° angle.

The 90° case results in a transition point where the majority of the events become full energy deposition due to the low energy protons, produced by high angle elastic recoils,

depositing their full energy into the PIN diode sensitive volume. Both the 45° and 90° angle measurements recorded energies above the 6-8 MeV shoulder in the 46.5 MeV quasimonoenergetic neutron beam measurements. This occurs from the higher energy deposition recoil protons, now being able to deposit more energy than in the silicon volume due to the angle than for the 0° and 180° incident radiation.

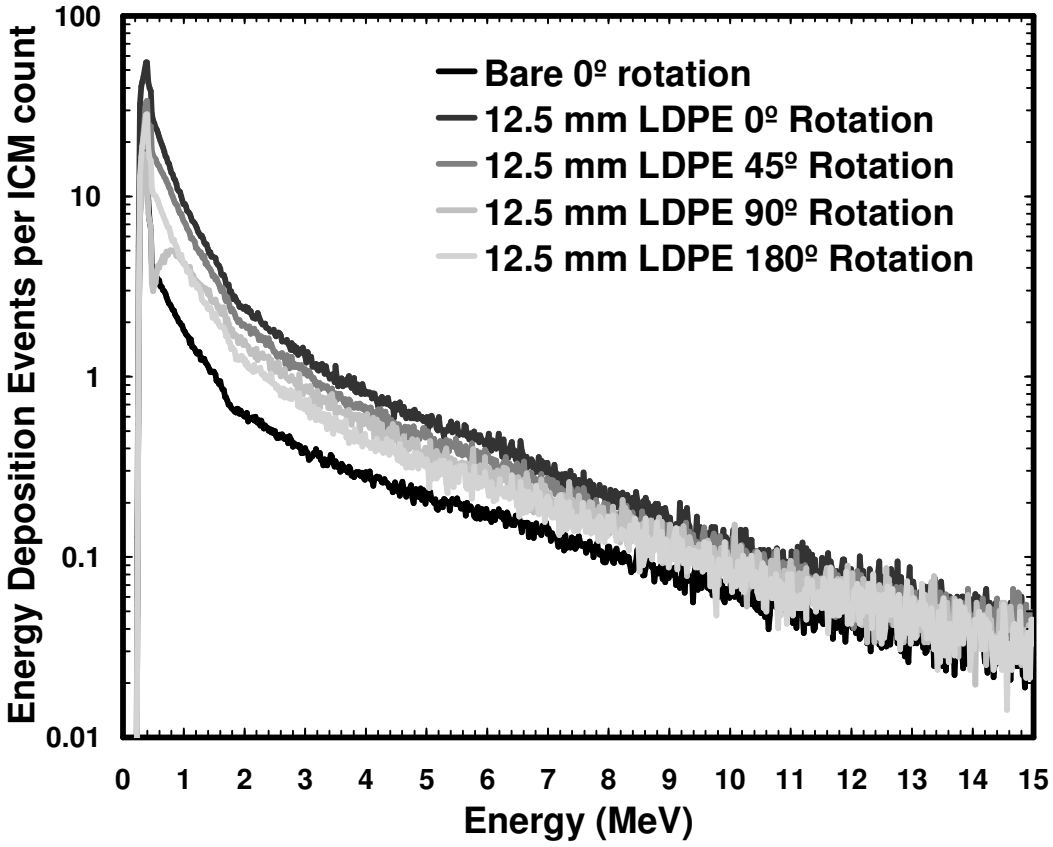

Fig. 7.14. Energy deposition event spectrum for a 300 μm PIN diode with 1.25 cm LDPE irradiated with various angles of incidence for the 174.35 MeV quasi-monoenergetic neutron beam.

The PIN diode angular dependence to the 174.35 MeV quasimonoenergetic neutron beam in Figure 7.13 shows the same response as the lower energy beam. The 90° incident neutron beam clearly shows the increased shift of the minimum energy depositions to about 500 keV with a peak observed at approximately 800 keV. This corresponds to the 1 cm width of the PIN detector volume.

The 180° measurements at both energies have a significant recoil proton contribution when compared with the respective bare measurements. The response of the rear side irradiation produces a greater proton recoil component than the 0.5 mm LDPE converter at 0°. This indicates that the ceramic PIN diode support contains a significant amount of hydrogen in the composition.

The response of the 0.5 mm LDPE covered PIN diode angular response for both neutron energies is similar to the angular response of the thicker 12.5 mm LDPE converter but with a reduced proton recoil component. Both of these can be observed in Figure 7.15. The complete data and graphs for all of the measurements can be found in Appendix 7.

This response to the angular distribution of the incident radiation is important when attempting to perform PIN diode dosimetry on radiation fields with large solid angles (i.e. from a neutron emitting point source at close range where field can be up to 2π solid angle) or an isotropic radiation field as encountered at high altitudes (where due to atmospheric reflection the neutron field at aviation altitudes approximately isotropic in 4π) and radiation protection applications from radiation sources where there are large amounts of backscatter.

Noteworthy is that the response of the detector to rear side irradiation (180°), for both neutron beam energies, exhibited a lower intensity proton peak at the same peak energy for normally incident recoil protons (0°). This is due to both the hydrogen in the adhesive used to bind the PIN diode to the ceramic diode support as well as hydrogen present within the porous ceramic PIN diode support.

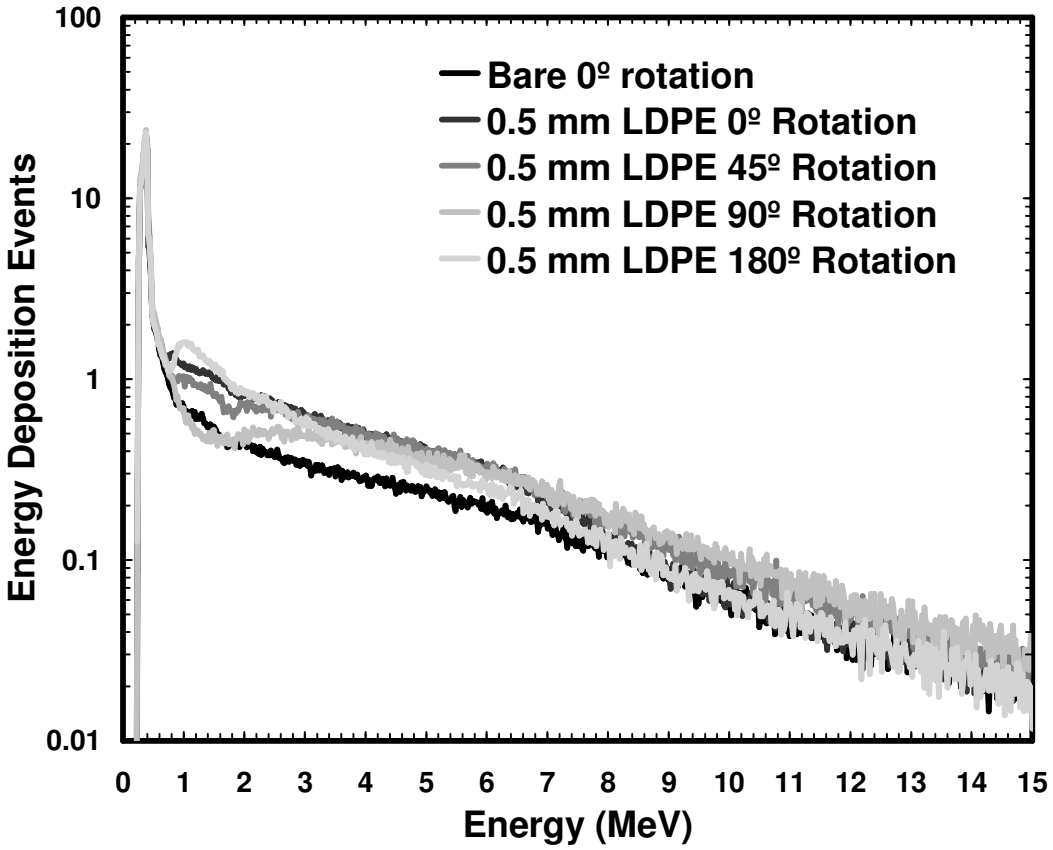

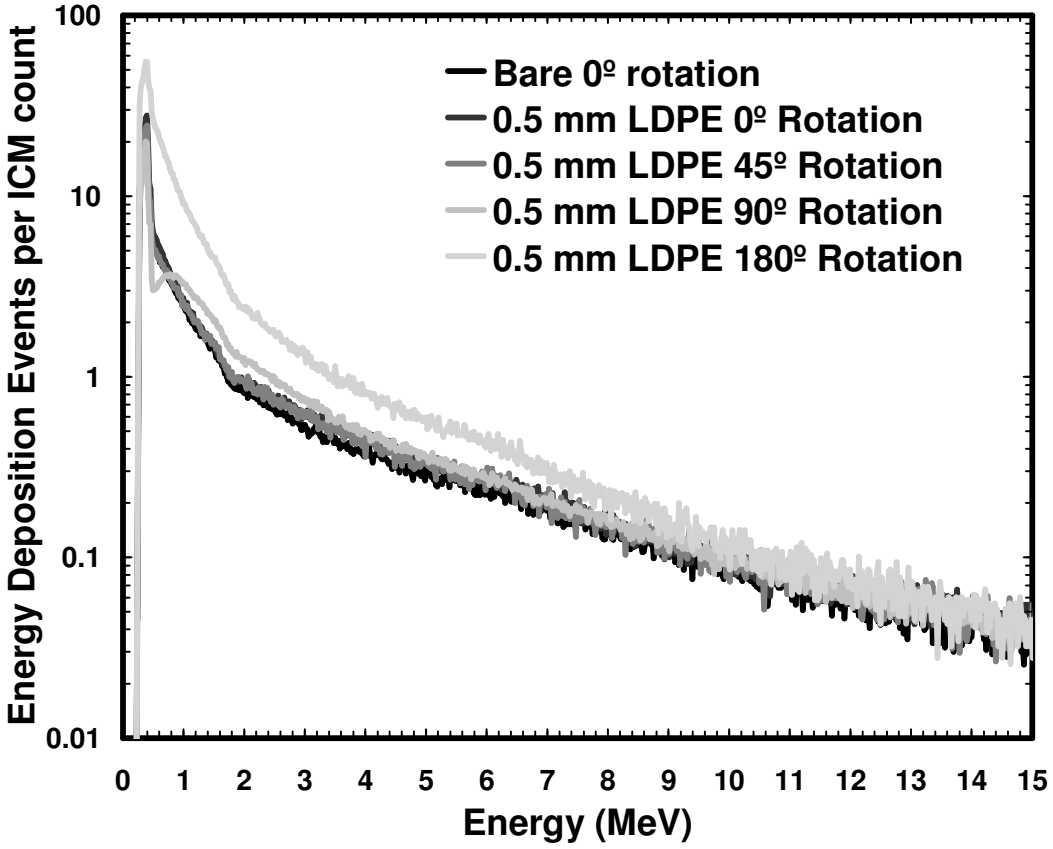

Figure 7.15. The angular response of the 0.5 mm thick LDPE converter to the two quasimonoenergetic neutron energies Top: 46.5 MeV Bottom 174.35 MeV

The peak at approximately 800 keV in the 90° angle 0.5 mm LDPE converter for the 174.35 MeV quasimonoenergetic beam energy is due to the same mechanism as the 12.5 mm LDPE converter. This indicates that for a high energy neutron field the choice of detector and converter dimensions is vital for the use of solid state detectors. Smaller detectors with dimensions similar in all directions will produce a ΔE spectrum without the irregularities observed with the PIN diode.

7.3.2 GEANT4 Simulated Results

The GEANT4 simulation used the input spectra for each of the quasimonoenergetic beam energies and was simulated using the accurate geometric setup for the same number of primary events as encountered in the experimental situation. This included the complete isotopic compositions for all of the materials used. The energy deposition events recorded in the SOI microdosimeter simulation were converted to *yd(y)* vs. lineal energy deposition spectra for microdosimetric analysis.

7.3.2.1 SOI Microdosimeter

The results of the simulated GEANT4 SOI microdosimeter results are shown in Figure 7.16. All of the results show a significant amount of high lineal energy deposition events above 100 keV/μm regardless of converter thickness or quasimonoenergetic beam energy. This is accounted for by the high energy of silicon recoils occurring in the sensitive volume being classified as “insiders” or “starters”.

The maximum energy from a silicon recoil due to a 46.5 MeV neutron is 6.2 MeV, this equates to a range in silicon of 3.5 μm, less than the SOI microdosimeter thickness used and hence the highest lineal deposition event of 1240 keV/μm .

The silicon recoil energy from a 174.35 keV neutron is 23.25 MeV which corresponds to a range in silicon of 8.97 μm. This corresponds to a maximum energy deposition in silicon of 10.6 MeV in 5 μm of silicon and a lineal energy deposition of 2120 keV/μm.

These maximum energy deposition events can be seen in the simulated lineal energy spectra in Figure 7.16 as well as the experimental lineal energy spectra in Figure 7.10.

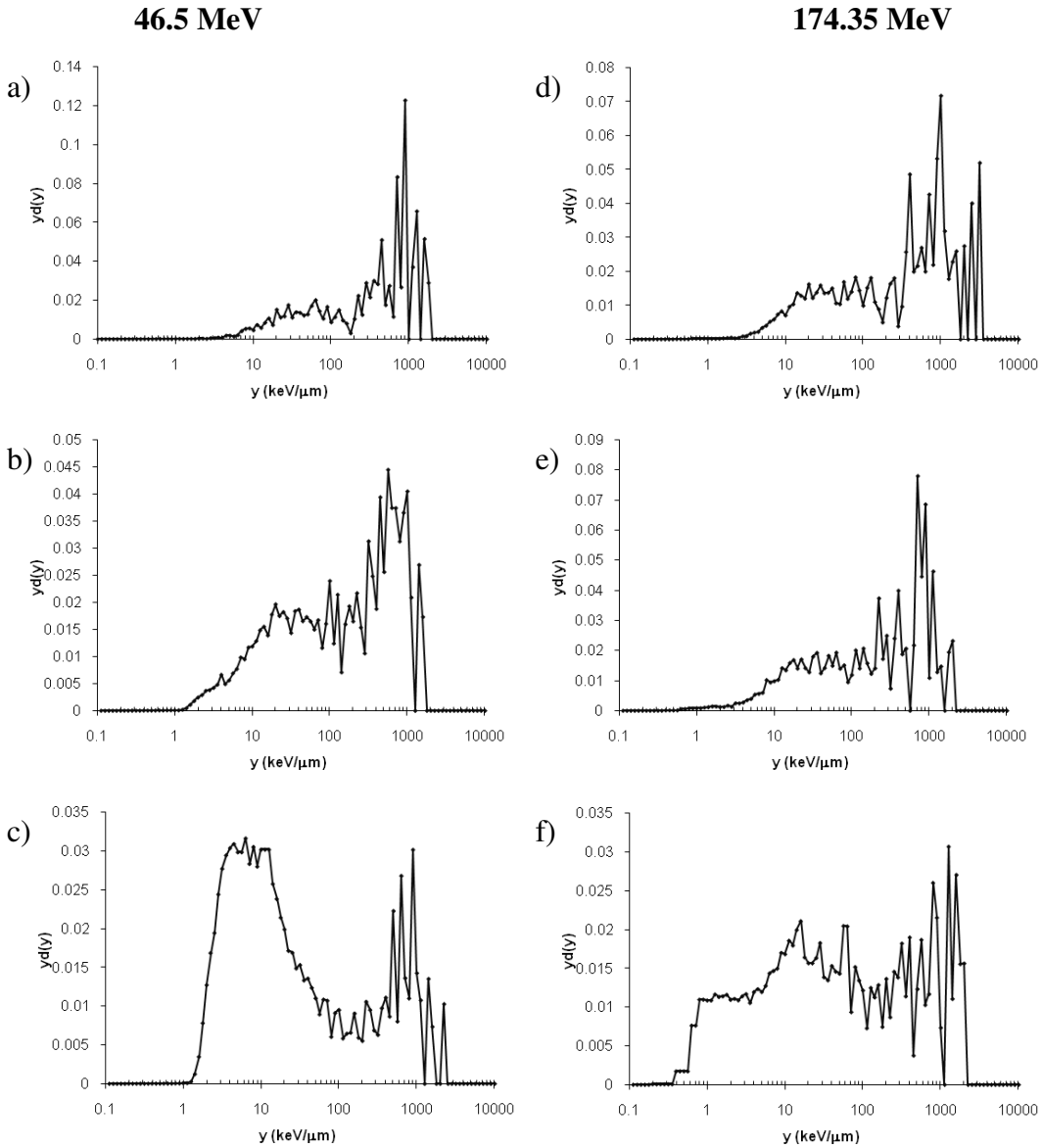

Figure 7.16. Microdosimetric spectra for the 49.5 MeV (left hand column) and 174.35 MeV (right hand column) simulated quasimonoenergetic neutron beam. The rows illustrate the thickness of LDPE layer a) No converter, b) 0.5 mm LDPE, c) 45 mm LDPE

There is a significant discrepancy between the simulated and experimental data in the 174.35 MeV quasimonoenergetic beam energy simulation of the SOI microdosimeter with the 45 mm LDPE layer below 15 keV/μm, as shown in spectrum (f) in Figure 7.16. Where a significant proton recoil peak is expected to be observed at lower lineal energies than is apparent in spectrum (c), the proton recoil component is not clearly observed as seen in the experimental measurements.

The over and under estimation appears to be due to overestimation of the neutron-silicon cross section at high energies in comparison to the neutron-proton cross section in GEANT4. The neutron data libraries used with GEANT4 end at 100 MeV for the ^{1}H elastic cross sections with 0.07493 barns and at 20 MeV for the ^{28}Si elastic cross sections with 0.9194 barns. Above 20 MeV the cross sections for elastic interactions are calculated using G4LElastic. Inelastic interactions are calculated using G4BertiniCascade which may lead to inaccuracies depending on the method used to evaluate the cross sections.

The published elastic high energy cross sections (JENDL/HE-2007, accessed through ENDF November 2009) for the ^{1}H elastic scattering with ^{28}Si is 0.075 barns at 100 MeV and 0.92 barns at 20 MeV . These value are consistent, however for the higher energies encountered in the experiment the published elastic cross sections for ^{1}H are 0.181 barns at 46.5 MeV and 0.046 barns at 174.35 MeV while the published ^{28}Si elastic cross sections are 1.14 barns at 46.5 MeV and 0.27 barns at 174.35 MeV.

For the 46.5 MeV quasimonoenergetic beam energy the hydrogen recoil cross section will be accurate, due to the presence of the data in the G4NDL3.13 table, however the silicon recoil cross section may have uncertainties up to about 10%. For the 174.35 MeV quasimonoenergetic beam simulations the uncertainties may be much larger and lead to the relative overestimation of the silicon recoil component that was observed.

The comparison of the bare SOI microdosimeter experimental results and simulation, as shown in Figure 7.18, appear to indicate a small discrepancy with the lower lineal energy component below 20 keV/μm and the region above 100 keV/μm. The features due to the silicon recoils are recognisable in both the experimental and simulated spectra. A possible explanation for this is the overestimation in the silicon recoil cross section leading to higher energy deposition events.

The discrepancy between the simulated and experimental spectra could also be due to the geometry of the simulated SOI microdosimeter. As the electric field and charge collection characteristics were not modelled, recording of higher energy silicon recoil events in the simulation compared to the experiment is possible. This could result if a

neutron produces an oblique recoil in the sensitive volume which in the simulation would deposit all of its energy along the projected path. In the experimental situation only a portion of the energy would be collected for oblique silicon recoils due to the cell consisting of a high charge collection efficiency region of 10x10 μm with a partial charge collection region between the 30 μm spaced cells. This experimentally confirmed in the IBIC maps described in chapter 8. These differences in charge collection can explain both the high and low lineal energy deposition results for high lineal energy deposition particles such as silicon recoils.

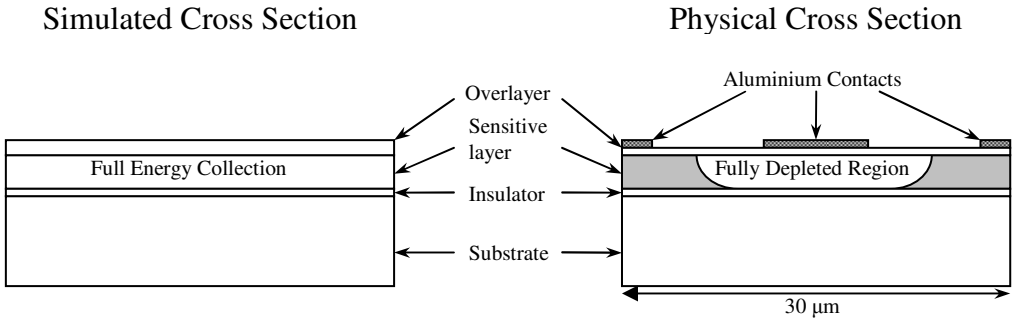

Fig. 7.17. Simulated and physical geometries of a SOI microdosimeter cell. The grey region in the schematic on the right indicates a region of partial depletion between the cells where charge recombination may take place and therefore result in only partial charge collection.

A comparison of the physical geometries in Figure 7.17 show that if a silicon recoil where to occur within the partially depleted region then it is likely the majority of the charge will recombine. This has previously been examined using a heavy ion beam with carbon nuclei (I. M. Cornelius, 2001) to test the charge collection efficiency of the SOI microdosimeter under different irradiations and bias voltages. The effect of a particle entering this region will vary depending on the lineal energy deposition and range of the particle for oblique energy depositions.

The GEANT4 SOI microdosimeter simulation results compared with the experimental measurements demonstrate good agreement. This is especially evident at the lower beam quasimonoenergetic beam energy of 46.5 MeV. The comparison of simulation and experimental results for the bare and different thicknesses of LDPE SOI

microdosimeter with the 46.5 MeV neutron beam are shown in Figures 7.18, 7.19 and 7.20. Similar results under different experimental conditions have been obtained previously using a therapeutic neutron beam (Bradley, P.D., 2001).

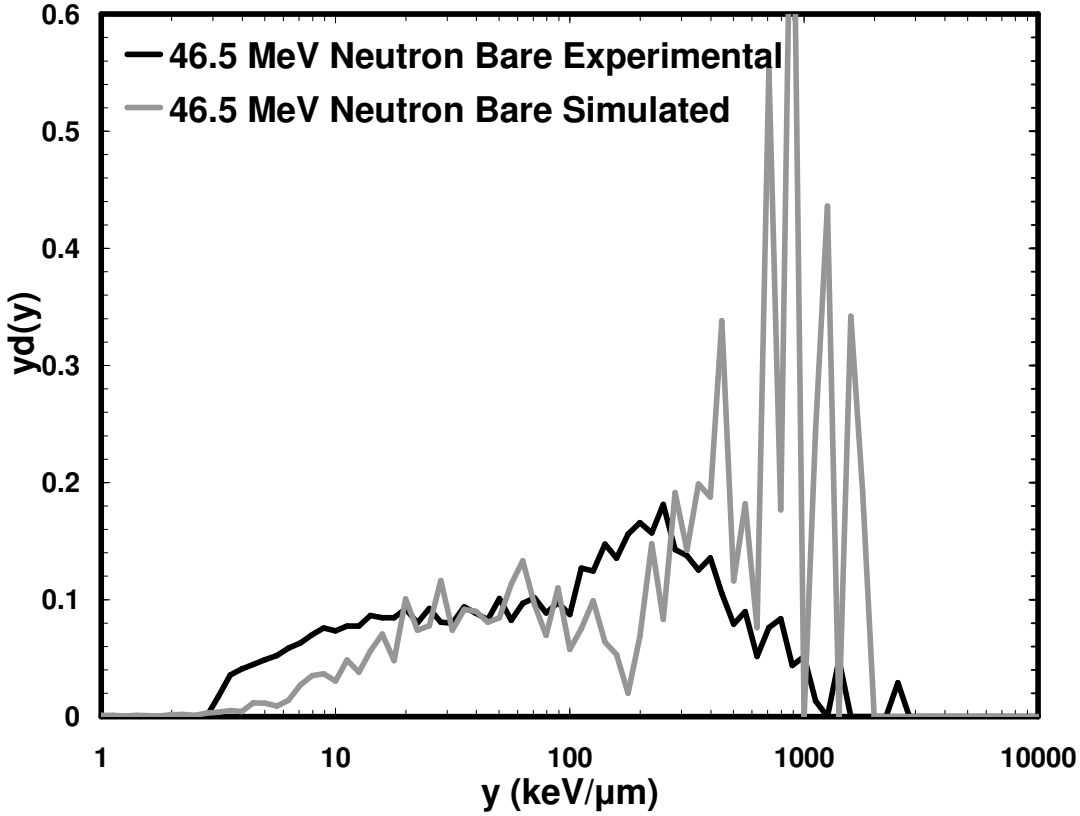

Fig. 7.18. Simulated and experimental microdosimetric spectra for a bare SOI microdosimeter irradiated with 46.5 MeV nominal quasimonoenergetic neutrons.

The overall shape for both of the lineal energy deposition spectra for a bare SOI microdosimeter is consistent with the expected energy deposition from a 46.5 MeV quasimonoenergetic beam. This includes the low lineal energy deposition events from maximum energy transfer recoil events occurring within the sensitive volume known as "Insider". If the energy deposition event originates nearby in the overlayer and loses all of its energy in the sensitive volume it is classified as a "Stopper" type of events. Stoppers cause the high lineal energy deposition "peak" above 100 keV/µm due to the silicon recoil events ending in a Bragg peak within the sensitive volume.

The lineal energy deposition events below 100 keV/µm are due to events where the silicon recoil originates near the rear side of the sensitive volume. These types of events

called “Starters” then escape from the volume before losing enough energy to approach the Bragg peak and therefore only deposit a small amount of energy within the sensitive volume.

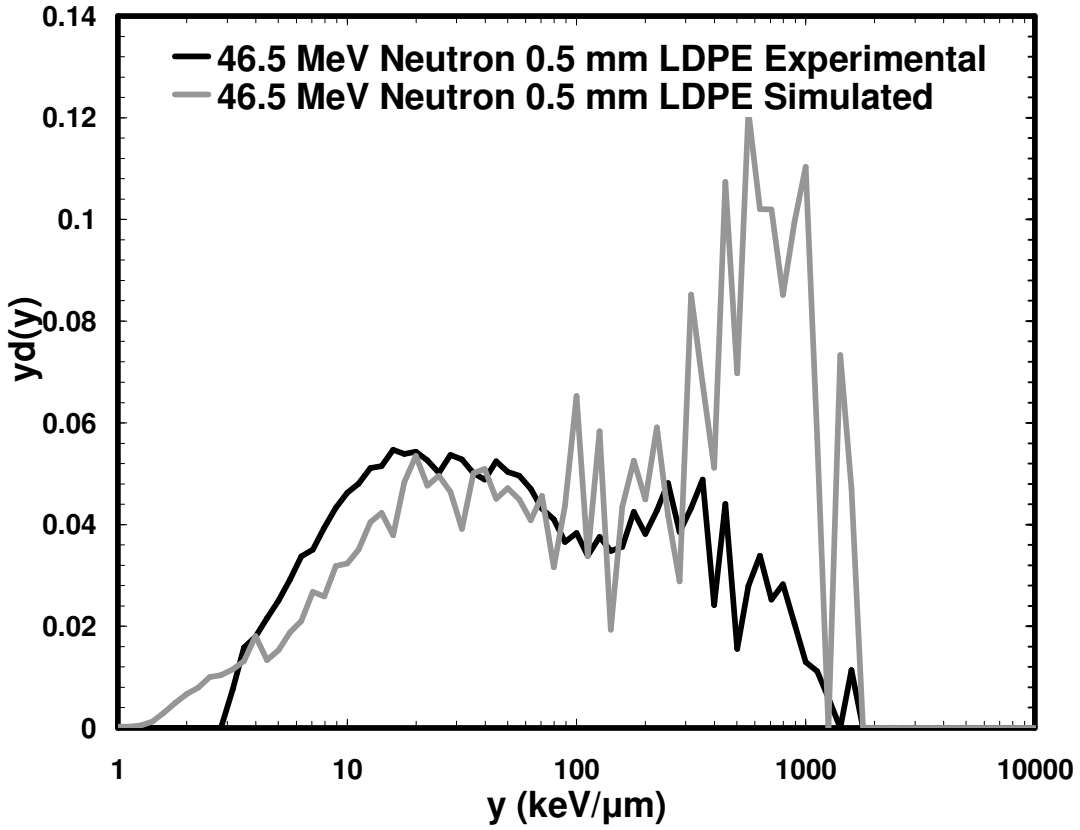

Fig. 7.19. Simulated and experimental microdosimetric spectra for an SOI microdosimeter with 0.5 mm LDPE irradiated with 46.5 MeV nominal quasimonoenergetic neutrons.

Figure 7.19 shows the comparison between the GEANT4 simulated results and the experimental results for the SOI microdosimeter covered with the 0.5 mm LDPE converter irradiated with the 46.5 MeV nominal quasimonoenergetic neutron beam. Both spectra have been normalised to unity for the energy range common to both spectra. For both of the different energies there is a noticeable increase in the recoil proton component of the spectra below 100 keV/µm relative to the silicon recoil component at higher lineal energies. Comparisons of the lineal energy deposition for the varying thicknesses of LDPE measured in the experiment are shown in Figure 7.10.

The recoil proton component becomes the most significant feature in the 45 mm LDPE measurement as shown in Figure 7.20. This recoil proton feature comes to a peak in the experimental data at 9 keV/μm while the feature in the simulated spectrum appears to be a plateau centred at approximately 7 keV/μm. The simulated spectrum has a more prominent lineal energy contribution below 6 keV/μm than for the case of the experimental measurement.

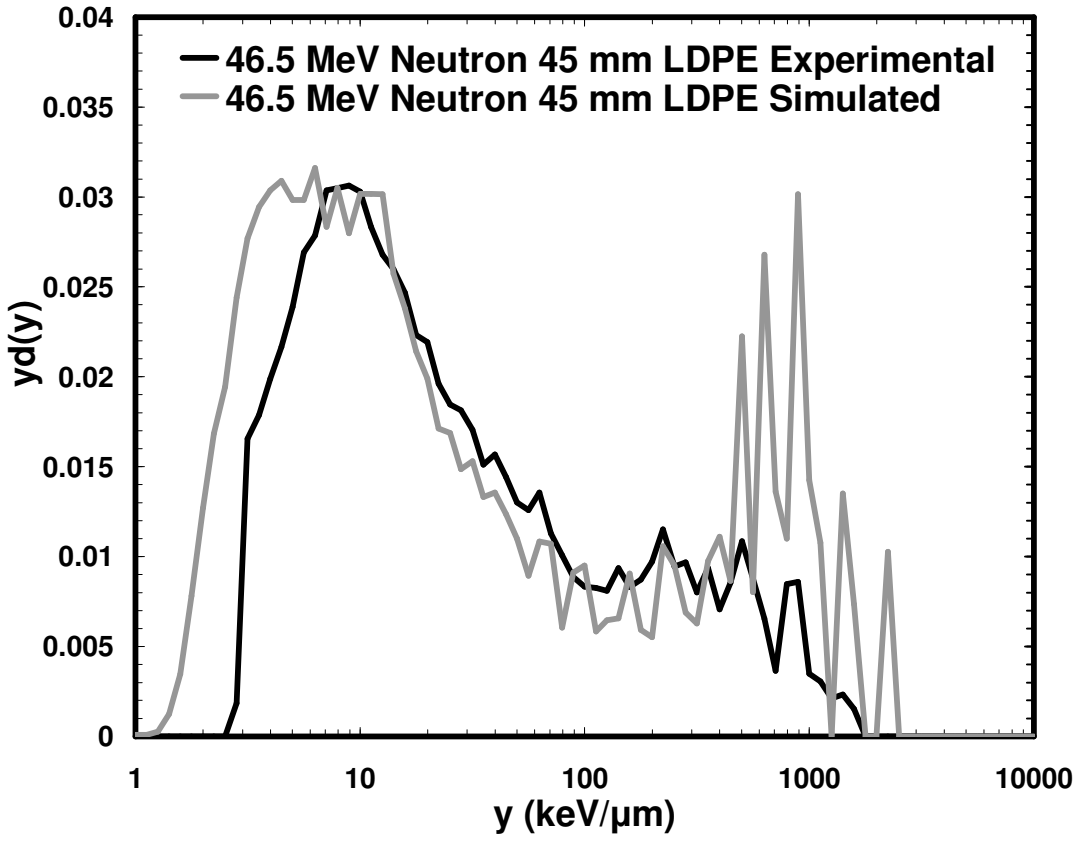

Fig. 7.20. Simulated and experimental microdosimetric spectra for an SOI microdosimeter with 45 mm LDPE irradiated with 46.5 MeV nominal quasimonoenergetic neutrons.

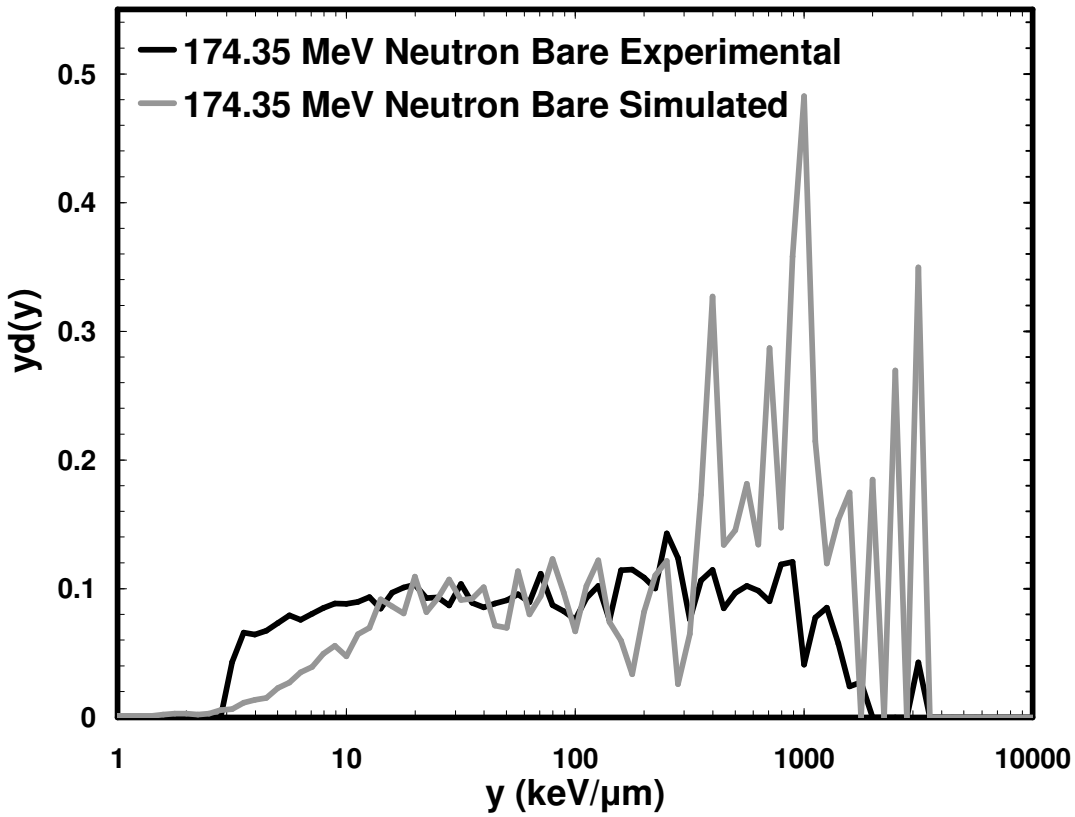

Fig. 7.21. Simulated and experimental microdosimetric spectra for a bare SOI microdosimeter irradiated with 174.35 MeV nominal quasimonoenergetic neutrons.

The comparisons of the experimental measurements and simulated results for the 174.35 MeV quasimonoenergetic beam are shown in Figures 7.21, 7.22 and 7.23.

A reasonable agreement is also seen in the case of the bare and 0.5 mm converter comparisons for the 174.35 MeV quasimonoenergetic neutron beam measurements. The same slight discrepancies occur for the high and low lineal energies as for the 46.5 MeV quasimonoenergetic beam.

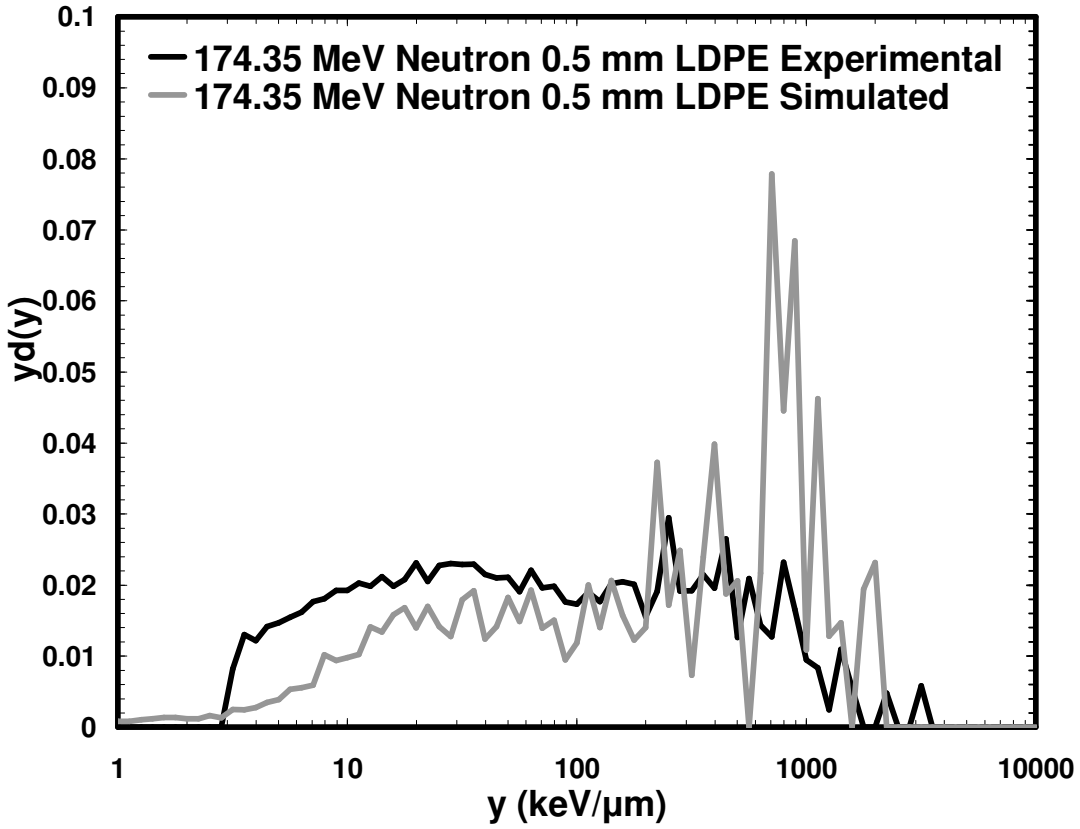

Fig. 7.22. Simulated and experimental microdosimetric spectra for a 0.5 mm LDPE covered SOI microdosimeter irradiated with 174.35 MeV nominal quasimonoenergetic neutrons.

The comparison between the experimental measurement and the GEANT4 simulation of the 45 mm LDPE layer at the 174.35 MeV quasimonoenergetic beam energy diverges below 10 keV/µm. This appears to be a limitation of the high energy proton elastic recoil cross section producing less high energy protons than lower energy angular protons and silicon recoil events.

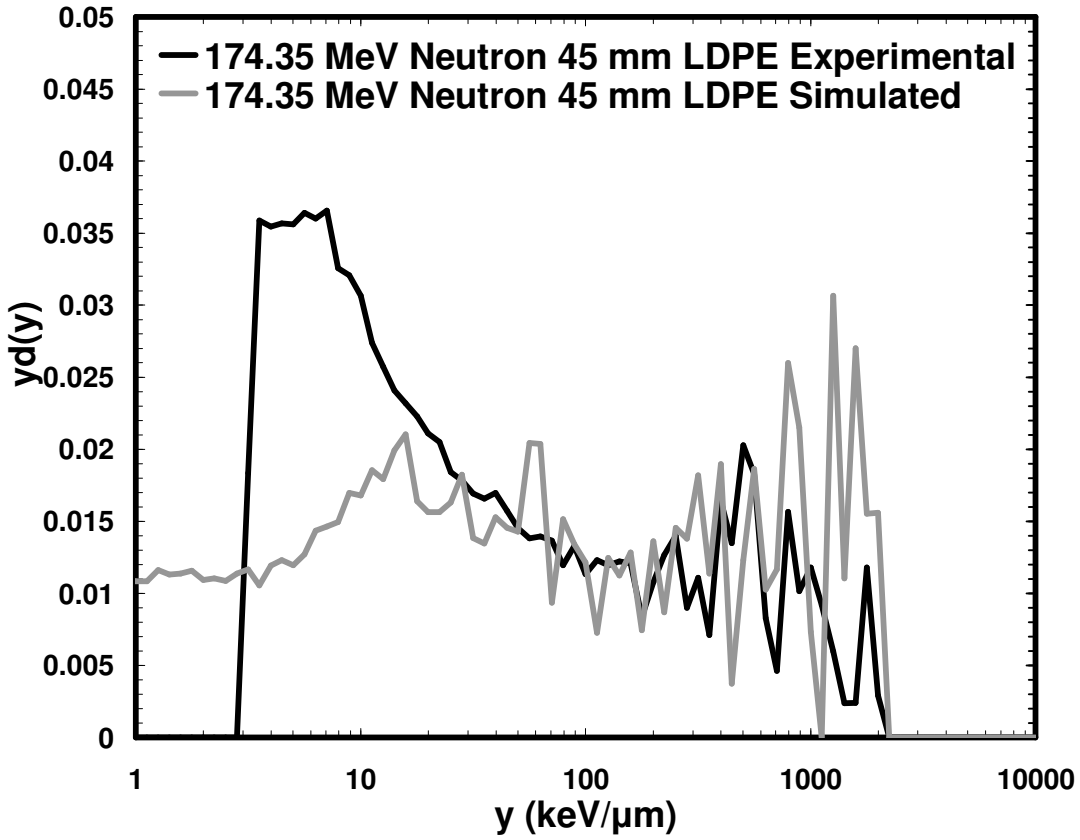

Fig. 7.23. Simulated and experimental microdosimetric spectra for a 45 mm LDPE covered SOI microdosimeter irradiated with 174.35 MeV nominal quasimonoenergetic neutrons.

The experimental measurement showed the expected lower lineal energy deposition contribution from the higher energy recoil protons. This continues down to the noise threshold of the measurement at 3 keV/µm. The lowest lineal energy deposition event from a high energy recoil proton at 174.35 MeV in silicon is 0.92 keV/µm. This is shown in the simulated response as the lowest lineal energy deposition events occurring at this energy.

7.3.2.2 PIN Diode

The GEANT4 simulated results of the PIN diode measurements display good agreement with the experimental results. Comparisons between the experimental and simulated results for the 46.5 MeV quasimonoenergetic neutron beam are shown in Figure 7.24.

The simulation only considered the neutron component of the beam. To conserve computing time only an area covering the LDPE converter for the neutron beam was simulated. This means that the experimentally observed gamma component of the radiation field produced within the lithium target, as well as the prompt neutron-gamma emissions from the surrounding environment, are not observable in the simulations of the 46.5 MeV neutron field. In the experimental data a sharp increase in the counts below 500 keV is evident before the noise cut off threshold at 200 keV.

The 46.5 MeV neutron beam comparison of the 12.5 mm thick LDPE converter shows a small difference in the low energy proton recoil peak due to the GEANT4 geometry not simulating an air gap or the thin detector dead layer between the LDPE converter and the sensitive volume of the PIN diode.

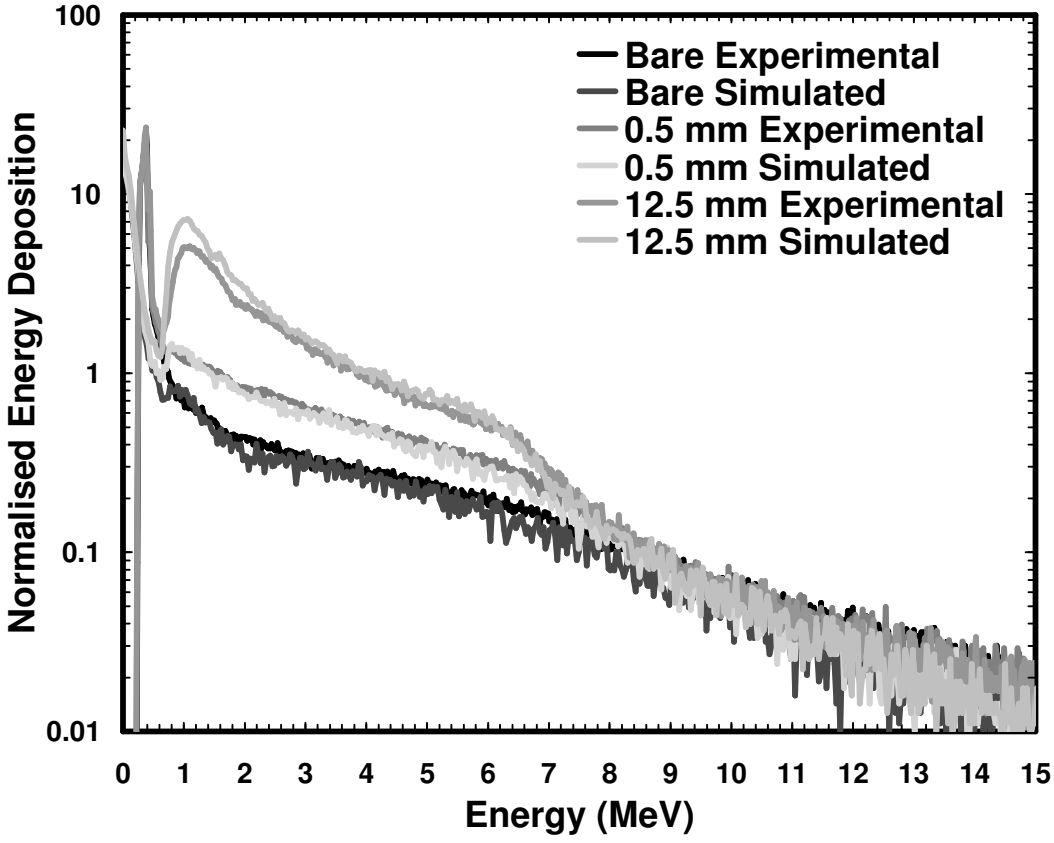

Fig. 7.24. Comparison of experimental and GEANT4 simulated energy deposition event spectrum for a 300 μm PIN diode with LDPE converter of given thickness for different quasi-monoenergetic neutron beam energies. 46.5 MeV

The 174.35 MeV PIN diode measurement comparisons with the simulation is in good agreement for the 12.5 mm LDPE converter, as shown is Figure 7.25, however there is a small increase in the experimental measurements below approximately 2.5 MeV for both the bare and 0.5 mm LDPE comparisons. This discrepancy is due to the much higher gamma background environment produced by the higher energy neutron beam within both the lithium target and associated with n,γ spallation reactions in the surrounding materials. These high intensity and high energy gamma rays produce a significant number of Compton interactions in the PIN diode, producing a Compton edge and continuum, which are not accounted for in the GEANT4 simulation.

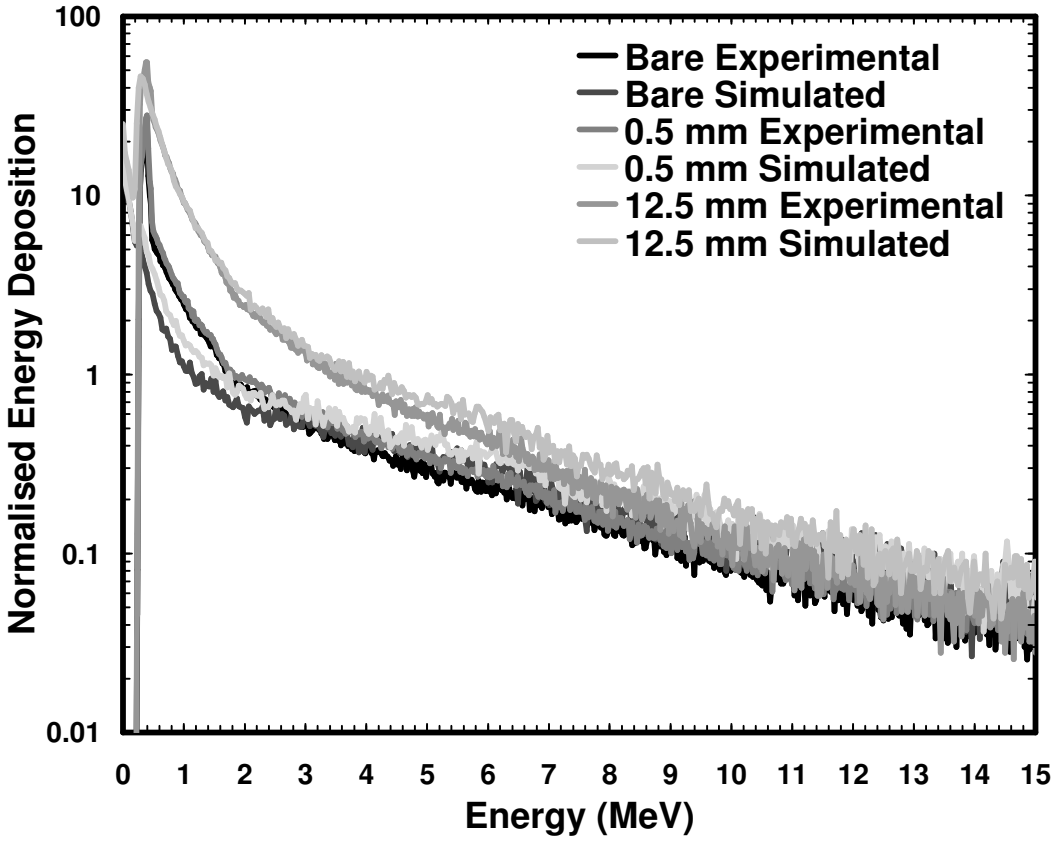

Fig. 7.25. Comparison of experimental and GEANT4 simulated energy deposition event spectrum for a 300 μm PIN diode with LDPE converter of given thickness for different quasi-monoenergetic neutron beam energies. 174.35 MeV

The simulated angular dependency shows a strong correlation with the directional incidence of radiation. As expected the 45° rotation is associated with a significant change in the 6 MeV maximum energy depositions due to the 300 μm thick silicon sensitive volume.

The simulated results of the angular PIN diode measurements for the 46.5 MeV beam are shown in Figure 7.26. The main difference between the simulated results and the measured results occur for the rear side irradiation (180°) at both neutron beam energies. This is due to the simulation geometry not including any hydrogen in the composition of the ceramic chip holder or the glue binding the photodiode to the chip holder.

The simulation also shows that for the 90° measurement that the minimum energy deposition has shifted to approximately 2.8 MeV. This is due to the proton recoils in the LDPE layer producing oblique energy depositions only. The theoretical maximum energy deposition for a 90° recoil proton completely traversing the 10 mm wide silicon sensitive volume is 44.75 MeV. In neither the simulation nor the experimental measurements could an energy deposition event of this magnitude be observed indicating that the vast majority of interactions were from much lower energy angular recoil protons obliquely striking the sensitive volume.

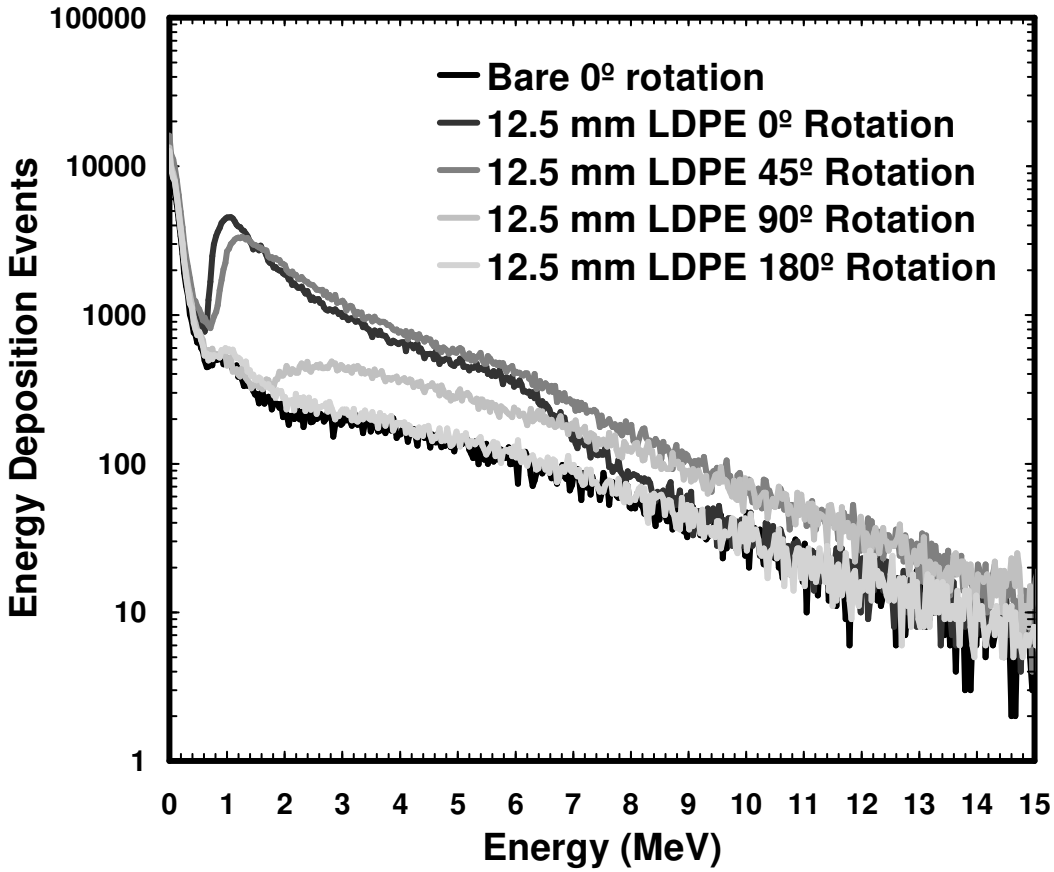

Fig. 7.26. GEANT4 simulated energy deposition event spectrum for a 300 μm PIN diode with 12.5 mm LDPE irradiated with a 46.5 MeV quasimonoenergetic neutron beam at various angles of incidence.

The simulated results of the 174.35 MeV neutron beam PIN diode angular response show the minimum proton recoil energy deposition peak that is not clearly seen in the experimental measurements due to the noise threshold. The 174.35 MeV incident neutron beam simulated at 90° shows the same 500 keV minimum energy deposition and approximately 800 keV peak as the experimental results.

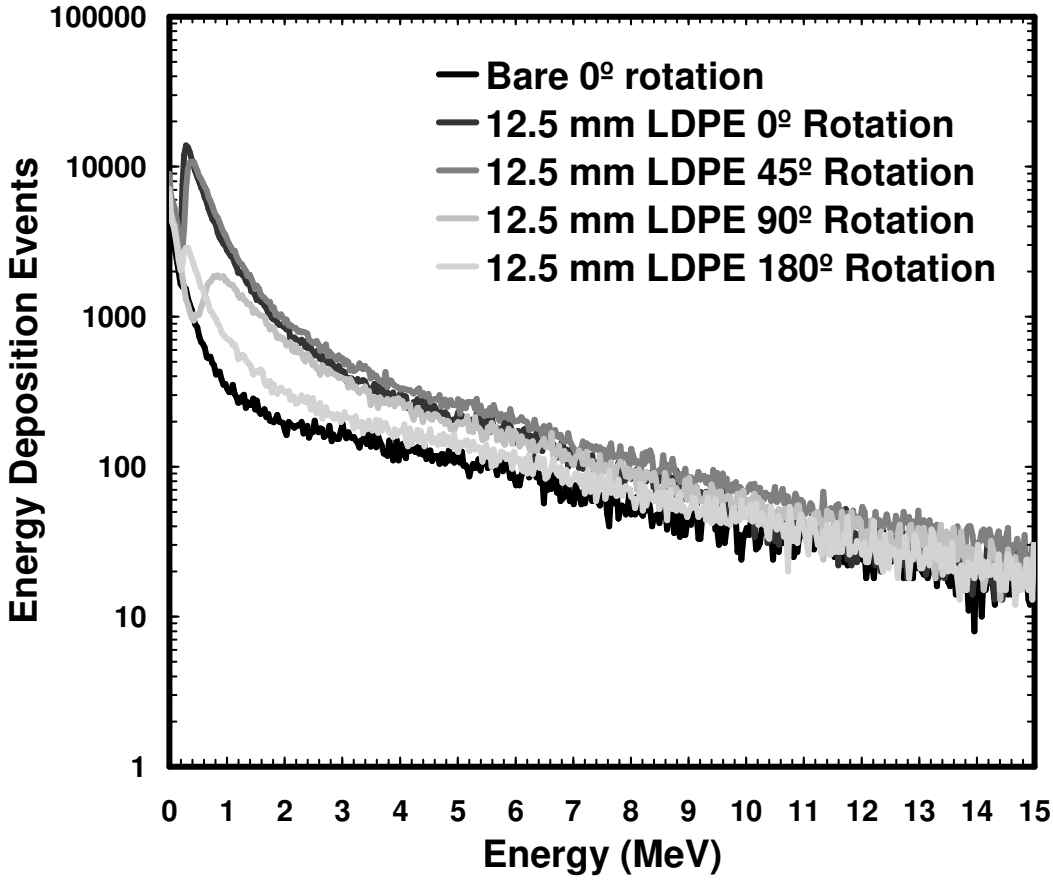

Fig. 7.27. GEANT4 simulated energy deposition event spectrum for a 300 μm PIN diode with 12.5 mm LDPE irradiated with a 174.35 MeV quasimonoenergetic neutron beam at various angles of incidence.

The angular response was also simulated for the 0.5 mm LDPE layer and bare PIN diode at both quasimonoenergetic beam energies. The response to the thinner LDPE layer was almost identical to that of the 12.5 mm LDPE thickness albeit with a reduced recoil proton component.

The bare PIN diode appeared to have minimal variation in energy deposition events. This is due to the low probability of a silicon recoil interaction occurring in a neutron field so that regardless of orientation the probability of a certain number of silicon recoil events occurring only depends on the volume of the detector. The PIN diode is therefore isotropic in response to an external high energy neutron field.

The angular response of the GEANT4 simulated results for both neutron beam energies is in good agreement with the experimental results. All of the experimental and simulated results along with all of the comparisons are shown in Appendix 7.

7.4 Discussion

The SOI microdosimeter experimental results compare reasonably well with the GEANT4 simulated response. The characteristics of SOI microdosimetry are more suitable for dose equivalent measurements in high energy isotropic neutron fields, such as those encountered at altitude, due to their inherent wider range of angular coverage. The results obtained in this study show that SOI microdosimetry is suitable for high energy neutron dominated fields.

A strong angular response of the PIN diode with an LDPE converter to a directional quasimonoenergetic neutron field was observed. From these results the use of a PIN diode with a thick converter is not well suited for the measurement of doses in high energy isotropic fields when based on calibrations from normally incident calibration neutron beams and mixed fields. It would be possible to shield the PIN diode to collimate the incoming neutron field however this would remove the advantage in having a large area for dosimetry applications.

A possible alternative is to have a cube of PIN diodes to allow for the various directional components of a neutron field to be deconvoluted and be able to determine field direction and be able to then calculate more of a dosimetric response to the neutron field. This can use the properties of the directional variations from the LDPE recoil protons with the angular invariance of the PIN diode volume to determine neutron fluence.

The effect of thickness of the converter on the response of the PIN diode for normal incidence is significant. For the use of a PIN diode for measurement of dose equivalent, a thorough investigation on optimal hydrogenous converter geometry for neutron dosimetry is needed as a single converter thickness will not give an adequate response for all neutron energies of interest for high energy applications.

8. Ion Beam Induced Charge Collection Analysis of SOI Microdosimeters

8.1 Introduction

8.1.1 Introduction to Ion Beam Induced Charge Collection (IBIC)

Ion Beam Induced Charge Collection (IBIC) (Breese et al., 1993) involves the use of a highly focused beam of charged particles from an accelerator to induce charge collection within the sensitive volume of a semiconductor. The setup for IBIC measurement is shown in Figure 8.1.

IBIC data was collected using the ANSTO Heavy Ion Microprobe (HIM) on the Australian National Tandem for Applied RESearch (ANTARES) accelerator. An ion beam of approximately one micron diameter was raster scanned across the sensitive surface of a SOI microdosimeter device using a magnetic scanning unit. SOI microdosimeters have previously been studied using IBIC (Cornelius et al., 2002) to investigate the charge collection efficiently as well as some preliminary studies into heavy ion damage with carbon ions. The aim of this present investigation was to investigate anomalous charge collection features, experimentally verify charge collection assumptions used in GEANT4 simulations and investigate the likelihood of radiation damage due to high energy light ions. An angular dependence investigation was also undertaken.

The signal readout of the SOI microdosimeter utilises a standard nucleonic charge sensitive preamplifier and shaping amplifier. The pulse height, together with the beam deflection voltages, read from the X and Y stage of the magnetic scanning stage, are read in by a series of ADCs to produce a data triplet. The X and Y deflections are digitised with a conversion gain corresponding to a granularity of 512 pixels in both X and Y. The energy channel had a conversion gain of 8192 channels.

The data was collected using a MicroDAS data acquisition system from MARC at Melbourne University, which also provided the control of the scanning ion beam. The list mode file consisting of X, Y and E data triplets allows for reconstruction of the

position and intensity of energy deposition events across the scanned surface of the device sensitive volume.

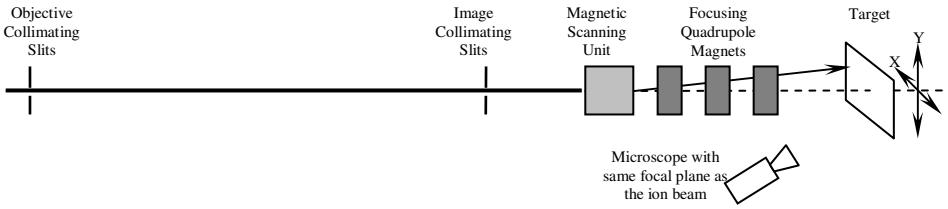

Figure 8.1. Illustration of the setup for IBIC measurements. The objective and imaging collimating slits produce a highly collimated monoenergetic ion beam. The quadrupole triplet focuses the spot down to an approximately micron spot size with the focal point in the target plane. The focused spot is then raster scanned over the target using the magnetic scanning unit. The microscope is used to ensure that the target remains in the focal plane of the focused beam.

8.2 Experimental Method

The ion beams used for the IBIC measurements were 5.5 MeV helium ions (LET in Si = 133.5 keV/µm) and 3 MeV hydrogen ions (protons) (LET in Si = 19.7 keV/µm). These were selected on account of the high LET from He ions being simular to the emission of ^{241}Am (5.486 MeV). The proton beam was used for comparison with proton recoils from the LDPE converter used in the experiments.

The SOI microdosimeters were mounted on a specialised aluminium stick within the vacuum chamber. A charge sensitive preamplifier was mounted adjacent to the device on the same mounting stick to minimise electronic noise. A fixed focal length zoom microscope with a camera attachment is used to ensure that all target objects were in the focal plane of the focused beam. A copper grid with a spacing of one thousand lines per inch was mounted on the stick to facilitate calibration of the dimensions used for the raster scans and monitor the spot size. An example of a grid measurement is shown in Figure 8.2, the 25.4 µm pitch allows calibration of the scan amplifier of the magnetic scanner. The image of the copper grid is created using Scanning Transmitted Ion Microscopy (STIM) where the transmitted ions are detected using a surface barrier detector behind the grid.

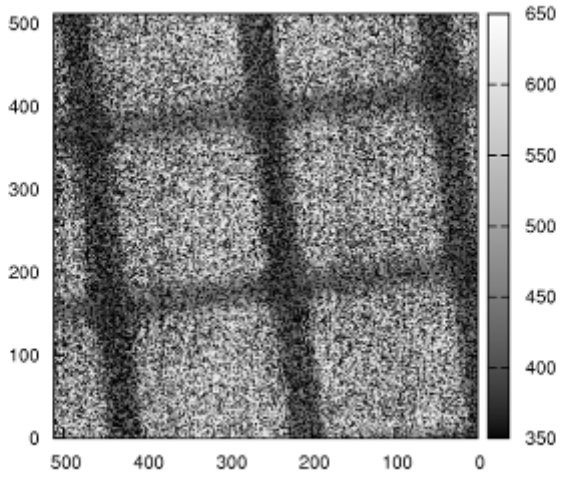

Figure 8.2. A median energy Scanning Transmitted Ion Microscopy (STIM) image of the 1000 lines per inch (25.4 µm pitch) copper grid used for calibration. The X and Y axes are in pixels. The total scan size in the X and Y dimensions are 60.2 µm.

Median energy mapping was used to produce images. The code used for the conversion of the list-mode file to the various maps and spectra is given in Appendix A8.1. The median energy for each pixel is obtained as it is less susceptible to contributions from outlying energy depositions. Such energy depositions can take the form of low energy stray ions scattered from the slits and high energy depositions due to pulse pile up from multiple ions arriving within the shaping amplifier integration time window.

The image shown in Figure 8.2 is 0.118 µm per pixel which equates to scan dimensions in X and Y of 60.2 µm. Using the grid and the gain setting on the scan amplifier the dimensions of all scans can be obtained. This assumes a linear response of the scan amplifier, which has been confirmed over the range used in our experiments.

Spectra and median energy maps for all of the scans were produced allowing comparison of the 10 µm and 5 µm thickness SOI microdosimeters used under different operating conditions. Angular measurements were taken from 0° and to a maximum of 70°, which is the upper limit due to the SOI microdosimeter being recessed slightly behind the mounting stick.

Bias dependant measurements were performed to investigate the effect of lateral depletion within the SOI microdosimeter as well as any charge collection from edge and corner effects and interconnect bonding.

8.3 Results

8.3.1 IBIC Characterisation and radiation damage

An image of the 5 µm SOI microdosimeter with 3 MeV protons is shown in Figure 8.3. The associated energy deposition spectrum is shown in Figure 8.4. This median energy map shows the A3 (right hand side) and A4 (left hand side) array biased at the operating bias of 10 volts.

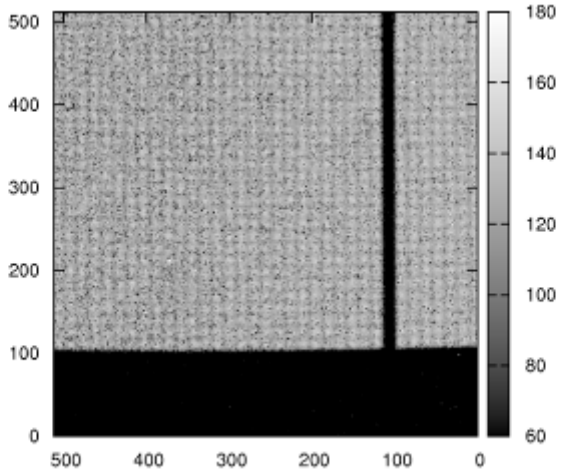

Figure 8.3. A median energy map of the 5 µm thick SOI microdosimeter used for the ^{252}Cf, TSL and some CERF measurements. Observable in this image are the brighter central p-n junctions of each "cell". The X and Y axes are in pixels. X and Y dimensions are 1184.4 µm.

The spectrum, shown in Figure 8.4, for the scan shows the position in the spectrum where the different charge collection regions in the image originates. This is more clearly shown in Figure 8.5 where the regions marked in Figure 8.4 are plotted.

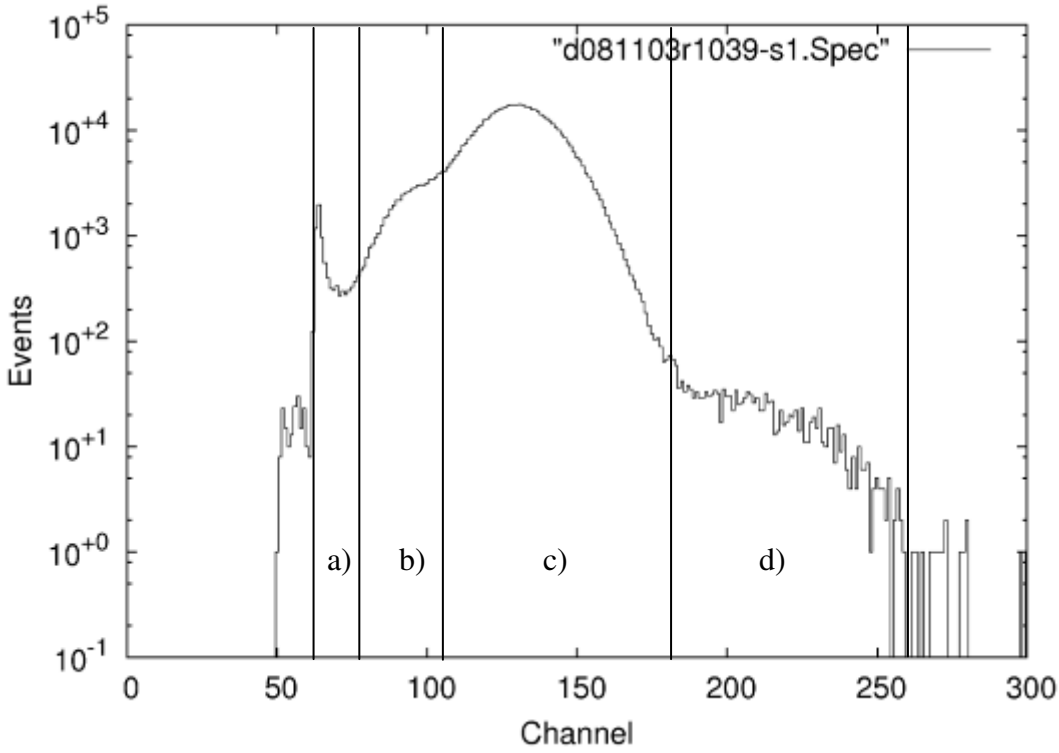

Figure 8.4. The spectra for the median map acquisition shown in Figure 8.3. Regions a, b, c and d are illustrated in Figure 8.5. The lower level discriminator cut off can be seen at the lower edge of region a.

The IBIC analysis on these scan shows that Region a) in the spectrum originates from a low charge collection region surrounding the edges of the arrays. Non spatially correlated events are also present which are associated with electronic noise. The lower level discriminator (LLD) was set to remove the majority of the noise generated events without losing real spatially resolved low energy events.

Region b reveals that the low energy “shoulder” observed on the spectrum in Figure 8.4 originates from both the “fringe” around the edges of the arrays as well as from partial charge collection from energy deposition events which occur between the SOI microdosimeter cells. The reduced charge collection seen between the cells is from the lower charge collection of the peak seen in region c). There is also a small contribution from channelling that will be discussed later in the section on angular measurements.

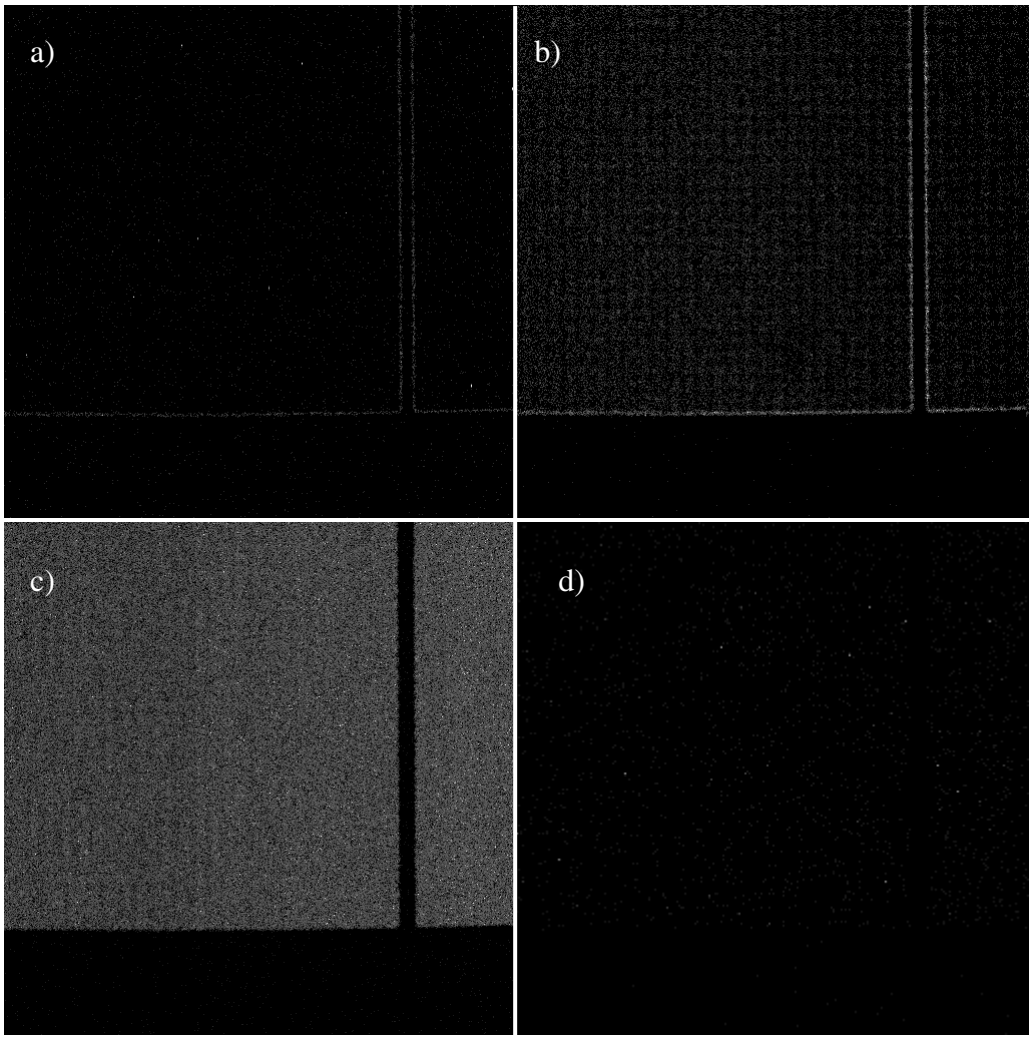

Figure 8.5. Charge collection maps for the 5 µm thick SOI microdosimeter. Charge collection regions are illustrated in Figure 8.4. Each pixel corresponds to a single hit within the windowed energy region. X and Y dimensions are 1184.4 µm.

Region c) is associated with the statistical majority of the charge collection events. This is the contribution from the fully depleted region of the SOI microdosimeter sensitive volume. The majority of the charge collection events are from the SOI microdosimeter collecting the lineal energy deposition of the proton in the depletion region beneath the p-n junction.

Region d) is from pulse pile up events due to multiple ions arriving within the integration window of the pulse processing electronics. This is seen as single events randomly distributed around the charge sensitive regions on the map.

The median charge collection map for an approximately 120 x 120 μm^2 region of the A3 array is shown in Figure 8.6. The scan covers approximately 16 of the 30 µm pitch cells

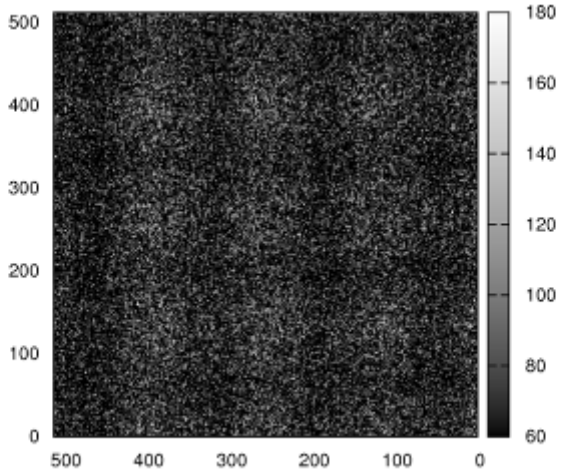

Figure 8.6. A median energy map of approximately 4x4 cells on the 5 µm thick SOI microdosimeter. The central p-n junctions of each "cell" can be seen. The X and Y axes are in pixels. X and Y dimensions of the map are 118.4 µm.

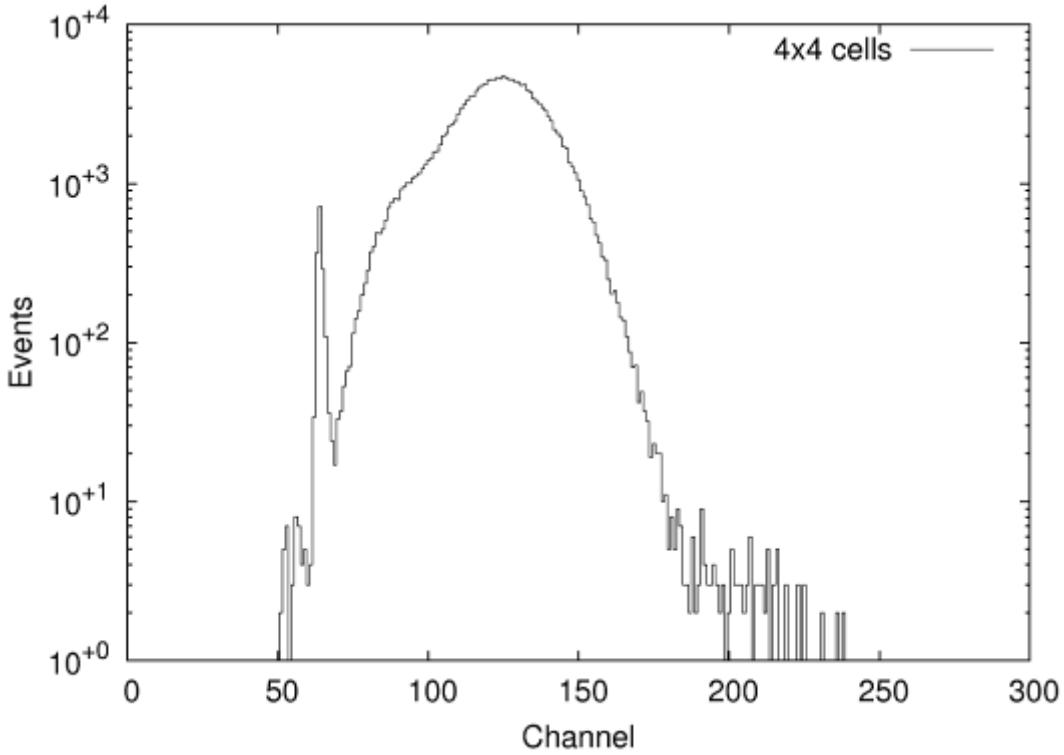

Figure 8.7. The spectrum of the charge collection from the region shown in Figure 8.6. The difference compared to the overall spectrum of Fig 8.4 can be seen in the strongly reduced intensity of the low and high energy regions.

The spectrum for the median energy map shown in Figure 8.6 is presented in Figure 8.7. The scan is 118.4 μm wide which covers 3.95 cells in the map width.

The spectrum when compared to the spectrum shown in Figure 8.4 only displays the contribution from the depletion beneath the p-n junction and the region of partial charge collection located between the cells.

The spectrum in Figure 8.7 shows the low energy noise peak as well as the structure associated with the lineal energy deposition from the protons. When the spectra of the zoomed in region is compared with the wide field of view the effect of the charge collection at the edge of the array can be observed. The comparison of the spectra is shown in Figure 8.8.

The contribution due to the partial charge collection at the edge of the array is manifest as a slight increase in the low energy "shoulder" down to the region above the noise. The slight downshift in the position of the main peak is due to a small amount of radiation damage that occurred due to the high particle flux of a small area scan which causes a local reduction in the minority carrier lifetime and the associated charge collection deficit.

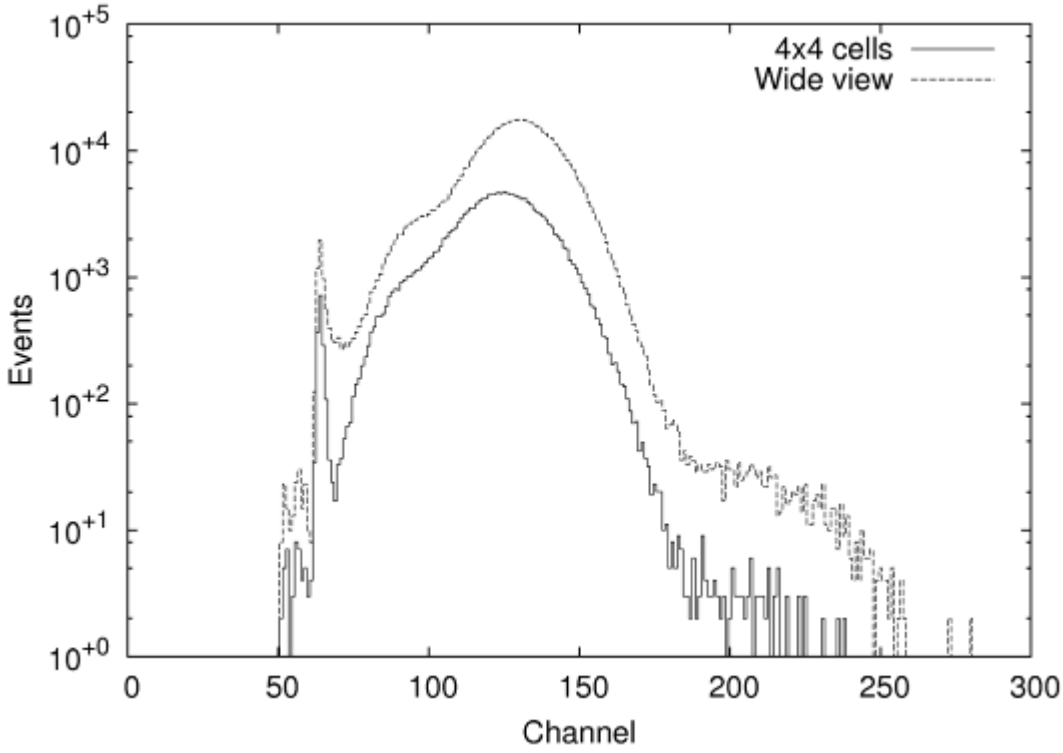

Figure 8.8. Comparison of the spectra including the array edges with the scan across 16 diodes.

The radiation damage can be seen by comparing the initial image shown in Figure 8.6 with the same image taken after multiple scans as shown in Figure 8.9. The same region was exposed to 1.38 x 10^6 protons in total between the start of the first scan and the end of the last scan. The total fluence for this exposure equates to 9.89 x 10^9 protons/cm^2.

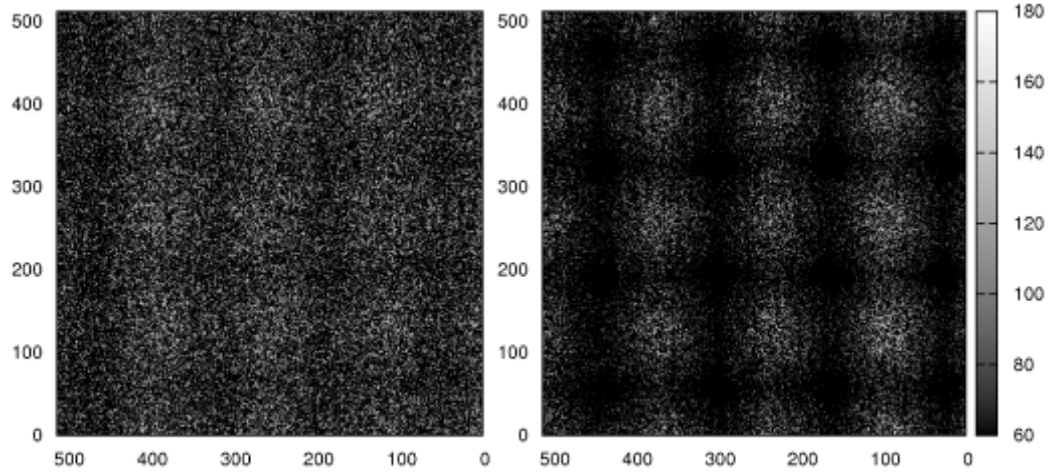

Figure 8.9. Comparison of the median energy maps due to proton radiation damage in the 5 µm thick SOI microdosimeter. The left hand median energy map is the initial close up scan and the left hand median map is after irradiation by 1.38x10^6 protons. Both maps are on the same energy scale.

The median energy maps show a distinct lack of charge collection between the cells of the irradiated scan in Figure 8.9. A comparison of the pre-irradiation and post-irradiation spectra is shown in Figure 8.10. The spectra show a shift to lower lineal energy deposition for the irradiation damaged cells.

The central part of the SOI microdosimeter cells, where the 10 µm wide p-n junctions are located, still collects the same amount of charge from the incident protons. The main difference between pre-irradiation and post-irradiation is that the pre-irradiation contribution to the charge collection from the spaces between the cells due to charge diffusion no longer occurs. The majority of the collected charge now comes from a much reduced region of charge collection where recombinations of the charges dominate. This indicated that there was reduction in the minority carrier lifetime due to trapping from radiation induced lattice defects.

Lineal energy deposition from 3 MeV protons incident upon the SOI microdosimeter is 19.712 keV/µm (3.158×10^{-15} J/µm) within a 5 µm thick SOI layer. This corresponds to a 98.56 keV (1.579×10^{-14} J) per proton energy deposition within the sensitive volume. The sensitive volume has dimensions of $5 \times 118.4 \times 118.4$ µm^3 which equates to 7×10^4 µm^3 (7×10^{-8} cm^3). Given the density of silicon of 2.33 g/cm^3 the mass of the irradiated volume is 1.633×10^{-7} g (1.633×10^{-10} kg). The corresponding dose per incident 3 MeV proton within the sensitive volume is 9.67×10^{-5} J/kg. Given the total number of ions during the irradiation was 1.38×10^6 protons, the total dose in silicon to the region where radiation damage occurred was 133.42 J/kg.

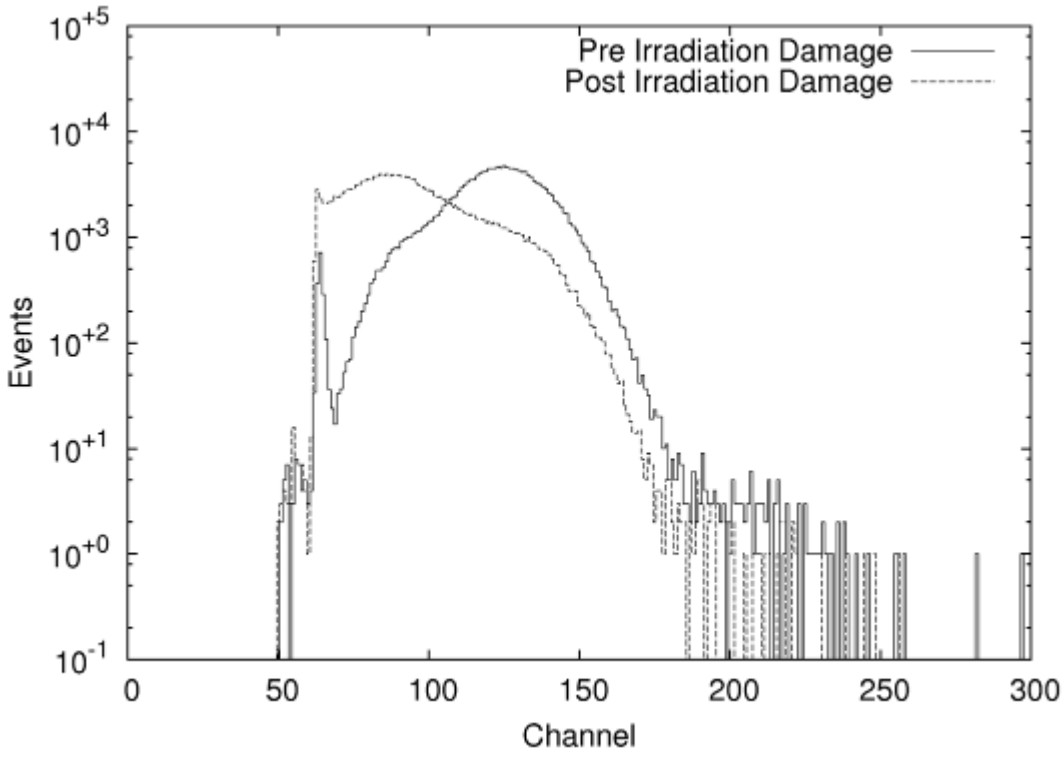

Figure 8.10. The pre-irradiation and post-irradiation damage spectra for the 5 µm thick SOI microdosimeter with 3 MeV protons.

Energy deposition from fewer protons per unit area resulted in a dose of 10.99 J/kg showing minimal charge collection degradation (Figure 8.11) and a dose of 1.53 J/kg resulting in an unobservable effect on the charge collection. Allowing for the 0.63 geometric tissue equivalence dose conversion the dose required to produce a degradation in the charge collection of the SOI microdosimeter is significantly higher than the 20 mSv dose limit for radiation worker within Australia and even higher than doses expected from most radiotherapy treatment fractions (1-2 Gy per fraction).

A square of reduced charge collection due to the damage from the 118.1 x 118.1 µm scans is observed in Figure 8.11. This region of reduced charge collection due to the proton irradiation creates a significant degradation in the lineal energy deposition. The spectra shown in Figure 8.10 illustrate a significant degradation of the maximum charge collection by approximately 60%.

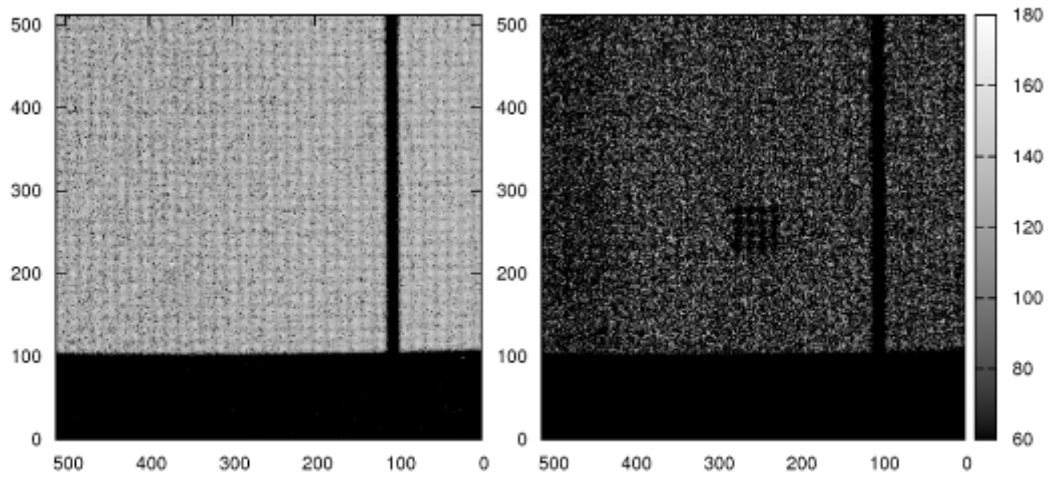

Figure 8.11. Comparison of the median energy maps due to proton radiation damage in the 5 µm thick SOI microdosimeter. The region of damage can be observed as the square of reduced charge collection in the centre. Both maps are on the same energy scale and both scans are 1181.4 µm wide. Due to concerns about radiation damage the scan on the right is for 22% of the incident ions used on the left hand scan.

The 9.89 x 10^9 protons/cm^2 incident on the small section of the array is equivalent to the recoil proton component from approximately 10^{14} neutrons/cm^2 (0.01% efficiency). This is well above the quantity of protons and neutrons encountered in acceptable radiation protection fields. For comparison the fluence in the small area scan is similar to those encountered proton therapy applications approximately 34.68 x 10^9 total fluence of protons at 180 MeV are used to give 1 Gy of proton therapy dose. The damage arising from the different proton energies is related to the total (electronic and nuclear) stopping power, for 3 MeV protons in silicon this is 19.712 keV/µm (1.970 x 10^1 keV/µm electronic and 1.197 x 10^{-2} keV/µm nuclear) while for 180 MeV protons in silicon this is 0.903 keV/µm (9.035 x 10^{-1} electronic keV/µm and 3.039 x 10^{-4} keV/µm nuclear). This means there is an order of magnitude less energy deposition within the sensitive volume from a 180 MeV proton (such as in hadron therapy or as a recoil proton from a high energy neutron) compared to the 3 MeV proton as used in the IBIC scan.

5.5 MeV helium ions were used to irradiate the SOI microdosimeters. The lineal energy deposition from these particles is an order of magnitude higher than for 3 MeV protons. The stopping power of a 5.5 MeV He ion is 133.500 keV/µm (1.334 x 10^2 keV/µm electronic and 1.004 x 10^{-1} keV/µm nuclear).

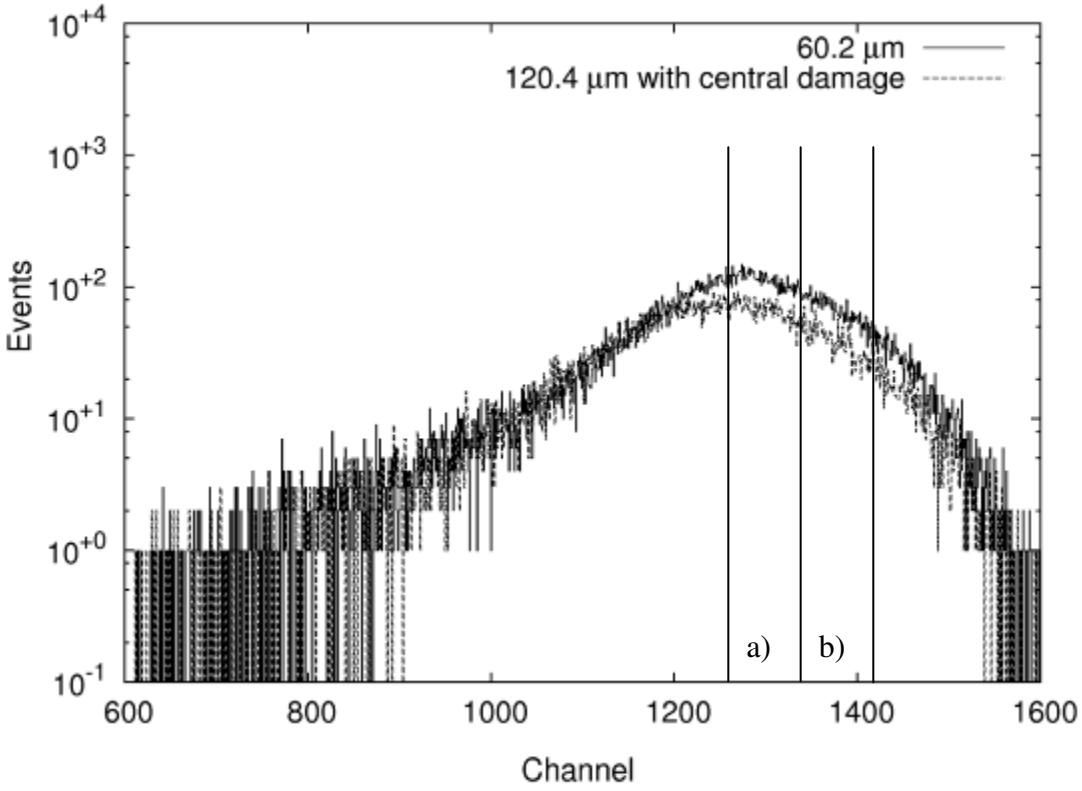

Figure 8.11. Effect of small amounts of radiation damage on a 10 µm thick SOI microdosimeter due to heavier 5.5 MeV helium ions. The intensity maps for the two cuts a) and b) are shown in Figure 8.12.

An energy slice from the 120.4 µm wide spectrum with central damage from a previous 60.3 µm scan is shown in Figure 8.12. The previous 60.2 µm scan was for 2.94 x 10^4 ions in total for the scan (8.11 x 10^8 ions/cm^2). This quantity of ions for the scan is not suitable for producing good statistics for production of median energy imaging maps.

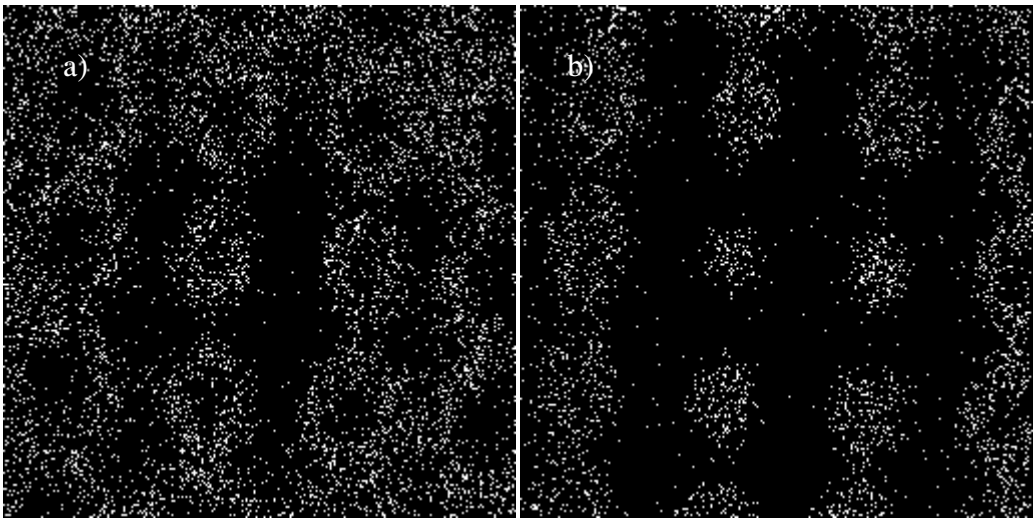

Figure 8.12. Intensity maps for the 120.4 µm wide scan on a after irradiation of the 60.2 µm region in the middle of the scan with 2.94 x 10^4 5.5 MeV He ions. Reduced charge collection in the central region is observable.

Increases in the area scan size will decrease the particle fluence (ions/cm^2). The result of this is a minimum limit on the size of IBIC scans achievable with such high lineal energy deposition radiation without degradation of the charge collection properties.

Charge collection from other regions around the SOI microdosimeters was observed during scans of the array edges. The spectrum showing the low energy charge collection artefact is shown in Figure 8.13.

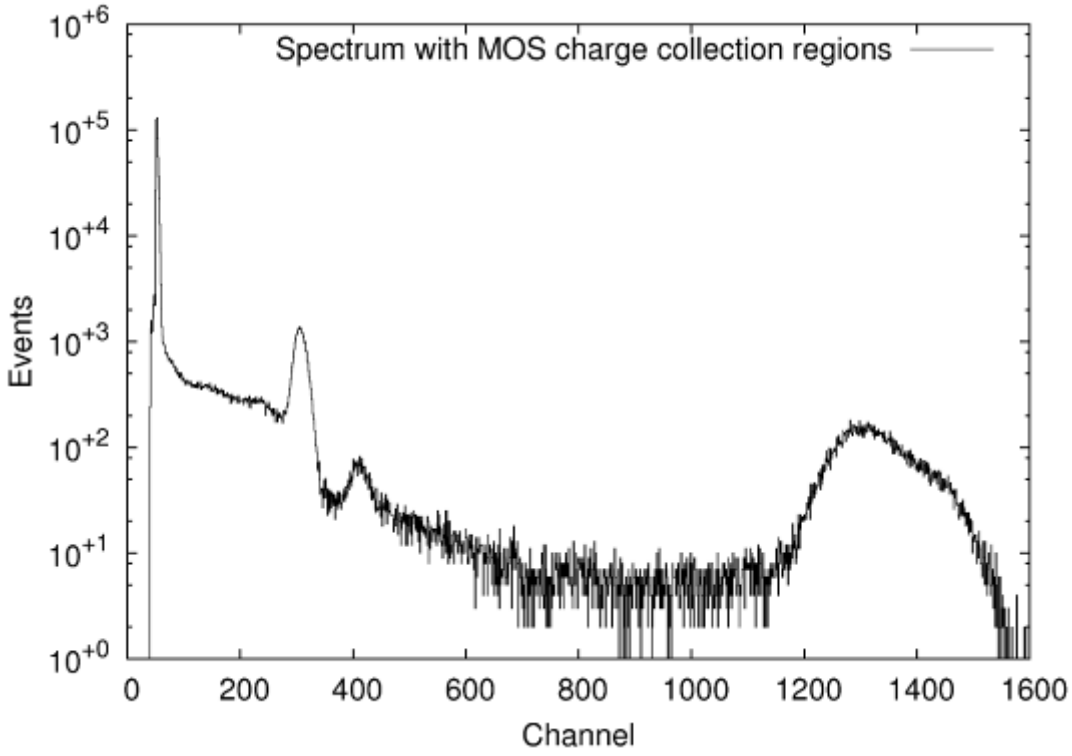

Figure 8.13. Spectrum from the IBIC scan on the edge of a 10 µm thick SOI microdosimeter with 5.5 MeV He ions. The main lineal energy charge collection peak can be seen above channel 1200. Anomalous charge collection peaks can be seen between channels 200 and 500.

These low energy charge collection artefacts are due to the aluminium track and bonding pad deposition. These aluminium regions are deposited on the 400 nm thick silicon dioxide passivation layer over the silicon. This creates a Metal-Oxide-Semiconductor (MOS) junction type structure as shown in Figure 8.14.

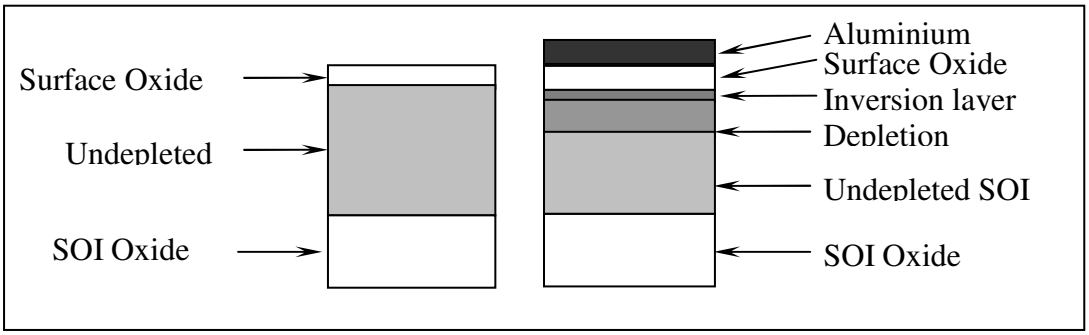

Figure 8.14. On the left hand side is the illustration of the layers for passivated silicon on insulator material. On the right hand side is the inclusion of a metallic layer on top of the passivating oxide. This metallic layer produces a thin inversion and depletion layer in the surface of the silicon. This depletion layer is created by the application of bias to the metal layer can collect charge from energy deposition events within the depletion layer.

The collection from the MOS region created by the aluminium tracks and bonding pads is easily discernable in Figure 8.15 as an extended region of reduced charge collection from the edge of the array with shadowing from a bonding wire. There is a "halo" of reduced charge collection from around the edge of the aluminium layer from charge diffusion into the depletion region of the MOS structure.

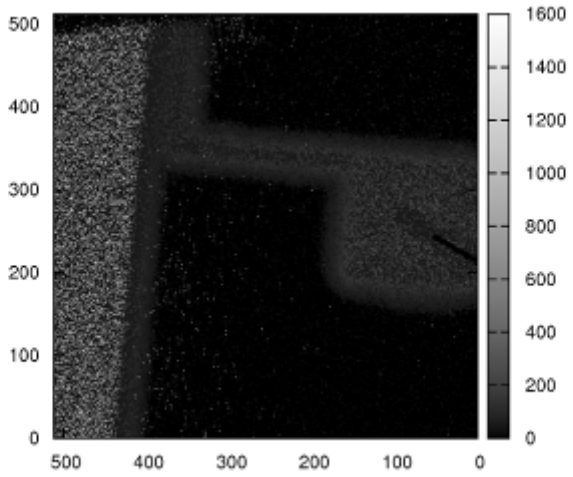

Figure 8.15. Median charge collection map of the spectrum for the 5.5 MeV He ions on the 10 µm thick SOI microdosimeter as shown in Figure 8.13. The scan is 1080.8 µm wide.

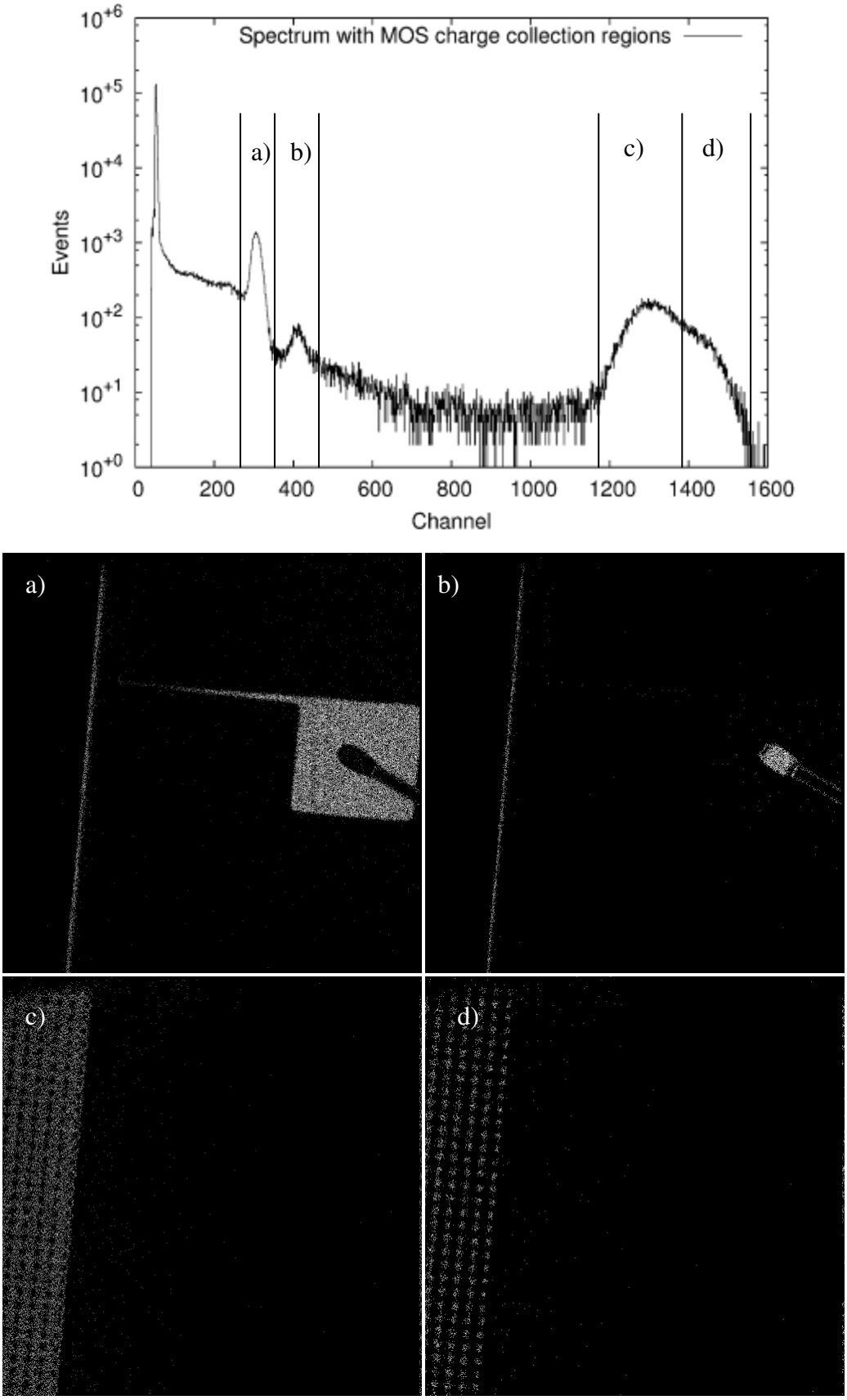

Figure 8.16. Windowed intensity charge collection map of the spectrum for the 5.5 MeV He ions on the 10 µm thick SOI microdosimeter as shown in Figure 8.13. The scan is 1080.8 µm wide.

An intensity map of the region of the spectra where charge was collected from the anomalies, shown in Figure 8.16, shows clearly the regions due to the MOS structure formation. By comparing the lineal energy deposition of the SOI microdosimeter region to the lineal energy deposition of the MOS region, a maximum MOS depletion region thickness of 2 µm at the 10 V bias can be estimated.

Observable in region b) is a low statistical region of high charge collection events attributable to the He ion losing energy from the compressed part of the aluminium wedge wire bond and depositing a higher lineal energy in the thin depletion region. This demonstrates that the effect is due to a thin depletion region and not from another effect such as channelling.

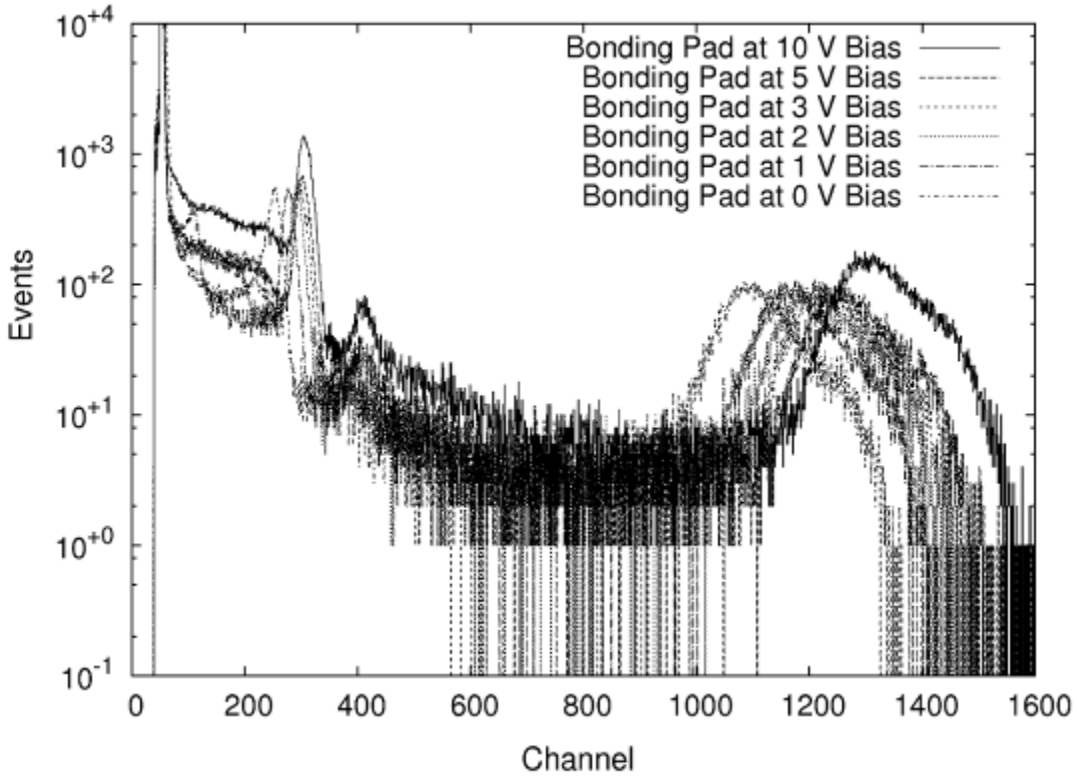

Figure 8.17. Spectrum from the IBIC scan on the edge of a 10 µm thick SOI microdosimeter with 5.5 MeV He ions at different applied bias.

The depletion region created by the MOS effect is dependant on bias as shown in Figure 8.17. The shift in the peak energy from the MOS region is proportional to the main lineal energy peak from the SOI microdosimeter cells showing that the depletion region under the MOS is an effect of the applied bias.

Regions of unwanted charge collection, namely the array edge, tracks and bonding pad, with an approximate total area of 0.02 mm^2, represent < 0.5 % of the total area of the A4 array. For larger arrays the contribution of the energy deposition events from around the edge of the arrays would be proportionally reduced.

8.3.2 Bias Dependence Results

The device charge collection dependence on bias was tested on the 5 µm and 10 µm thick SOI microdosimeters. This was performed to investigate the variation in both the charge sharing between cells as well as the charge collection in the array border.

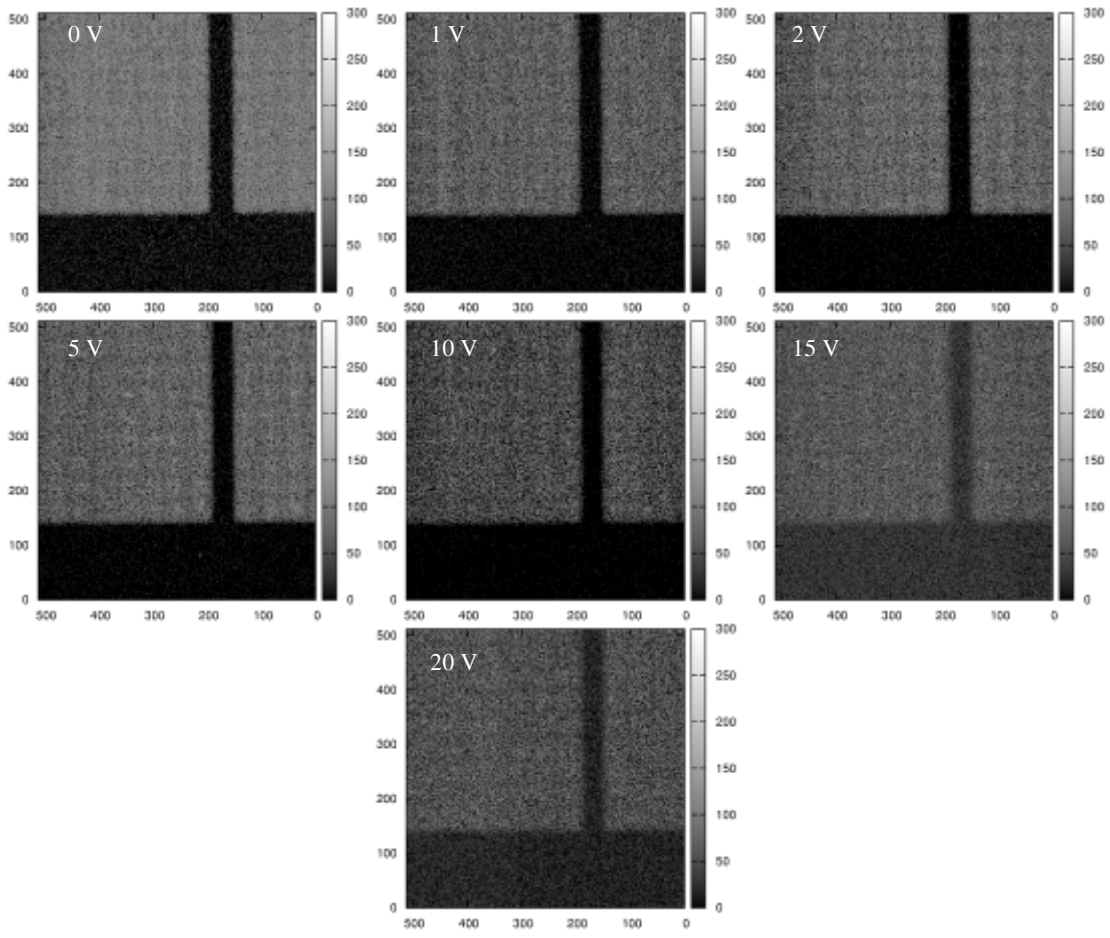

Figure 8.18. The median energy maps of the 5 µm SOI microdosimeter under different bias conditions. The spectra for these maps is shown in Figure 8.19

Figure 8.18 shows the bias dependence of the median energy maps for the 5 µm thick SOI microdosimeter with 3 MeV protons for bias voltages from 0 to 20 V. The

nominal operating voltage of the device is 10 V. Above the normal operating bias an increase in leakage current begins to produce a substantial increase in the noise.

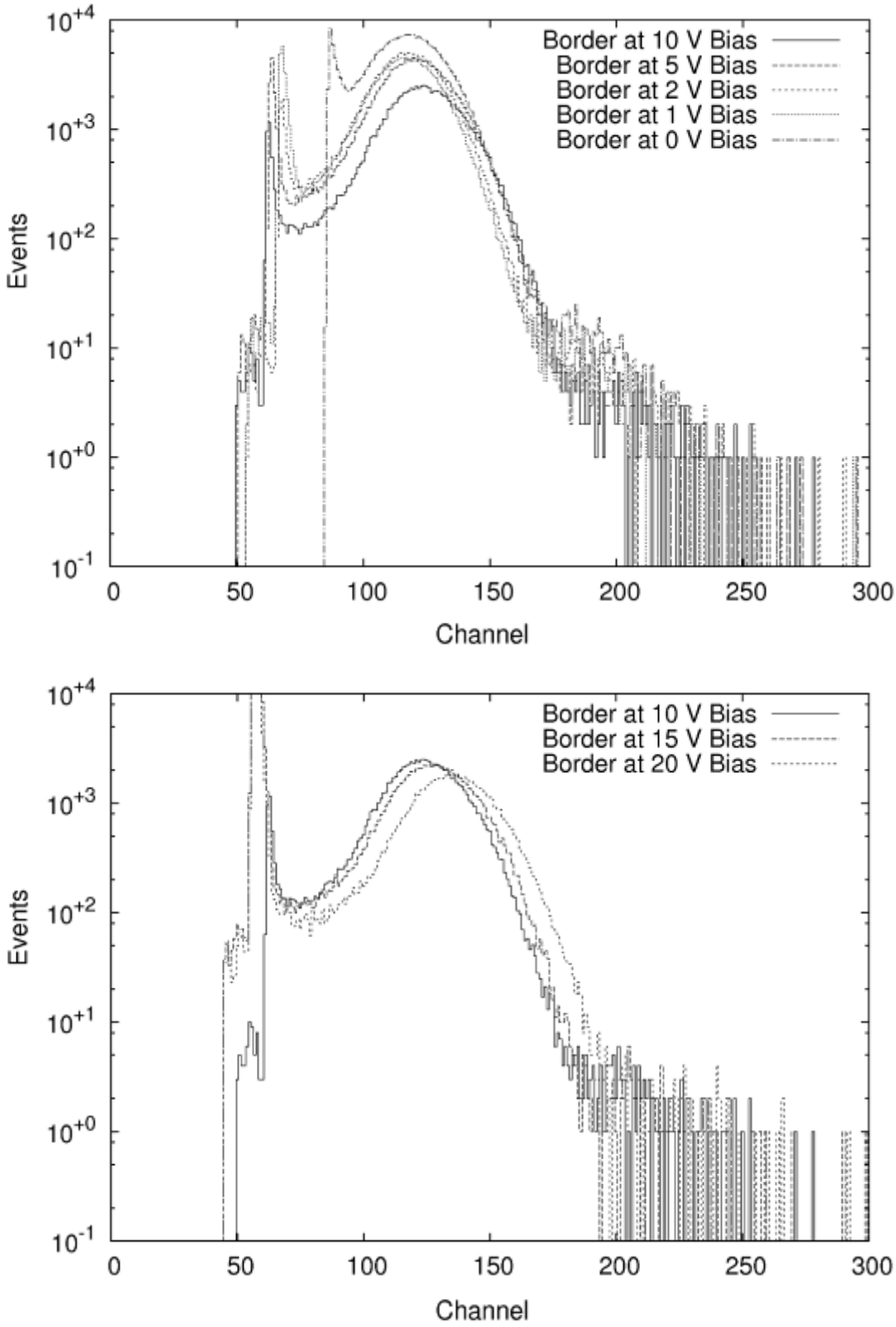

Figure 8.19. The spectra of the 5 µm SOI microdosimeter region shown in Figure 8.18.

The fringe of partial charge collection around the array is not observable due to the excessive noise level. Between 0 V and 10V bias the charge collection below the p-n junction increases with the expansion of the depletion region. For bias voltages above 10 V the charge collection under the p-n junction continues to increase however the noise also increases significantly as can be seen in Figure 8.19.

The bias dependant median energy map measurements of the 10 µm thick SOI microdosimeter are shown in Figure 8.20. The region scanned includes the track and bonding pad to investigate changes in the energy deposition in these regions as well as with respect to the bias.

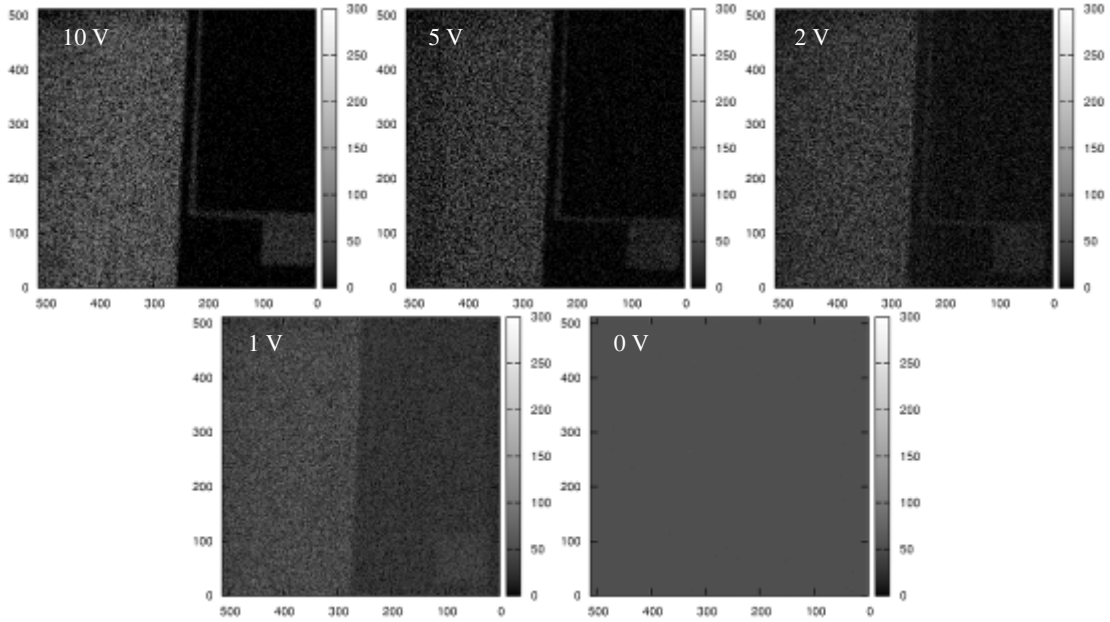

Figure 8.20. The median energy maps of the 10 µm SOI microdosimeter under different bias conditions. The spectra for these maps is shown in Figure 8.21

The spectra for the median energy maps shown in Figure 8.20 are shown in Figure 8.21. The spectra show the expected increase in noise and decrease in charge collection with reduction in bias.

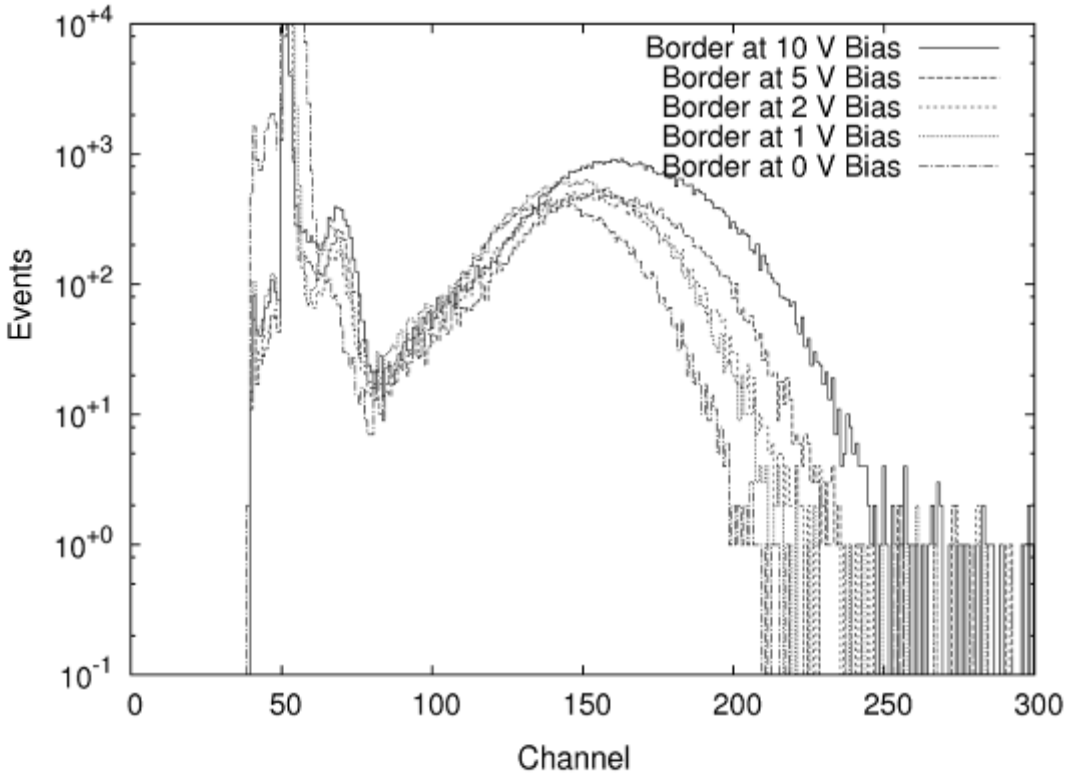

Figure 8.21. The spectrum of the 5 µm SOI microdosimeter region shown in Figure 8.20.

8.3.3 Angular Dependence Results

An investigation into the angular dependence the SOI microdosimeter device response was performed on both the 5 µm and 10 µm thick devices. The median energy map for the measurements on the 10 µm thick SOI microdosimeter with 3 MeV protons is shown in Figure 8.22.

The angle of the beam with respect to the normal of the SOI microdosimeter surface was limited to 70°. This was due to the SOI microdosimeter being recessed behind the axis of rotation. The central portion of the SOI microdosimeter remained in focus, however, due to parallax effects from rotation relative to the plane of beam focus and scanning calibration there is some distortion of the images.

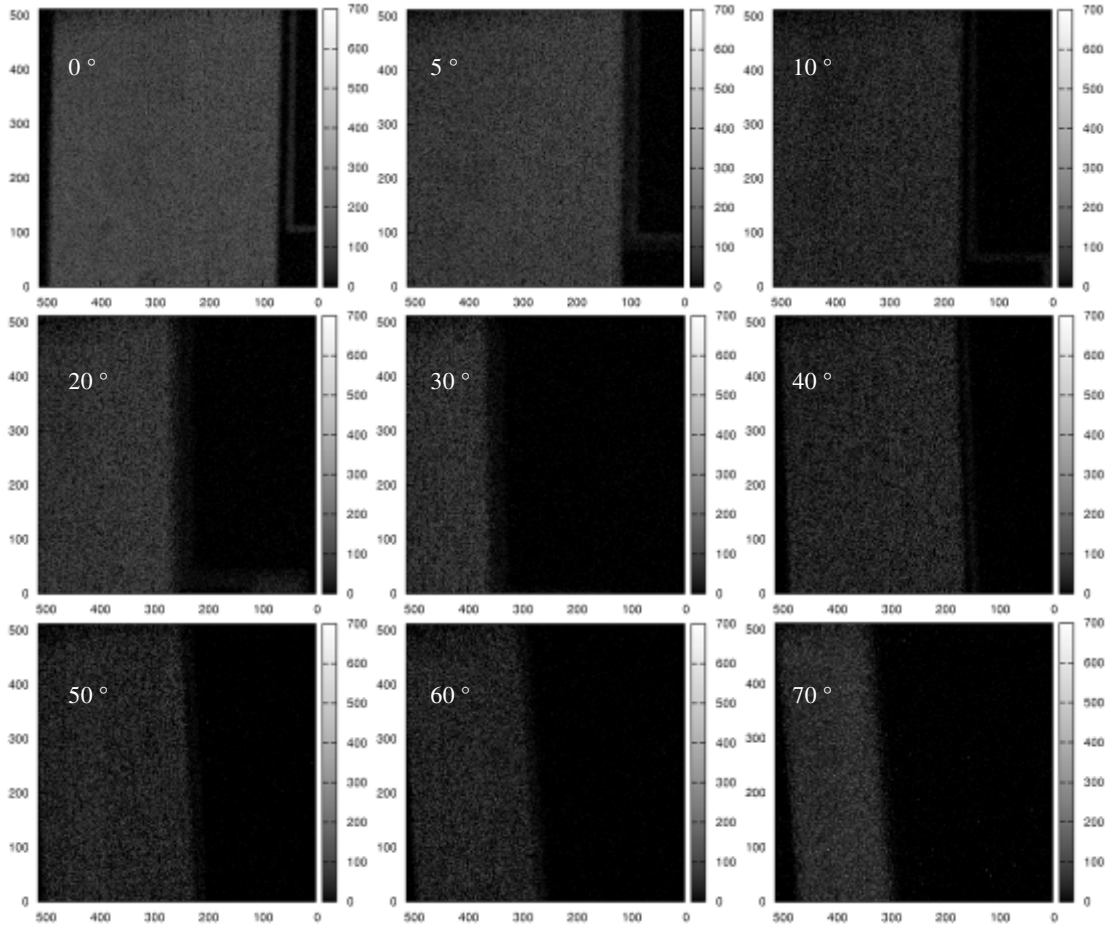

Figure 8.22. Angular dependence median energy maps of the 10 µm thick SOI microdosimeter under 3 MeV proton irradiation. Between 30° and 40° the sample was moved laterally by 600 µm to keep the array in the field of view. All of the maps cover the same range of energy and are 1693.34 µm wide.

The spectra of the angular response of the 3 MeV protons incident on the 10 µm thick SOI microdosimeter is shown in Figure 8.23. The spectra show the expected increase in lineal energy for the longer chord length lineal energy deposition events. The increase in lineal energy deposition at an angle 70° corresponds to the 2.92 times increase in chord length. The range of the 3 MeV protons in silicon is 92.05 µm, which is 3.15 times longer than the maximum chord length at the 70° angle.

Significant change in the lineal energy deposition is only observed at angles greater than 30 degrees. This is where the peak lineal energy deposition increase of approximately 15% exceeds the FWHM of the main lineal energy deposition peak.

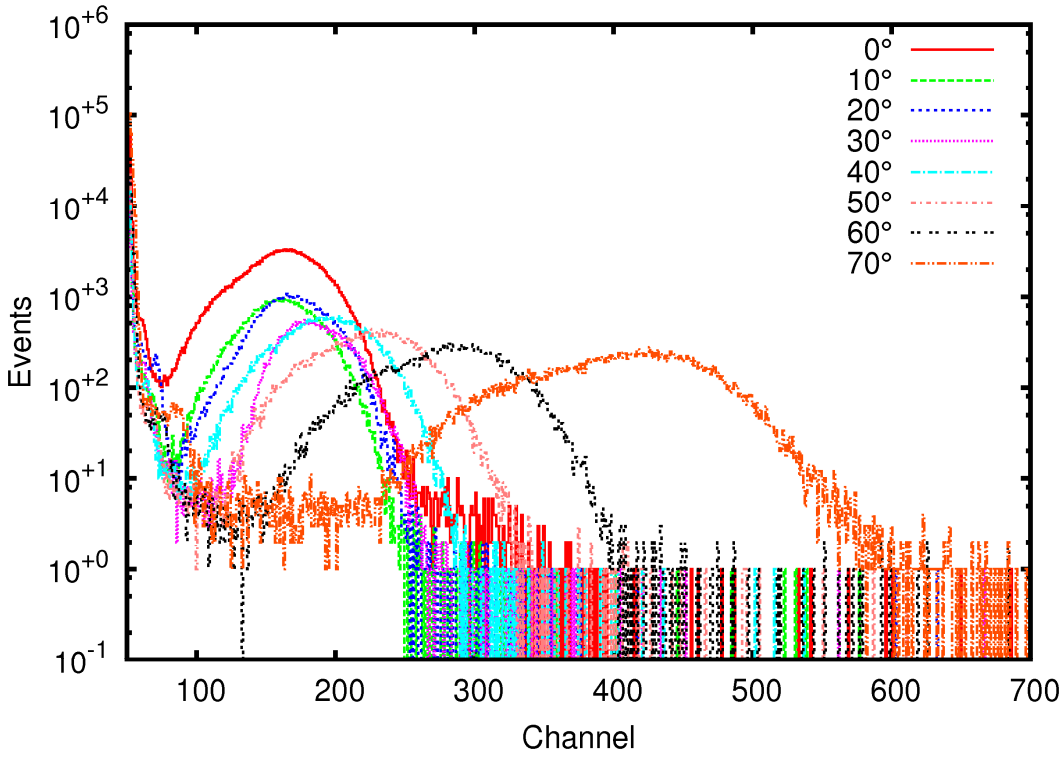

Figure 8.23. Spectra for the irradiation of a 10 µm thick SOI microdosimeter by 3 MeV protons at different angles.

The angular dependence of the 5 µm thick SOI microdosimeter median energy maps is shown in Figure 8.24. These median energy maps show a shift in the lineal energy deposition events to higher values, similar to the effect observed in the 10 µm thick device.

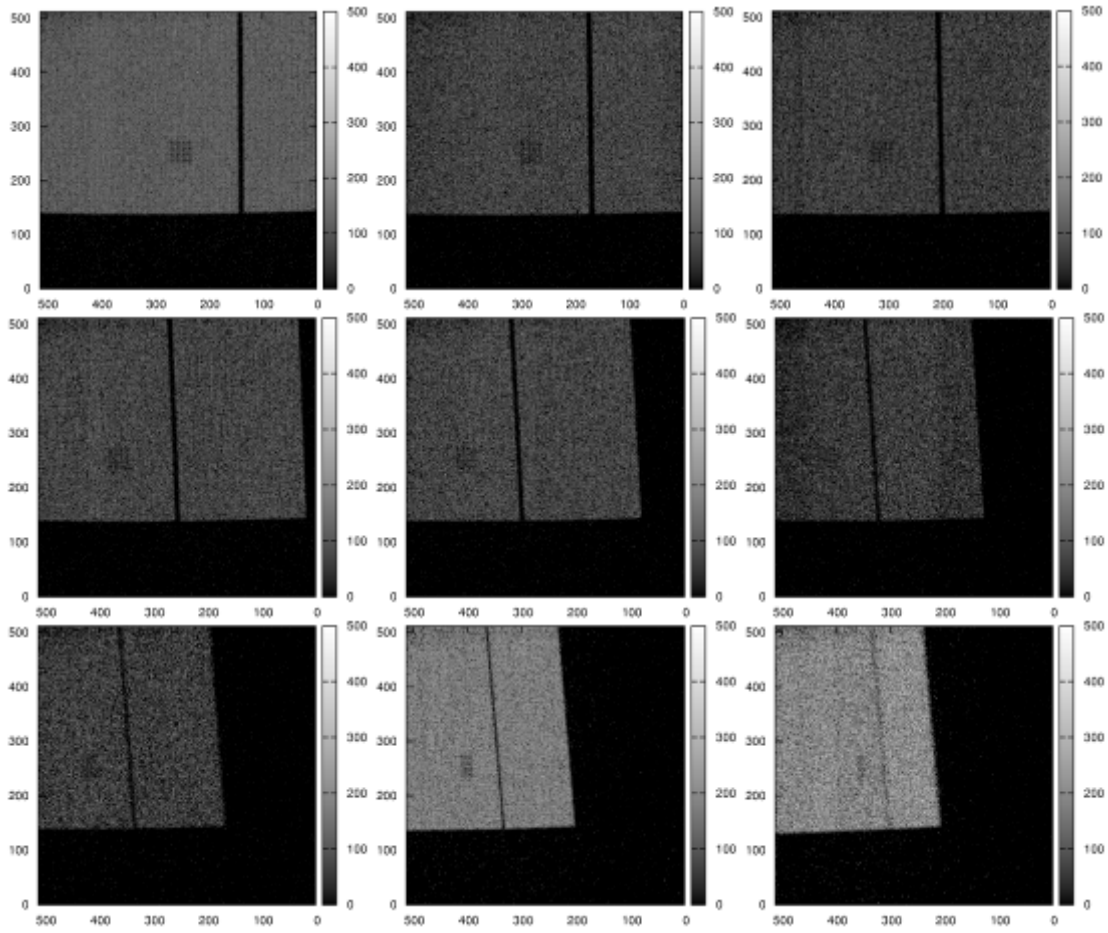

Figure 8.24. Angular dependence median energy maps of the 5 µm thick SOI microdosimeter under 3 MeV proton irradiation. All of the maps cover the same range of energy and are 1575.2 µm wide.

The spectra for the 5 µm thick SOI microdosimeter under different irradiation angles with a 3 MeV proton beam are shown in Figure 8.25. These spectra indicate the same angular variance for the 5 µm thick SOI microdosimeter as was previously observed on the 10 µm thick SOI microdosimeter. This is where the angular dependence of the lineal energy deposition centroid position begins to become significantly larger than the FWHM of the normal lineal energy deposition centroid position.

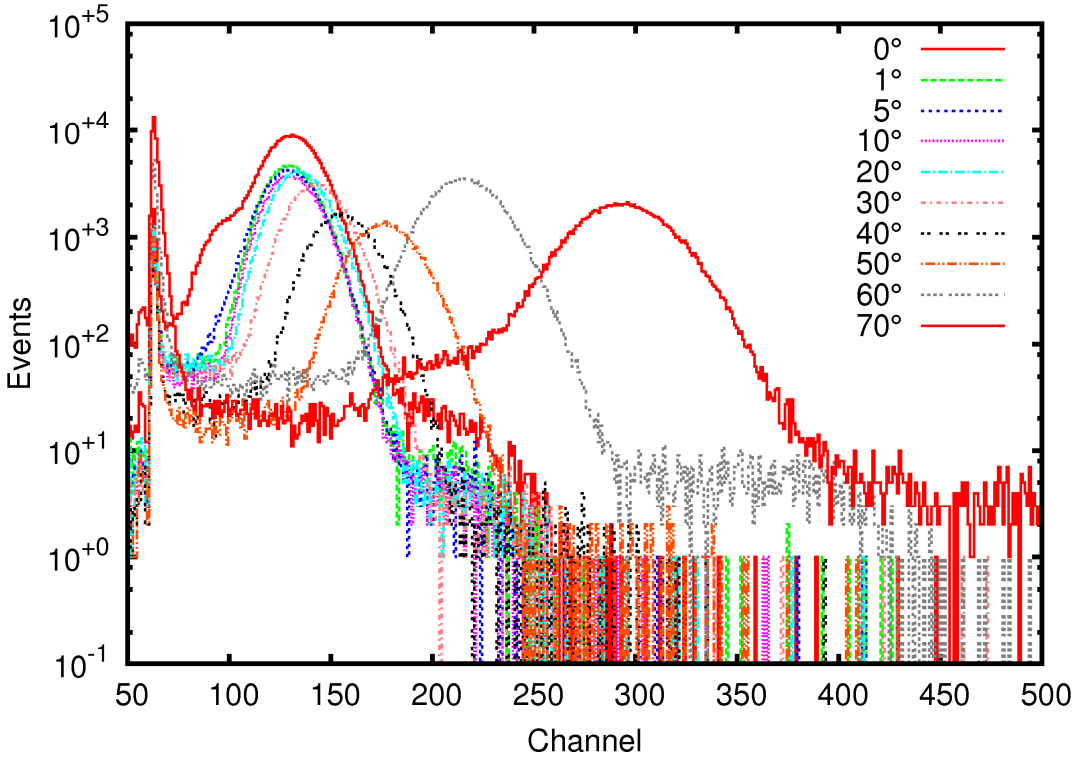

Figure 8.25. Spectra for the irradiation of a 5 µm thick SOI microdosimeter by 3 MeV protons at different angles.

The maximum range of 5.5 MeV helium ions in silicon is 28.02 µm. This means that the 29.4 µm chord length of a 10 µm thick SOI microdosimeter at 70° exceeds the range of the helium ion leading to full energy deposition. Therefore the angular measurements were only performed with the 3 MeV protons (range 92.05 µm) to ensure only lineal energy deposition with respect to angle was measured.

8.4 Discussion

The observations from the IBIC mapping of the SOI microdosimeters used for the measurements in this thesis show that under normal operating conditions the charge collection regions from adjacent cells overlap. The collection of charge from diffusion charge collection around the fringe of the array and from under the MOS regions formed by the aluminium tracks is not significant enough in depletion region volume, charge collection efficiency or area when compared to the main SOI microdosimeter array to cause any significant microdosimetric features.

The assumption of the GEANT4 geometry to simulate the response of the SOI microdosimeter as a uniform sensitive region is appropriate under normal operating conditions (i.e. no radiation damage and fully depleted bias of 10 V).

The charge collection from the SOI microdosimeter array at angles, relative to the normal, showed that only under relatively large angles (> 30 degrees) the SOI microdosimeter measurement of the lineal energy deposition became significantly distorted. This allows for an acceptance angle of approximately 60 degrees for the incident radiation. The recoil protons produced by the neutron fields investigated in earlier chapters in this thesis follow a $\cos^2\theta$ angular energy dependence. This indicates that, with the small air gap between the LDPE layer and the SOI microdosimeter, the majority of the lineal energy deposition events are likely to fall within the angular acceptance window.

The IBIC data indicates that the SOI microdosimeter is suitable for high energy low lineal energy deposition neutron dominated mixed fields such as those encountered at aviation altitudes. The limiting factors affecting the SOI microdosimeter are from lateral depletion of the sensitive volumes outside of the array area and regions of charge collection due to MOS structures. These MOS structures and regions of charge collection are minimal in area compared to the total area of the SOI microdosimeter, larger arrays would further minimise the contribution from these low energy deposition regions.

9. Discussion

This thesis had proposed the investigation of SOI microdosimetry in high energy neutron dominated radiation fields. The fields under investigation ranged from a few MeV up to several hundred MeV. The SOI microdosimeter has been successfully tested in several high energy neutron dominated fields with a focus on radiation protection applications. The lineal energy spectra acquired experimentally showed very good agreement with GEANT4 simulated results as well as with results obtained using a TEPC in the case of the CERF facility field. A summary of the significant results for each of the different radiation fields tested follows.

The ^{252}Cf source neutron irradiation results:

- SOI microdosimetry demonstrated suitability for radiation protection applications with mid range neutron energies.
- A compact online dosimetry system is possible for neutrons produced by radioactive neutron sources (energy range approximately 10 keV to 10 MeV)
- Optimising the thickness of the polyethylene converter for the energy of the operational situation could provide online dosimetry for occupational exposure in industry applications and therapy situations. It would also be possible to have multiple SOI microdosimeters covered with different thicknesses and types of converter materials (e.g. ^{6}Li, ^{10}B and other fissionable material) to give an approximate energy dependant response for thermal to mid range neutron energies.

CERN-EU High Energy Radiation Field (CERF) facility simulation results:–

- The GEANT4 simulation of the facility showed good agreement between the neutron spectra produced and previously published results from both FLUKA simulations and experimental Bonner sphere measurements.
- GEANT4 was able to recreate the properties of the field with respect to the non neutron components of the field that had previously not been considered significant to the overall dose contribution.
- Simulation of the facility showed the spectra of the field to consist of primarily gammas and neutrons with charged particles being a minority component of the field. The contribution from the charged particles and gamma ray components of

the CERF facility field can increase to approximately 25% of the total ambient dose equivalent.

- The ambient dose equivalent varies significantly at the irradiation positions around the facility. The contribution from the charged particles can vary from approximately 15% up to approximately 25% depending on the irradiation position.

CERN-EU High Energy Radiation Field (CERF) facility experimental results:–

- SOI microdosimetry is capable of determining the different LET components of the CERF facility high energy aviation test beam. Using the lineal energy deposition in combination with the simulated results for the different field components the neutron and charged particle contribution can be estimated.
- The major contribution to the energy deposition in a PIN diode and SOI microdosimeter from the CERF facility field comes from the charged particles in the field. The ability of the SOI microdosimeter to differentiate the different components of the field allows the proton recoil component to be separated from the other charged particles. The neutron component can be separated from the other components of the field due to their contribution above 10 keV/μm.
- The measurements of the CERF facility radiation field showed excellent agreement with measurements taken using a HAWK TEPC. The HAWK TEPC is currently marketed as an aviation specific TEPC for online measurements of aviation doses.

TSL high energy quasimonoenergetic neutron field results:

- Response of PIN diodes to the quasimonoenergetic neutrons showed unsuitability for high energy neutron dosimetry and detection due to detector thickness resulting in problems with the energy deposition limits of the secondaries and resulting in large amounts of silicon recoils.
- The angular distribution of radiation with respect to the normal of the PIN diode detector face results in poor response due to angular distribution of aviation fields.
- Response of SOI microdosimetry to high energy quasimonoenergetic neutron field showed expected response according to GEANT4 Simulations
- Response of SOI microdosimetry chord length distribution overcomes limitations occurring due to a 4π radiation field as encountered in aviation radiation fields due to differing radiation angle of incidence.

- The response of the SOI microdosimetry is capable of measuring recoil protons created by neutrons up to several hundred MeV.

IBIC analysis of SOI microdosimeter:

- The SOI microdosimeter showed charge collection from adjacent cells was overlapping under normal operation conditions.
- Angular dependence results showed that for 3 MeV protons and 5.5 MeV helium that there was a negligible shift in the energy deposition spectrum up to an angle of 30 degrees from the normal. This acceptance angle is suitable for the use of the microdosimeter in the experiments undertaken in this thesis.
- The energy deposition over the SOI microdosimeter cells shows a very good lineal energy deposition spectrum. The median charge collection imaging does not show very good charge isolation between the cells.
- There was an observed contribution to the lineal energy spectrum from the edge of the arrays outside of the cell volumes and from underneath the track metallisation. This contribution can create a small low charge collection peak if the border area of the cell is significant compared to the area of the array such as can occur during IBIC imaging. The size of the array used in this thesis does not contribute significantly to the charge collection spectrum.
- Radiation damage due to very intense proton and helium ion irradiation can occur in the SOI microdosimeter sensitive volume reducing the charge collection efficiency. The fluence required to create damage in the SOI microdosimeter is several magnitudes greater than for the applications explored in this thesis.

9.1 Recommendations for future solid state Microdosimetry development

During the undertaking of this study into the radiation protection applications of SOI microdosimetry several limitations of the 1st Generation SOI microdosimeter were observed. The recommendations for improvement to overcome these limitations are outlined in this section.

During the duration of this thesis, work commenced and is progressing on the development of a next generation SOI microdosimeter. The author has been heavily involved in the developments taking place with the next generation SOI

microdosimeter. This next generation attempts to resolve some issues identified with the 1st generation SOI microdosimeter and as such the next generation includes:

- Cylindrical junction design for a more uniform chord length distribution
- Better charge collection isolation from adjacent SOI microdosimeter cells
- Improvement in the charge collection properties and the possibility of having a high electric field close to the anode allowing for proportional electron multiplication.

9.2 Suggestions for future solid state microdosimetric designs

Considerations and recommendations are intended to improve solid state microdosimetry to a more "ideal" microdosimetric cell volume. These suggestions are based on the current knowledge of the SOI microdosimeter limitations.

- Better isolation of the individual microdosimeter cells. Highly conductive implanted doping between each cell to create a "guard grid" to completely isolate the individual junctions from each other.
- Thinning of the semiconductor substrate to allow rear side illumination. This would remove the bulk semiconductor material past the insulator layer and allow the sensitive volumes to be directly exposed. This will remove over layer effects from the spectrum for high LET radiations. Currently several semiconductor foundries are offering silicon thinning services down to approximately 50 micron thick wafers and are hoping to offer 10 micron in the near future.
- Creation of a very high electric field at a small anode to allow electron multiplication close to the anode. Ideally these devices will operate in a proportional mode allowing for lower LET radiation measurements. To allow for this the cell would require a cylindrical (currently being attempted with the next generation SOI microdosimeter) or hemispherical design, both of which give a better chord length distribution.
- 3D voxelisation of the design to greatly increase efficiency and the ability to read out in layers. The thinning of semiconductor material is allowing semiconductor manufacturers to "sandwich" several thin device layers together to increase the density of microelectronics. This could be used for a microdosimetric application where thinned layers are sandwiched between layers of tissue equivalent material to allow for an increase in efficiency as well as a dose depth profile. Ideally a tissue equivalent semiconductor material could be used to minimise aberration of the radiation field being measured.

- If a thin enough rear illuminated semiconductor is used, it would be possible to read out each pixel individually using a bump bonded ASIC design. This would possibly allow for compensation of charge sharing or an ion strike that interacts in multiple cells which are currently summed up in existing SOI microdosimeter designs.
- Integration of the front end electronics into the detector material itself. It would be possible to create small amplification stage into the semiconductor adjacent to the sensitive volume. This would allow for lower LET radiations to be measured.

9.3 Future semiconductor materials to consider for semiconductor Microdosimetry

Silicon has served well as a good material for solid state microdosimetry allowing for small sensitive volumes closer to the ideal micron scale site size outlined by Rossi et. al. than conventional gas filled tissue equivalent proportional counters. A criticism of the use of silicon for dosimetry is that silicon is not tissue equivalent. Another criticism of silicon is the radiation hardness of the material which is not a problem with TEPC's.

One suggested material to overcome some of the limitations of silicon is to use silicon carbide. The average atomic number of the material, Z=10 (Si Z=14, C Z=6) is closer to tissue than silicon alone. Silicon Carbide is also extremely radiation hard and physically durable with band gap energy of 3.28 eV for 4H and 3.03 eV for 6H polytypes. The wide band gap allows for high temperature operation and low noise.

Amorphous silicon would have the advantage of being resistant to radiation damage from high LET radiation and the ability to deposit the sensitive volume directly onto tissue equivalent materials. Drawbacks of this material are the dangling bonds produced by the amorphous nature of the material causing electrical defects and trapping states in the material. Passivation using hydrogen is possible but can degrade with time and cause large area inconsistencies in the material.

Diamond has the advantage of being regarded as tissue equivalent resulting in a better microdosimetric measurement. It also has the advantage of a 5.5 eV band gap which allows for high temperature operation. One drawback in the past has been the difficulty of the crystal growth resulting in polycrystalline material deposition leading to problems in producing active volumes. Currently several companies are able to grow

reasonable areas and thicknesses of single crystal diamond (approximately 4 x 4 mm area with up to 500 micron thickness)

Organic materials have been of interest in recent years for the fields of optoelectronics, biological sensors and medical applications. The application of these to radiation detection is a natural extension of the semiconductor properties of these materials.
Organic semiconductors are currently being used and researched for use in organic light emitting diodes (OLED), organic field effect transistors (OFET), organic light emitting field effect transistors (OLET), organic solar cells, electrochemical transistors and for organic biosensors. The advantage of organic semiconductors is that being polymer based they are closer to tissue equivalency than most non organic semiconductors and can be processed into any form or printed onto a given substrate. This allows for a very flexible arrangement of semiconductor structures and designs.
A current drawback of the organic semiconductor is the reduction in efficiency over time and use. This is currently observable with OLED's having a usage "half life" which is actually dependant on their emission wavelength (blue OLED's have a much shorter lifespan than red or orange OLED's). Newer organic semiconductor materials with extended lifetimes and promising characteristics are currently in development.

Small organic scintillators mounted or grown directly onto a photosensitive detector could allow for tissue equivalency and lower LET measurements. The advantage of this as a system is the ability to have very large three dimensional arrays of scintillators.

Carbon nanotubes have shown semiconducting or semimetal properties depending on the chiral vector. Construction of carbon nanotube diodes could allow for the transition towards solid state nanodosimetry. Research into carbon nanotube devices is currently under intense study and reliably working device arrays are possible within several years. Alternatively there is also interest in single sheets of graphene for use in nanometre sized semiconductor devices which could also be investigated for micro-nano dosimetric applications.

10. References

1. "Henri Becquerel." Encyclopædia Britannica. 2010. Encyclopædia Britannica Online. 03 Sep. 2010 <http://www.britannica.com/EBchecked/topic/58020/Henri-Becquerel>.
2. "GEANT4 Physics Reference Manual", Available online at http://geant4.web.cern.ch/geant4/UserDocumentation/UsersGuides/PhysicsReferenceManual/fo/PhysicsReferenceManual.pdf
3. Agostinelli S., et al., 2003, "Geant4: a simulation Toolkit", Nuclear Instruments and Methods in Research A, vol. 506, pp. 250-303.
4. Allison J., et al., 2006, "Geant4 Developments and Applications", IEEE Transactions on Nuclear Science", vol. 53 (1), pp. 270-278
5. Amsler C., et al., 2008, "Review of Particle Physics", (Particle Data Group), Physics Letters B, Vol 667, No. 1, pp. 1-1340
6. Annals of the ICRP, Publication 103, 2007. "The 2007 Recommendations of the International Commission on Radiological Protection." Pergamon Press ISSN 0146-6453
7. Annals of the ICRP, Publication 51, 1987. "Data for use in Protection Against External Radiation." Vol. 17, No. 2/3, Pergamon Press ISBN 0-08-035587-0
8. Annals of the ICRP, Publication 60, 1991. "1990 Recommendations of the International Commission on Radiological Protection." Pergamon Press ISBN 0-08-041998-4
9. Annals of the ICRP, Publication 74, 1996. "Conversion Coefficients for Radiation Protection.", Pergamon Press ISSN 0146-6453
10. Annals of the ICRP, Publication 92, 2003. "Relative Biological Effectiveness (RBE), Quality Factor (Q), and Radiation Weighting Factor (wR)" Pergamon Press ISSN 0146-6453
11. Asaro, F., Stephens, Jr., F. S., Harvey, B. G. and Perlman I., "Complex Alpha and Gamma Spectra of $Cf^{250,252}$", Physical Review, 100, 1955, pp 137–142
12. Baba, M., "Quasi-Monoenergetic Neutron Sources", International Workshop on Fast Neutron Detectors, April 3-6, 2006, University of Cape Town, South Africa.
13. Badhwara G.D., et. al. "Response of a tissue equivalent proportional counter to neutrons", Radiation Measurements, 35, 2002, pp 551-556

14. Bartlett, D.T., “Radiation protection aspects of the cosmic radiation exposure of aircraft crew”, Rad. Prot. Dosim. vol. 109, No. 4, 2004, pp. 349-355
15. Battistoni, G., Ferrari, A., Pelliccioni, M. and Villari, R., “Monte Carlo Calculation of the Angular Distribution of Cosmic Rays at Flight Altitudes”, Rad. Prot. Dosim., vol. 112, No. 3, 2004, pp. 331-343
16. Berger, M.J., Hubbell, J.H., Seltzer, S.M., Chang, J., Coursey, J.S., Sukumar, R., Zucker, D.S. and Olsen, K., NIST Standard Reference Database 8 (XGAM), “XCOM: Photon Cross Sections Database”, http://www.nist.gov/pml/data/xcom/index.cfm, accessed December 2010.
17. Bolshakova A., et. al., 2008, “Comparison of GEANT4 hadron generation with data rom the interactions with beryllium nuclei of +8.9 GeV/c protons and pions and -8.0 Gev/c pions”, European Physical Journal C, vol. 56, pp. 323-332.
18. Bradley P.D. and A.B. Rosenfeld, 1998, “Tissue Equivalence Correction for Silicon Microdosimetry Detectors in Boron Neutron Capture Therapy”. Medical Physics, vol. 25, pp. 2220-2225.
19. Bradley, P. D., Rosenfeld, A. B., et al. (1998). "Charge collection and radiation hardness of a SOI microdosimeter for medical and space applications." IEEE Transactions on Nuclear Science 45(6): 2700-2710.
20. Bradley, P. D., Rosenfeld, A. B., et al. (1999). "Performance of silicon microdosimetry detectors in boron neutron capture therapy." Radiation Research 151(3): 235-243.
21. Bradley, P.D., Rosenfeld, A.B. and Zaider, M., 2001. “Solid State Microdosimetry”, Nuclear Instruments and Methods in Research B, vol. 184, issue 1-2, pp. 135-157.
22. Breese M. B. H., “A theory of ion beam induced charge collection”, J. Appl. Phys. 74, (1993) 3789; doi:10.1063/1.354471
23. Brenner D. J., 1989. “Appropriate uses of the proposed quality factor, Q(y)”, Journal of Radiological Protection. Vol. 9, No.1, pp 51-52.
24. Brugger M. and Roesler S., “Remanent dose rates around the collimators of the LHC beam cleaning insertions”, Radiation Protection Dosimetry, 115, 2005, pp.470-474

25. Brugger M., Khater H., Mayer S., Prinz A., Roesler S., Ulrici L., and Vincke H., “Benchmark studies of induced radioactivity produced in LHC materials, part I: Specific activities”, Radiation Protection Dosimetry, 116, 2005, pp.6-11
26. Brugger M., Khater H., Mayer S., Prinz A., Roesler S., Ulrici L., and Vincke H., “Benchmark studies of induced radioactivity produced in LHC materials, part II: Remanent dose rates”, *Radiation Protection Dosimetry*, 116, 2005, pp.12-15
27. C. Amsler, et al., 2008, “Review of Particle Physics”, (Particle Data Group), *Physics Letters B*, Vol 667, No. 1, pp. 1-1340
28. Cornelius I., Rosenfeld A., Siegele R., and Cohen D., “LET dependence of the charge collection efficiency of silicon microdosimeters,” IEEE Trans. Nucl. Sci., vol. 50, pp. 2373–2379, Dec. (2003)
29. Cornelius I., Siegele R., Rosenfeld A.B., Cohen D.D., “Ion beam induced charge characterisation of a silicon microdosimeter using a heavy ion microprobe”, Nuc. Inst. Meth. B, (2002), 190 (1-4), pp. 335-338.
30. Cornelius I.M. and Rosenfeld A.B., 2004, “Verification of Monte Carlo Calculations in Fast Neutron Therapy Using Silicon Microdosimetry”, IEEE Transactions on Nuclear Science, Vol 51, no. 3, pp 873-877
31. Cornelius I.M., Siegele R.N., Rosenfeld A.B. and Cohen D., 2001, “Ion Beam Induced Charge Collection Imaging of a Silicon Microdosimeter Using a Heavy Ion Microprobe”, Nuclear Instruments and Methods in Research B, Vol 184, pp 135-157
32. Coursey, J.S., Schwab, D.J., and Dragoset, R.A. (2005), Atomic Weights and Isotopic Compositions (version 2.4.1). [Online] Available: http://physics.nist.gov/Comp [2008, June 10]. National Institute of Standards and Technology, Gaithersburg, MD.
33. Crowther, I.A., 1924, “Some considerations relative to the action of X-rays on tissue cells,” Proc. Roy. Soc. 96, 207.
34. Daquino, G.G., Corti, G and Folger, G., 2006, “Background Radiation Studies at LHCb Using GEANT4”, IEEE Transactions on Nuclear Science”, vol. 53 (5), pp. 2907-2915
35. Dessauer, F., 1922, “Uber einige Wirkungen von Strahlen. I.,”, Z. Phys. 12, 38.

36. Dicello J. F., et al., “Radiation Quality of Californium-252”, 1972, Phys. Med. Biol., Vol. 17, No. 3, 345-355
37. European Commission. Council Directive 96/29/EURATOM of 13 May 1996 “Laying down the basic safety standards for protection of the health of workers and the general public against the dangers arising from ionising radiation.”, Off. J. Eur. Commun. 39, L159 (29 June 1996).
38. Falcão, R. C., Facure, A., and Silva, A. X. “Neutron dose calculation at the maze entrance of medical linear accelerator rooms” Radiation Protection Dosimetry, 123(3), 2007, pp 283-287, first published online September 27, 2006 doi:10.1093/rpd/ncl144
39. Far West Technology Inc., Environmental radiation monitor with 5 inches tissue equivalent proportional counter, Operations and repair manual, December, (2000).
40. Farahmand M. et al., 2004, “First microdosimetric measurements with a TEPC based on a GEM”, Rad. Prot. Dosim., Vol. 110, No 1-4, 839-843
41. Federal Aviation Administration, CARI6 Radiobiology Research Team webpage, Last updated March 2 2009, Accessed October 23 2009, Current version dated July 7 2004 available at http://www.faa.gov/data_research/research/med_humanfacs/aeromedical/radiobiology/cari6/
42. Fröman, N., 1 December 1996, The Nobel Foundation, “Marie and Pierre Curie and the Discovery of Polonium and Radium”, (http://nobelprize.org/nobel_prizes/physics/articles/curie/index.html)
43. Fuerstner M., Theis C. and Vincke H., Private communication on the 04/04/2007, CERN, CH-1211 Geneva 23, Switzerland
44. Ghassoun J, Mostacci D, Molinari V and Jehouani A., “Detailed dose distribution prediction of Cf-252 brachytherapy source with boron loading dose enhancement”, Applied Radiation and Isotopes, 68(2), 2010, pp 265-70. Epub 2009 Oct 14.
45. GEANT4 collaboration, “GEANT4 Physics Reference Manual”, Available online at http://geant4.web.cern.ch/geant4/UserDocumentation/UsersGuides/PhysicsReferenceManual/fo/PhysicsReferenceManual.pdf
46. Goodfellow datasheet for LDPE, ET311452, www.goodfellow.com

47. Hajek M., Berger T. and Vana N., “Passive In-Flight Neutron Spectrometry by means of Bonner Spheres”, Rad.Prot.Dosim., vol. 110, No. 1-4, 1999, pp. 343-346
48. Cornelius, I., Rosenfeld, A., Siegele, R., and Cohen, D., “LET dependence of the charge collection efficiency of silicon microdosimeters,” IEEE Trans. Nucl. Sci., vol. 50, pp. 2373–2379, Dec. (2003)
49. IAEA, Technical Report Series No. 403., 2001. “Compendium of Neutron Spectra and Detector Responses for Radiation Protection Purposes” ISBN 92–0–102201–8
50. IAEA, TRS403, 2001. “Compendium of Neutron Spectra and Detector Responses for Radiation Protection Purposes” ISBN 92–0–102201–8
51. International Commission on Radiation Units and Measurements (ICRU), Report 33, Issued 15 April 1980. “Radiation Quantities and Units”, ISBN 0-913394-27-0
52. International Commission on Radiation Units and Measurements (ICRU), Report 36, Issued 31 December 1983. “Microdosimetry”, ISBN 0-913394-30-0
53. International Commission on Radiation Units and Measurements (ICRU), Report 39, Issued 1 February 1985. “Determination of Dose Equivalents Resulting from External Radiation Sources”, ISBN 0-913394-33-5
54. International Commission on Radiation Units and Measurements (ICRU), Report 40, Issued 15 March 1986. “The Quality Factor in Radiation Protection”, ISBN 0-913394-34-3
55. International Commission on Radiation Units and Measurements (ICRU), Report 43, Issued 15 December 1988. “Determination of Dose Equivalents Resulting from External Radiation Sources – Part 2”, ISBN 0-913394-33-5
56. International Commission on Radiation Units and Measurements (ICRU), Report 44, Issued 15 January 1989. “Tissue Substitutes in Radiation Dosimetry and Measurement”, ISBN 0-913394-38-6
57. International Commission on Radiation Units and Measurements (ICRU), Report 57, Issued 01 August 1998. “Conversion Coefficients for Use in Radiological Protection Against External Radiation”, ISBN 0-913394-56-4

58. International Commission on Radiation Units and Measurements (ICRU), Report 60, Issued 30 December 1998. “Fundamental Quantities and Units for Ionising Radiation”, ISBN 0-913394-59-9
59. Kellerer, A. M. (1984). "A survey of microdosimetric quantities and concepts." Ultramicroscopy 14(3): 169-174.
60. Kellerer, A.M., Rossi, H.H. 1972. “The theory of dual radiation action”. Curr. Topics Radiat. Res. 8, 85-158
61. Kellerer, A. M. and K. Hahn (1988). "Considerations on a Revision of the Quality Factor." Radiation Research 114(3): 480-488.
62. Knoll, Glenn F., 2000, “Radiation Detection and Measurement”, Third Edition, John Wiley & Sons, ISBN 0-471-07338-5.
63. Latocha, M., Beck, P. and Rollet, S., “AVIDOS—A Software Package for European Accredited Aviation Dosimetry”, Rad. Prot. Dosim. vol. 136, No. 4, 2009, pp. 286–290
64. Lindborg, L. et al. Eds. “Cosmic radiation exposure of aircraft crew—compilation of measured and calculated data.” European Commission, Radiation Protection Issue No. 140. (2004). ISBN 92-894-8448-9.
65. Martin, R.C., Knauer J.B. and Balo P.A., (2000). "Production, distribution and applications of californium-252 neutron sources." Applied Radiation and Isotopes 53(4-5): 785-792.
66. McDonald J. C., Schwartz, R. B. and Thomas, R. B., “Neutron Dose Equivalent Conversion Coefficients Have Changed in the Last Forty Years… Havent’t They?”, Radiation Protection Dosimetry. 78, 1998, pp.147–149
67. Mitaroff, A. and Silari, M. “The CERN-EU High-Energy Reference Field (CERF) facility for dosimetry at commercial flight altitudes and in space” Rad. Prot. Dosim. 102(1), 2002, pp.7–22
68. Mukherjee B.,Cross P. and Alsop R. “Measurement of the Neutron and Gamma Doses Accumulated during Commercial Jet Flights from Sydney to Several Major Destinations in the Northern and Southern Hemisphere”, Radiat Prot Dosimetry, (2002) 100(1-4): 515-518
69. NIST, Physical Reference Data, Atomic Weights and Isotopic Compositions http://www.physics.nist.gov/PhysRefData/Compositions/index.html, accessed December 14th 2007.

70. Nobel-Winners.com website, Acessed, 2003, “Antoine-Henri Becquerel” (http://www.nobel-winners.com/Physics/antoine_henri_becquerel.html)
71. Perez-Nunez, D. and Braby, L. A., “Replacement tissue-equivalent proportional counter for the International Space Station”, Radiation Protection Dosimetry, 143(2-4), 2011, pp394-397 first published online November 28, 2010 doi:10.1093/rpd/ncq409
72. Pelliccioni, M. “Overview of fluence-to-effective dose and fluence-to-ambient dose equivalentconversion coefficients for high energy radiation calculated using the FLUKA code.”, Radiation Protection Dosimetry, 88, 2000, pp279-297.
73. Pomp, S., Blomgren, J., Hayashi, M., Mermond, P., Öhrn, A., Olsson, N., Österlund M., Prokofiev, A. and Tippawan, U., “Light-ion production and fission studies using the MEDLEY facility at TSL”, International Workshop on Fast Neutron Detectors, April 3-6, 2006, University of Cape Town, South Africa.
74. Prokofiev, A., Chadwick, M., Mashnik, S., Olsson, N. and Waters, L., “Development and Validation of the 7Li(p,n) Nuclear Data Library and Its Application in Monitoring of Intermediate Energy Neutrons”, International Conference on Nuclear Data for Science and Technology, October 7-12, 2001 Tsukuba, Japan. (http://lib-www.lanl.gov/lapubs/00818636.pdf)
75. Prokofiev, A.V., Blomgren, J., Byström, O., Ekström, C., Pomp, S., Tippawan, U., Ziemann, V. and Österlund M. “The TSL Neutron Beam Facility”, Rad.Prot.Dosim., vol. 126, No. 1-4, 2007, pp. 12-22.
76. Prokofiev, A.V., Byström, O., Ekström, C., Ziemann, V., Blomgren, J., Pomp, S., Österlund M. and Tippawan, U., “A New Neutron Beam Facility at TSL”, International Workshop on Fast Neutron Detectors, April 3-6, 2006, University of Cape Town, South Africa.
77. Prokopovich, D.A., Reinhard, M.I., Cornelius, I.M. and Rosenfeld A.B., “SOI microdosemetry for mixed field radiation protection”, Radiat. Meas., Vol. 43, issue 2-6, Feb-Jun, 2008, pp. 1054-1058
78. Prokopovich, D.A., Reinhard, M.I., Cornelius, I.M., Rosenfeld, A.B., 2010. “Geant4 simulation of the CERN-EU high-energy reference field (CERF) facility.” Radiat Prot Dosim 141, 106-113.

79. Reistad D., “Recent developments at the Gustaf Werner Cyclotron and CELSIUS”, IEEE, Proceedings of the Particle Accelerator Conference., Vol 3, 1993, pp. 1744-1746
80. Rollet, S. et. al. “Measurement and Simulation of Lineal Energy Distribution at the CERN High Energy Facility with a Tissue Equivalent proportional Counter” Rad.Prot.Dosim., Vol. 125, No. 1–4, pp. 425–428, (2007)
81. Rollet, S., et. al. “Dosimetric Considerations on TEPC FLUKA-Simulation and Measurements”, Rad.Prot.Dosim., Vol. 110, No. 1-4, pp. 833-837, (2004)
82. Rosenfeld A.B., “Semiconductor microdosimetry in mixed radiation field: present and future,” Rad.Prot.Dosim., vol. 84, No. 1-4, 1999, pp. 385-388
83. Rossi, H.H. and Zaider, M., 1996, “Microdosimetry and Its Applications”, Springer, ISBN 3-54058541-9.
84. Spurný F., Ploc O. and Dachev T., “On the neutron contribution to the exposure level onboard space vehicles”, Rad. Prot. Dosim., Vol. 126, No. 1–4, 2007, pp. 519–523
85. Theis, C., Forkel-Wirth, D., Perrin, D., Roesler R. and Vincke H. “Characterisation of ionisation chambers for a mixed radiation field and investigation of their suitability as radiation monitors for the LHC”, Radiation Protection Dosimetry, 116, 2005, pp.170–174
86. Wroe, A., Rosenfeld, A., Reinhard, M., Pisacane, V., Ziegler, J., Nelson, M., Cucinotta, F., Zaider, M., Dicello, J., “Solid State Dosimetry with Heavy Ions for Space Applications”, IEEE Trans. Nucl. Sci., NS-2007

11. APPENDIX

A3.1
C++ code for the conversion of energy deposition spectra into microdosimetric spectra

```
#include <fstream>
#include <iostream>
#include <iomanip>
#include <string>
#include <cstdlib>
#include <math.h>

using namespace std;

int main(int argc, char *argv[])
{
  int num_args = argc-1; // number of arguments
  cout << "This program is intended to read in a linearly binned calibrated energydeposition
spectrum and rebin the data for microdosimetric display" << endl;
  // This program is intended to only take one argument which is the normalised linearly binned y
vs yd(y) spectrum with errors
  if(num_args!=1){
    cout << "Usage: MicroDisp [f(e)_filename]" << endl;
    exit(1);
  }

  // count the number of lines in the file
  int linecount = 0;
  int MAXI = 16385; // Will never have more than 16384 linear bins in spectrum due to MCA
limitations

  double Edep[MAXI];
  double Dist[MAXI];
  double Error[MAXI];

  double LinLinealE[MAXI];
  double Linydy[MAXI];
  double LinErrydy[MAXI];

  double Lin_yfy[MAXI];
  double LinErr_yfy[MAXI];

  /*****************************************************************************************/

  // This section reads in the imput file

  ifstream infile(argv[1]);

  if(infile.is_open()){
    while(!infile.eof()){
      string temp="";
      infile >> temp;
      char* pEnd;
      Edep[linecount] = strtod(temp.c_str(),&pEnd);
      infile >> temp;
      Dist[linecount] = strtod(temp.c_str(),&pEnd);
      Error[linecount] = sqrt(Dist[linecount]);
      //infile >> temp;
      //LinErrydy[linecount] = strtod(temp.c_str(),&pEnd);
      //getline(infile, temp);
      linecount++;
    }
  }else{
    exit(1);
```

```
}

cout << "There are " << linecount-1 << " lines in the file" << endl;

/*******************************************************************************************/
// Ask for mean chord length.

int MeanChordLength;
cout << "What is the mean chord length (um)? (default 5 um)- ";
string UserInput="";
getline(cin, UserInput);
if(UserInput=="") MeanChordLength=5;
else MeanChordLength=atoi(UserInput.c_str());
cout << MeanChordLength << endl;

// calculate lineal energy deposition
for(int i=0;i<linecount-1;i++){
  LinLinealE[i]=Edep[i]/MeanChordLength;
}

double LinBinWidth=LinLinealE[1]-LinLinealE[0];

// Integral F(E)dE
double Integral_FY=0;
for(int i=0;i<linecount-1;i++){
  Integral_FY += LinBinWidth*Dist[i];
}

// yf(y) and Err yf(y)
for(int i=0;i<linecount-1;i++){
  Lin_yfy[i]=(Dist[i]/Integral_FY)*LinLinealE[i];
  LinErr_yfy[i]=(Error[i]/Integral_FY)*LinLinealE[i];
}

// yF = Integral yf(y)
double yF=0;
for(int i=0;i<linecount-1;i++){
  yF += LinBinWidth*Lin_yfy[i];
}

cout << "The frequency mean lineal energy yF is " << yF << endl;

// Integral y^2f(y)dy
double Integral_y2fy=0;
for(int i=0;i<linecount-1;i++){
  Integral_y2fy += LinBinWidth*Lin_yfy[i]*LinLinealE[i];
}

// yD = 1/yF Integral y^2f(y)dy
double yD=(1/yF)*Integral_y2fy;

cout << "The dose mean lineal energy yD is " << yD << endl << endl;

// calculation of d(y)=y/yF f(y)
double dy[MAXI];
double Err_dy[MAXI];
for(int i=0;i<linecount-1;i++){
  dy[i]=Lin_yfy[i]/yF;
  Err_dy[i]=LinErr_yfy[i]/yF;
}

double ydy[MAXI];
double Err_ydy[MAXI];
for(int i=0;i<linecount-1;i++){
  ydy[i]=(LinLinealE[i]*Lin_yfy[i])/yF;
  Err_ydy[i]=(LinLinealE[i]*LinErr_yfy[i])/yF;
}

// Normalise yd(y)
```

```
double Integral_Norm=0;
for(int i=0;i<linecount-1;i++){
  Integral_Norm+=ydy[i]*LinBinWidth;
}

cout << "Pre normalisation : " << Integral_Norm << endl;

for(int i=0;i<linecount-1;i++){
  Linydy[i]=ydy[i]/Integral_Norm;
  LinErrydy[i]=Err_ydy[i]/Integral_Norm;
}

//Post Normalisation check
Integral_Norm=0;
for(int i=0;i<linecount-1;i++){
  Integral_Norm+=Linydy[i]*LinBinWidth;
}

cout << "Post normalisation : " << Integral_Norm << endl;


/*****************************************************************************************/

double Miny=0.0;
int bpd=0;
int NumberDecades=0;

cout << "What is the minimum lineal energy (keV/um)? (default 0.1 keV/um)- ";
UserInput="";
getline(cin, UserInput);
if(UserInput=="") Miny=0.1;
else Miny=atof(UserInput.c_str());
cout << Miny << endl;

cout << "How many bins per decade? (default 20 bin per decade)- ";
UserInput="";
getline(cin, UserInput);
if(UserInput=="") bpd=20;
else bpd=atoi(UserInput.c_str());
cout << bpd << endl;

cout << "How many decades? (default 3 decades)- ";
UserInput="";
getline(cin, UserInput);
if(UserInput=="") NumberDecades=3;
else NumberDecades=atoi(UserInput.c_str());
cout << NumberDecades << endl;

cout << endl;

/*****************************************************************************************/

int LengthLogArray = NumberDecades*bpd+1;

double LogLinealE[LengthLogArray];
double Logydy[LengthLogArray];
double LogErrydy[LengthLogArray];
double DeltaLogX[LengthLogArray];
double LowLogLinealE[LengthLogArray];
double HighLogLinealE[LengthLogArray];
double count[LengthLogArray];
int FullBinCounter[LengthLogArray];

for(int i=0;i<LengthLogArray;i++){
  LogLinealE[i] = Miny*pow(10,(double)i/(double)bpd);
  Logydy[i] = 0;
  LogErrydy[i] = 0;
  DeltaLogX[i] = sqrt((Miny*pow(10,(double)i/(double)bpd))*
                      (Miny*pow(10,(double)(i+1)/(double)bpd)))-
```

```
                    sqrt((Miny*pow(10,(double)i/(double)bpd))*
                          (Miny*pow(10,(double)(i-1)/(double)bpd)));
    LowLogLinealE[i] = sqrt((Miny*pow(10,(double)i/(double)bpd))*
                            (Miny*pow(10,(double)(i-1)/(double)bpd)));
    HighLogLinealE[i] = sqrt((Miny*pow(10,(double)i/(double)bpd))*
                            (Miny*pow(10,(double)(i+1)/(double)bpd)));
    count[i] = 0;
  }

  double DeltaLinX=LinLinealE[1]-LinLinealE[0];
  double LinLowE[linecount-1];
  double LinHighE[linecount-1];

  for(int i=0;i<linecount-1;i++){
    LinLowE[i] = LinLinealE[i]-(DeltaLinX/2);
    LinHighE[i] = LinLinealE[i]+(DeltaLinX/2);
  }

  double IntegralPreNorm = 0;
  double IntegralPostNorm = 0;

  // In this section calcultate the fraction of bins that overlap and put that fraction into the
count instead of just incrementing it.
  for(int i=0;i<LengthLogArray;i++){
    for(int j=0;j<linecount-1;j++){
      if((LinLinealE[j]>LowLogLinealE[i])&&(LinLinealE[j]<HighLogLinealE[i])){
        Logydy[i]+=Linydy[j];
        LogErrydy[i]+=LinErrydy[j];
        count[i]++;
      }
    }
    IntegralPreNorm+=(HighLogLinealE[i]-LowLogLinealE[i])*Logydy[i];
  }

  double sum=0;

  for(int i=0;i<LengthLogArray;i++){
    if(count[i]>0){
      Logydy[i]=(Logydy[i]/((double)count[i]));// The factor of (log(10)/((double)bpd)); is not
required
      LogErrydy[i]=(LogErrydy[i]/(((double)count[i])));
      sum+=Logydy[i];
      IntegralPostNorm+=(HighLogLinealE[i]-LowLogLinealE[i])*Logydy[i];
    }
  }

  /*****************************************************************************************/

  cout << "Enter a filename to save data to or press enter to output to screen: ";
  UserInput="";
  getline(cin, UserInput);
  if(UserInput==""){
    cout
<<"count"<<setw(11)<<"LowE"<<setw(12)<<"MidE"<<setw(12)<<"HighE"<<setw(13)<<"yd(y)"<<setw(13)<<"Er
r yd(y)\n";

    for(int i=0;i<LengthLogArray;i++){
      cout
        << count[i] << setw(15)
        << LowLogLinealE[i] << setw(12)
        << LogLinealE[i] << setw(12)
        << HighLogLinealE[i] << setw(12)
        << Logydy[i] << setw(12)
        << LogErrydy[i] << endl;
    }
    cout << "\nPreNormInt: " << IntegralPreNorm << "\n\nPostNormInt: " << IntegralPostNorm <<
"\nsum: " << sum << endl << endl;
    cout << "The error in normalisation between linear and logarithmic binning is " << (1-
(Integral_Norm/IntegralPostNorm))*100 << " %" << endl;
```

```
    cout << endl;
    cout << "The frequency mean lineal energy yF is " << yF << " keV/um" << endl;
    cout << "The dose mean lineal energy yD is " << yD << " keV/um" << endl;
  }
  else{
    ofstream outfile;

    outfile.open(UserInput.c_str());
    if(outfile.is_open()){

      cout << "Writing output to " << UserInput << endl;

      outfile
<<"count"<<setw(11)<<"LowE"<<setw(12)<<"MidE"<<setw(12)<<"HighE"<<setw(13)<<"yd(y)"<<setw(13)<<"Er
r yd(y)\n";

      for(int i=0;i<LengthLogArray;i++){
         outfile
           << count[i] << setw(15)
           << LowLogLinealE[i] << setw(12)
           << LogLinealE[i] << setw(12)
           << HighLogLinealE[i] << setw(12)
           << Logydy[i] << setw(12)
           << LogErrydy[i] << endl;
      }
      outfile << "\nPreNormInt: " << IntegralPreNorm << "\n\nPostNormInt: " << IntegralPostNorm <<
"\nsum: " << sum << endl << endl;
      outfile << "The error in normalisation between linear and logarithmic binning is " << (1-
(Integral_Norm/IntegralPostNorm))*100 << " %" << endl;
      outfile << endl;
      outfile << "The frequency mean lineal energy yF is " << yF << " keV/um" << endl;
      outfile << "The dose mean lineal energy yD is " << yD << " keV/um" << endl;
    }
  }
}
```

A5.1 GEANT4 tracking of a single neutron inelastic interaction

```
*********************************************************************************************
* G4Track Information:   Particle = neutron,   Track ID = 230,   Parent ID = 50
*********************************************************************************************

Step#    X(mm)    Y(mm)    Z(mm) KinE(MeV)  dE(MeV) StepLeng TrackLeng  NextVolume ProcName
    0     64.9     1.17     14.7       256        0        0         0   Converter initStep
    1       81    -27.3     4.86         0  0.00021     34.2      34.2   Converter NeutronInelastic

*********************************************************************************************
* G4Track Information:   Particle = Fe56[0.0],   Track ID = 269,   Parent ID = 230
*********************************************************************************************

Step#    X(mm)    Y(mm)    Z(mm) KinE(MeV)  dE(MeV) StepLeng TrackLeng  NextVolume ProcName
    0       81    -27.3     4.86       1.3        0        0         0   Converter initStep
    1       81    -27.3     4.86         0      1.3  0.00115   0.00115   Converter ionIoni

*********************************************************************************************
* G4Track Information:   Particle = gamma,   Track ID = 268,   Parent ID = 230
*********************************************************************************************

Step#    X(mm)    Y(mm)    Z(mm) KinE(MeV)  dE(MeV) StepLeng TrackLeng  NextVolume ProcName
    0       81    -27.3     4.86      3.61        0        0         0   Converter initStep
    1     81.6    -34.7     4.71      3.61        0     7.38      7.38    Scoring1 Transportation
    2     81.6    -34.7     4.71      3.61        0   0.0102      7.39       World Transportation

*********************************************************************************************
* G4Track Information:   Particle = gamma,   Track ID = 267,   Parent ID = 230
*********************************************************************************************

Step#    X(mm)    Y(mm)    Z(mm) KinE(MeV)  dE(MeV) StepLeng TrackLeng  NextVolume ProcName
    0       81    -27.3     4.86      5.06        0        0         0   Converter initStep
    1     64.5      -35    -1.54      5.06        0     19.3      19.3    Scoring1 Transportation
    2     64.4      -35    -1.55      5.06        0   0.0244      19.3       World Transportation

*********************************************************************************************
* G4Track Information:   Particle = alpha,   Track ID = 266,   Parent ID = 230
*********************************************************************************************

Step#    X(mm)    Y(mm)    Z(mm) KinE(MeV)  dE(MeV) StepLeng TrackLeng  NextVolume ProcName
    0       81    -27.3     4.86      6.43        0        0         0   Converter initStep
    1       81    -27.3     4.86         0     6.43   0.0135    0.0135   Converter ionIoni

*********************************************************************************************
* G4Track Information:   Particle = proton,   Track ID = 265,   Parent ID = 230
*********************************************************************************************

Step#    X(mm)    Y(mm)    Z(mm) KinE(MeV)  dE(MeV) StepLeng TrackLeng  NextVolume ProcName
    0       81    -27.3     4.86      5.72        0        0         0   Converter initStep
    1     80.9    -27.3     4.89         0     5.72   0.0986    0.0986   Converter hIoni

*********************************************************************************************
* G4Track Information:   Particle = neutron,   Track ID = 264,   Parent ID = 230
*********************************************************************************************

Step#    X(mm)    Y(mm)    Z(mm) KinE(MeV)  dE(MeV) StepLeng TrackLeng  NextVolume ProcName
    0       81    -27.3     4.86      48.3        0        0         0   Converter initStep
    1     81.9      -35     1.27      48.3        0      8.5       8.5    Scoring1 Transportation
    2     81.9      -35     1.26      48.3        0   0.0113      8.52       World Transportation

*********************************************************************************************
* G4Track Information:   Particle = neutron,   Track ID = 263,   Parent ID = 230
*********************************************************************************************

Step#    X(mm)    Y(mm)    Z(mm) KinE(MeV)  dE(MeV) StepLeng TrackLeng  NextVolume ProcName
    0       81    -27.3     4.86      44.7        0        0         0   Converter initStep
    1     98.1    -31.2    -15.8      44.7        0     27.1      27.1    Scoring1 Transportation
    2     98.1    -31.2    -15.8      44.7        0   0.0212      27.2       World Transportation

*********************************************************************************************
* G4Track Information:   Particle = neutron,   Track ID = 262,   Parent ID = 230
*********************************************************************************************

Step#    X(mm)    Y(mm)    Z(mm) KinE(MeV)  dE(MeV) StepLeng TrackLeng  NextVolume ProcName
    0       81    -27.3     4.86       110        0        0         0   Converter initStep
    1     80.3    -29.8     5.28       110   0.0652     2.59      2.59   Converter hElastic
    2     80.3      -30     5.34         0        0    0.178      2.76   Converter NeutronInelastic
```

A 5.1 GEANT4 tracking of a single neutron inelastic interaction. This interaction produces particles that escape from the copper target, reach a stable state or undergo further interactions. The reaction for this listing is given in Equation 5.4.1

A5.2 The neutron particle spectra and conversion coefficient

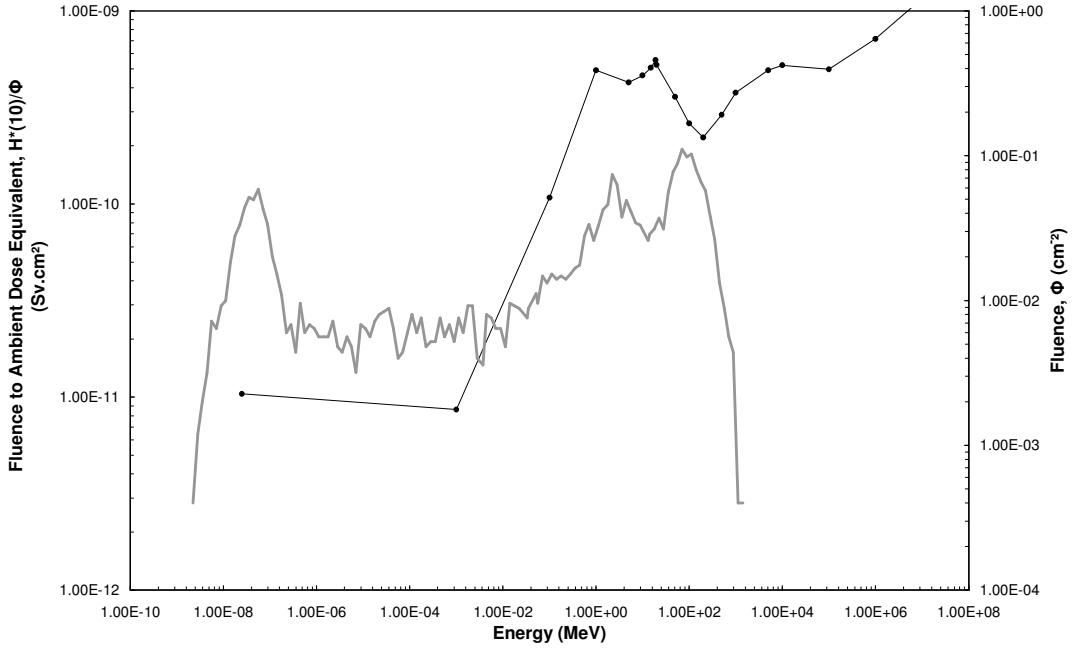

A 5.2 The neutron particle spectra from position CS1 with the associated fluence to ambient dose equivalent conversion coefficient reference points from (Pellicccioni, M. 2000).

A5.3 Published ambient dose equivalent conversion coefficients

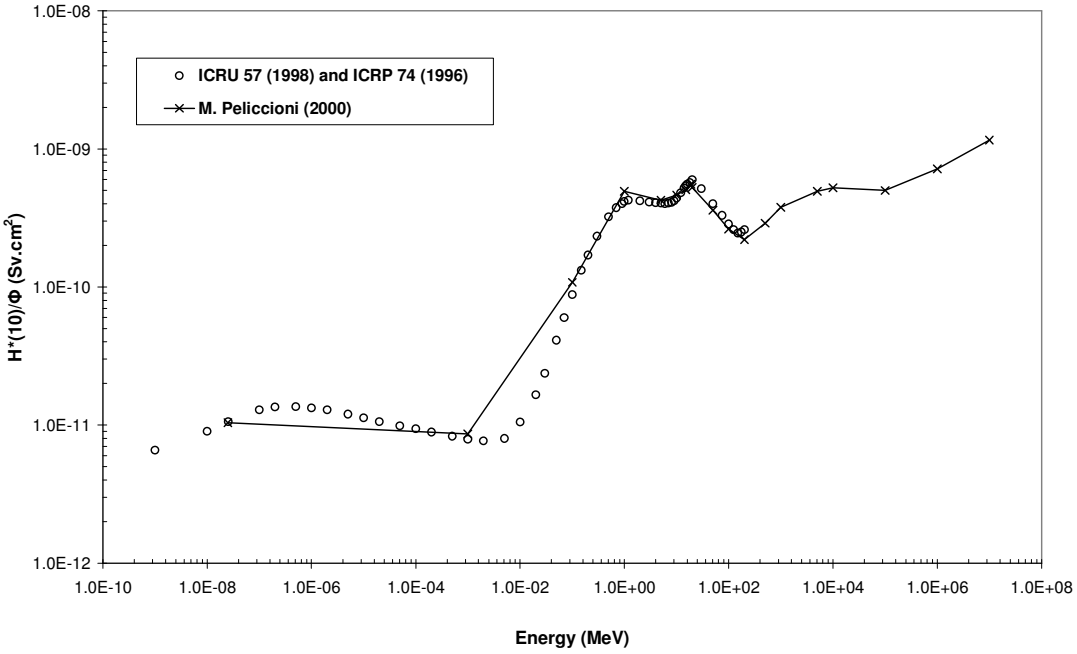

A 5.3 Published ambient dose equivalent conversion coefficients. The line drawn for the data from (Peliccioni, M., 2000) is for, as in the original publication, a guide to the eye only.

A8.1

Code to convert the listmode IBIC output into spectra, Median, Mode and Mean energy maps

```
#include <fstream>
#include <iostream>
#include <string>
#include <vector>

using namespace std;

int main(int argc, char* argv[])
{
  int num_args = argc-1; // Number of argumments following command
  if (num_args==0){
    cout << "This program only takes a single filename" << endl;
    exit(1);
  }
  // the following lines set the
  const int ResX = 512;//11;
  const int ResY = 512;//11;
  //const int Depth = 0; // set to 1000 for testing.
  const int NumChannels = 8192; // the ADC uses a maximum 8192 conversion gain

  for(int l=1;l<=num_args;l++){

    string inputfilename = argv[l];
    cout << "Input File: " << inputfilename << endl;
    int linecount = 0;
    int fileline = 0;

    // this creates an empty [3D] vector for the data
    vector< vector< vector< int> > > E;
    E.resize(ResX);
    for(int i=0;i<ResX;++i){
      E[i].resize(ResY);
      //for(int j=0;j<ResY;++j){
      //E[i][j].resize(Depth);
      //}
    }
    // This creates an array to store the spectra of the data
    int Spectrum[NumChannels] = {0};

    ifstream infile(argv[l]);
    if(infile.is_open()){
      while(!infile.eof()){
         string temp="";
         infile >> temp;

         int fileline = atoi(temp.c_str());
         if(fileline!=linecount){
           infile.close();
           break;
         }
         infile >> temp;
         int Ch = atoi(temp.c_str());
         infile >> temp;
         infile >> temp;
         int Y = atoi(temp.c_str());//+ResX/2;
         infile >> temp;
         int X = atoi(temp.c_str());//+ResY/2;
```

```
        ++linecount;

        if(X>=0 && X<=ResX && Y>=0 && Y<=ResY) {
          E[X][Y].push_back(Ch);
          Spectrum[Ch]++;
        }else{
          cout << "X: " << X << " or Y: " << Y << " is out of bounds" << endl;
        }
        /*
        cout << "Line: " << fileline << " X: " << X <<
          " Y: " << Y << " Ch: " << Ch <<
          " Size: " << E[X][Y].size() <<
          " Last: " << E[X][Y].back() <<
          endl;
        */
      }
    }else{
      cout << argv[1] << " is not a file" << endl;
    }
    /*************************************************************************/
    // sorting the data more efficiently by only sorting once if there is more than 1 event in the
pixel

    for(int i=0;i<ResX;++i){
      for(int j=0;j<ResY;++j){
        if(E[i][j].size()>1){
          std::sort(E[i][j].begin(),E[i][j].end());
        }
      }
    }

    /*************************************************************************/

    // this method displays the matrix with x on the horizontal and y in the vertical
    /*
    cout << endl;
    // this outputs the sorted list of events for each pixel
    for(int i=0;i<ResX;++i){
      for(int j=0;j<ResY;++j){
        int k;
        for(k=0;k<E[i][j].size();++k){
          //if(E[i][j].size()==0){
          //cout << "0";
          //}else{
          cout << E[i][j][k];
          //}
          if(k>0-1 && k<E[i][j].size()-1) cout << ",";
        }
        if(k<E[i][j].empty()) cout << "0";
        cout << " ";
      }
      cout << endl;
    }
    cout << endl;
    */
    /*************************************************************************/

    // this initialises the output file streams
    ofstream outfile;
    string outputfilename = "TestOutput.out";

    /*************************************************************************/

    // This outputs the spectrum of the file
```

```
outputfilename = inputfilename.substr(0,inputfilename.rfind("."))+".Spec";
cout << "Writing file: " << outputfilename << endl;
outfile.open(outputfilename.c_str());

for(int i=0;i<NumChannels;i++){
  outfile << i << " " << Spectrum[i] << endl;
}

outfile.close();
outfile.clear();
//cout << endl;

/*************************************************************************/


// this outputs the number of events in each pixel
outputfilename = inputfilename.substr(0,inputfilename.rfind("."))+".Stats";
cout << "Writing file: " << outputfilename << endl;
outfile.open(outputfilename.c_str());

for(int i=0;i<ResX;++i){
  for(int j=0;j<ResY;++j){
    //cout << E[i][j].size();
    outfile << E[i][j].size();
    //cout << " ";
    outfile << " ";
  }
  //cout << endl;
  outfile << endl;
}

outfile.close();
outfile.clear();
//cout << endl;

/*************************************************************************/

// Median charge collection map

outputfilename = inputfilename.substr(0,inputfilename.rfind("."))+".MedMap";
cout << "Writing file: " << outputfilename << endl;
outfile.open(outputfilename.c_str());

//i,j,k = 0;
for(int i=0;i<ResX;++i){
  for(int j=0;j<ResY;++j){
    if(E[i][j].size()==0){
      //cout << "0";
      outfile << "0";
    }else{
      //cout << E[i][j][E[i][j].size()/2];
      outfile << E[i][j][E[i][j].size()/2];
    }
    //cout << " ";
    outfile << " ";
  }
  //cout << endl;
  outfile << endl;
}

outfile.close();
outfile.clear();
// End of median map output
//cout << endl;
```

```
    /*************************************************************************/

    // Average Charge collection Map
    outputfilename = inputfilename.substr(0,inputfilename.rfind("."))+".MeanMap";
    cout << "Writing file: " << outputfilename << endl;
    outfile.open(outputfilename.c_str());

    for(int i=0;i<ResX;++i){
      for(int j=0;j<ResY;++j){
         int k;
         int sum=0;
         for(k=0;k<E[i][j].size();++k){

           sum+= E[i][j][k];

         }
         if(k<E[i][j].empty()){
           //cout << "0";
           outfile << "0";
         }else{
           //cout << sum/E[i][j].size();
           outfile << sum/E[i][j].size();
         }
         //cout << " ";
         outfile << " ";
      }
      //cout << endl;
      outfile << endl;
    }
    outfile.close();
  }
  return 0;
}
```